Ching-Hua Su

Vapor Crystal Growth and Characterization

ZnSe and Related II–VI Compound Semiconductors

Springer

Vapor Crystal Growth and Characterization

Ching-Hua Su

Vapor Crystal Growth and Characterization

ZnSe and Related II–VI Compound Semiconductors

Springer

Ching-Hua Su
Huntsville, AL, USA

ISBN 978-3-030-39654-1 ISBN 978-3-030-39655-8 (eBook)
https://doi.org/10.1007/978-3-030-39655-8

© Springer Nature Switzerland AG 2020
This work is subject to copyright. All rights are reserved by the Publisher, whether the whole or part of the material is concerned, specifically the rights of translation, reprinting, reuse of illustrations, recitation, broadcasting, reproduction on microfilms or in any other physical way, and transmission or information storage and retrieval, electronic adaptation, computer software, or by similar or dissimilar methodology now known or hereafter developed.
The use of general descriptive names, registered names, trademarks, service marks, etc. in this publication does not imply, even in the absence of a specific statement, that such names are exempt from the relevant protective laws and regulations and therefore free for general use.
The publisher, the authors and the editors are safe to assume that the advice and information in this book are believed to be true and accurate at the date of publication. Neither the publisher nor the authors or the editors give a warranty, expressed or implied, with respect to the material contained herein or for any errors or omissions that may have been made. The publisher remains neutral with regard to jurisdictional claims in published maps and institutional affiliations.

This Springer imprint is published by the registered company Springer Nature Switzerland AG
The registered company address is: Gewerbestrasse 11, 6330 Cham, Switzerland

For Wen-Jer Yu and Yuk Yin

Preface

With a simple processing setup, the crystal growth of physical vapor transport (PVT) transforms the original starting source material into the final form of crystal inside a closed ampoule. The vapor species are transported from the source at one end of the ampoule to form the crystal at the other end. The driving force for the transport is the pressure gradient between the source and the crystal ends created by an imposed temperature difference. Hence, the PVT process can be treated as three processes occurring in series:

(1) The corresponding vapor species sublime from the source material at higher temperature,
(2) The vapor species transport through the vapor phase to the crystal site at lower temperature, and
(3) The condensation of vapor species on the crystal surface for its growth.

Besides its simplicity, crystallization by PVT has several advantages over the conventional melt growth. These advantages result mostly from (1) the lower processing temperatures, (2) the purification process associated with PVT, and (3) the improved surface morphology of the grown crystals. The high melting temperatures of the wide bandgap materials make the melt growth process very difficult to handle. For instance, in the Si–C binary system, the SiC compound melts at 2830 °C into Si-rich liquid and C solid, i.e., there is not even a stoichiometric melt of SiC to conduct melt growth at this extremely hot environment. The PVT process enables crystal growth at unique and advantageous environments than the melt growth would allow. The PVT process also acts as a purification process because of the differences in the vapor pressures of the native elements and the impurities. Additionally, most solid–vapor interfaces exhibit higher interfacial morphological stability during growth because of their low atomic roughness.

On the other hand, the main disadvantage of vapor growth techniques, compared to other growth techniques, is that the growth rates are low and inconsistent and the grown crystals are small with variable single crystal yields. To achieve a reasonable growth rate, an intrinsic requirement for the PVT process of multielements compounds is that the partial pressure of each element needs to be comparable to each

other and at least above the level of 10^{-4} atm under the growth conditions. This requirement excludes the possible PVT growth of III–V compounds because the equilibrium partial pressures of group III are usually orders of magnitude lower than those of the group V elements. It also excludes the PVT growth of any II–VI compounds consisting of oxygen and mercury due to their high pressures.

In this book, the PVT process will be focused on ZnSe-based materials, such as ZnSe, Cr- and Fe-doped ZnSe and ZnSeTe, as well as other wide bandgap II–VI compounds, such as CdTe, CdS, and ZnTe. The contents of the book are intended for the professional crystal growers, either academic researchers or commercial operators, by providing the details of the operating procedures and the theoretical bases behind them. After a short Introduction, Chap. 2 will present the fundamentals of PVT process, including partial pressure measurements and one-dimensional diffusion model for the transport of vapor species. The experimental measurements of the vapor transport rate, i.e., mass flux, as well as the heat treatments of the starting materials to maximize the mass flux for various material systems will be discussed in Chap. 3. The detailed crystal growth procedures and in situ real-time optical monitoring techniques will be given in Chap. 4. Chapters 5 and 6 will present the results of various characterization techniques, including morphology of the grown crystals, structural crystalline quality, impurity distribution, dopant levels, and optical properties. The measured results of thermal and electrical properties and the effects of post-growth annealing will be included in Chap. 7. The formulation and calculated results from two-dimensional and three-dimensional numerical simulation on the vapor transport process of ZnSe will be presented in Chap. 8.

Huntsville, USA Ching-Hua Su

Acknowledgements

First of all, I would like to show my appreciation to my Ph.D. advisor, Prof. Robert F. Brebrick, who inspired and taught everything I know about compound semiconductors and was highly involved throughout the project. I am also indebted to my colleagues for their accomplishments to the project: Drs. A. Burger, M. Dudley, S. Feth, M. A. George, D. G. Gillies, S. L. Lehoczky, R. Matyi, K. Mazuruk, W. Palosz, N. Ramachandran, Yi-Gao Sha, F. R. Szofran, M. P. Volz, and Ling Jun Wang.

Contents

1 Introduction 1
1.1 Group II–VI Wide Bandgap Compound Semiconductors 1
1.2 Crystallization by Physical Vapor Transport 3
References 6

2 Fundamentals of Physical Vapor Transport Process 9
2.1 Sublimation of Source Materials 10
2.1.1 Vapor Pressures of Pure Elements 10
2.1.2 Thermodynamics of Solid and Vapor Phases in Compound Semiconductors 11
2.1.3 Partial Pressure Measurements 15
2.1.4 Thermodynamic Analyses 24
2.2 Physical Vapor Transport Process (One-Dimensional Diffusion Model) 26
2.2.1 Diffusive Transport in Binary Systems 26
2.2.2 Diffusive Transport in Multi-nary Systems 30
2.2.3 Diffusive Transport with Residual Gas of Impurities 31
2.2.4 Summary of One Dimensional Diffusion Analysis 33
2.2.5 Convective Transport 33
Appendix 35
References 37

3 Vapor Transport Rate (Mass Flux) Measurements and Heat Treatments 39
3.1 Mass Flux of CdS by PVT 40
3.1.1 CdS Ampoules Sealed Under Vacuum 40
3.1.2 CdS Ampoules Sealed with Ar Pressure 44
3.1.3 CdS Samples Annealed Under Controlled Cd Over-Pressure 46
3.1.4 Summary on PVT of CdS 47

3.2 Mass Flux and Heat Treatments of CdTe 48
3.2.1 Vapor Phase Stoichiometry 48
3.2.2 Heat Treatments of CdTe for PVT 49
3.3 Mass Flux and Heat Treatments for ZnSe System 53
3.3.1 In-Situ Dynamic Mass Flux Measurements 53
3.3.2 Heat Treatments of Source Materials 54
3.3.3 Measurements of Residual Gas Pressure and Composition 56
3.3.4 Simultaneous Measurements of Partial Pressure and Mass Flux in PVT of ZnSe 58
3.3.5 Optimum Heat Treatment Procedures for ZnSe Starting Materials 60
3.3.6 Summary of Heat Treatment of Starting Material of ZnSe 63
3.4 Mass Fluxes in ZnSe-Related Ternary Systems 64
3.4.1 One-Dimensional Diffusion Model for Ternary Case 64
3.4.2 Mass Flux of PVT for $ZnSe_{1-x}Te_x$ System 65
3.4.3 Mass Flux of PVT for $ZnSe_{1-x}S_x$ System 67
3.4.4 Mass Flux of $Zn_{1-x}Cd_xSe$ System from One-Dimensional Diffusion Model 71
3.4.5 Summary of Mass Flux of ZnSe-Related Ternary Systems 71
References 72

4 Crystal Growth 75
4.1 Growth Ampoule Preparations 75
4.2 Heat Treatments of Starting Materials 77
4.3 Crystal Growth Environments 79
4.3.1 Temperature Profile 79
4.3.2 Growth Configurations 80
4.3.3 Crystal Growth of ZnSe by PVT 82
4.3.4 Crystal Growth of ZnSe Doped with Transition Metals by PVT 84
4.3.5 Crystal Growth of ZnSeTe by PVT 86
4.3.6 Crystal Growth of CdTe by PVT 88
4.3.7 Crystal Growth of CdS by PVT 90
4.3.8 Crystal Growth of ZnTe by PVT 91
4.4 In-situ Real Time Optical Monitoring During Growth 91
4.4.1 Optical Absorption Measurements 92
4.4.2 Optical Interferometry Measurements 94
4.5 Recent Advancement on the Enhancement of Transport Rate by PVT 101
References 106

5 Residual Gas Measurements and Morphology Characterization on Grown Crystals 109
5.1 Residual Gas Measurements 110
5.2 Morphology of the Grown Crystals 112
5.2.1 Self-seeded Grown Crystals of ZnSe in Horizontal Configuration 112
5.2.2 Self-seeded Grown Crystals of ZnSe in Vertical Configuration 115
5.2.3 Seeded Grown Crystals of ZnSe 118
5.2.4 Analysis on Contactless Growth 118
5.2.5 Growth Kinetics 124
5.2.6 Growth Direction from X-ray Diffraction 126
5.2.7 Transition Metal Doped Crystals of ZnSe 127
5.2.8 Morphology of Grown Crystals of ZnSeTe 128
5.2.9 Morphology of Grown Crystals of CdTe 129
5.2.10 Morphology of Grown Crystals of CdS 132
5.2.11 Morphology of Grown Crystals of ZnTe 135
References 135

6 Characterizations on Crystalline Structures and Defect Distributions 137
6.1 Synchrotron White Beam X-ray Topography and High Resolution X-ray Diffraction Analysis 138
6.1.1 ZnTe Crystals Grown by Self-seeded Horizontal PVT . . . 138
6.1.2 ZnSe Crystals Grown by Self-seeded Horizontal PVT . . . 146
6.1.3 High Resolution Triple X-ray Diffraction (HRTXD) 148
6.1.4 ZnSe Crystals Grown by Self-seeded Vertical PVT 153
6.1.5 ZnSe Crystals Grown by Seeded PVT 153
6.2 Chemical Etching 157
6.2.1 Etching of ZnSe Crystals 158
6.2.2 Etching of CdTe Crystals 158
6.2.3 Etching of CdS Crystals 159
6.3 Cathodoluminescence (CL) 160
6.4 Characterization on Distributions of Impurities and Point Defects 161
6.4.1 Secondary Ion Mass Spectroscopy (SIMS) 161
6.4.2 Photoluminescence (PL) Spectroscopy 165
6.5 Impurity and Dopant Analyses on ZnSe Crystals by Glow Discharge Mass Spectroscopy (GDMS) 177
6.6 Dopant Levels in Cr-Doped ZnSe Crystals Measured by Optical Absorption 178

6.7 Characterizations of ZnSeTe Crystals . . . 179
6.7.1 Compositional Variation by Wavelength Dispersive X-ray Spectroscopy (WDS) . . . 179
6.7.2 Compositional Variation by Optical Transmission Measurements . . . 184
6.7.3 Axial Compositional Variation by Precision Density Measurements . . . 186
References . . . 187

7 Measurements on Thermal and Electrical Properties and Characterizations on Annealed Samples . . . 189
7.1 Thermal, Electrical Conductivity and Seebeck Coefficient of CdTe Grown by PVT . . . 189
7.1.1 Thermal Conductivity . . . 190
7.1.2 Electrical Conductivity . . . 191
7.1.3 Seebeck Coefficient . . . 193
7.2 Effects on Post-growth Annealing of CdS Crystals Grown by PVT . . . 194
References . . . 197

8 Two-Dimensional and Three-Dimensional Numerical Simulation of Vapor Transport Process . . . 199
8.1 The Problem Set Up . . . 200
8.2 Governing Equations . . . 200
8.3 Benchmark Simulations . . . 202
8.4 The Zn–Se System with a Residual Gas Component . . . 204
8.4.1 Two-Dimensional Calculation . . . 206
8.4.2 Three-Dimensional Calculations . . . 210
8.4.3 Limitations of Mathematical Modeling and Future Developments . . . 213
References . . . 215

Abbreviations

2-D	Two-dimensional
3-D	Three-dimensional
AFM	Atomic force microscopy
CL	Cathodoluminescence
CVD	Chemical vapor deposition
CVT	Chemical vapor transport
D	Diffusion coefficient
D/L	Diffusion limited
DAP	Donor-acceptor pair
EDS	Energy dispersive X-ray spectroscopy
FWHM	Full width at half maximum
g	Gram
GDMS	Glow discharge mass spectroscopy
h	Hour
HRTXD	High resolution triple axis X-ray diffraction analysis
I.D.	Inner diameter
LED	Light-emitting diodes
LWIR	Long wavelength infrared
MBE	Molecular beam epitaxy
min	Minute
MOCVD	Metal-organic chemical vapor deposition
MWIR	Mid-Wavelength Infrared
O.D.	Outer diameter
P_A	Partial pressure of A
P_{B_2}	Partial pressure of B_2
PL	Photoluminescence
PVT	Physical vapor transport
P_Z	Partial pressure of residual gases
QZR	Quadruple zone refined
R.T.	Room temperature

s	Second
SCVT	Seeded chemical vapor transport
SEM	Scanning electron microscopy
SIMS	Secondary ion mass spectroscopy
SPVT	Seeded PVT
SSMS	Spark source mass spectroscopy
SWBXT	Synchrotron white beam X-ray topography
T_C	Crystal temperature
T_d	Deposition temperature
T_H	Hot zone temperature
THM	Traveling heater method
T_{Hom}	Homogenization temperature CdTe
TM	Transition metals
T_{op}	Optical cell temperature
T_P	Central peak temperature
T_R	Reservoir temperature
T_S	Source temperature
T_{Sup}	Supersaturation temperature
WDS	Wavelength dispersive X-ray spectroscopy
wt.%	Weight %

Chapter 1
Introduction

Abstract Interest in optical devices which can operate in the visible spectrum has motivated research interest in the semiconductors of wide bandgap II–VI compounds, such as ZnSe, ZnS, ZnTe, CdS and CdSe and their solid solutions, which are expected to be the vital materials for high-performance optoelectronics devices such as light-emitting diodes (LEDs) and laser diodes operating in the blue spectrum and ultraviolet detectors. Compounds of the group II–VI elements, specifically, ZnS, ZnSe, ZnTe, CdS and CdSe, providing as matrix materials for doping with transition metal as activator ions, also promise wide coverage of the mid-IR spectrum for the development of solid-state lasers. In the bulk growth of some technologically important semiconductors, growth technique of physical vapor transport (PVT) have significant advantages over melt growth because of the high melting points of these materials. The continued improvement in overall device performance requires bulk crystals with less structural defects such as twins, lattice strain, dislocations, grain boundaries and second phase inclusions. The electrical and consequently the optical properties of the materials depend on the deviation from stoichiometry, the impurity or dopant distribution, and native point defects. The compositional homogeneity becomes extremely important for the ternary alloys because the non-uniformity in composition implies a response at different wavelengths across the crystal wafer. The realization of high performance devices is dependent on the routine production of high-quality, single-crystalline wafers which requires systematic investigations on the correlations between the process conditions of the PVT and various properties of grown crystal.

Keywords Physical vapor transport (PVT) · II–VI compound semiconductors · Zinc selenide (ZnSe) · Cadmium sulfide (CdS) · Zinc telluride (ZnTe) · Zinc selenide telluride ($ZnSe_{1-x}Te_x$)

1.1 Group II–VI Wide Bandgap Compound Semiconductors

Interest in optical devices which can operate in the visible spectrum has motivated research interest in the semiconductors of wide bandgap II–VI compounds which

© Springer Nature Switzerland AG 2020

C.-H. Su, *Vapor Crystal Growth and Characterization*,
https://doi.org/10.1007/978-3-030-39655-8_1

are expected to be the vital materials for high-performance optoelectronics devices such as light-emitting diodes (LEDs) [1–3] and laser diodes [4–10] operating in the blue spectrum and ultraviolet detectors [11]. Additionally, the high ionicity of these compounds makes them good candidates for high electro-optical and electro-mechanical coupling. With an energy gap of 2.69 eV at room temperature and an efficient direct band-to-band transition, ZnSe has been studied extensively [12–16] in the applications for blue LEDs and lasers for optical displays, high density recording, and military communications. By employing a ternary [17, 18] or quaternary [19] system, the energy band gap of II–VI materials can be tuned to a specific range. ZnSe bulk crystals [20, 21] and ZnSe-based structures such as ZnSe/ZnSeS [22, 23], ZnSe/ZnCdSe [24–26] and ZnCdSe/ZnSeS [27] have showed photopumped lasing capability in the blue-green region at a low threshold power and high temperatures. The demonstration of its optical bistable properties in bulk and thin film forms [28, 29] also make ZnSe a possible candidate material for the building blocks of a digital optical computer. ZnSe has also been grown on GaAs substrates with alternating orientations for the applications of second harmonic generation and optical parametric oscillation devices [30]. Despite these research efforts, developments in the crystal growth of bulk II–VI semiconductor materials has not advanced far enough to provide the needed bulk and thin film growth technologies [31].

In general, the wide bandgap materials of the group II–VI class, such as ZnSe, ZnS, ZnTe, CdS, CdSe and their solid solutions have been studied in thin film, bulk crystal and coatings and have had a significant impact on modern technologies. High-quality bulk crystals have been grown by physical vapor transport (PVT) method [32–39] for a variety of applications. There has been a continuous effort to develop high power lasers operating in mid-wavelength infrared (MWIR) using these materials specifically for applications in infrared counter measures, surveillance, medicine and environmental monitoring. The technologies require the development of suitable optical quality crystalline samples. The two major approaches toward developing optical quality crystals have utilized bulk single crystals and thick film based quasi phase materials (QPM). For both bulk crystal and QPM approaches, ZnSe has been an exciting material since it covers the spectral regions of the near IR extending to the long wavelength infrared (LWIR) region and can utilize high power 1.06 μm and 9.6 μm lasers for frequency conversion. Another approach that has been developed is to dope this class of materials with transition metals (TM) to generate emission in the infrared region [40–42]. Specific dopants have been used to study growth, fluorescence quenching mechanisms, and materials performance. There are numerous studies on the site occupancies and electronic energy levels of specific TM dopants such as iron (Fe), chromium (Cr), cobalt (Co), nickel (Ni), copper (Cu), vanadium (V), and manganese (Mn) in II-VI and other host material systems. When a II-VI crystal such as ZnSe, which has an unfilled d-shell, is doped with a transition metal, the 3d and 4p orbitals can be mixed at noncentro-symmetric sites. As a result, transitions among the d levels occur and the MWIR radiation appears due to these new electronic transitions. The TM ions (tetrahedral coordinated) give almost half crystal field splitting due to octahedral coordination at the dopant sites and the resulting TM

dopant transitions occur in the infrared region. The absorption and emission properties of these dopants in chalcogenides suggest they are most likely to luminance in the 2–5 μm region. Compounds of the class II–VI elements, specifically, ZnS, ZnSe, ZnTe, CdS and CdSe, have been suggested as good matrix materials for doping. The selection of transition metal ions as activator ions, each having different transition-energy ranges, promises wide coverage of the mid-IR spectrum for the development of solid-state lasers. However, most of the reports on the doping of these compounds were conducted by solid-state diffusion of dopants into the polycrystalline materials [43] which inevitably creates a dopant compositional distribution. The PVT crystals grown from a source material mixing with dopant will provide high crystalline quality compounds with uniform dopant distribution.

The electrical and optical properties of semiconductor materials depend on the native point defects (deviation from stoichiometry) and the impurity (or dopant) distribution. To date, the bulk growth of ZnSe has been plagued with problems related to defects such as non-uniform distributions of native defects, impurities and dopants, lattice strain, dislocations, grain boundaries, and twins which greatly affect the device performance. Compositional non-homogeneity is also important in ternary alloys because the non-uniformity in the composition causes optical responses at different wavelengths across the crystal wafer. In the bulk growth of some technologically important semiconductors, such as ZnTe, CdS, ZnSe and ZnS, vapor growth techniques have significant advantages over melt growth because of the high melting points of these materials. The realization of routine production of high-quality single crystals of these semiconductors requires a fundamental, systematic, and in-depth study on the crystal growth process.

1.2 Crystallization by Physical Vapor Transport

Crystallization from physical vapor transport (PVT) has several intrinsic advantages over the conventional melt growth. These advantages result mostly from (1) the lower processing temperatures, (2) the purification process associated with PVT and (3) the improved surface morphology of the grown crystals. The high melting temperatures of the wide band gap materials make the melt growth process very difficult to handle. The PVT process enables crystal growth at significantly lower temperatures than melt growth would allow. Table 1.1 summarizes the semiconductor compounds grown by PVT, the energy bandgap, the melting points of the compound, and the temperature

Table 1.1 List of II-VI semiconducting compounds grown by PVT

Compounds	CdTe	ZnTe	CdS	ZnSe	ZnS
Energy Bandgap at 300 K (eV)	1.46 [49]	2.28 [50]	2.36 [51]	2.69 [52]	3.69 [52]
Melting points (°C)	1092	1295 [53]	1405 [54]	1526 [54]	1718 [54]
PVT growth temperature (°C)	850	1000	985	1120	1150

used for the successful PVT crystal growth in our laboratory. The PVT process also acts as a purification process [44] because of the differences in the vapor pressures of the native elements and the impurities. Additionally, most solid-vapor interfaces exhibit higher interfacial morphological stability [45–47] during growth because of their low atomic roughness [48]. An earlier book [35], which reported the crystal growth from the vapor phase, has provided some information on PVT. Recently, reviews and general comparisons of growth methods for the seeded PVT (SPVT) growth of ZnSe crystal and seeded chemical vapor transport (SCVT) were given in Ref. [36, 37]. Under optimized growth conditions, in contrast to the growth from the melt, twin-free single crystals without morphological instability could be grown by SPVT and SCVT.

The main disadvantage of vapor growth techniques compared to other growth techniques is that the growth rates are low and inconsistent and the grown crystals are small with a variable single crystal yield [14]. To achieve a reasonable growth rate, an intrinsic requirement for the PVT process of multi-elements compounds is that the partial pressure of each element needs to be comparable to each other and at least above a level of 10^{-4} atm at the growth conditions. This requirement excludes the possible PVT growth of III–V compounds because the equilibrium partial pressures of group III are usually orders of magnitude lower than those of the group V elements. It also excludes the PVT growth of any II–VI compounds consisting of oxygen and mercury due to their extremely high pressures. While a seeded growth technique can be adopted to improve the yield of single crystals, the transport process needs to be studied carefully in order to increase the growth rates.

To increase the transport rate and consequently reduce the growth temperature the introduction of a transport agent, such as I_2, was employed for the vapor growth of CdS [55], ZnSe [56–63], ZnTe [62], ZnS [62–64] and ZnSeS [56, 63]. The disadvantage of this chemical vapor transport (CVT) is that the grown crystals are usually contaminated by the transport agent. This causes difficulties in the control of the electrical properties of the crystals because of the unintentionally doped by the transport agent [56, 59, 63]. On the other hand, different variations of the PVT technique have been applied. These variations include the growth in semi-open system originally developed by Piper and Polich [65–67], the stationary seeded growth in a closed system for CdS [68], CdS and CdSe [69], and ZnSe [70], the translational self-seeded growth in a closed system for CdS [32, 71], ZnTe [33, 72], ZnSe [73–78] as well as seeded growth for CdTe [76] and the growth of CdS [79–81], ZnSe [36, 82–84], ZnSeS [36, 84, 85] and CdSeS [86] under the controlled partial pressure of one (or two) of the constituent elements in a closed ampoule.

It was believed that a slow but practical transport rate improves the morphological and crystalline quality of the grown crystals [70] and, therefore, in some cases inert gas was intentionally introduced into the system [87]. The thermally induced strain and defects caused by the crucible wall were eliminated in the seeded contactless growth of CdS and CdSe reported in Ref. [68, 69] and in a novel self-seeded contactless growth of CdTe [88]. The growth of doped-ZnTe by introducing a small amount of In into the growth system was also reported [89].

It has also been reported that the growth kinetics varies on different seed orientations. The growth rate on ZnSe (111)B Se face was reported to be two and half times faster than that on the (111)A Zn face [56] and this may cause twinning of the grown crystal in order to preserve the overall axial growth direction [82]. It was argued by Yoshioka et al. [90] that an off-oriented substrate can provide surface with steps which promotes step-growth mechanism and results in twin-free crystals whereas two-dimensional nucleation growth on (111) surface results in nucleation in two opposite direction because of the freedom in rotation and, consequently, produces in twinned crystals. The report [90] showed experimentally that twin-free CdTe crystals were produced when CdTe (211) seed was adopted whereas the CdTe (111) seeds always resulted in twinned crystals.

In the studies described above the effects of gravity on the grown crystals were neither examined nor reported. Several vapor crystal growth experiments have been conducted under low-gravity conditions by investigators from the U.S. [91–94], Europe [95], and the USSR [96]. Wiedemeier et al. [93, 94] have obtained significant improvements in size and morphology of their space-grown GeSe, GeTe, and GeS crystals as compared to Earth-grown samples. The improvements in surface morphology, compositional uniformity, and structural micro-homogeneity in the epitaxial CVT growth of HgCdTe were also demonstrated. Van den Berg et al. [94] grew HgI_2 crystals in space that were superior in structural quality, measured by gamma ray rocking curves, to ground-grown samples and showed mobility twice higher than ground-growth samples for both holes and electrons. Siffert et al. [95] found a remarkable decrease in the dislocation etch pit density in the space-grown CdTe crystal. All low-gravity vapor growth experiments conducted to date have been carried out in closed ampoules, i.e., all constituents of the system are loaded and sealed inside a (silica) tube at room temperature and then brought to processing conditions by various heating arrangements. The main external control consists of imposing a specific temperature distribution and its translation rate that may vary with time.

The continued improvement in overall device performance requires bulk crystals with less structural defects such as twins, lattice strain, dislocations, grain boundaries and second phase inclusions. The electrical and consequently the optical properties of the materials depend on the deviation from stoichiometry, the impurity or dopant distribution, and native point defects. The compositional homogeneity becomes extremely important for the ternary alloys because the non-uniformity in composition implies a response at different wavelengths across the crystal wafer. The realization of high performance devices is dependent on the routine production of high-quality, single-crystalline wafers which requires systematic investigations on the correlations between the process conditions and the growth and properties of grown crystal.

Following Introduction, Chap. 2 will present the fundamentals of PVT process, including partial pressure measurements and one-dimensional diffusion model for the transport of vapor species. The experimental measurements of the vapor transport rate, i.e., mass flux, as well as the heat treatments of the starting materials to maximize the mass flux for various material systems will be discussed in Chap. 3. The detailed

crystal growth procedures and in situ real time optical monitoring techniques will be given in Chap. 4. Chapters 5 and 6 will present the results of various characterization techniques, including morphology of the grown crystals, structural crystalline quality, impurity distribution, dopant levels and optical properties. The measured results of thermal and electrical properties and the effects of post-growth annealing will be included in Chap. 7. Lastly, the formulation and calculated results from two-dimensional and three-dimensional numerical simulations of vapor transport process will be presented in Chap. 8.

References

1. H. Morkoc, S. Strite, G.B. Gao, M.E. Lin, B. Sverdlov, M. Burns, J. Appl. Phys. **76**, 1363 (1994)
2. A.N. Krasnov, Y. Purtov, Y. Vaksman, V.V. Sverdyuk, J. Crystal Growth **125**, 373 (1992)
3. H. Kukimoto, Semicond. Sci. Technol. **6**, A14 (1991)
4. X.H. Yang, J.M. Hays, W. Shan, J.J. Song, E. Cantwell, Appl. Phys. Lett. **62**, 1072 (1993)
5. H. Jeon, J. Ding, A.V. Nurmikko, W. Xie, D.C. Grillo, M. Kobayashi, R.L. Gunshor, G.C. Hua, N. Otsuka, Appl. Phys. Lett. **60**, 2045 (1992)
6. K. Nakanishi, I. Suemune, Y. Fujii, Y. Kuroda, M. Yamanishi, Appl. Phys. Lett. **59**, 1401 (1991)
7. G.F. Neumark, R.M. Park, J.M. Depuydt, Phys. Today **47**, 26 (1994)
8. V. Daneu, D.P. DeGloria, A. Sanchez, F. Tong, R.M. Osgood Jr., Appl. Phys. Lett. **49**, 546 (1986)
9. L.H. Kuo, L. Salamanca-Riba, B.J. Wu, G.M. Haugen, J.M. Depuydt, G. Hofler, H. Cheng, J. Vac. Sci. Technol. **B13**, 1694 (1995)
10. M. Hovinen, J. Ding, A. Salokatve, A.V. Nurmikko, C. Hua, D.C. Grillo, L. He, J. Han, M. Ringle, R.L. Gunshor, J. Appl. Phys. **77**, 4150 (1995)
11. J.A.B. Howie, G.K. Rowles, P. Hawkins, Meas. Sci. Technol. **2**, 1070 (1991)
12. M.E. Ozsan, J. Woods, J. Phys. **D10**, 1335 (1977)
13. W. Stutius, Appl. Phys. Lett. **33**, 657 (1978)
14. J. Nishizawa, K. Itoh, Y. Okuno, F. Sakurai, J. Appl. Phys. **57**, 2210 (1985)
15. X.W. Fan, Z.K. Tang, H. Tian, J. Crystal Growth **101**, 944 (1990)
16. H. Kukimoto, J. Crystal Growth **101**, 953 (1990)
17. X.H. Yang, J. Hays, W. Shane, J.J. Song, E. Cantewell, J. Aldridge, Appl. Phys. Lett. **60**, 926 (1992)
18. H. Jeon, J. Ding, W. Patterson, A.V. Nurmikko, W. Xie, D.C. Grillo, M. Kobayashi, R.L. Gunshor, Appl. Phys. Lett. **59**, 3619 (1991)
19. K. Ichino, Y.-H. Wu, Y. Kawakami, S. Fujita, S. Fujita, J. Crystal Growth **117**, 527 (1992)
20. I.M. Catalano, A. Cingolani, M. Ferrara, M. Lugara, Solid State Commun. **43**, 371 (1982)
21. X.H. Yang, J. Hays, W. Shan, J.J. Song, E. Cantwell, J. Aldridge, Appl. Phys. Lett. **59**, 1681 (1991)
22. I. Suemune, K. Yamada, H. Masato, Y. Kan, M. Yamanishi, Appl. Phys. Lett. **54**, 981 (1989)
23. K. Nakanishi, I. Suemune, H. Masato, Y. Kuroda, M. Yamanishi, Jap. J. Appl. Phys. **29**, L2420 (1990)
24. H. Jeon, J. Ding, A.V. Nurmikko, H. Luo, N. Samarth, J.K. Furdyna, W.A. Bonner, R.E. Nahory, Appl. Phys. Lett. **57**, 2413 (1990)
25. J. Ding, H. Jeon, A.V. Nurmikko, H. Luo, N. Samarth, J.K. Furdyna, Appl. Phys. Lett. **57**, 2756 (1990)
26. H. Jeon, J. Ding, A.V. Nurmikko, H. Luo, N. Samarth, J. Furdyna, Appl. Phys. Lett. **59**, 1293 (1991)

27. Y. Kawakami, S. Yamaguchi, Y.-H. Wu, K. Ichino, S. Fujita, S. Fujita, Jap. J. Appl. Phys. **30**, L605 (1991)
28. V.A. Stadnik, Optics Commun. **68**, 445 (1988)
29. J. Eichler, V. Glaw, A. Kummrow, V. Penschke, A. Wahi, J. Crystal Growth **101**, 695 (1990)
30. N.B. Singh, G.S. Kanner, A. Berghmans, D. Kahler, A. Lin, B. Wagner, S.P. Kelley, D.J. Knuteson, R. Holmstrom, K.L. Schepler, R. Peterson, M.M. Fejer, J.S. Harris, J. Crystal Growth **312**, 1142 (2010)
31. R. Triboulet, Semicon. Sci. Technol. **6**, A18 (1991)
32. C.-H. Su, S.L. Lehoczky, F.R. Szofran, J. Crystal Growth **101**, 221 (1990)
33. C.-H. Su, M.P. Volz, D.C. Gillies, F.R. Szofran, S.L. Lehoczky, M. Dudley, G.-D. Yao, W. Zhou, J. Crystal Growth **128**, 627 (1993)
34. K. Chattopadhyay, S. Feth, H. Chen, A. Burger, C.-H. Su, J. Crystal growth **191**, 377 (1998)
35. M.M. Faktor, I. Garrett, *Growth of Crystals from the Vapour* (Chapman and Hall, London, 1974)
36. D. Siche, H. Hartmann, K. Bottcher, E. Krause, Phys. Status Solidi B **194**, 101 (1996)
37. H. Hartmann, D. Siche, J. Crystal Growth **138**, 260 (1994)
38. C.-H. Su, M.A. George, W. Palosz, S. Feth, S.L. Lehoczky, J. Crystal Growth **213**, 267 (2000)
39. C.-H. Su, Y.-G. Sha, M.P. Volz, P. Carpenter, S.L. Lehoczky, J. Crystal Growth **216**, 104 (2000)
40. S.B. Mirov, V.V. Fedorov, D. Martyshkin, I.S. Moskalev, M. Mirov, S. Vasilyev, IEEE J. Select Topics Quantum Electron. **21**, 1601719 (2015)
41. A.E. Dormidonov, K.N. Firsov, E.M. Gavrishchuk, V.B. Ikonnikov, SYu. Kazantsev, I.G. Kononov, T.V. Kotereva, D.V. Savin, N.A. Timofeeva, Appl. Phys. B **122**, 211 (2016)
42. N.B. Singh, C.-H. Su, B. Arnold, F.-S. Choa, B. Cullum, Stacey Sova, and Christopher Cooper, Crystal Res. Tech. 180023 (2019)
43. A. Burger, K. Chattopadhyay, J.-O. Ndap, X. Ma, S.H. Morgan, C.I. Rablau, C.-H. Su, S. Feth, Ralph H. Page, Kathleen I. Schaffers, S.A. Payne, J. Crystal Growth **225** 249 (2001)
44. R. Lauck, G. Muller-Vogt, W. Wendl, J. Crystal Growth **74**, 520 (1986)
45. A.A. Chernov, J. Crystal Growth **24**(25), 11 (1974)
46. F. Rosenberger, M.C. Delong, D.W. Greenwell, J.M. Olson, G.H. Westphal, J. Crystal Growth **29**, 49 (1975)
47. R.-F. Xiao, J.I. Alexander, F. Rosenberger, J. Crystal Growth **100**, 313 (1990)
48. J.-S. Chen, N.-B. Ming, F. Rosenberger, J. Chem. Phys. **84**, 2365 (1986)
49. S.M. Johnson, S. Sen, W.H. Konkel, M.H. Kalisher, J. Vac. Sci. Technol. **B9**, 1987 (1991)
50. K. Sato, S. Adachi, J. Appl. Phys. **73**, 926 (1993)
51. H. Tai, S. Nakajima, S. Hori, J. Japan. Inst. Metals **40**, 474 (1967)
52. A. Ebina, E. Fukunaga, T. Takahashi, Phys. Rev. B **10**, 2495 (1974)
53. J. Carides, A.G. Fischer, Solid State Commun. **2**, 217 (1964)
54. L.A. Sysoev, E.K. Raiskin, V.R. Gur'ev, Inorg. Mater. **3,** 341 (1967)
55. E. Kaldis, J. Crystal Growth **5**, 376 (1969)
56. A. Catano, Z.K. Kun, J. Crystal Growth **33**, 324 (1976)
57. E. Kaldis, J. Phys. Chem. Solids **26**, 1701 (1965)
58. S. Parker, J. Crystal Growth **9**, 177 (1971)
59. T. Koyama, T. Yodo, H. Oka, K. Yamashita, T. Yamasaki, J. Crystal Growth **91**, 639 (1988)
60. K. Recker, R. Schoepe, J. Crystal Growth **9**, 189 (1971)
61. S.G. Parker, J.E. Pinnell, Trans. Meta. Soc. AIME **245**, 451 (1969)
62. H. Hartmann, J. Crystal Growth **42**, 144 (1977)
63. S. Fujita, H. Mimoto, H. Takebe, T. Noguchi, J. Crystal Growth **47**, 326 (1979)
64. T. Ohno, K. Kurisu, T. Taguchi, J. Crystal Growth **99**, 737 (1990)
65. W. Piper, S.J. Polich, J. Appl. Phys. **32**, 1278 (1961)
66. G.J. Russell, J. Woods, J. Crystal Growth **47**, 647 (1979)
67. J. Morimoto, T. Ito, T. Yoshioka, T. Miyakawa, J. Crystal Growth **57**, 362 (1982)
68. E.V. Markov, A.A. Davydov, Neorg. Mater. **7**, 575 (1971)
69. A.A. Davydov, V.N. Ermolov, S.V. Neustroev, L.P. Pavlova, Neorg. Mater. **28**, 42 (1992)

70. G. Cantwell, W.C. Harsch, H.L. Cotal, B.G. Markey, S.W.S. McKeever, J.E. Thomas, J. Appl. Phys. **71**, 2931 (1992)
71. N. Hemmat, M. Weinstein, J. Electrochem. Soc. **114**, 851 (1967)
72. T. Taguchi, S. Fujita, T. Inuishi, J. Crystal Growth **45**, 204 (1978)
73. E. Anderson, H.-Y. Cheng, M.J. Edgell, Mater. Res. Soc. Symp. Proc. **152**, 51 (1989)
74. H.-Y. Cheng, E. Anderson, J. Crystal Growth **96**, 756 (1989)
75. F. Allegretti, A. Carrara, S. Pizzini, J. Crystal Growth **128**, 646 (1993)
76. C.-H. Su, Y.-G. Sha, K. Mazuruk, S.L. Lehoczky, H.-C. Liu, R. Fang, R.F. Brebrick, J. Crystal Growth, 736 (1996)
77. C.-H. Su, Y.-G. Sha, M.P. Volz, D.C. Gillies, F.R. Szofran, S.L. Lehoczky, W. Zhou, M. Dudley, H.-C. Liu, R.F. Brebrick, J.C. Wang, Proc. AIAA 32nd Aerospace Sciences Meeting, paper 94–0564 (1994)
78. S. Ching-Hua, Y.-G. Sha, Curr. Topics Crystal Growth Res. **2**, 401 (1995)
79. L. Clark, J. Woods, J. Crystal Growth **3**(4), 126 (1968)
80. G.J. Russell, N.F. Thompson, J. Woods, J. Crystal Growth **71**, 621 (1985)
81. P.D. Fochs, W. George, P.D. Augustus, J. Crystal Growth **3**(4), 122 (1968)
82. K.F. Burr, J. Woods, J. Crystal Growth **9**, 183 (1971)
83. J.R. Cutter, J. Woods, J. Crystal Growth **47**, 405 (1979)
84. J.R. Cutter, G.J. Russell, J. Woods, J. Crystal Growth **32**, 179 (1976)
85. K. Mochizuki, J. Crystal Growth **58**, 87 (1982)
86. K. Mochizuki, K. Igaki, J. Crystal Growth **45**, 218 (1978)
87. Y. Morimoto, I. Igarashi, H. Sugahara, S. Nasu, J. Non-Cryst, Solids **139**, 35 (1992)
88. K. Grasza, U. Zuzga-Grasza, A. Jedrzejczak, R.R. Galazka, J. Majewski, A. Szadkowski, E. Grodzicka, J. Crystal Growth **123**, 519 (1992)
89. A.S. Jordan, L. Derick, J. Electrochem. Soc. **116**, 1424 (1969)
90. T. Yoshioka, J. Crystal Growth **115**, 705 (1191)
91. H. Wiedemeier, F.C. Klaessig, E.A. Irene, S.J. Wey, J. Crystal Growth **31**, 36 (1975)
92. H. Wiedemeier, H. Sadeek, F.C. Klaessig, M. Norek, R. Santandrea, J. Electrochem. Soc. **124**, 1095 (1977)
93. H. Wiedemeier, NASA Conf. Publ. **3272**, 263 (1993)
94. L. van den Berg, W.F. Schnepple, Nucl. Inst. Meth. Phys. Res. **A283**, 335 (1989)
95. P. Siffert, B. Biglari, M. Samimi, M. Hage-Ali, J.M. Koebel, R. Nitsche, M. Bruder, R. Dian, R. Schdnholz, Nucl. Inst. Meth. Phys. Res. **A283**, 363 (1989)
96. Manufacturing in Space: Processing Problems and Advances, V. S. Avduyevsky Editor, MIR Publishers, Moscow (1985)

Chapter 2
Fundamentals of Physical Vapor Transport Process

Abstract The crystal growth of physical vapor transport (PVT) transforms the original source material powder into the final form of compound semiconducting crystal in a closed ampoule. The vapor species were transported from the source at one end of the ampoule to the crystal at the other end because of the applied temperature gradient between the source and the crystal. To understand the fundamentals of PVT, one of the most important parameters during PVT, the partial pressures of the vapor species in equilibrium with the compounds as a function of temperature with different stoichiometry, have been measured by optical absorption technique to establish the three-phase curve. Then using an associated solution model for the liquid phase, which is assumed to consist of certain atomic/molecular species, the Gibbs energy of mixing for the liquid can be expressed in terms of the interaction parameters between these species. After the establishment of the best-fit parameters, the complete phase diagram and thermodynamic properties of the system can be generated for the applications of crystal growth experiments. The thermodynamic analysis has been applied to binary, ternary and quaternary systems such as Hg–Te, Cd–Te and Hg–Cd–Te as well as In–Sb, Ga–Sb and In–Ga–Sb, Hg–Cd–Zn–Te, Zn–Se and Zn–Se–Te. Then, a one-dimensional diffusion model, which includes the vapor species in equilibrium with a binary compound and the residual inert gases, was established to identify the critical growth parameters such as the heat treatment conditions, the thermal field for the growth process, the composition of the grown (ternary) crystal as well as the growth rate. From the results of the one-dimensional diffusion analysis, four experimentally adjustable parameters: the source temperature, the deposition temperature, the partial pressure ratio over the source and the residual gas pressure, determine the diffusive mass flux in a PVT system. However, two of these four parameters, the partial pressure ratio over source and the residual gas pressure, are more critical than the others.

Keywords Partial pressure · Three-phase curve · Associated solution model · One-dimensional diffusion model

The crystal growth of physical vapor transport (PVT) transforms the original source material chunk/powder into the final form of compound semiconducting crystal in a closed ampoule. The vapor species were transported from the source at one end of the

© Springer Nature Switzerland AG 2020

C.-H. Su, *Vapor Crystal Growth and Characterization*,
https://doi.org/10.1007/978-3-030-39655-8_2

ampoule to the crystal at the other end because of the applied temperature gradient between the source and the crystal. This PVT process consists of three steps:

(1) The corresponding vapor species sublime from the source material at higher temperature,
(2) The vapor species transport through the vapor phase to the crystal site at lower temperature,
(3) The condensation of vapor species on the crystal surface for its growth.

Crystal growth by PVT can be treated as these three processes occurring in series. Thus, it is the slowest of the processes that limits the growth rate. In this chapter, the fundamental physics and thermodynamics of these steps will be discussed in detail.

2.1 Sublimation of Source Materials

2.1.1 Vapor Pressures of Pure Elements

In a closed system, i.e. no exchange of matter with the surroundings, the vapor species sublime from the condensed materials (usually solid), at temperatures above absolute zero, and reach the corresponding equilibrium vapor pressures when the species sublime and condense at the same rate. The magnitude of the pressure depends on the temperature and physical nature of the corresponding element. The mechanism of vapor transport process in II–VI semiconductors is different from those of the IV–VI and II–VII_2 compounds. In the systems of IV–VI semiconductors under metal (Group IV) saturation conditions, the predominant vapor species are the congruent subliming molecular species such as PbTe [1–3], SnTe [3–5] and GeTe [3].

In the case of the II–VI compounds and the temperature range of PVT process, the vapor species sublime from solid material are the atomic Group II elements, such as Zn and Cd, and the diatomic Group VI elements, i.e. S_2, Se_2, Te_2 [6–12]. There are various thermodynamically possible chalcogen vapor species in equilibrium with the condensed phase. However, as shown in Fig. 2.1, from the plots of the partial pressures of the various species as functions of total pressures, it is evident that the chalcogen vapor is dominated by dimmers, or the diatomic molecules. The other thermodynamically possible chalcogen species have partial pressures at least two orders of magnitude lower than the favorable growth conditions, i.e., $P_{total} > 10^{-4}$ atm. The partial pressures of the species II and VI_2 in equilibrium with the II–VI semiconducting compounds, at a fixed temperature, can vary by orders of magnitude as the composition of the compound varies over the narrow homogeneity range from Group II saturation to Group VI saturation [9, 12–14]. As a result, the transport rate of the vapor species can also vary from a maximum transport rate corresponding to the condition of congruent sublimation, (i.e. the compositions of the solid phase and the equilibrium vapor phase are the same), to a transport rates that are orders of magnitude lower when the solid composition deviates significantly from the congruent

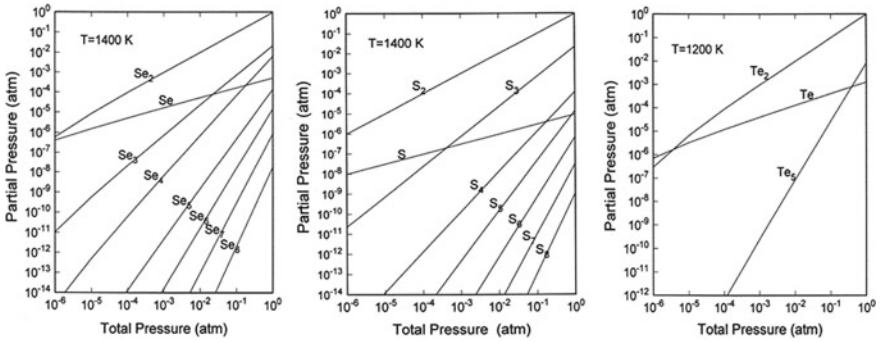

Fig. 2.1 The vapor species in equilibrium with the condensed phase of group VI elements, i.e., Se, S and Te, at the growth conditions

sublimation condition. Generally speaking, in the growth temperature range usually adopted, the congruent sublimation condition does exist inside the homogeneity range of these II–VI materials [9, 12] but a precise control of the stoichiometry of the starting materials from the weighing of the constituent elements is practically impossible. However, with certain heat treatments the partial pressures over the starting compound material can be reasonably optimized and reproduced.

The pressure of predominant vapor species, P, over the pure elements is related to the Gibbs energy of formation from the vapor phase, ΔG_f, and the corresponding enthalpy ΔH_f and entropy ΔS_f as:

$$RT\ln P = \Delta G_f^o = \Delta H_f - T\Delta S_f \tag{2.1}$$

where R is gas constant and T in K. Therefore, the vapor pressures can be expressed in the form of $\log_{10}P$ (atm) $= -A/T + B$. The values of A and B for the vapor species over the pure elements relevant to the compound semiconductors discussed here are given in Table 2.1. From these values, the vapor pressures are calculated and plotted as function of 1000/T in Fig. 2.2.

2.1.2 Thermodynamics of Solid and Vapor Phases in Compound Semiconductors

When the elements are mixed and reacted to form intermediate compounds, the equilibrium vapor pressure decreases from the value for pure element because its chemical potential decreases. Considering a simple case of compound semiconductor, such as AB, the Gibbs energy, G, as functions of composition x_B, for each phase at a fixed temperature, T_g, below the melting temperature, T_M, can be shown schematically as Fig. 2.3. The curve, L, is the Gibbs energy for the liquid phase and the other sharply curved one, S, is for the solid compound phase where the narrow homogeneity range

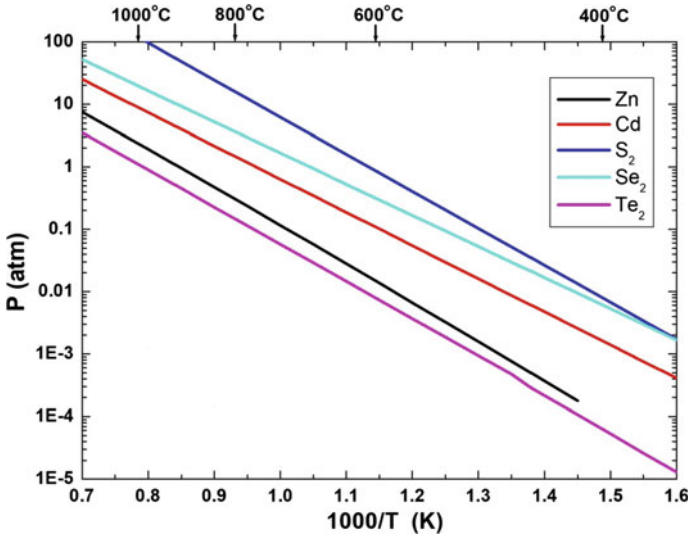

Fig. 2.2 The pressures of various vapor species over the pure elements as functions of 1000/T (K)

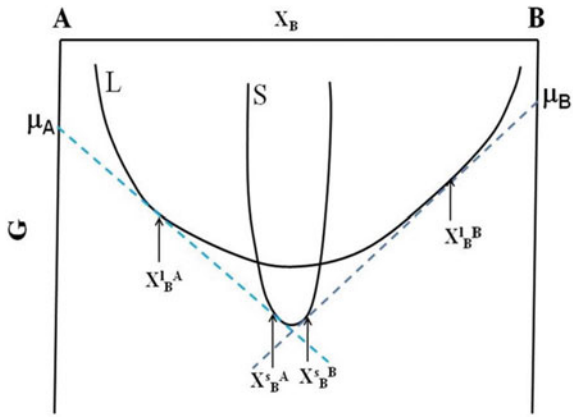

Fig. 2.3 The schematics of Gibbs energy isotherms for the liquid and solid phases

has been exaggerated. As shown, two simultaneous tangents can be drawn to the L-and S-curve at different compositions and intercept the element A and B at μ_A and μ_B. The common tangents mean that these two compositions have the same chemical potential, μ_A or μ_B, and therefore, co-exist in the solid and liquid phases.

The complete phase diagram can be constructed from the Gibbs energy isotherm for different temperatures as shown in Fig. 2.4. The existence of narrow homogeneity range of the stoichiometric compounds is the material's nature to reduce the Gibbs energy of formation by increasing the entropy term [17]. Therefore, the existing homogeneity range is zero at temperature of absolute zero as well as at the maximum melting temperature due to the phase transition. Along the temperatures in-between,

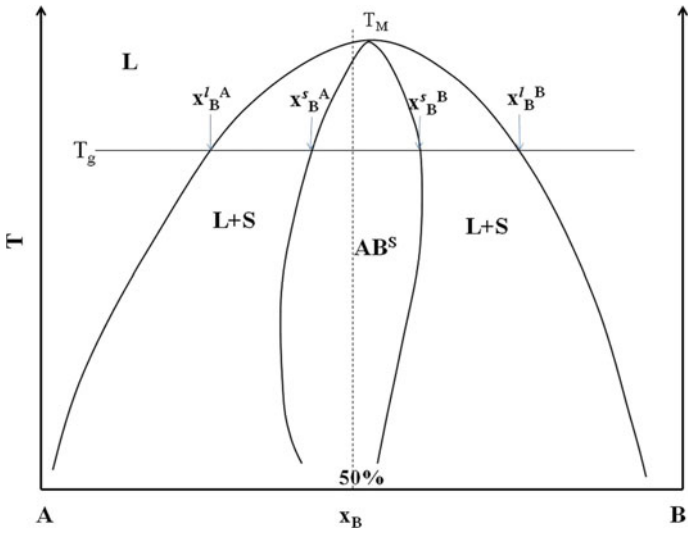

Fig. 2.4 A schematic phase diagram of the compound semiconductor AB (taken from Fig. 1 of Ref. [18])

the homogeneity range goes through a maximum as a function of temperature, known as retrograde solubility. The AB compound has a maximum melting point of T_M, at a composition slightly larger than 50% in this case. At a fixed temperature T_g, lower than T_M, as shown in Fig. 2.4, the phase boundaries, from low to high x_B, between liquid (L), liquid + solid (L + S), AB solid (AB^S), liquid + solid (L + S), and liquid (L), are marked by four different compositions of x_B [18].

As shown schematically in Fig. 2.5, at temperature T_g, the chemical potential of B, μ_B, as functions of x_B, increases monotonically with x_B in the one-phase region, L or S, and remain constant as μ_B^A and μ_B^B in the two-phase (liquid + solid) regions.

In a closed system, the partial pressures of the predominant vapor species, A and B_2, in equilibrium with the condensed phase at a constant temperature T (in K), with the assumption of ideal gas for the vapor phase, are related to their chemical potentials as:

$$RT \ln P_A = \mu_A - \mu_A^o(T) \tag{2.2}$$

and

$$RT \ln P_{B_2}^{1/2} = \mu_B - \frac{1}{2}\mu_{B_2}^o(T) \tag{2.3}$$

where P_A and P_{B_2} are the partial pressure of A and B_2, respectively, μ_i^o is the chemical potential of the vapor species, i, at 1 atm and T in K.

Figure 2.6 presents the schematic plot of $\log(P_{B_2})$ versus 1/T. The slanting straight line on the top of the figure gives the vapor pressure of B_2 for the pure element B. The

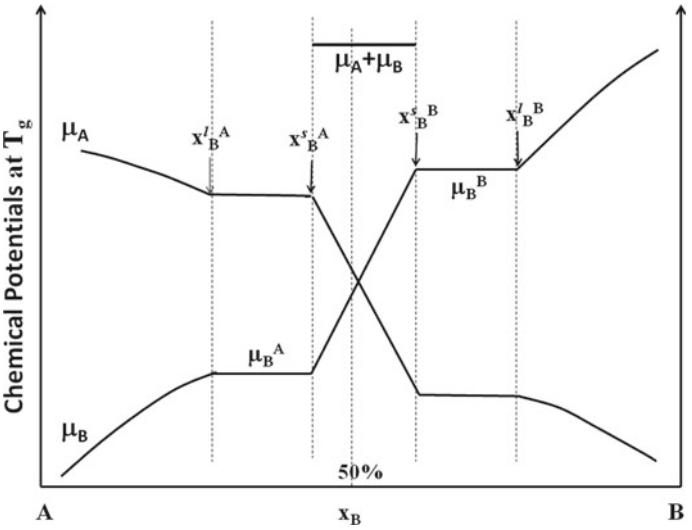

Fig. 2.5 Schematic plots of chemical potentials of A, μ_A and B, μ_B, as a function of X_B at temperature T_g (taken from Fig. 2 of Ref. [18])

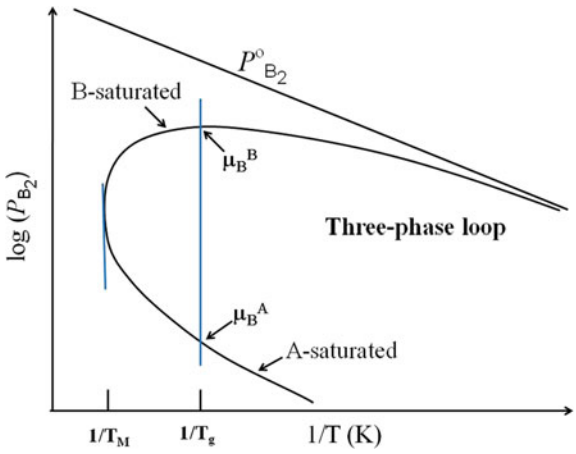

Fig. 2.6 Three-phase loop of partial pressure of B_2 over compound AB

three-phase loop/curve below it delineates the partial pressure of B_2 along the boundary of the homogeneity range. The B-saturated curve, with higher partial pressure, follows the B-rich boundary of the homogeneity range to the melting temperature T_M, then comes down toward the A-saturated boundary with the lower partial pressure. At the temperature of T_g, the partial pressure follows the chemical potential of B which increases tremendously (as shown in Fig. 2.5) from, μ_B^A, at one end of the solid of composition of x_B^{sA} that saturated with A element to, μ_B^B, at the other end of x_B^{sB} that saturated with element B. As a result, the partial pressures of the species

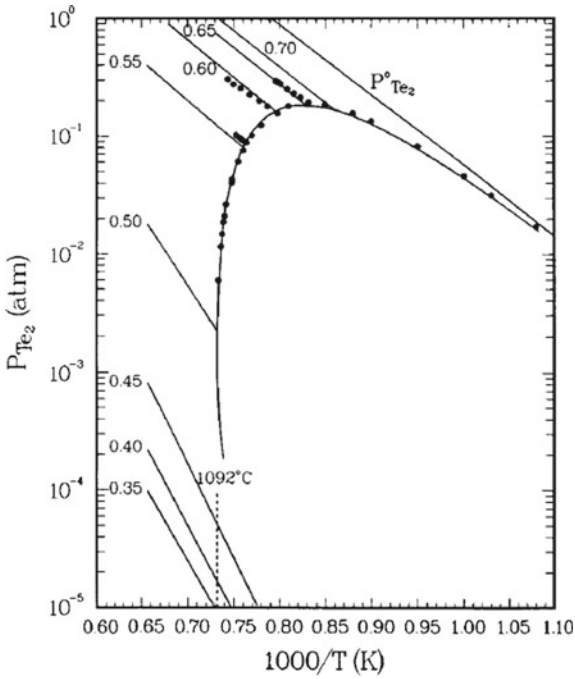

Fig. 2.7 Partial pressure of Te_2 along the three-phase loop of CdTe(s) and over the various melts with the composition X_{Te} labeled. (Reproduced with permission from *J. Electrochem. Soc.*, 118, 2014 (1971). Copyright 1971, The Electrochemical Society, Ref. [19])

A and B_2 in equilibrium with the AB compounds, at a fixed temperature, can vary by orders of magnitude as the composition of the compound varies over the narrow homogeneity range from A-saturation to B-saturation [9, 12, 14].

As an example, the measured partial pressures of Te_2 over the Cd-Te system [19] are shown in Fig. 2.7, which includes the three-phase curve over the CdTe(s) and the segments of Te_2 partial pressure in equilibrium with the melts of various composition of x_{Te} as labeled.

2.1.3 Partial Pressure Measurements

There are various methods to measure the partial pressures over the condensed compound, including isopiestic, transpiration method, Bourdon or Spoon gauge, self-manometer, Knudsen cell, torsion cell, electrochemical techniques, solid state coulometry, oxygen gauge, calorimetric method and optical absorption of the vapor phase. The optical absorption technique has the advantage of simultaneously measuring partial pressures of different vapor species and has been adopted extensively on the systems of ZnSe [13, 14], HgTe [20, 21], HgSe [22], CdTe [19], PbTe [1, 2], SnTe [4, 5], PbSnTe [1], CdZnTe [23], HgCdTe [24–26] and HgZnTe [27].

The basic principles for the measurements and the experimental procedure were described in detail in the references above. In brief, the T-shape cell for the optical measurement was made of fused silica. The sample beam of a double beam monochromator passed through the optical windows on the top of the T which was held at a fixed temperature and the sample was located at the bottom of the vertical leg of the T (see Fig. 2.8). The sample temperature was held at one of a set of temperatures lower than the optical path temperature for measurement. For the measurements of partial pressures over ZnSe at temperatures above 1100 °C [13] some modifications are required. Figure 2.9 shows the optical density of the vibronic spectra for the vapor species O_2 between 190 and 220 nm at various temperatures. The vibronic spectra at room temperature does not extend into the 195 nm range, but for temperatures above 1100 °C, it extends out to the Zn absorption line, 213 nm, as can be seen in the figure. To eliminate this problem, a modification of the cell, shown in Fig. 2.10 was employed. This configuration eliminates the spectrum of hot O_2, reduces the noise in the optical density that would arise in an air path from density fluctuations and reduces the pressure differences across the interior windows and thus eliminates their possible long-term distortion [13]. For the partial pressure measurements of the pure elements as calibration standards, spectroscopically pure Se and pure Zn were loaded into a triple cell such as that shown in Fig. 2.10.

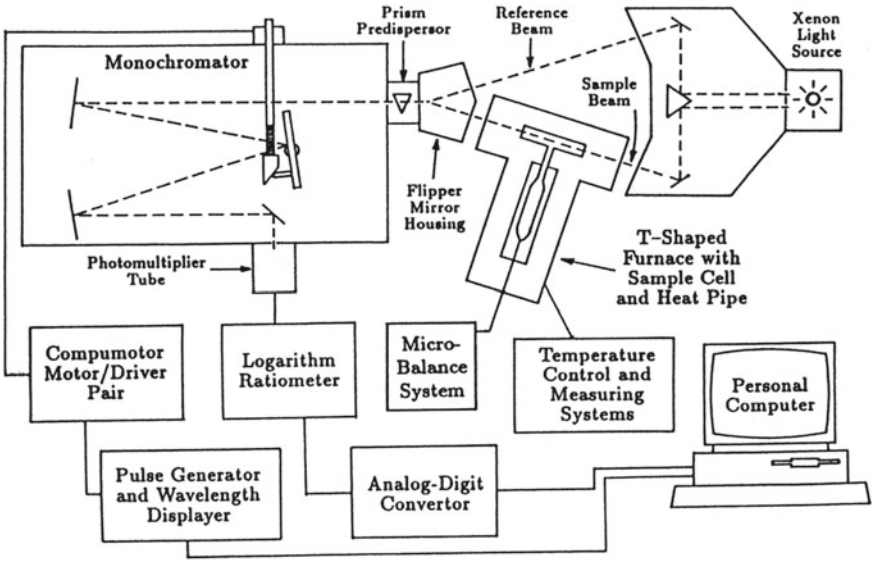

Fig. 2.8 Schematic of the partial pressure experiment setup and control/recording systems

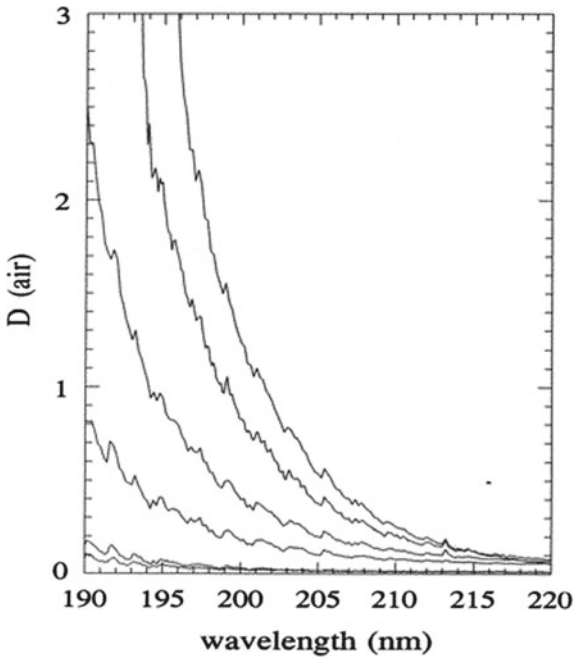

Fig. 2.9 Optical density of the O_2 vibronic spectra in the UV range for various temperatures. The optical path consisted of approximately 10 cm of air plus two 2-mm thick fused silica disks. The temperatures plotted from top to bottom are; 1150 °C, 1100 °C, 860 °C, 500 °C, 420 °C and room temperature (taken from Fig. 3 of Ref. [8])

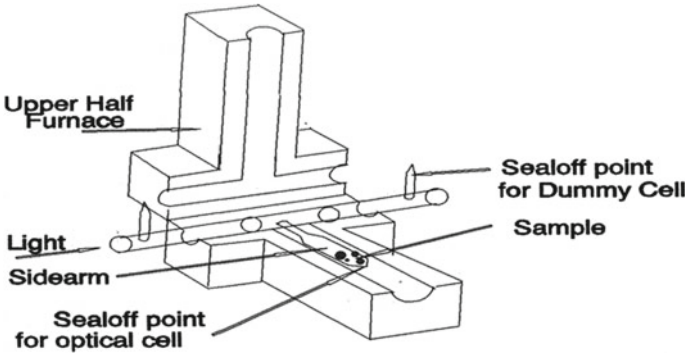

Fig. 2.10 Schematic of a triple optical cell placed in an opened T-shaped, split furnace (taken from Fig. 1 of Ref. [8])

2.1.3.1 Selenium Partial Pressure Calibrations

Figure 2.11 shows the spectrum of Se_2(g) for an optical path length of 9.5 cm at 410, 432, 551 and 603 °C. The maximum absorption between 200 and 700 nm occurs as broad vibronic peaks with a maximum at 330 nm. With an increase in the partial pressure of Se_2, the absorption extends further into the visible region and a broad minimum in the UV range develops between 230 and 260 nm. An isolated maximum at 212.4 nm is also observed at the higher temperatures (i.e. higher partial pressures). The optical density as a function of 1000/T(K) for four vibronic maxima is plotted on a logarithmic scale in Fig. 2.12. The upper dashed line is the total vapor partial pressure of Se_2, as read on the right ordinate of the graph. This pressure is given by:

$$\log P^0_{Se_2}(\text{atm}) = -4989.5/T + 5.2078 \tag{2.4}$$

From the selenium vapor species equilibrium constants published by Mills [28] and the vapor pressures determined from the equation above, it was estimated that Se_2 comprises 95% of the vapor in the optical cell at the lowest temperature and 99% at the highest temperature. The remaining 1–5% is predominantly the monatomic species. By assuming Beer's law, the net optical density, D_λ, can be determined by;

$$D_\lambda = P_2 L/\alpha_\lambda \tag{2.5}$$

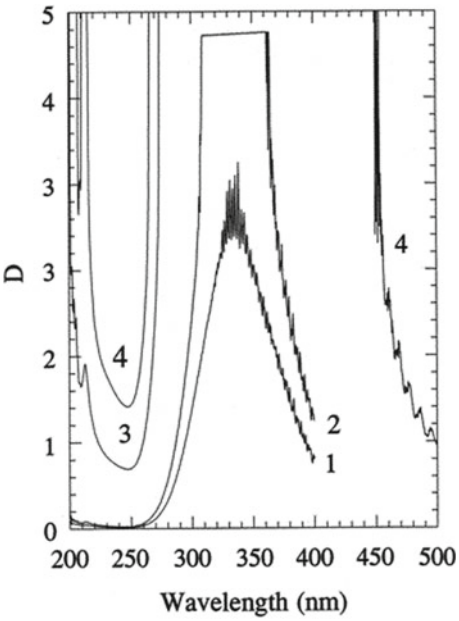

Fig. 2.11 Optical absorption spectra for Se_2(g). The optical path is 9.5 cm. The temperatures and total Se vapor pressures for each curve are as follows: Curve #1 410 °C and 0.008 atm, #2 432 °C and 0.013 atm, #3 551 °C and 0.142 atm and for #4 603 °C and 0.325 atm (taken from Fig. 4 of Ref. [8])

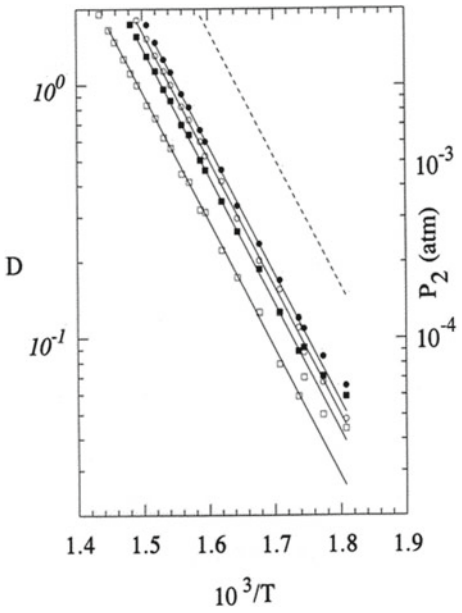

Fig. 2.12 Calibration measurements of Se_2 optical density. The optical density of pure selenium sample for a 9.75 cm optical path at 1150 °C is plotted as a function of 1000/T(K) for 4 vibronic peaks. Solid circles are for 340.5 nm, open circles for 350.8 nm, solid squares for 361.3 nm and open squares for 379.2 nm. The upper dashed line is the vapor pressure (read from the right ordinate) as described in the text (taken from Fig. 5 of Ref. [8])

Table 2.2 Beer's Law constants, α_λ, of Se_2 for four different wavelengths at three different optical path temperatures

λ (nm)	α_λ (atm–cm)		
	1150 °C	1100 °C	1000 °C
340.5	0.0278 ± 7%	0.0269 ± 6%	0.0278 ± 6%
350.8	0.0313 ± 4%	0.0296 ± 6%	0.0267 ± 6%
361.3	0.0363 ± 9%	0.0353 ± 5%	0.0315 ± 7%
379.2	0.0544 ± 11%	0.0531 ± 11%	0.0500 ± 7%

where P_2 is the partial pressure of Se_2 in atm, L is the optical path length in cm and α_λ is the Beer's law constant in atm–cm. α_λ depends on the wavelength, the optical path temperature, and to some extent on the band-pass. Using a linear least squares fit to log D_λ versus 1000/T (sample temperature in K) data, with the constraint that the slope be identical to that of P_2, the Beer's law constants were obtained. These are tabulated in Table 2.2 for optical path temperatures of 1150, 1100 and 1000 °C.

2.1.3.2 Zinc Partial Pressure Calibrations

The optical density at the maximum of the 213.8 nm Zn(g) absorption line is shown in Fig. 2.13 for a 9.55 cm optical path at 1150 °C and for nominal instrumental band-pass of 0.1 and 0.2 nm as a function of the reciprocal temperature of a pure Zn sample. The vapor pressure of Zn is shown by the dashed line and can be seen to be significantly less curved than the experimental optical density lines. The solid lines

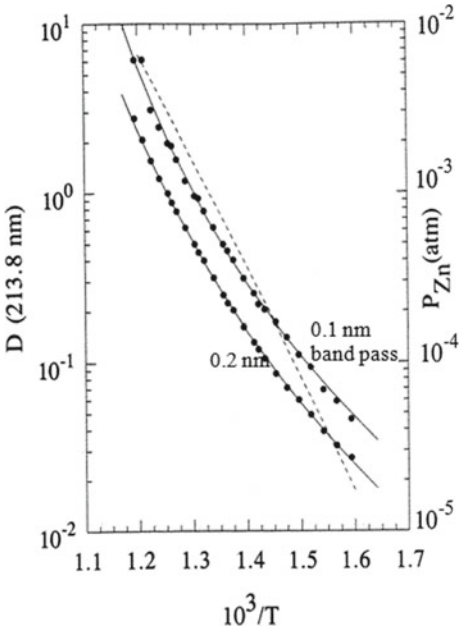

Fig. 2.13 Optical Density at the maximum of the 213.8 nm Zn(g) absorption line as a function of reciprocal temperature of a pure Zn sample. The optical path is 9.55 cm, the temperature is 1150 °C and the nominal band-pass is 0.1 and 0.2 nm. The solid curves are calculated assuming a triangular slit function and a Voigt line profile. The dashed line is the vapor pressure of Zn as read from right ordinate (taken from Fig. 6 of Ref. [8])

through the optical density points are calculated assuming a triangular slit function for the spectrophotometer and a Voight line profiles for the Zn peak. The curve for the 0.2 nm instrumental band-pass can be written as:

$$\log P_{Zn}(\text{atm}) = A + B(\log D) + C(\log D)^2 \tag{2.6}$$

The constants in the expression $\log P_{Zn}(\text{atm}) = A + B(\log D) + C(\log D)^2$ under various experimental conditions have been determined in Ref. [13] and are given in Table 2.3.

Table 2.3 The constants in Eq. (2.6) for different experimental conditions. (T_{op} is optical cell temperature; taken from Table 25 of Ref. [13])

T_{op} (°C)	Instrumental band pass (nm)	Optical path length (cm)	A	B	C
1000	0.48	9.75	−2.2672	0.8604	−0.2494
1050	0.48	9.75	−2.2425	0.8919	−0.2339
1100	0.48	9.75	−2.1979	0.9363	−0.2184
1150	0.48	9.75	−2.2126	0.8850	−0.2378
1150	0.26	9.60	−2.4800	0.9373	−0.2815

2.1.3.3 Partial Pressures Over ZnSe and Gibbs Energy of Formation

The optical absorbance was measured between 190 and 800 nm and the partial pressures of individual vapor species were calculated using the data of calibration runs. A total of six ZnSe optical cells, with optical path length about 10 cm, were measured. The starting ZnSe compound was extracted from a vapor-grown crystal from Cleveland Crystals, Inc., and followed by various treatments to modify its stoichiometry. Two samples of the six cells were un-treated, one sample was added with an extra small amount (22 mg) of Se, and the rest starting materials were baked out under dynamic vacuum conditions at various temperatures for different periods of time. The partial pressure of Se_2 was determined from the absorbance of the Se_2 vibronic peaks at 340.5, 350.8, 361.3, and 379.2 nm and that of Zn was determined from the atomic absorption peak at 213.8 nm and are given in Figs. 2.14 and 2.15 between 1000 and 1130 °C.

It will be discussed later in the theoretical derivation of vapor transport that one of the critical parameters in determining the diffusion rate of vapor species is the vapor composition, i.e., the contents of Zn and Se in the vapor phase. Therefore, it should be interesting to study the vapor compositions of these vapor-grown samples. From the measured P_2, the partial pressure of Se_2, the partial pressures of other vapor species, Se_n, n = 1, 3, 4, 5…8, can be calculated as shown in Fig. 2.1. The

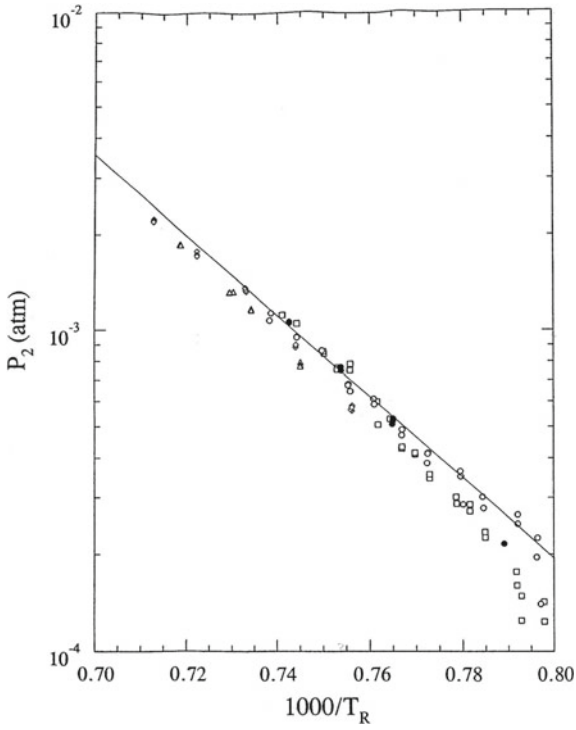

Fig. 2.14 Partial pressures of Se_2, P_2, are plotted against 1000 over reservoir temperature, T_R(K), for various ZnSe(s) samples. The solid line is the result from fitting the data over the high T_R range (taken from Fig. 23 of Ref. [13])

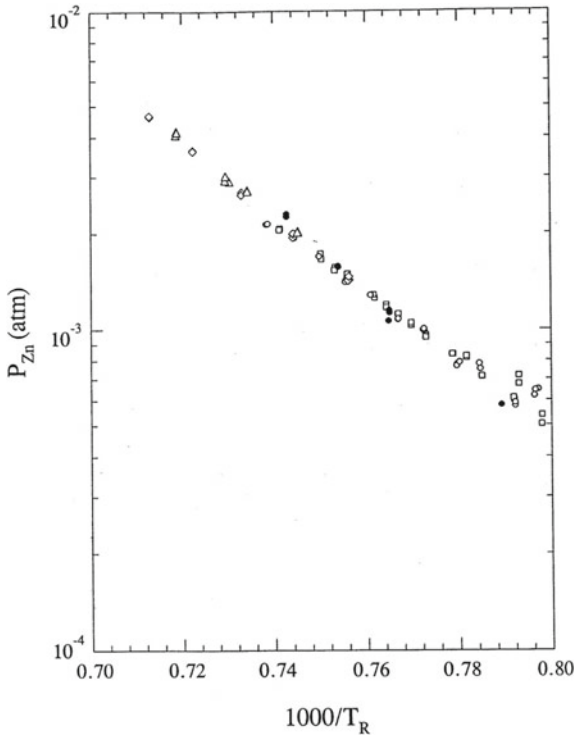

Fig. 2.15 Partial pressures of Zn, P_{Zn}, are plotted against 1000 over reservoir temperature, T_R(K), for various ZnSe(s) samples (taken from Fig. 24 of Ref. [13])

vapor composition, defined as $X_v = P_{Zn}/P_B$ with $P_B = \sum_{n=1}^{8} n P_n$, where P_n is the partial pressure of vapor species Se_n, n = 1, 2, 3,…8. In the case of $X_v = 1.0$, the ZnSe material has the composition of congruent sublimation, i.e., the solid and vapor phases have the same composition $x_{Zn}/x_{Se} = 1.0$. From the measured partial pressures of Zn and Se_2, X_V has been calculated for these starting materials and is plotted in Fig. 2.16 as a function of temperature for one un-treated sample, i.e., sample ZnSe-93B in Ref. [13] with the Zn and Se_2 partial pressures shown as open squares in Figs. 2.14 and 2.15, respectively. It can be seen in the figure that, at the low temperature range of 980 °C, X_V started at about 2.0, i.e., the content of Zn to Se in the vapor phase has a ratio of 2:1. As the temperature increased, the composition of the ZnSe solid shifted toward the Se-rich direction as more Zn has been sublimed to the vapor phase than Se. The shifting in composition stopped at about 1045 °C when the solid reached congruent sublimation, i.e., $X_v = 1.0$.

One important thermodynamic characteristic for the narrow homogeneity range compounds is that the Gibbs free energy of formation from the vapor phase is, within experimental error, independent of the deviation from stoichiometry and a function of temperature only [17]. The Gibbs energy of formation for AB(s) from the vapor phases of A(g) and 0.5 B_2(g), ΔG_f, as a function of temperature can be expressed from the partial pressures as:

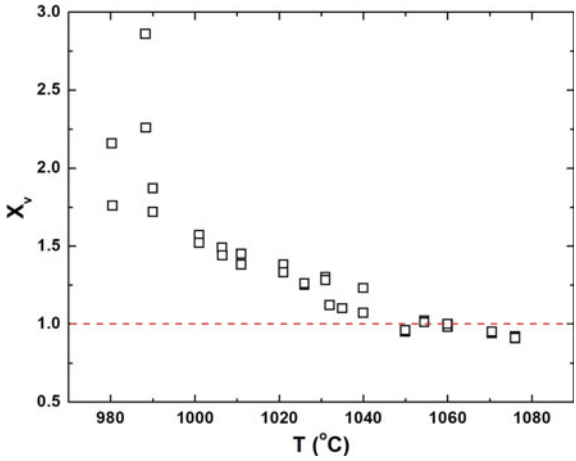

Fig. 2.16 The vapor composition, $X_V = P_{Zn}/P_B$, derived from the measured P_{Zn} and P_2 as a function of temperature

$$\Delta G_f = RT\ln\left(P_A P_{B_2}^{\frac{1}{2}}\right) \tag{2.7}$$

This stoichiometric invariant has provided the useful information in that, when one partial pressure at a fixed temperature is known for the compound, the other one can be determined from the relationship using the general expression of enthalpy H and entropy S:

$$\Delta G_f = \Delta H - T\Delta S \tag{2.8}$$

The Gibbs energy of formation for ZnSe(s) from Zn(g) and 0.5 Se_2(g) as a function of temperature was determined from the partial pressure measurements [8]. Figure 2.17 is a plot of the Gibbs energy of formation versus temperature. The upper solid line is the least squares fit to the 4 sets of partial pressure measurements. The various lines in Fig. 2.17 are from other studies. The Gibbs energy of formation can be expressed as:

$$\begin{aligned} \Delta G_f(\text{J/mol}) &= RT\ln(P_{Zn}P_{Se_2}^{1/2}) \\ &= -361,807(\pm 7979) + 191.485(\pm 5.883)T \end{aligned} \tag{2.9}$$

and the relationship can be written as: $\log_{10} P_A P_{B2}^{1/2}(\text{atm}) = -C/T + D$ for the easy conversion from one partial pressure to the other. Since R = 8.314 J/mole-K and ln(10) = 2.303, the constants of C and D can be calculated for ZnSe and listed in Table 2.4 where the equilibrium constants C and D for various compound semiconductors have also been determined.

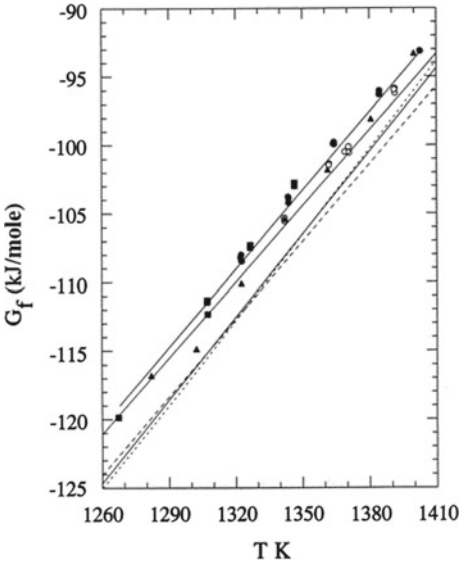

Fig. 2.17 The standard Gibbs energy of formation of ZnSe versus temperature from 4 samples comparing with other reports (taken from Fig. 8 of Ref. [8])

Table 2.4 The equilibrium constants C and D in $\log_{10} P_A P_{B2}^{1/2}(\text{atm}) = -C/T + D$ for the partial pressures of various II–VI compound semiconductors AB

Compounds	C	D	References
ZnSe	18900	10.003	[8, 13]
ZnTe	16350	9.680	[9]
CdS	17247	10.466	[10]
CdSe	16632	10.092	[11]
CdTe	15003	9.8224	[12]

2.1.4 Thermodynamic Analyses

With the available experimental phase diagram and thermodynamic data, certain solution models have been adopted for the solid and liquid phases to practice phase diagram calculation. Assuming an associated solution model for the liquid phase, the thermodynamic analyses has been applied to binary, ternary and quaternary systems such as Hg–Te, Cd–Te and Hg–Cd–Te as well as In–Sb, Ga–Sb and In–Ga–Sb [29], Hg–Cd–Zn–Te [15] and Zn-Se [14]. In the associated solution model, the phase is assumed to consist of certain atomic/molecular species and Gibbs energy of mixing for the phase can be expressed in terms of the interaction between these species with interaction parameters. A simultaneous, quantitatively good, and thermodynamically self-consistent fit to the experimental data can be obtained by varying the interaction parameters of the models. After the establishment of the best-fit parameter set, the complete phase diagram and thermodynamic properties of the system can be generated for the applications of crystal growth experiments with certain level of confidence.

2.1.4.1 Analyses of Zn–Se System

The phase diagram was analyzed using an associated solution model for the liquid by fitting the experimental results of Se-rich liquidus points, Gibbs energy of formation for ZnSe(s) and the partial pressure measurements discussed in the previous section. The liquid phase was assumed to consist of three species; Zn and Se unassociated species with mole fractions y_1 and y_2, respectively, and the molecular species ZnSe with mole fraction y_3. The excess Gibbs energy of mixing per mole of species is given by:

$$\Delta G_{mix}^{ex} = \sum\sum \left(\alpha_{ij} + \beta_{ij} y_j\right) y_i y_j - y_3 \Delta G_D \tag{2.10}$$

where $\alpha_{ij} = \alpha_{ji}$, $\alpha_{jj} = 0$ and $\beta_{ij} = -\beta_{ji}$ and ΔG_D is the standard Gibbs energy of dissociation of the ZnSe species. The Gibbs energy of formation for the solid phase $Zn_{1-x}Se_x$(s) from Zn(l) and Se(l) is independent of the composition, x, for this narrow homogeneity range compound and can be derived from the Gibbs energy of formation from the gas phase described in the previous section:

$$\Delta G_f(\text{J/mole}) = -197,022 + 44.330T \tag{2.11}$$

After the liquid model parameters were fixed by a best fit to the liquidus points, the entire liquidus curve was generated as well as the partial pressure of Zn and Se_2 along the ZnSe(s) three-phase curve as shown in Fig. 2.18a, b. Inside the narrow homogeneity range just below the melting temperature, there exists a congruent sublimation composition, shown as the straight line segments in the figures, that the equilibrium partial pressures ratio, $P_{Zn}/P_{Se_2} = 2.0$.

2.1.4.2 Analysis of Zn–Se–Te System

The associated solution model was extended to the Zn–Se–Te ternary system and there are five species in the melt, Zn, Se, Te, ZnSe, and ZnTe molecules. The interaction parameters determined from the Zn–Se binary system described above and those for the Zn–Te system [15] were adopted. For the Se-Te system, the Se and Te species were assumed to interact as a quasi-regular solution and the interaction parameters were determined from the best fit to the Se-Te phase diagram. An ideal solution was assumed for the solid solution of $ZnSe_{1-x}Te_x$. The calculated results included the liquidus and solidus lines for the ZnSe–ZnTe pseudobinary system and the partial pressures of the elements along the three-phase curves for nine different solid solution compositions. Two of these compositions, $x = 0.05$ and $x = 0.20$ are shown in Fig. 2.19. The short, dashed line segments shown for $x = 0.20$ are the partial pressures for a stoichiometric vapor, i.e. $P_{Zn} = 2\left(P_{Se_2} + P_{Te_2}\right)$. However, these are not the congruent sublimation condition because $P_{Te_2}/\left(P_{Se_2} + P_{Te_2}\right) > 0.98$ from 940 to 1220 °C.

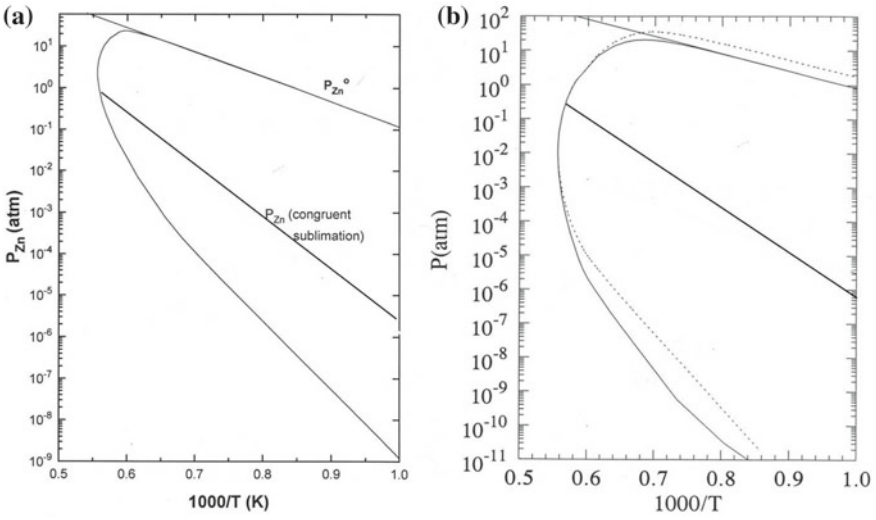

Fig. 2.18 Calculated partial pressure of **a** Zn and **b** Se_2, along the three-phase curve for ZnSe(s). The short line segment at the upper right is for pure Zn/Se liquid and the straight line inside the three-phase curve is for congruently subliming ZnSe(s) The total pressure of all of the Se species along the three-phase curve is the closely following dashed curve. (taken from Figs. 4 and 5 of Ref. [14])

2.2 Physical Vapor Transport Process (One-Dimensional Diffusion Model)

As discussed in the beginning of this chapter, the PVT process consists of three steps in series: (1) sublimation, (2) transport and (3) condensation, and the slowest one of these steps limits the crystal growth rate. During the experiments of partial pressure measurement by optical absorption, after adjusting the sample to a new temperature, the measured optical density usually reached its final steady value within minutes. Hence, the transport of the vapor species would be the growth-rate limiting step and an in-depth theoretical study of the PVT process is needed to find out the critical growth parameters in determining the transport rate.

2.2.1 Diffusive Transport in Binary Systems

It is clearly shown from last section that the equilibrium pressure of a vapor species goes up monotonically as the temperature of the condensed phase gets higher. In a closed system, the non-uniform partial pressure profile caused by a temperature variation along the transport length will result in mass diffusion in the vapor phase and the resultant flux of mass transport. To have a better understanding of the effects of

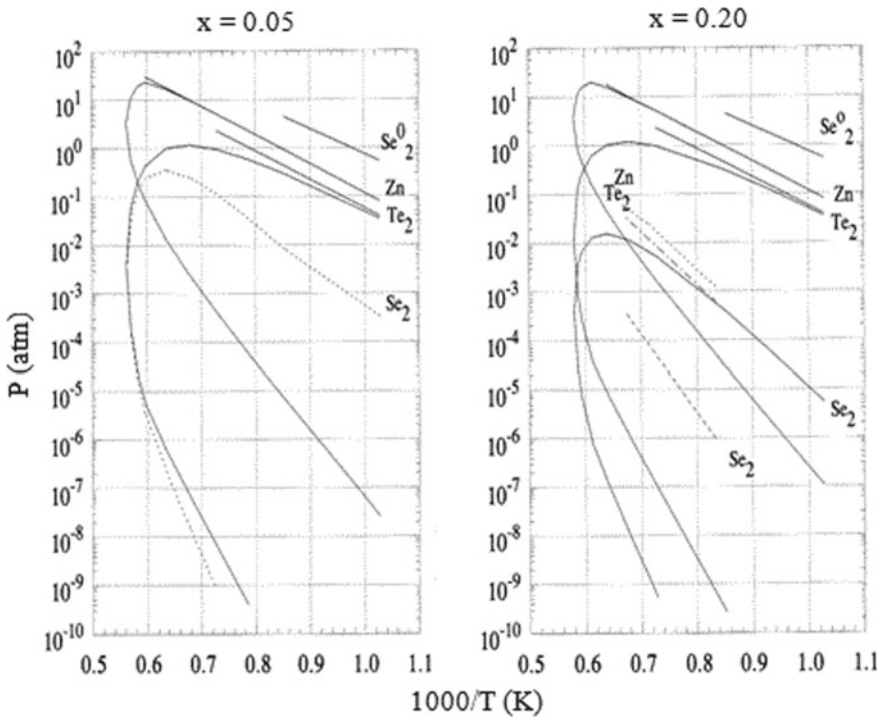

Fig. 2.19 Three-phase curves for $ZnSe_{1-x}Te_x$ solid solutions x = 0.05 and 0.20. The short, dashed line segments shown for x = 0.20 are the partial pressures for a stoichiometric vapor phase, i.e. $P_{Zn} = 2(P_{Se_2} + P_{Te_2})$

various growth parameters and the thermal field, a simple one-dimensional diffusion model was established to identify the critical growth parameters such as the heat treatment conditions, the thermal field for the growth process, the composition of the grown (ternary) crystal as well as the transport rate. The theory of diffusion in ideal multi-species gases was developed about a century ago mainly by Maxwell and Stefan. The original form of a Maxwell equation for diffusion of species A through species B was

$$-dP_A = \alpha_{AB} \frac{\rho_A \rho_B}{M_A M_B} (u_A - u_B) dy \tag{2.12}$$

where P_A is the partial pressure of A along the distance y, ρ's the partial densities, M's the molecular weights, u's the velocities of the species in the direction of net diffusion, and α_{AB} a proportionality constant. Conventionally, the mass flux, or the rate of diffusion of the species A in moles per unit time per unit cross section area, $J_A = u_A \rho_A / M_A$, is used and for a multi-species system the Maxwell equations have the form

$$-\frac{dP_i}{dy} = \sum_{j \neq i} r_{ij}\left(J_i P_j - J_j P_i\right) \; i = A, B, \ldots \tag{2.13}$$

where $r_{ij} = \alpha_{ij}/RT = RT/D_{ij}P$, $r_{ij} = r_{ji}$, and D_{ij} is the binary diffusion coefficients.

In the PVT process, a binary II–VI compound $A^{II}B^{VI}$ sublimes dissociatively according to the following reaction:

$$AB(s) \rightarrow A(g) + \frac{1}{2}B_2(g) \tag{2.14}$$

Two Maxwell equations need to be solved. A correlation between two fluxes has to be assumed in order to solve them since only one of the equations is independent due to the constant total-pressure condition. Obviously, $J = J_A = 2J_B$ ($B \equiv B_2$ in subscript) is justified because of the fact that all the II–VI compounds have a very narrow homogeneity range and no secondary phase was observed in the grown crystals. Using this and the constant total-pressure constraint $P = P_A + P_B$, the two Maxwell equations can be decoupled and reduced to

$$J = \frac{3}{2}\frac{J}{P}P_A - \frac{1}{r_{AB}P}\frac{dP_A}{dy} \tag{2.15}$$

$$J = 3\frac{J}{P}P_B - \frac{2}{r_{AB}P}\frac{dP_B}{dy} \tag{2.16}$$

respectively. Equations (2.15) and (2.16) are equivalent to those derived by Faktor and Garrett [30], where the first term on the right-hand side is called the Stefan flow and the second term is the diffusive flow. The integration of Eqs. (2.15) and (2.16) leads to:

$$P_A(y) = \frac{2}{3}P + \left[P_A(L) - \frac{2}{3}P\right]\exp\left[\frac{3}{2}Jr_{AB}(L - y)\right] \tag{2.17}$$

$$P_B(y) = \frac{1}{3}P + \left[P_B(L) - \frac{1}{3}P\right]\exp\left[\frac{3}{2}Jr_{AB}(L - y)\right] \tag{2.18}$$

and the flux is given by:

$$J = \frac{2}{3}\frac{D_{AB}P}{RTL}\ln\frac{P_A(0) - \frac{2}{3}P}{P_A(L) - \frac{2}{3}P} = \frac{2}{3}\frac{D_{AB}P}{RTL}\ln\frac{P_B(0) - \frac{1}{3}P}{P_B(L) - \frac{1}{3}P} \tag{2.19}$$

in which $y = L$ is where the source is located, 0 is where the crystal is. Equation (2.19) has been used by Su [31] and Sha et al. [7] to analyze the CdS and ZnSe system, respectively. Three parameters, T(L), T(0), and α, defined as $\alpha \equiv P_A/P_B$, determine the mass flux in this PVT system. One important thermodynamic property for the narrow homogeneity range compounds is that the Gibbs free energy of formation from the vapor phase is, within experimental error, independent of the deviation

from stoichiometry and a function of temperature only, as observed experimentally earlier on the ZnSe system. Figure 2.20 shows the results calculated from Eq. (2.19) for the mass flux in ZnSe system as a function of $\Delta T \equiv T(L) - T(0)$ for different stoichiometries, α, of the source.

In the calculation, the diffusion coefficient for a binary gas system AB at low pressure can be estimated by the Chapman-Enskog formula using the collision integral given by Neufield et al. [32]:

$$D_{AB} = 0.001858 T^{3/2} \frac{[(M_A + M_B)/(M_A M_B)]^{1/2}}{P \sigma_{AB}^2 \Omega_D} \tag{2.20}$$

where D_{AB} is in cm^2/s, T in K, M_i is the weight of atom/molecule i, P in atm, σ_{AB} in $\dot{A}$ and

$$\Omega_D = \frac{A}{T_r^B} + \frac{C}{\exp(DT_r)} + \frac{E}{\exp(FT_r)} + \frac{G}{\exp(HT_{r)}} \tag{2.21}$$

where $T_r = kT/\varepsilon_{AB}$, $\varepsilon_{AB} = (\varepsilon_A \varepsilon_B)^{1/2}$, $\sigma_{AB} = (\sigma_A + \sigma_B)/2$, $A = 1.06036$, $B = 0.15610$, $C = 0.19300$, $D = 0.47635$, $E = 1.03587$, $F = 1.52996$, $G = 1.76474$, $H = 3.89411$; and k is the Boltzmann constant, ε_i, the Lennard-Jones potential well depth (see Appendix at the end of this chapter) between species i and σ_i is the radius of atom/molecule i.

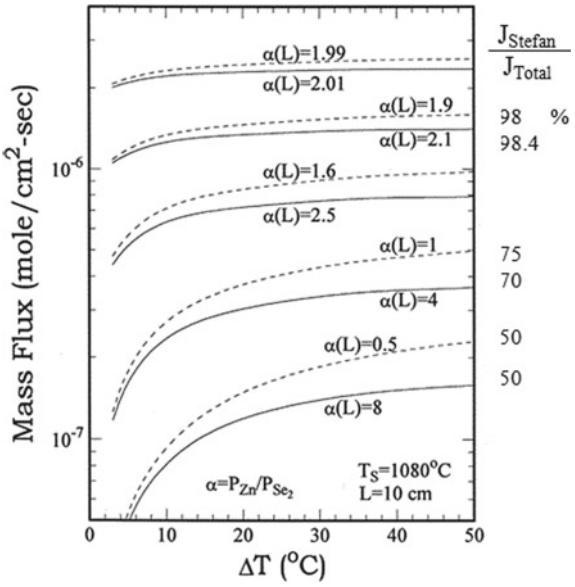

Fig. 2.20 Calculated mass flux of ZnSe as a function of ΔT and different values of $\alpha(L)$. The source temperature was 1080 °C. Solid lines are for $\alpha(L) > 2$ and dashed lines are for $\alpha(L) < 2$ (taken from Fig. 2 of Ref. [7])

2.2.2 *Diffusive Transport in Multi-nary Systems*

In a gas system with multiple species, the diffusion coefficient can be approximated by substituting the total pressure for P in the denominator of Eq. (2.20). The molecular parameters used for the computation are given in Table 2.5. From Eq. (2.19), one can find that when $P_A = (2/3)P$, or equivalently, $\alpha(L) = P_A(L)/P_{B2}(L) = 2$, the flux J is infinite. In this case, the mass transport is no longer limited by diffusion or by stoichiometric excess. As the source material approaches congruent sublimation, or $\alpha(L) = 2.0$, the mass flux increases rapidly. Figure 2.20 also shows that the mass flux reaches an upper limit at about $\Delta T = 30$ °C for non-congruently subliming vapor and this limiting value of ΔT reduces when $\alpha(L)$ is closer to 2.0. This is because the ΔT-dependence of the mass flux is mainly due to that of the diffusion of the minority species whose partial pressure at T(0) becomes very low at a certain ΔT-value. A further increase in ΔT does not produce much change in the partial pressure and therefore cannot effectively increase the transport rate. In fact, a source material with an α-value either higher than 8 or lower than 0.5 could result transport rates which are 2 or more orders of magnitude lower than the highest values shown in Fig. 2.20. The right ordinate of Fig. 2.20 gives the contribution of Stefan flux, i.e., the first term on the right hand side in Eqs. (2.15) and (2.16).

The calculated mass fluxes for T_S between 900 and 1200 °C for a fixed value of $\alpha(L)$ remain almost constant with very slight increase with increasing T_s. This can be attributed to a weak increase in the minority partial pressure (more so for larger values of $|\alpha(L) - 2|$) and a decrease in the diffusion coefficient with the increasing total pressure. However, this should not to be confused with the reality where the

Table 2.5 Molecular parameters used for computing binary diffusion coefficients

Species	σ (Å)	ε/k (K)	References
Zn (g)	4.70	522	[33]
Cd (g)	4.10	557	[33]
S_2 (g)	3.97	1183[c]	[34]
Se_2 (g)	3.576[a]	1130[b]	[32]
Te_2 (g)	3.887[a]	1490[b]	[32]
CO (g)	3.690	91.7	[35]
CO_2 (g)	3.941	195.2	[35]
N_2 (g)	3.798	71.4	[35]
H_2 (g)	2.827	59.7	[35]
Ar(g)	3.54	92.8	[35]

[a]Estimated from the molar volume at the melting point
[b]Estimated from the normal boiling temperature
[c]Reference [35] gave the parameter, Z, in Sutherland equation for viscosity. Comparing it with our viscosity equation in Appendix, $1 + Z/T = \Omega_v$. The value of 1183 K makes $1 + Z/T$ and Ω_v agree within +1.5% between 1000 and 1200 K

mass flux is likely to increase with T_s because the amount of excess element is fixed within an ampoule and α(L) is approaching 2 with increasing T_s.

2.2.3 *Diffusive Transport with Residual Gas of Impurities*

In a real PVT process, however, volatile impurities, such as H_2, H_2O, CO, CO_2, N_2, and O_2 resulting from the outgassing of the silica ampoule and/or from source material [36–38], form a significant amount of residual gas. Systematic studies [39–42] have reported on the residual gas formation in sealed silica ampoules. Since these residual species remain in the vapor phase, a third, stagnant component should be included in the diffusion analysis. The analytical solutions to the Maxwell equations for a three-species problem were first given by Gilliland [43] and can be derived in the following way.

The third equation can be decoupled by setting $J_Z = 0$ with Z standing for the residual gas component which represents all the residual species in the vapor phase other than the two transport species (A and B_2) and whose molecular parameters can be calculated as weighted averages based on the composition of the residual gas. We have

$$\frac{J_A}{D_{AZ}} + \frac{J_B}{D_{BZ}} = \frac{P}{RT(L-y)} \ln \frac{P_Z(y)}{P_Z(L)} \tag{2.22}$$

$$\frac{J_A + J_B}{D_{AB}} = \frac{P}{RT(L-y)} \ln \frac{\left(1 + J_B/J_A\right)P_A(y) - a\left(1 + J_A/J_B\right)P_B(y) - b}{\left(1 + J_B/J_A\right)P_A(L) - a\left(1 + J_A/J_B\right)P_B(y) - b} \tag{2.23}$$

where

$$J_B \equiv J_{B_2},\ a = \frac{r_{AB} - r_{AZ}}{r_{AB} - r_{BZ}},\ b = \frac{r_{AZ} - r_{BZ}}{r_{AB} - r_{BZ}} P \tag{2.24}$$

and

$$P = P_A(y) + P_{B_2}(y) + P_Z(y) \tag{2.25}$$

Again, $J = J_A = 2J_B$ should be used in the calculation. Equations (2.22) and (2.23) have been used by Sha et al. [7] and Palosz et al. [44] to analyze the mass transport in the PVT systems of ZnSe and CdTe, respectively.

For the given values of T(L), T(0), and α(L), $P_A(L)$ and $P_{B2}(L)$ can be calculated from the Gibbs energy of formation $P_A(L)P_{B2}^{1/2}(L) = K(T(L)) = \exp(\Delta G_f/RT)$. Then $P_A(0)$, $P_{B2}(0)$, $P_Z(0)$, and the mass flux J can be solved from Eqs. (2.22) and (2.23) with $y = 0$, $P_A(0)P_{B2}^{1/2}(0) = K(T(0))$, and the constant total-pressure condition with an input value of $P_Z(L)$. The second step can be repeated for different $P_Z(L)$ until the average residual pressure defined as:

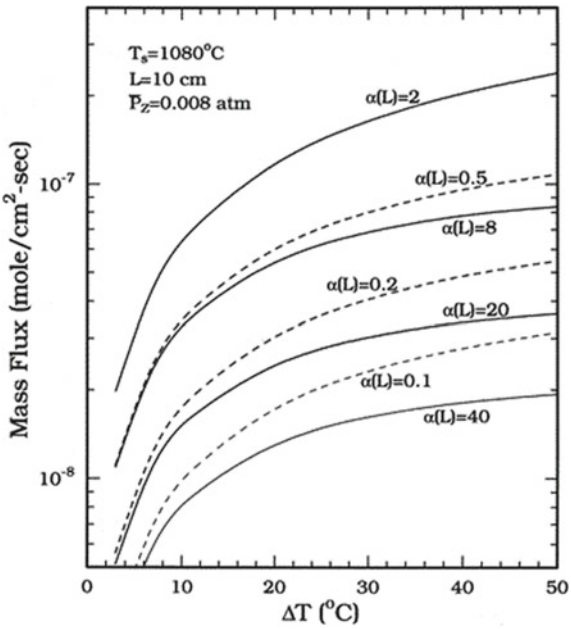

Fig. 2.21 Calculated mass flux of ZnSe as a function of ΔT under the same conditions as Fig. 2.20 except a residual gas pressure of 0.008 atm is present in the system. The composition of the residual gas used in the calculation is 36% CO_2, 26% each for CO and N_2 and 12% H_2

$$\bar{P}_Z = \frac{1}{L}\int_0^L P_Z(y)dy, \tag{2.26}$$

matching the experimentally determined pressure of the residual gas.

Figure 2.21 shows the calculated results for the mass flux in the ZnSe-residual gas system as a function of ΔT. The residual pressure adopted, 0.008 atm, was a typical value measured on the ZnSe growth ampoules by a total pressure gauge technique described later. By comparing the calculated results shown in Figs. 2.20 and 2.21, the mass flux decreases rapidly with the presence of the residual gas. For instance, at $T_S = 1080$ °C and $\Delta T = 30$ °C, with the presence of residual gas of 0.008 atm, the mass flux of ZnSe decreases about 13 and 2 times, respectively, for $\alpha(L) = 2.0$ and 8.0.

Figure 2.22 shows the mass flux as a function of total residual gas pressure for different stoichiometries of the source, α(L). The composition of the residual gas was chosen to be 25% each for CO and N_2 and 50% CO_2. The curves in Fig. 2.22 indicate that the residual gas starts to measurably reduce the mass flux when its total pressure approaches the excess pressure $|P_A - 2P_B|$. Beyond this region, the residual gas becomes the rate-limiting factor and the α(L) dependence of the flux becomes weak. The temperature dependence of the mass flux becomes relatively strong in the presence of residual gas. For instance, the mass flux for $\alpha(L) = 2.7$ and $P_z(L) = 0.01$ atm increases by almost 70 times when T_S changes from 900 to 1200 °C.

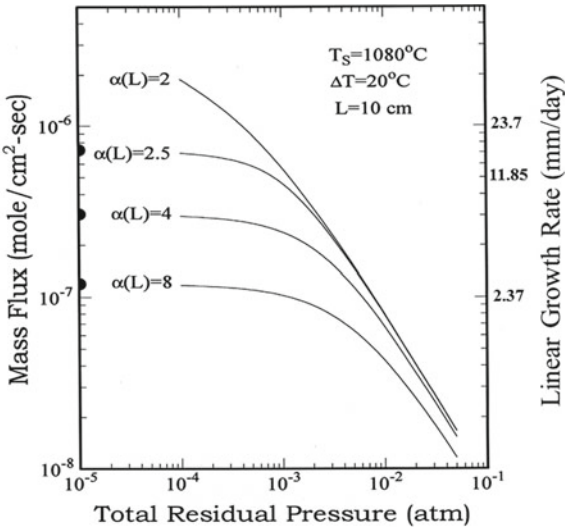

Fig. 2.22 Calculated mass flux of ZnSe as a function of $P_Z(L)$ for source temperature at 1080 °C and different values of α(L). The solid dots on the left axis are those under the same conditions but with a zero residual gas pressure (taken from Fig. 3 of Ref. [7])

2.2.4 Summary of One Dimensional Diffusion Analysis

From the results of the one-dimensional diffusion analysis, four experimentally adjustable parameters: the source temperature, the deposition temperature, the partial pressure ratio over the source and the residual gas pressure, determine the diffusive mass flux in a PVT system. However, two of these four parameters, the partial pressure ratio over source and the residual gas pressure, are more critical than the others. The source material with the composition closest to the congruent sublimation will have the highest transport rate of vapor species from the source to the crystal for all of the compound semiconductors, whether this composition is inside the homogeneity range of the compounds. At the same time, the residual gas pressure in the closed ampoule during the processing condition needs to be minimized to enhance the vapor transport rate. As shown in the later section, these two parameters are significantly dependent on the proper heat treatments of the starting materials for the optimum mass flux.

2.2.5 Convective Transport

Besides the mass flux from the diffusive transport, there will be contribution from convective transport caused by the Earth gravity. In a two-dimensional enclosure with side length of l and d, shown in Fig. 2.23a, if there is a thermal (T) or species concentration (N) gradient perpendicular to the gravitational field, which is directing toward–**Y** direction as shown in Fig. 2.23b, then a thermal convective flow, **V**, as shown in Fig. 2.23a will occur. The interaction between this convective flow and a

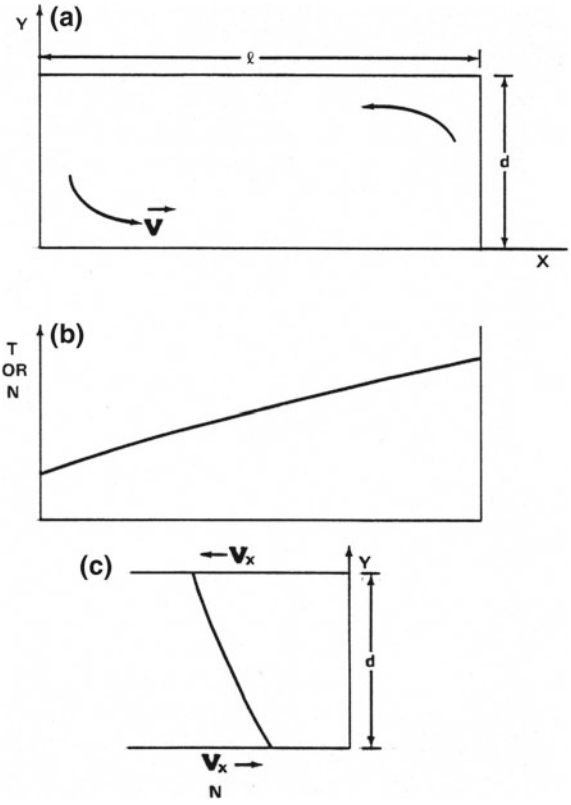

Fig. 2.23 **a** In a two-dimensional enclosure with **b** a positive thermal gradient perpendicular to the gravitational field directing toward –Y direction then **c** a thermal convective flow, **V**, will occur

concentration gradient along the **X** direction as shown in Fig. 2.23b gives rise to a concentration gradient $\frac{\partial N}{\partial Y}$ along the Y direction shown in Fig. 2.23c. The net mass flux resulting from this gradient is the convective contribution to the total flux and is in the order of

$$V_X d\left(\frac{\partial N}{\partial Y}\right) \approx V_x N|_{Y=0} - V_X N|_{Y=d} \tag{2.27}$$

Klosse et al. [45] have calculated this convective contribution to the total mass flux caused by a horizontal thermal gradient and a vertical gravity in a rectangular enclosure. The result is given in terms of a dimensionless quantity K, which is defined as the ratio of the mass transport of convection to diffusion:

$$J_T = (1 + K)J_D \tag{2.28}$$

where J_T is the total flux and J_D the diffusive flux given in last section. The expression for K is:

$$K = [A/(N_{Sc}N_{Gr})^2 + B]^{-1} \tag{2.29}$$

where A and B are geometrical parameters depending on the dimension of the enclosure. The numerical values for A and B as a function of the aspect ratio of l/d can be found in Fig. 4 of Ref. [45]. N_{Sc} and N_{Gr} are the Schmidt and Grashof numbers given by:

$$N_{Sc} = \mu/\rho D \tag{2.30}$$

$$N_{Gr} = d^3 g\alpha\rho^2[T(l) - T(0)]/\mu^2 \tag{2.31}$$

where μ is the viscosity, ρ the density, D the molecular diffusion coefficient, g the gravity and α the thermal expansion coefficient. Under the assumption of ideal gas for the transport fluid, ρ and α can be approximated as:

$$\rho = \sum_i \frac{P_i M_i}{RT_a} \tag{2.32}$$

and

$$\alpha \cong -\frac{1}{\rho}\frac{\partial\rho}{\partial T} \cong \frac{1}{T_a} \tag{2.33}$$

where P_i and M_i are the partial pressure and molecular weight of the species i, respectively, and T_a the average temperature of the enclosure. The detailed calculation of these thermophysical properties of the vapor phase, derived by Reid et al. [32], is given in the Appendix.

Appendix

A.1 Thermophysical Properties of Vapor Phase

A.1.1 Viscosity

The viscosity of a one-component gas phase can be calculated by assuming a Lennard-Jones 6-12 intermolecular potential between species as:

$$\Psi(r) = 4\varepsilon\left(\left(\frac{\sigma}{r}\right)^{12} - \left(\frac{\sigma}{r}\right)^{6}\right) \tag{34}$$

The two interaction parameter, ε and σ, are, respectively, the potential well depth and the intermolecular distance at $\Psi = 0$. The viscosity μ is then given by:

$$\mu = 26.69\frac{\sqrt{MT}}{\sigma^2\Omega_\upsilon} \tag{35}$$

where μ is in micro-poise, T in K, σ in $\dot{A}$ and

$$\Omega_\upsilon = \frac{A}{T_r^B} + \frac{C}{\exp(DT_r)} + \frac{E}{\exp(FT_r)} \tag{36}$$

where $T_\mathrm{r} = \mathrm{kT}/\varepsilon$ and $A = 1.16145$, $B = 0.14874$, $C = 0.52487$, $D = 0.77320$, $E = 2.16178$, $F = 2.43787$.

The viscosity of a gas mixture, μ_m, at low pressure is given by:

$$\mu_m = \sum_{i=1}^{n} \frac{y_i\mu_i}{\sum_{j=1}^{n} y_j\varphi_{ij}} \tag{37}$$

where

$$\phi_{ij} = \frac{\left(1 + \left(\mu_i/\mu_j\right)^{1/2}\left(M_j/M_i\right)^{1/4}\right)^2}{\left(8\left(1 + M_i/M_j\right)\right)^{1/2}} \tag{38}$$

and μ_i, and y_i are the viscosity of pure-component i and mole fraction of species i, respectively.

A.1.2 Thermal Conductivity

The thermal conductivity of a gas system, κ, is related to its viscosity, μ, by the Eucken factor, $\mathrm{f_{Eu}}$:

$$f_{Eu} = \frac{\kappa M}{\mu C_{\upsilon,m}} = 1.32 + 1.77\left(\frac{R}{C_{\upsilon,m}}\right) \tag{39}$$

where M is the molar weight, $C_{\upsilon,m}$ the molar heat capacity at constant volume and R the gas constant.

A.2 Thermophysical Properties of a Typical ZnSe PVT Growth System

T (source)	1160 °C	μ (viscosity)	4.3×10^{-4} poise (g/s cm)
T (crystal)	1130 °C	ν (kinematic viscosity) $= \mu/\rho$	36 stoke (cm^2/s)
P_{Zn}	0.11 atm	a (radius)	0.75 cm
P_{Se2}	0.0007 atm	L (length)	10 cm
$P_{residual\ gas}$ (36% CO_2, 26% CO 26% N_2 and 12% H_2)	0.01 atm	g_0 (gravitational acceleration)	980 cm/s^2
$\beta = 1/T$ (thermal expansion)	7.1×10^{-4} K^{-1}	κ (thermal conductivity)	5.42×10^{-4} J/cm s K
ρ (density)	1.2×10^{-5} g/cm^3	C_v (heat capacity)	0.76 J/g K

References

1. Y. Huang, R.F. Brebrick, J. Electrochem. Soc. **135**, 486 (1988)
2. R.F. Brebrick, A.J. Strauss, J. Chem. Phys. **40**, 3230 (1964)
3. D.A. Northrup, J. Phys. Chem. **75**, 118 (1971)
4. R.F. Brebrick, A.J. Strauss, J. Chem. Phys. **41**, 197 (1964)
5. Y. Huang, R.F. Brebrick, J. Electrochem. Soc. **135**, 1547 (1988)
6. R.C. Sharma, U.A. Chang, J. Cryst. Growth **88**, 193 (1988)
7. Y.G. Sha, C.H. Su, W. Palosz, M.P. Volz, D.C. Gillies, F.R. Szofran, S.L. Lehoczky, H.-C. Liu, R.F. Brebrick. J. Cryst. Growth **146,** 42 (1995)
8. R.F. Brebrick, H.-C. Liu, High Temp. Mater. Sci. **35**, 215 (1996)
9. R.F. Brebrick, J. Electrochem. Soc. **116**, 1274 (1969)
10. P. Goldfinger, M. Jeunehomme, Trans. Faraday Soc. **59**, 2851 (1963)
11. P.Z. Floegel, Anorg. Allg. Chem. **370**, 16 (1969)
12. R.F. Brebrick, J. Electrochem. Soc. **135**, 486 (1971)
13. H. Liu, Ph.D. Dissertation, Marquette University, March 1995
14. R.F. Brebrick, H.-C. Liu, J. Ph. Equilib. **17**, 495 (1996)
15. T.-C. Yu, R.F. Brebrick, J. Ph. Equilib. **13**, 476 (1992)
16. A.N. Nesmeyanov, *Vapor Pressure of the Chemical Elements* (Elsevier Publishing Co., Amsterdam/London/New York, 1963)
17. R.F. Brebrick, Prog. Solid State Chem. **13**, Ch. 5. in *Non Stoichiometry in Binary Semiconductor Compounds*, ed. by H. Reiss (Pergamon Press, Oxford 1967), p. 213
18. Su Ching-Hua, Mater. Sci. Semicond. Proc. **90**, 259 (2019)
19. R.F. Brebrick, J. Electrochem. Soc. **118**, 2014 (1971)
20. R.F. Brebrick, A.J. Strauss, J. Phys. Chem. Solids **26**, 989 (1965)
21. C.H. Su, P.-K. Liao, T. Tung, R.F. Brebrick, High Temp. Sci. **14**, 181 (1981)
22. R.F. Brebrick, J. Chem. Phys. **43**, 3846 (1965)

23. Su Ching-Hua, Cryst. Growth **281**, 577 (2005)
24. J.P. Schwartz, T. Tung, R.F. Brebrick, J. Electrochem. Soc. **128**, 438 (1981)
25. T. Tung, L. Golonka, R.F. Brebrick, J. Electrochem. Soc. **128**, 451 (1981)
26. C.H. Su, P.-K. Liao, R.F. Brebrick, J. Electrochem. Soc. **132**, 942 (1985)
27. K.-T. Chen, Y.-G. Sha, R.F. Brebrick, J. Vac. Sci. Technol. **A8**, 1086 (1990)
28. K.C. Mills, *Thermodynamic Data for Inorganic Sulfides, Selinides, and Tellurides* (Butterworth, London, 1974)
29. R.F. Brebrick, C.H. Su, P.K. Liao, *Semiconductors and Semimetals,* vol. 19, ed. by R.K. Willardson, A.C. Beer (Academic Press, NY, 1983)
30. M.M. Faktor, I. Garrett, *Growth of Crystals from the Vapour* (Chapman and Hall, London, 1974)
31. Su Ching-Hua, Cryst. Growth **80**, 333 (1987)
32. R.C. Reid, J.M. Prausnitx, T.K. Sherwood, *The Properties of Gasses and Liquids*, 3rd edn. (McGraw-Hill, New York, 1977), p. 113
33. C.H. Su, P.K. Liao, Y. Huang, S.-S. Liou, R.F. Brebrick, J. Chem. Phys. **81**, 11 (1984)
34. D.M. Shteingradt, V.E. Lyusternik, Russ. J. Phys. Chem. **56**, 1379 (1982)
35. R.A. Svehla, NASA Tech Report R-132 (Lewis Research Center, Cleveland, Ohio 1962)
36. G.J. Russell, J. Woods, J. Cryst. Growth **46**, 323 (1979)
37. G. Schmidt, R. Gruehn, J. Cryst. Growth **57**, 585 (1982)
38. Y. Morimoto, T. Igarashi, H. Sugahara, S. Nasu, J. Non-Cryst. Solids **139**, 35 (1992)
39. T.C. Harman, J.P. McVittie, J. Electron. Mater. **3**, 843 (1974)
40. W. Palosz, H. Wiedemeier, J. Cryst. Growth **131**, 193 (1993)
41. W. Palosz, F.R. Szofran, S.L. Lehoczky, J. Cryst. Growth **142**, 215 (1994)
42. W. Palosz, J. Cryst. Growth **267**, 475 (2004)
43. T.K. Sherwood, *Absorption and Extraction* (McGraw-Hill, New York, 1937)
44. W. Palosz, H. Wiedemeier, J. Cryst. Growth **129**, 653 (1993)
45. K. Klosse, P. Ullersma, J. Cryst. Growth **18**, 167 (1973)

Chapter 3
Vapor Transport Rate (Mass Flux) Measurements and Heat Treatments

Abstract The vapor transport rates have been measured experimentally for the systems of CdS, CdTe and ZnSe under various experimental conditions. To enhance the transport rate, the optimum procedures in the preparations of fused silica ampoule and heat treatments of starting materials have been established experimentally. From the theoretical results, the heat treatments were aimed at reducing the residual gas as well as shifting the source material toward congruent sublimation. A hydrogen reduction treatment was established in reducing the oxygen-related residual gas species and a baking under dynamic vacuum procedure was effective in changing the stoichiometry of source materials. Hence, the hydrogen reduction followed by the dynamic vacuum treatment procedure was established for the source to maximize the mass flux. Several in-situ dynamic measurements have been employed to monitor the partial pressures and transport rates. The mass flux in the ternary systems of $ZnSe_{1-x}Te_x$, $ZnSe_{1-x}S_x$ and $Zn_{1-x}Cd_xSe$ have been calculated from the one-dimensional diffusion model for the ternary systems and experimentally measured on the systems of $ZnSe_{1-x}Te_x$ and $ZnSe_{1-x}S_x$.

Keywords Mass flux · Vapor transport rate · Heat treatment of starting material · Hydrogen reduction · In-situ dynamic mass flux measurement

Measurements on vapor transport rate have been reported using various techniques which can be classified into two categories. The first involves visual observation of the linear growth velocity of the deposition in sealed ampoules inside a transparent furnace for systems such as HgI_2 [1, 2], CdTe and PbTe [3], and CdS [4]. The second type of transport rate measurement takes measurements of the total change in the mass of the source/deposition in a closed ampoule after the transport process has been conducted for a period of time. The latter method has been used for systems such as the chemical vapor transport (CVT) of GeSe-GeI_2 [5], the PVT of CdTe [6] and those investigations on the effects of controlled over pressures on the transport rate of CdTe [7–10], ZnSe [11], $CdSe_{1-x}S_x$ [12] and $ZnSe_{1-x}S_x$ [13]. The growth temperatures for ZnTe, ZnS and ZnSe compounds are too high to be processed in a transparent furnace which usually provides a maximum temperature of 900–950 °C. This precludes the use of the first technique on ZnTe and ZnSe-based compounds. The disadvantages of the second technique above are: (1) it yields the average transport rates and (2) it

© Springer Nature Switzerland AG 2020

C.-H. Su, *Vapor Crystal Growth and Characterization*,
https://doi.org/10.1007/978-3-030-39655-8_3

produces limited results since only one data point is determined, i.e. mass flux for a fixed set of T(source) and T(deposit), from each ampoule. Therefore, an in-situ dynamic mass flux measurement method [14, 15], discussed later in Sect. 3.3.1, was developed to be reused for the continuous measurement of the total mass transported in a closed ampoule as a function of time under different thermal conditions.

3.1 Mass Flux of CdS by PVT

The measurements of CdS transport rate by PVT were conducted by the first experimental type, i.e., observation of the transport in sealed ampoules inside a transparent furnace [4]. The testing conditions were divided into three categories:

(1) CdS PVT ampoules were sealed under vacuum.
(2) CdS PVT ampoules were sealed under different Ar pressures.
(3) CdS samples were annealed under controlled Cd vapor pressure before loading into the PVT ampoules which were then sealed under vacuum.

In these experiments, the 99.995% purity CdS source materials were provided by Eagle-Picher Inc. as a mixture of small chunks and powder. The test ampoules were made from T08 commercial grade of 16 mm outer diameter (O.D.), 10 mm inner diameter (I.D.) fused silica tubing supplied by Heraeus Amersil. After cleaning with distilled water, HF, methanol and acetone, the ampoules were baked out at 1140 °C for 3 h. They were sealed off under 10^{-2} Torr vacuum or certain Ar pressure after the CdS was loaded. Typically, an ampoule was 14 cm long with the CdS source at one end covering about 3 cm of its length. The ampoule was then placed inside a four-zone gold-coated transparent furnace mounted in such a way that it can be tilted to give different gravitational configuration. The typical thermal profile for the PVT measurements was 880 °C at the CdS source end and 850 °C at the cold end. Table 3.1 lists the experimental conditions for all of the 9 CdS runs.

The theoretical calculation on the diffusive mass flux for each experimental condition was performed by the procedure described in Sect. 2.2 with the transport parameters of viscosity and diffusion coefficient for a low pressure gas mixture estimated from kinetic theory of gas [16, 17] as described in Sect. 2.2 and Appendix of Chap. 2.

3.1.1 CdS Ampoules Sealed Under Vacuum

To study the convective contribution to the mass flux, the transport rates for ampoule CdS-1 were measured with the furnace in vertical stabilized (hot end on the top) and horizontal configurations. Ampoule CdS-1 was sealed off under vacuum and transport rate was determined from the time, observed in the transparent furnace, to transport all material from the hot to the cold end. It is known that under the vertical

Table 3.1 Experimental conditions and results for CdS transport rate measurements

Run	Source (g)	P_{Cd} anneal	P_{Ar} (atm)	T(L) °C	T(0) °C	Transport amount (g)	Time (h)	Rate (mole/cm^2-s)	Rate (mm/day)
CdS-1$^+$	1.798	No	0	880	845	1.798	59	7.5×10^{-8}	1.94
CdS-1	1.798	No	0	880	845	1.798	52	8.5×10^{-8}	2.20
CdS-2	1.791	No	0.23	880	835	0.13	328	9.3×10^{-10}	0.0240
CdS-4	1.803	No	0.07	895	850	0.22	306	1.8×10^{-9}	0.0466
CdS-5	1.145	No	0.13	895	850	0.19	306	1.5×10^{-9}	0.0388
CdS-6	1.239	Yes	0	880	850	Black residue left at the source end, contaminated by Si			
CdS-7	0.443	Yes	0	880	850				
CdS-8	0.653	Yes	0	880	850				
CdS-9*	0.639	Yes	0	880	850				

1. Column 3 indicates whether source materials have been annealed under P_{Cd} pressure
2. Column 4 gives the back-filled Ar pressure at room temperature
3. All runs are in horizontal configuration except the CdS-1$^+$ run

$^+$Vertical stabilized configuration

*Graphitized ampoule

stabilized configuration the gravity driven convection should be at its minimum. The two data of transport rates, given in Table 3.1 and presented in Fig. 3.1, were almost the same, within experimental error, which showed almost no convective contribution in this case. Figure 3.1 also shows the calculated diffusive mass flux, J, for $T(L) = 880\ ^\circ C$ and $L = 10$ cm, as a function of $\Delta T = T(L) - T(0)$ with various values of $\alpha(L) \equiv P_{Cd}(L)/P_{S2}(L)$. As the source material approaching congruent sublimation, or $\alpha(L) = 2.0$, the transport rate increases rapidly. The figure also shows that, for $\alpha(L) = 0.1$ or 10, the mass flux reaches saturation at $\Delta T \approx 30\ ^\circ C$ and a larger ΔT does not effectively further increase the mass flux.

Figure 3.2 shows the calculated profiles of partial pressure for Cd and S_2 along the 10 cm long ampoule for two ΔT values of 10 and 30 °C, $T(L) = 880\ ^\circ C$ and $\alpha(L)$

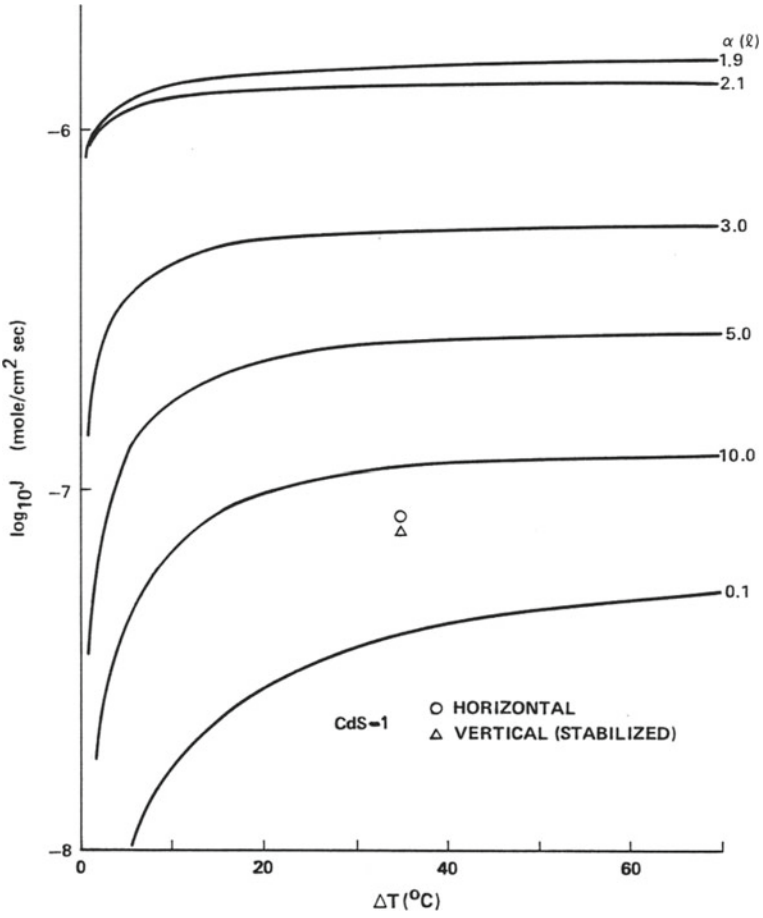

Fig. 3.1 Mass transport flux of CdS, J, in $\log_{10}$ scale for $T(L) = 880\ ^\circ C$ and $L = 10$ cm, as a function of $\Delta T = T(L) - T(0)$ with various values of $\alpha(L) \equiv P_{Cd}(L)/P_{S2}(L)$ (taken from Fig. 3 of Ref. [4])

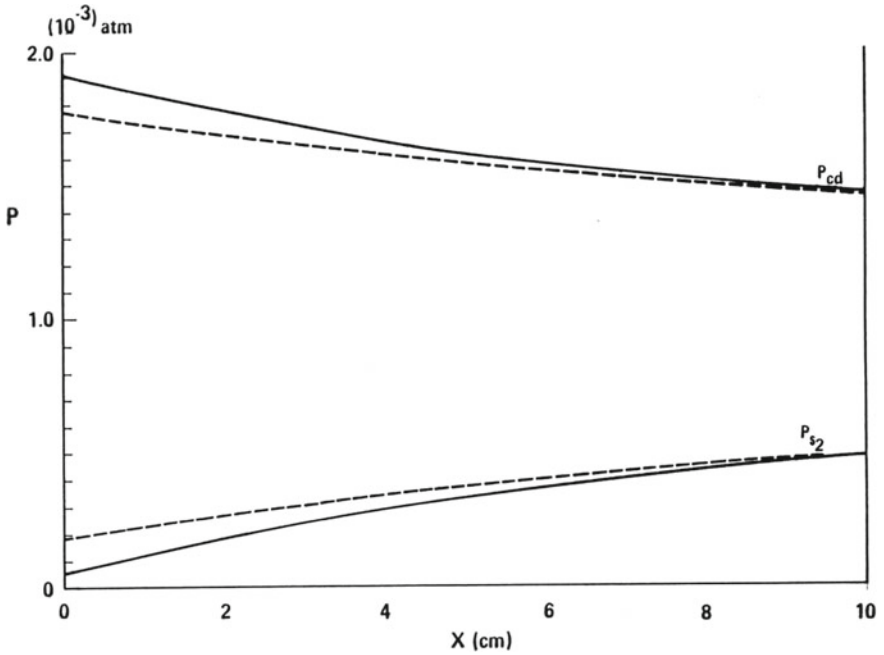

Fig. 3.2 Calculated partial pressures profiles along a 10 cm transport path for T(L) = 880 °C and α(L) = 3.0. Solid curves are for ΔT = 30 °C and dashed curves for ΔT = 10 °C

= 3.0. In the physical sense of the PVT process as given by Eqs. (2.15) and (2.16) in Chap. 2, the mass flux is the sum of (1) Stephen flow which is proportional to the partial pressure of the species and (2) the diffusive flow which is proportional to the pressure gradient. However, the formation of the CdS compound at the crystal end means that the flux needs to satisfy the equality, $J_{Cd} = 2J_{S2}$. From Fig. 3.2, with α(L) greater than 2.0, the Stephen flow carries flux of Cd more than twice of that of S_2 so that the diffusive flux of Cd is actually from the crystal toward the source end to fulfill the equality.

Figure 3.3 shows that, for a fixed α(L) and ΔT, the mass flux increases a small amount when T(L) increase from 800 to 1000 °C. Because as T(L) increases, although partial pressures increases, the corresponding diffusion coefficients decrease. The convective contribution to the mass flux in the horizontal configuration was also calculated as described in Sect. 2.2.5 and the value of $K \equiv J_T/J_D - 1$ was found to be negligible, in the order of 10^{-9} for 10 cm long, 1 cm diameter ampoule as demonstrated by the results from the CdS-1 run.

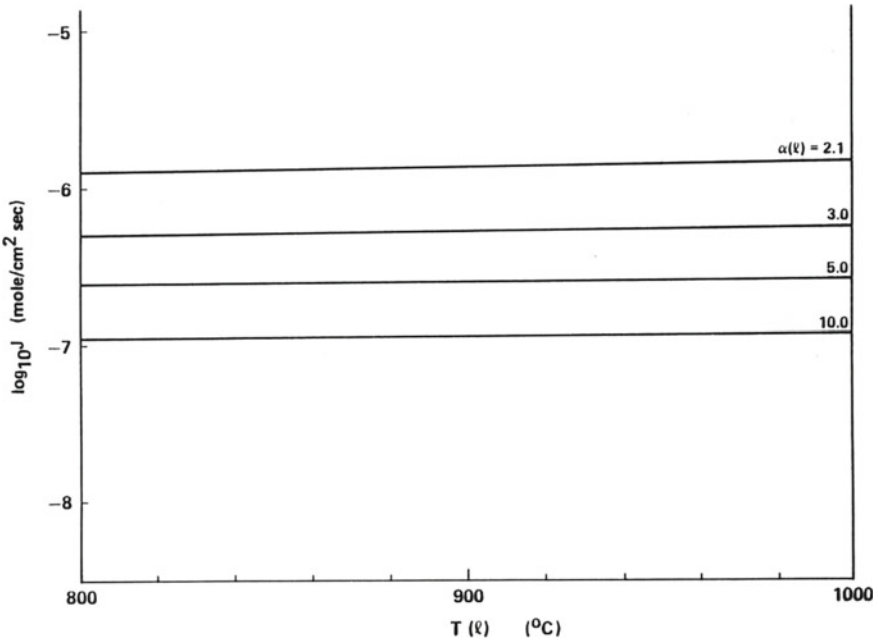

Fig. 3.3 Calculated diffusive mass flux, J, in $\log_{10}$ scale, as a function of T(L) for $\Delta T = 30$ °C and different values of α(L) (taken from Fig. 4 of Ref. [4])

3.1.2 CdS Ampoules Sealed with Ar Pressure

With the CdS samples loaded, the ampoules CdS-2, 4 and 5 were evacuated first and then back-filled with 0.07–0.23 atm of Ar before sealing by H_2–O_2 torch. The mass flux was measured from the amount of CdS transported in a period of about 2 weeks in the horizontal configuration with a thermal gradient given in Table 3.1. The fluxes were 5–8 times slower than that of the CdS-1, $P_{Ar} = 0$ atm run. Figure 3.4 shows the plot of the measured and calculated flux versus Ar pressure in a log-log scale. The Ar pressure in the figure is the value at 25 °C sealed-off environment and the actual Ar pressure inside the ampoule at 880 °C is about four times higher.

In Fig. 3.4, the calculated mass flux in the horizontal configuration, including the convective contribution, is shown as dashed curves whereas the diffusive-only flux is shown as solid curves. The convective contribution is essentially negligible for P_{Ar} less than 1 atm and the total mass flux reaches a maximum at $P_{Ar} \cong 7$ atm. The sum of the partial pressures of Cd and S_2 at 880 °C are 1.912×10^{-3} and 2.40×10^{-3} atm, respectively, for $\alpha = 2.0$ and 10.0. For the range of P_{Ar} shown in Fig. 3.4, the total pressure P_T ($\equiv P_{Cd} + P_{S2} + P_{Ar}$) is much larger than $P_{Cd} + P_{S2}$. Using the approximation of $\ln(1 - x) \cong -x$ when $x \ll 1$, Eq. (2.19) in Chap. 2 becomes:

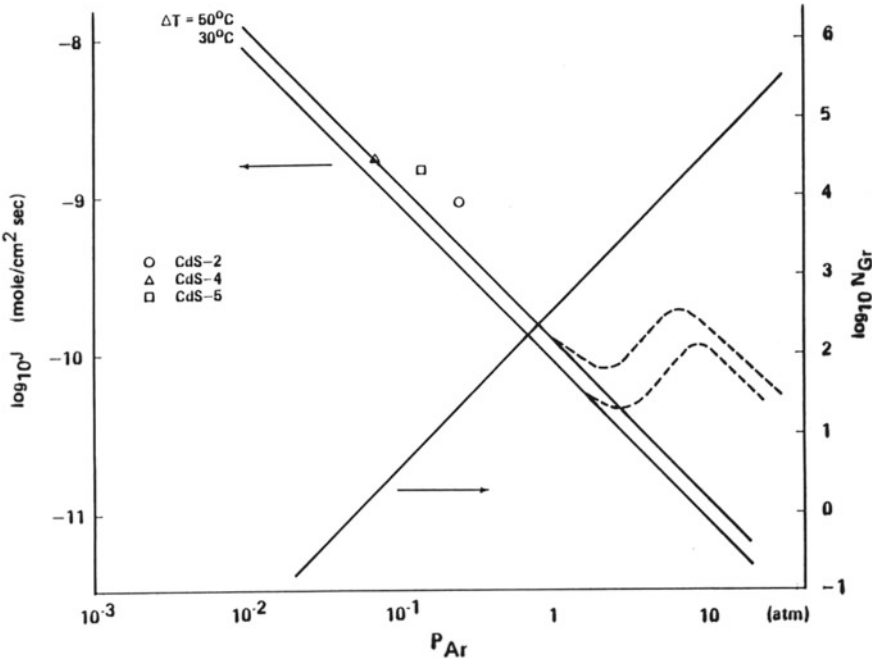

Fig. 3.4 Measured and calculated mass flux, J, as a function of P_{Ar} (at 25 °C) in a log-log scale for T(L) = 800 °C, for for α(L) = 3.0, L = 10 cm, inner diameter of 1 cm and ΔT = 30 °C, 50 °C. Solid curves are the calculated diffusive mass flux and the dashed curves are the results for horizontal configuration. Also shown is the calculated Grashof number (right scale), N_{Gr}, as a function of Ar pressure for the case of ΔT = 50 °C (taken from Fig. 6 of Ref. [4])

$$J \propto \frac{D_{AB}}{RT_a L}[P_A(L) - P_A(0)] \approx \frac{2D_{AB}}{RT_a L}[P_{B_2}(L) - P_{B_2}(0)] \tag{3.34}$$

Since $D_{AB} \propto \frac{1}{P_T}$ and the difference $P_A(L) - P_A(0)$ is almost independent of P_T, the diffusive mass flux $J \propto \frac{1}{P_T}$. As shown in Fig. 3.4, the plot of J versus P_{Ar} in a log-log scale is almost a straight line with a slope of −1.

The calculated Groshof number, N_{Gr}, for the case of ΔT = 50 °C, is also plotted as a function of P_{Ar} in Fig. 3.4 on the right hand scale. It goes almost linearly with P_{Ar} in the log-log scale and has the value of 3.69 and 3.25×10^5 at $P_{Ar} = 0.1$ and 30 atm, respectively.

3.1.3 CdS Samples Annealed Under Controlled Cd Over-Pressure

In an attempt to control the value of α(L), the CdS powder was annealed under Cd pressure before the mass flux experiments. First, about 6 g of CdS and 5.0 g of 99.9999% purity Cd, from Cominco Ltd, American were loaded and sealed under vacuum inside an ampoule. The annealing was conducted with a thermal profile as shown in Fig. 3.5 with CdS at 880 °C and Cd at 393 ± 3 °C. After 22 h of annealing, the ampoule was opened and the CdS material was retrieved as the source material for the subsequent mass flux experiment. Using the expression for the Cd pressure as a function of temperature (393 °C), Table 1.1 in Chap. 1, and the equilibrium constant for $\log_{10} P_A P_{B2}^{1/2}$ (at 880 °C), the partial pressure ratio, α, was calculated to be 2.45. The CdS-6 ampoule was loaded with the annealed material and sealed under vacuum. However, the transport rate was much slower and some black residues were observed at the hot (source) end after the transport was completed. Using energy dispersive x-ray spectrometry (EDS), the residues were identified essentially to be Si, or SiO_2, as shown in Fig. 3.6. Ampoules CdS-7 and-8 were repeated with the Cd element purified by a distillation process before loading in the transport ampoules. However, results similar to the CdS-6 run were observed. Actually, small pieces of fused silica were observed to detach from the wall of the hot end after the distillation. Therefore,

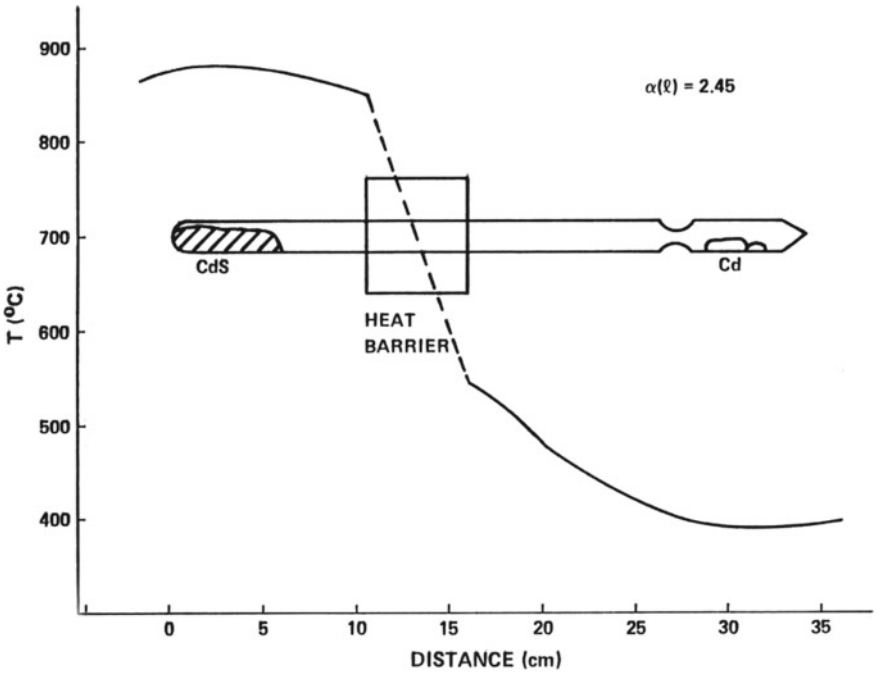

Fig. 3.5 Thermal profile for the annealing of CdS source material (taken from Fig. 2 of Ref. [4])

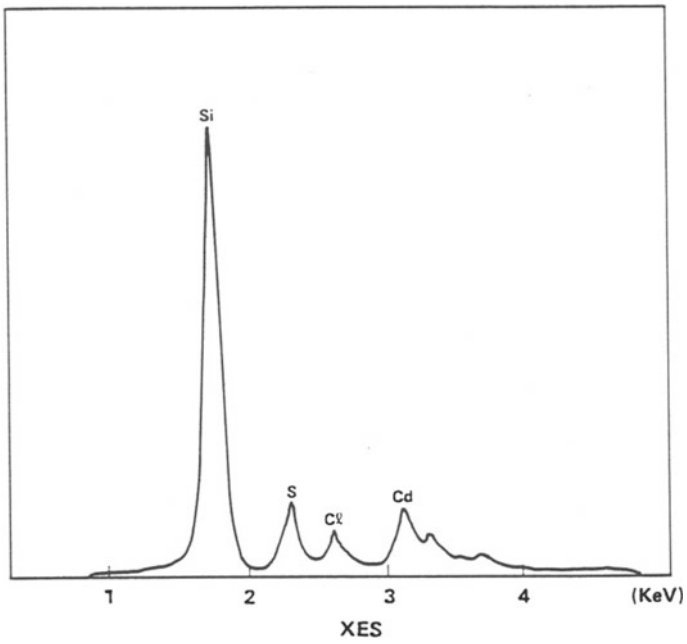

Fig. 3.6 Energy dispersive x-ray (EDS) spectrum on the black residues (taken from Fig. 7 of Ref. [4])

the annealing ampoule for the CdS-9 run was graphitized (or carbon coated) by pyrolysis of methane at 1050 °C for 80 min. After the run, the black residues, in much smaller amount than CdS-6, 7 and 8, were still found at the hot end.

3.1.4 Summary on PVT of CdS

In summary, the transport rates measured for the horizontal and vertical-stabilized configurations show that the convective contribution is negligible in this case. Using the density of CdS, the measured transport rates (mole/cm^2-s) give in Table 3.1 can be converted into linear growth rate in mm/day, which is given in the last column in Table 3.1. The growth rates of about 2 mm/day for the ampoule sealed under vacuum are too low and the 0.047 mm/day with residual gas of 0.07 atm is unpractical for production. Among the four parameters that control the mass flux, i.e., T(L), ΔT, α(L) and P_{Ar}, the results clearly show that the last two parameters are much more critical than the first two. As shown in Fig. 3.1, the mass flux can be as high as 1 $\times$ 10^{-6} mol/cm^2 s, or 27 mm/day, if the stoichiometry of the source material can be adjusted to close to α(L) = 2.0 and the residual gas minimized to 10^{-4} atm and lower.

It should be noted that the comparison between the theoretical and experimental mass flux of CdS-1 given in Fig. 3.1 does not necessarily imply that the α(L) for CdS-1 to be about 0.1 or 10. In this run, all of the source CdS has be transported so that the α(L) value changed continuously during the run. The final part of the source material could be very Cd-rich or S-rich, corresponding to very high or low values of α(L), respectively, and would take a long time to transport. The annealing method used here should be able to fulfill the purpose of controlling α(L) if it were not contaminated by Si during anneal. The reactions between elements and fused silica have been reported in many studies. Fochs et al. [18] found that silica particles were carried upwards into the growing crystal of CdS in a vapor growth experiment. But they concluded that the contamination of silica was originated from the starting material and not the result from chemical reaction between CdS and ampoule material. During the annealing of CdTe, the contamination of CdTe by Al and Si was reported [19] to be originated from the quartz tubing and Cd reservoir. Using secondary ion mass spectroscopy (SIMS), Morimoto et al. [20] found impurities of Si and Al in the remainder of the CdS source material after part of it has been transported. Russell et al. [21] associated the incidence of voids found in vapor-grown CdS crystals with the minute particles of SiO_2 that originated from the fused silica ampoule wall. Su et al. [22] recognized that the adhesion of samples to the silica wall, or "wetting", during the homogenization of HgCdTe was caused by the chemical reaction between Cd and silica ampoule and, consequently, eliminated the "wetting" problem by adopting a slower heating rate to reduce the chemical potential of Cd. It was also reported recently [23] that after a simple pre-treatment of HF etching of the fused silica growth ampoule for 30 min to modify the surface features of its inner wall, the reduction in contact area between ampoule and grown crystal results in less chemical interaction between the sample and the container, which causes fewer "wettings" and better structural quality of the vapor-grown crystals of ZnSe, Fe-doped ZnSe and melt-grown PbTe.

3.2 Mass Flux and Heat Treatments of CdTe

3.2.1 Vapor Phase Stoichiometry

From the experimental and theoretical results, to enhance the crystal growth rate, or to improve the mass flux, the first requisite is to adjust the stoichiometry of the source material closer to congruent sublimation, i.e., $\alpha(L) = 2.0$. However, the partial pressures of the species A and B_2 in equilibrium with the AB semiconducting compounds, at a fixed temperature, can vary by orders of magnitude as the composition of the compound varies over the narrow homogeneity range from A-saturation to B-saturation. To demonstrate that it is essentially impossible to weigh in the exact amount of elements of A and B to reproducibly synthesize the compound into the composition at congruent sublimation, several batches of CdTe were synthesized from pure Cd and Te elements and their vapor phase compositions were determined

Table 3.2 Amounts of Cd and Te, the corresponding Te content, the homogenization temperature, T_{Hom}, and the homogenization duration for each batch

Batch	Cd (g)	Te (g)	$X_{Te} - ½$	T_{Hom} (°C)	Time at T_{Hom} (h)
6	61.1715	69.4311	-4.6×10^{-5}	925	63
7	71.1613	80.7791	-1.7×10^{-5}	925	16
9	64.3485	73.0792	9.8×10^{-5}	955	64
10	77.0927	87.5088	-2.6×10^{-5}	1015	39
11	95.1116	107.9900	3.8×10^{-5}	985	40
13	46.5623	52.8885	13.8×10^{-5}	940	21

by optical absorption technique [24]. The synthesis ampoules were made from either 27 × 25 (27 mm O.D., 25 mm I.D.), 23 × 20 or 22 × 20 mm fused silica tubing supplied by Heraeus Amersil, Inc. The ampoules were cleaned and baked at 1045 °C under vacuum for over 16 h and, except for one batch, #13, were graphitized to form a carbon layer inside by flowing a mixture of 10% methane-Ar gas at 1045 °C for 10 min. The starting elements were quadruple zone refined (QZR), six-nine grade, Cd rods and QZR, six-nine grade Te bars from Johnson Matthey, Inc. The elements were weighed to the resolution of 0.1 mg. The ampoules were sealed under vacuum after the elements had been loaded with the Cd short rods surrounded by the Te chunks. The sealed ampoules were heated inside a furnace with an isothermal heat-pipe liner from room temperature to the homogenization temperatures in several hours and maintained at the homogenization temperature, T_{Hom}, for certain hours before cool down. On batch #6 the furnace was heated from room temperature to 500 °C in 1 h and maintained at 500 °C for 22 h before being heated to 925 °C in 2 h. The amounts of Cd and Te, the corresponding gross Te mole fraction, T_{Hom} and the time at T_{Hom} for each ampoule are listed in Table 3.2. During the heat-up the homogenization reaction took place at the CdTe-Te eutectic temperature of 447.2 °C [25]. The readings of the thermocouple attached to the ampoule jumped from 450 °C to over 500 °C (600 °C on batch #11) within 1 min because of the heat from the exothermic eutectic reaction.

3.2.2 Heat Treatments of CdTe for PVT

After the homogenization process, the ampoule for each batch was opened and the reacted sponge like CdTe was crushed, ground and mixed with mortar and pestle into particles of diameter less than 0.5 mm. The partial pressures of Cd and Te_2 were measured by the optical absorption technique described in Sect. 2.1.3. One set of the optical cells was loaded with the as-synthesized CdTe material from various batches and sealed under vacuum. The other set of the cells were loaded with the as-synthesized materials followed by a heat-treatment process to adjust the stoichiometry prior to seal off. The heat treatment of these cells was performed by connecting the loaded cell horizontally to a turbo-molecular vacuum pump. After

Table 3.3 Amounts of CdTe loaded, heat-treatment conditions, the measured partial pressure of Te_2, P_{Te_2}, and the pressure ratio, $\alpha \equiv P_{Cd}/P_{Te_2}$, at 870 °C for as-synthesized and heat treated batches

Cell	Amount of CdTe (g)	Heat-treated temperature (°C)	Heat-treated duration (min)	P_{Te_2} (atm) at 870 °C	$\alpha \equiv P_{Cd}/P_{Te_2}$ at 870 °C
6	15.0	–	–	4.06×10^{-3}	1.92
7	15.0	–	–	1.65×10^{-1}	0.00742
7A	13.0	870	8	3.44×10^{-3}	2.47
9	12.4	–	–	8.90×10^{-2}	0.0187
10	14.9	–	–	4.95×10^{-3}	1.43
10A	20.3	870	8	2.74×10^{-3}	3.47
11	6.9	–	–	1.51×10^{-2}	0.268
11A	20.0	860	8	2.96×10^{-3}	3.11
13A	17.9	800	8	4.18×10^{-3}	1.84

the vacuum level stabilized, a horizontal tubular furnace at the processed temperature was slid into cover the cell which was then baked out under dynamic vacuum. Table 3.3 lists the cell number (corresponding to the CdTe batch in Table 3.2), the amounts of CdTe loaded, the bake-out temperature and the bake-out duration for each optical cell. The amounts of CdTe as well as the bake-out temperatures were selected to match the growth conditions usually employed for the crystal growth of CdTe by PVT. The loss of the material during the baking process under vacuum was measured. After baking at 870 °C for 8 min the loss of a typical 18 g charge of CdTe was 1.8 g, i.e. about 10%.

The optical absorption spectra were measured on these cells and the partial pressures of Te_2 were taken as the average of the values calculated from the Beer's law constants established in the calibration runs of pure Te for several wavelengths between 363.4 and 537.2 nm [26]. For each cell the partial pressure of Te_2 was measured while the sample was held at 870 °C and the optical cell was at 900 °C. The base line was established with the sample at 400 °C and, for each cell, the sample was held at the 870 °C for at least 24 h prior to the measurements. The measured partial pressure of Te_2 at 870 °C for each optical cell is given in the 5th column of Table 3.3. The given values were usually the average of two measurements obtained after the cells were held at temperature for 24 and 48 h. The corresponding partial pressures of Cd can be obtained from the stoichiometric invariant, ΔG_f, the Gibbs energy of formation of CdTe from the vapor phase [27]:

$$\Delta G_f = RTln\left(P_{Cd}P_{Te_2}^{\frac{1}{2}}\right) = -68640 + 44.94T\left(\frac{cal}{mole}\right) \tag{3.35}$$

The stoichiometry of the vapor phase at 870 °C, defined as $\alpha \equiv P_{Cd_2}/P_{Te_2}$ was then calculated for each cell using the measured P_{Te_2} and the calculated P_{Cd} and is

given in the last column of Table 3.3. The vapor-phase stoichiometry at temperatures other than 870 °C was also measured for cell 10A and is plotted in Fig. 3.7. The first series of measured P_{Te_2} are shown as open circles which started at about 825 °C (1000/T = 0.91). Several measurements were taken as the sample temperature was increasing to above 880 °C before the sample was cooled to 795 °C. The second series of measurements is shown as solid squares and agreed well with the results of the first series. The time between each run is also given in the figure. Comparing with the solid line shown as the P_{Te_2} for the congruent sublimation condition, i.e. $\alpha = 2.0$, the CdTe sample in Cell 10A maintained slightly Cd-rich over the temperature range.

The measured results show that the vapor composition at 870 °C over various as-synthesized CdTe batches, having total amounts of material from 99 to 203 g and gross Te mole fraction, X_{Te}, from 0.499954 to 0.500138, were always Te-rich, i.e., $\alpha < 2.0$. A possible cause for the Te-rich nature of the optic cell samples is that during the grinding of the synthesized material, occasionally, a small smear of un-reacted Cd element was found and was taken out. To estimate the stoichiometry of our as-synthesized materials, we studied the previously measured partial pressures of Te_2 in equilibrium with four CdTe samples of known condensed-phase compositions

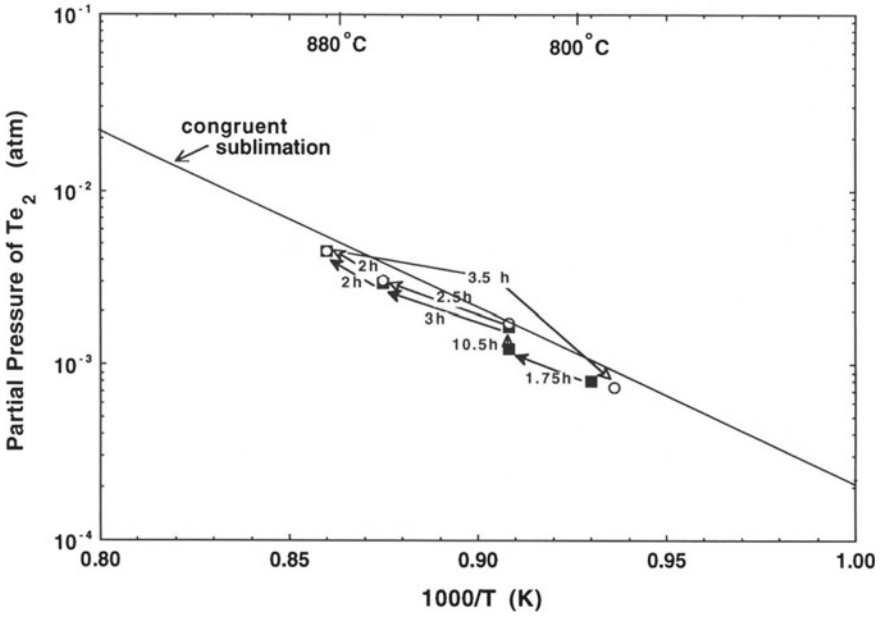

Fig. 3.7 The measured P_{Te_2} as a function of 1000/T for cell 10A. The first series of measured P_{Te_2}, shown as open circles, was started at about 825 °C (1000/T = 0.91). Several measurements were taken when the sample temperature was raised to above 880 °C before it was cooled to 795 °C. The second series of measurements is shown as solid squares. The time between each run is also given (taken from Fig. 1 of Ref. [24])

Table 3.4 Te mole fraction, X_{Te}, and measured P_{Te_2}, at 870 °C for CdTe samples from Ref. [28]

Samples	$X_{Te} - 0.5$	P_{Te_2} (atm)
CT-93E	4.4×10^{-5}	0.135
CT-92A	2.2×10^{-5}	0.105
CT92-C	1.4×10^{-5}	0.0595
CT92-D	1.2×10^{-5}	0.0306
Congruent sublimation[a]	0.3×10^{-5}	0.00396

[a]Reference [29]

over the temperature range 635–1025 °C [28]. The measured P_{Te_2} at 870 °C and the corresponding Te contents for these four samples were scaled from Figs. 2 and 4 of Ref. [28], respectively, and are tabulated in Table 3.4. By comparing the measured P_{Te_2} of our as-synthesized samples with those in Table 3.4, it can be summarized that (a) the samples in cell #6 and #10 were near the congruent sublimation composition at 870 °C (from a defect chemistry analysis [29], the congruent sublimation composition is $X_{Te} - 0.5 = 0.3 \times 10^{-5}$); (b) having $P_{Te_2} = 0.165$ atm at 870 °C the sample in cell #7 was almost Te-saturated with $(X_{Te} - 0.5)$ greater than 4.4×10^{-5} (note: the equilibrium P_{Te_2} for Te-saturated condition at 870 °C is 0.18 atm [28]); (c) the sample in cell #9, with the measured $P_{Te_2} = 0.089$ atm at 870 °C, has composition $(X_{Te} - 0.5)$ in the range $1.4–2.2 \times 10^{-5}$; (d) the CdTe in cell #10 and #11 have $(X_{Te} - 0.5)$ values below 1.2×10^{-5} and above that for congruent sublimation as given in Table 3.4, i.e. $(X_{Te} - 0.5) = 0.3 \times 10^{-5}$, with the value for cell #10 lower than that for cell #11.

Table 3.3 clearly shows that after the heat treatment of baking under dynamic vacuum, the vapor-phase compositions moved toward that of congruent sublimation with the final measured α values varying from 1.84 to 3.47. The change in composition stopped when the sample reached the congruent sublimation condition because the sample started to lose Cd and Te at the same rate through the sublimation process. The rate-controlling step for the heat treatment should be the solid-state diffusion inside each CdTe particle. The composition of the sample in each cell changed from its original value as outlined in the last paragraph to a value close to that of congruent sublimation during the 8 min bake out even when the starting composition was near the Te-saturated condition such as the case of cell #7. The required baking time can be estimated from the CdTe inter-diffusion coefficient reported by Brown et al. [30] which gave $D_{CdTe} = 3.4 \times 10^{-5}$ cm^2/s at 870 °C. The estimated diffusion length $(Dt)^{1/2}$ for 8 min annealing time is 0.128 cm, which is about 5 times the radius of the ground particle. Furthermore, although the heat treatment was performed at 870 °C the heat-treated sample remains close to the congruent sublimation condition in the temperature range 800–880 °C as indicated in Fig. 3.7. This was also evident from the defect chemistry analysis in Ref. [29] which reported that the congruent sublimation composition almost follows a constant X_{Te} curve for temperatures below 900 °C.

The large range of α for the as-synthesized CdTe source materials implies that the assumption of $\alpha(L) = 2.0$ in the analyses of CdS PVT process [31, 32] is not justified. Ballentyne et al. [33] claimed to make the CdS source material "more stoichiometric"

by heating the material at 900 °C in a slow flow of Ar for 4 to 5 h which can be related to the method of baking under dynamic vacuum.

3.3 Mass Flux and Heat Treatments for ZnSe System

3.3.1 In-Situ Dynamic Mass Flux Measurements

A continuous measurement of the total mass change in a closed ampoule by an in-situ dynamic technique was developed [14, 15]. A schematic of the experimental ampoule used is shown in Fig. 3.8. The two legs attached to the left end of the ampoule serve as a fulcrum. A three-zone tubular resistance furnace was employed to provide the thermal profile for the transport experiments. A temperature maximum was intentionally set up to create a steep thermal gradient just inside the deposition area so that its location was limited to the narrow region near the ampoule end. The right end of the ampoule was connected, via a ceramic block, to a ceramic lever which extended out of the furnace and rested on a wire suspended from a Mettler AE 100 electronic balance. The temperatures, at the source and at the deposition region, were measured by two thermocouples placed at the ends of the ampoule and together with the balance readings were recorded by a computer at 15 or 30 min intervals. The balance readings were then converted to the amount of mass transported using the dimensions of the ampoule/lever assembly. These data were plotted versus time and the mass flux was obtained from the slope of the curve. For most of the runs a few

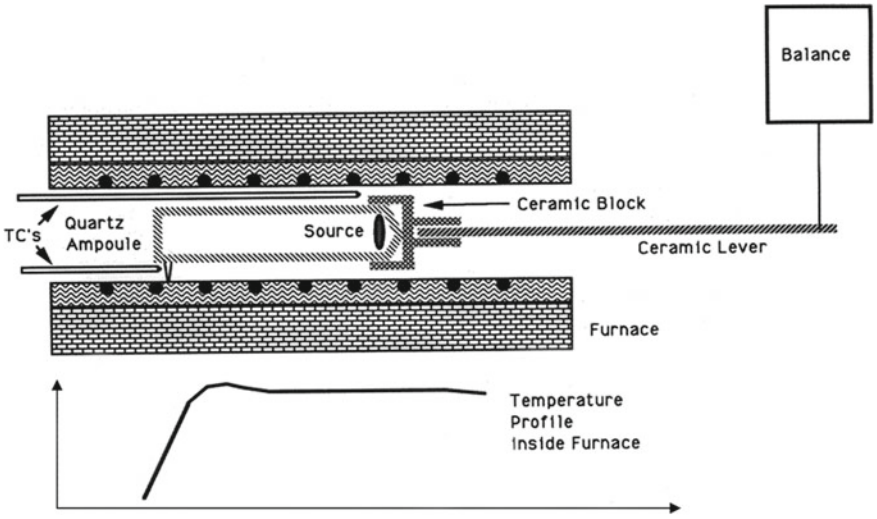

Fig. 3.8 Schematic of set-up for in-situ dynamic mass-flux measurements (taken from Fig. 1 of Ref. [14])

different temperature settings were used to determine the dependence of the mass flux on the source temperature. After all the material has transported the accuracy of the measuring system can be confirmed by comparing the total transport mass measured with the total mass loaded and another run using the same ampoule can proceed by simply reversing the temperature gradient.

3.3.2 Heat Treatments of Source Materials

Two methods were adopted to adjust the stoichiometry of the starting source materials. One is to bake out the material at the processing temperature under dynamic vacuum (method A). The change in stoichiometry stops when the material sublimes congruently. The other method is to distill the material by subliming it from one end of the ampoule to the other under dynamic vacuum and an auxiliary heater can be used to confine the deposition to a designated region (method B). Commercially available ZnSe was obtained from both Cleveland Crystals, Inc. (purity 99.995 or 99.999%) and Eagle Picher Research Laboratory (high purity grade). Both heat-treatment methods were applied after these starting materials were ground into powder. In method A, the bake-out was performed for about 10 min at 1080 °C. This temperature was also used in method B at the subliming end. At the end of the distillation all of the starting ZnSe was transported in most of the runs. The measurements of mass flux for the PVT experiments of ZnSe [14, 15] were performed using this in-situ dynamic technique. The experiment ampoules were made of 15 mm ID, 18 mm OD silica tubing and were about 12 cm in length. The cleaned and outgassed ampoule was loaded with 2–3 g of heat-treated ZnSe and sealed at a pressure of 5×10^{-6} Torr or less. Figure 3.9 shows the measured mass transported as a function of time for a typical run.

A series of transport experiments was performed and the results of the mass flux are plotted in Fig. 3.10 versus the reciprocal of the source temperature. Each mass

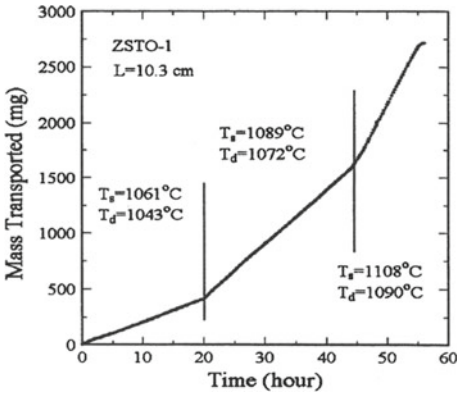

Fig. 3.9 Measurements of ZnSe mass flux as a function of time for three different temperatures of source (T_s) and deposition (T_d)

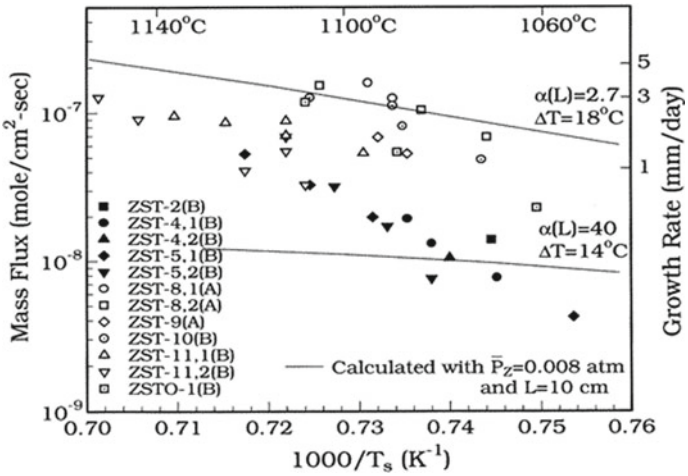

Fig. 3.10 Mass flux versus the reciprocal of the source temperature from different ampoules tested. Each mass flux value was derived from a well defined straight line on a plot of mass transported versus time and was normalized to a transport length of 10 cm (taken from Fig. 4 of Ref. [14])

flux value was derived from a well defined straight line generally consisting of 40 or more data points on the mass versus time plot and was normalized to L = 10 cm. Solid symbols represent the runs where the source materials were from Cleveland Crystals and open symbols from Eagle Picher. With a few exceptions, the difference in temperature between the source and deposition region, ΔT, was set between 13 and 20 °C. In general, the source materials from Cleveland Crystals (ZST-2, 4, and 5) result in somewhat lower fluxes with stronger temperature dependence than those of source materials from Eagle Picher. The methods of heat treatment, given in parentheses, method A and B described above, showed that samples heat treated by method A exhibited slightly higher transport rates than those heat treated by method B. The total residual pressure were measured (details described in next section), which ranges from 0.0011 to 0.0041 atm at room temperature and four different species were found—H_2, CO, N_2, and CO_2. The majority species is CO_2 which accounts for 28–43% of the total amount. CO and N_2, being indistinguishable by the measuring method, together contributes 35–64% and H_2 accounts for the remaining 8–22% of the residual vapor.

For a comparison with the experimentally measured transport rates, four parameters are needed to perform the one-dimensional diffusion limited calculation. The source temperature, T_s, and the average of the pressures and compositions of the residual gas measured from four experiment ampoules, were used as input values for two parameters. Two theoretical curves were calculated. The first one is the upper limit for the mass flux and was calculated with ΔT = 18 °C and α over the source, α(L) = 2.7 and the lower limit of the mass flux was calculated using ΔT = 14 °C and α(L) = 40. The composition of the residual gas used in the calculations was 36% CO_2, 26% each for CO and N_2, and 12% for H_2. Most of the experimental data points

fall between these two curves and some agree with the upper curve which represents the highest mass flux achievable under the experimental conditions. The stronger temperature dependence of the mass flux measured from some ampoules could be caused by a progressive improvement towards the congruent subliming condition of the source materials with increasing source temperature.

3.3.3 Measurements of Residual Gas Pressure and Composition

As discussed early, beside the stoichiometry of the source materials, the other parameter which hinders the transport rate in a closed vapor transport system is the residual vapor species outgassed during the growth process. The technique and the apparatus for the residual gas measurement were described in Refs. [34–37]. Briefly, the processed ampoule was placed in a vacuum chamber connected to a pressure gauge and a vacuum system. After outgassing the chamber with the ampoule inside at room temperature under high vacuum, the valve between the chamber and the vacuum system was closed. Then, the ampoule was broken by sliding and striking its L-shape tip against an obstacle and the pressure change in the chamber was recorded. The residual pressure in the sealed ampoule was calculated based on the chamber-to-ampoule volume ratio. Determination of the gas composition was made by selectively freezing-out the gas components with a cold finger cooled to a predetermined temperature with appropriate cold bath mixtures. Based on the literature [38–40], it has been assumed that the residual gas may consist of H_2, H_2O, CO, CO_2, N_2, and O_2 molecules, although, the amount of CO, N_2, and O_2 could not be determined separately by this technique. From the mass spectroscopic studies [40, 41], it has been found that the presence of O_2 and N_2 in residual gas can be ignored. Also, the presence of H_2 in most of our ampoules precludes the simultaneous presence of O_2 at elevated temperatures. Therefore, it was assumed that the amount of O_2 in the residual gas under our experimental condition is negligible. After the vapor transport measurements, the pressures and the compositions of the residual gas inside several ZnSe ampoules were measured and listed in Table 3.5. For the first five ampoules which were heat treated by method A or B, the majority species is CO which accounts for 35–64% of the total except for the ZSTO-3 ampoule. The comparison of the residual gas pressures between the ZnSe processed ampoules and those ampoules heat treated under similar conditions but without the presence of ZnSe [35] indicates that the total residual gas pressures in the ZnSe ampoules are about one order of magnitude or more higher than the empty one. The fact that the residual gas composition of the ZnSe ampoules is dominated by carbon oxides (CO and CO_2) whereas that of the empty ampoules consists of a high percentage of hydrogen and water implies that the ZnSe starting material was the potential source of carbon and oxygen in these processed ampoules. Therefore, some of the starting materials of ZnSe were treated by H_2 reduction before the heat treatment. During this reduction process

Table 3.5 Residual gas pressures and compositions in the processed ZnSe ampoules

	Pressure (10^{-3} atm) at R.T.			Composition (vol. %)			
Run #	Total	$H_2 + H_2O$	$H_2O + CO + 2CO_2$	H_2O	CO_2	CO	H_2
ZST-6[b]	2.90	0.25	3.6	<1	30	62	8
ZST-7[b]	0.77	0.16	0.93	<1	43	35	21
ZST-9[a]	1.16	0.12	1.5	<1	42	48	10
ZST-10[b]	1.36	0.14	1.7	<1	28	64	8
ZSTO-3[b]	2.68	0.05	2.6	<2.5	<1	96	<1.5
Empty[d]	0.23	0.10	0.23	40	<1	60	<1
ZST-13[e]	0.25	–	0.38	<1.5	53	47	<1
ZST-15[c]	0.58	0.36	0.30	<1.5	13	25	61

[a]Ground sample, heat treated by baking under dynamic vacuum (method A)
[b]Ground sample, heat treated by baking and distillation (method B)
[c]Ground sample, heat treated by H_2 reduction and baking under vacuum (method C, optimum method)
[d]Palosz et al. [35]
[e]Chunky sample, heat treated by baking under vacuum

the ZnSe ampoules were back filled with high purity H_2 gas and baked at elevated temperatures. General conclusions from the results listed in Table 3.5:

1. CO_2 might have been generated by the reaction between H_2O and CO
2. No H_2 was found in the chunky sample (ZST-13)—ground ZnSe is the primary source of H_2 (H_2O)
3. Relatively large amount of H_2 was trapped during the heat treatment under H_2 atmosphere (61% for ZST-15).
4. Other ampoules (ZST-6, 7, 9 and 10) have H_2 contents of 8–21%, which were probably generated by H_2O trapped in the samples and released later when reacting with CO.

The residual gas pressures for the last two ampoules, ZST-13 and 15 were about 12 times lower than that of the first five ampoules. In ZST-13, un-ground, chunky, starting materials were loaded directly into the ampoule and the residual gas pressure was close to that of the empty reference ampoule. As for the ZST-15 ampoule, the as-supplied chunks were ground and then treated by H_2 annealing as well as baking under vacuum prior to sealing. The residual gas pressure in the ampoule was about three times higher than that in the empty ampoule, but most of the gas consisted of hydrogen. The major factor in limiting the diffusive rates of the transport species in our system is the presence of carbon oxides. The high content of oxides in the ampoules loaded with ZnSe is apparently due to the presence of solid oxides and/or graphite in the original source material. The oxygen amount is significantly reduced in the second group where the source materials either had a limited surface area or were hydrogen treated prior to sealing. Evidently, oxidation of the source surface from exposure to air plays a major role in contributing to the amount of residual

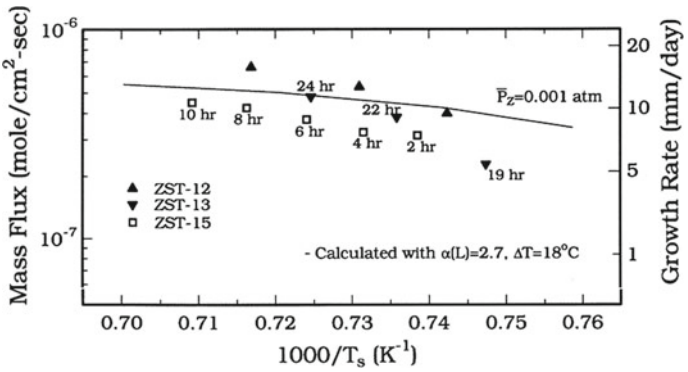

Fig. 3.11 Mass flux of ZnSe for ZST-12, 13 and 15 measured by the in-situ dynamic technique and plotted against the reciprocal source temperature

gas in the ZnSe ampoules annealed at elevated temperatures. Even a short, 1 min exposure to air (ZSTO-3 was ground in a glove box under Ar) may lead to some oxidation of the material. Removal of the oxides can be achieved by H_2 annealing without any subsequent exposure of the material to air. Mass flux of ZnSe for ZST-13 and -15 were measured by the in-situ dynamic technique and are plotted against the reciprocal source temperature in Fig. 3.11. The detailed heat treatment processing of the three ampoules are the followings: (1) ZST-12, chunky sample (3.3 g in 7 chunks from Yamanaka Hutech Corp.), baking at 1040 °C under vacuum for 10 min; (2) ZST-13, chunky sample (3.5 g in 8 chunks from Eagle, Picher, Inc.), baking at 1040 °C under vacuum for 10 min; and (3) ZST-15, ground sample (5.3 g from Eagle, Picher, Inc.), baking with 0.54 atm H_2 at 900 °C for 20 min then baking under vacuum at 1010 °C for 8 min. The mass fluxes were measured in the range of 1050–1140 °C with $\Delta T = T_s - T_d$ between 13 and 17 °C. The measurements started from the lowest temperature and the furnace temperature was raised to several different settings to determine the dependence of the mass flux on the source temperature.

Figure 3.11 shows that the mass flux of the ground, H_2 back filled and heat treated sample (ZST-15) were almost as high as the chunky, un-ground sample, ZST-12 and 13, and reached 10 mm/day at 1135°C. However, to have the reproducibility in the deviation of stoichiometry in the source material, the procedures of sample grinding and vacuum baking are necessary.

3.3.4 Simultaneous Measurements of Partial Pressure and Mass Flux in PVT of ZnSe

The general agreement observed between the experimental and theoretical results of the mass flux is satisfactory. However, the actual value of α over the source, or the

deposition region, during the vapor transport process was not known for these measurements. In principle, this α-value can vary during the transport process because the stoichiometry of the deposit is usually different from that of the source and, therefore, the stoichiometry of the source and that of the deposit, change continuously during the transport process.

To have a better understanding of the transport process, a simultaneous in-situ measurement of the transport rates and the partial pressures was designed and performed [15, 42]. The ampoule configuration, as shown in Fig. 3.12, has a short optical path length, 1.95 cm, which was made intentionally to have an almost constant cross-section area for the mass flux measurements throughout the length of the ampoule. An amount of 3 g heat treated ZnSe was loaded and sealed under vacuum. The transport length was 10.3 cm. During the run, the material transported from the reservoir, at 1160 °C, to the window end, at 1130 °C and the partial pressures over the deposited material were measured. The optical absorbance and the balance readings were simultaneously recorded at 30 min intervals. The pressure and compositions of the residual gas were measured after the experiments using the technique described previously.

The measured partial pressure of Zn and the mass transported were plotted versus time in Fig. 3.13. The measured optical absorption of the Se_2 peaks was too low to

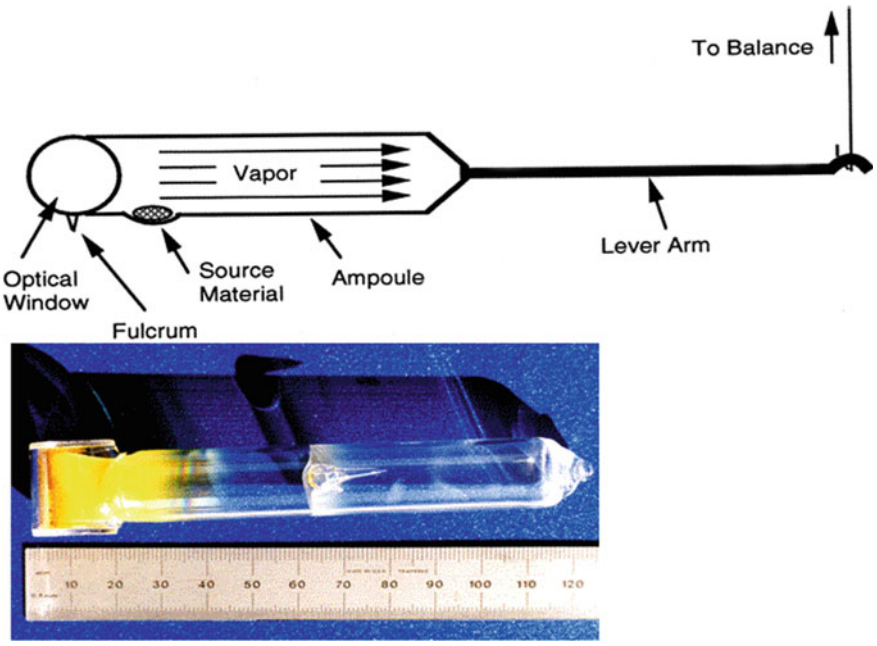

Fig. 3.12 Schematic and photograph of ampoule used in simultaneous in-situ measurement of the transport rates and the partial pressures in a closed ampoule. The two legs attached to the left side of the ampoule serve as a fulcrum

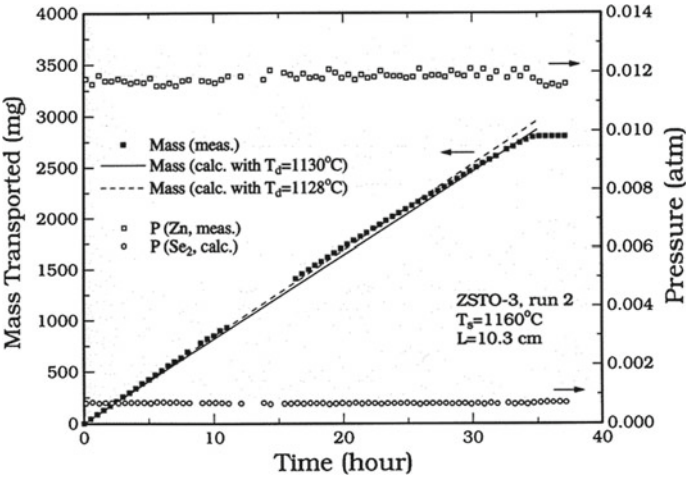

Fig. 3.13 Measured partial pressure of Zn and the mass transported versus time. P_{Zn}/P_{Se2}, α(deposit) = 17. The calculated transport rate and the sensitivity of deposition temperature, T_d, are also shown (taken from Fig. 4 of Ref. [15])

give an accurate measurement of Se_2 pressure due to the combination of the low Se_2 pressure and the short optical path length used. Therefore, the equation for the Gibbs free energy of formation, Eq. (2.11), together with the measured Zn partial pressures were used to calculate the partial pressures of Se_2 which is also plotted in Fig. 3.13. The measured pressures of Zn scattered but remained almost constant throughout the run at about 0.012 atm which corresponds to a value of P_{Zn}/P_{Se2}, α(deposit) = 17. The theoretical flux was calculated by the one-dimensional diffusion theory, using the measured parameters, i.e., thermal field, partial pressures over the deposition and the residual gas pressure. For the first time, the mass fluxes in a PVT system were calculated, without any adjustable parameters, by assuming a one-dimensional diffusion model with all of the input parameters measured experimentally. The calculated mass flux, i.e., the slope of the transported mass versus time, agrees well with the experimental data.

3.3.5 Optimum Heat Treatment Procedures for ZnSe Starting Materials

It is clear from the mass flux experiments above that a combination of H_2 reduction followed by dynamic baking under vacuum provides the heat treatment processes to enhance the transport rate. To establish the detailed procedures for optimum heat treatment, four optical cells were prepared with ground starting ZnSe materials from Eagle-Picher, Inc. and were heat treated by various procedures prior to sealing under vacuum [44]. The measured partial pressure of Se_2 over these heat treated ZnSe

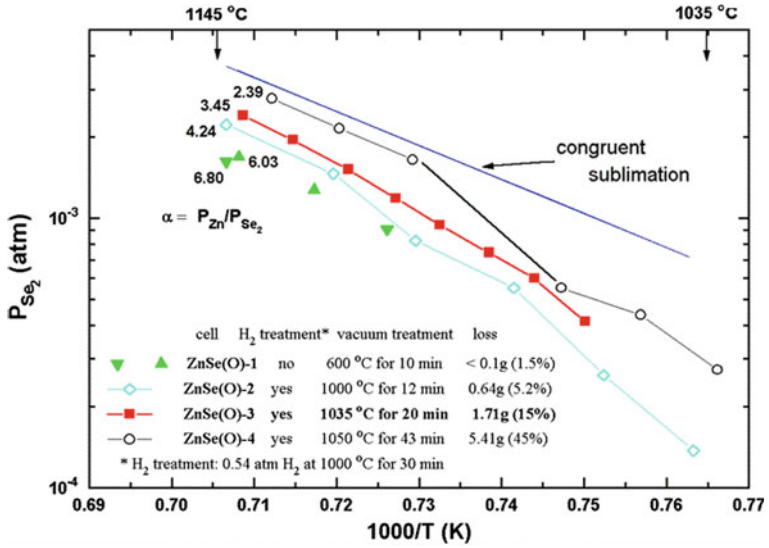

Fig. 3.14 Measured partial pressure of Se_2, P_{Se2} vs. 1000/T for optical cells, ZnSe(O)-1, -2, -3, -4 for temperatures of 1035–1145 °C. The pressure ratio, $\alpha \equiv P_{Zn}/P_{Se2}$, at the highest experimental temperature for each cell was calculated and labeled (taken from Fig. 2 of Ref. [44])

samples, P_{Se2}, for the optical cells ZnSe(O)-1, -2, -3 and -4 are plotted against 1000/T in Fig. 3.14 for temperatures between 1035 and 1145 °C. The pressure ratio, $\alpha \equiv P_{Zn}/P_{Se2}$, at the highest experimental temperature for each cell was calculated and labeled. The P_{Se2} for the condition of congruent sublimation was also calculated using Eq. (2.11). The measured partial pressure in the ZnSe(O)-1 cell, which was heat treated by baking at 600 °C under vacuum for 10 min to sublime the moisture and other volatile impurities in the ground sample, shows that the typical stoichiometry for the Eagle-Picher starting ZnSe material was moderately Zn-rich; with the pressure ratio $\alpha = 6.0$–6.8 at 1145 °C. A heat treatment by baking at 1000 °C for 12 min improved this ratio to 4.24 as measured on the ZnSe(O)-2 cell. Another baking at 1035 °C for 20 min on the sample retrieved from ZnSe(O)-2 cell further improved the stoichiometry to $\alpha = 3.45$ at 1145 °C as indicated from the results of ZnSe(O)-3. With a treatment by baking under vacuum at 1050 °C for 43 min on the ground ZnSe sample as shown by ZnSe(O)-4, the stoichiometry reached a value corresponding to $\alpha = 2.39$. The error associated with the measured P_{Se_2} is estimated to be 15%. The error for the Gibbs energy of formation given in Eq. (2.11), was estimated to be 2.5% [43]. The combined estimated error in α is about 29% and the measured value of 2.39 is within the estimated uncertainty range for the congruent sublimation condition. For ZnSe(O)-2 and 3 the sample loss during the heat treatment of baking under dynamic vacuum was reasonable; 5% for ZnSe(O)-2 and 15% for ZnSe(O)-3. The loss of 45% of the starting material for ZnSe(O)-4 during the heat treatment was considered to be high. Therefore, the optimum heat treatment procedure for the ground experiments was determined to be that for ZnSe(O)-3, i.e., annealing under

0.5 atm H_2 pressure at 1000 °C for 30 min followed by baking under dynamic vacuum at 1035 °C for 20 min.

To verify the effectiveness of the heat treatment procedures on the mass transport rate, crystal growth experiments using source materials provided by different vendors were performed. Two self-seeded growth experiments were performed and the starting material was 69's purity ZnSe supplied by Furukawa Co. Ltd. One ampoule was loaded with 12 g of ZnSe chunks (~0.35 g per piece) and the sample was baked at 280 °C for 13 min under vacuum to remove residual moisture before sealing. The other growth ampoule was loaded with 16 g of ground ZnSe and heat treated first by annealing under 0.5 atm H_2 at 1015 °C for 30 min, followed by baking at 1045 °C for 20 min under dynamic vacuum before sealing. For the PVT growth experiments a horizontal three-zone translational furnace, as described later, was used. The growth conditions were identical for both experiments. The source was held at 1140 °C and the furnace translation rate was 4.9 mm/day. Figure 3.15 shows the photos of the two growth ampoules after 6 days of the growth process. The first ampoule, which has been loaded with chunk starting material, as shown in Fig. 3.15a, had a very limited transport rate. Only specks and spots of ZnSe deposited on the cooler conical part of the ampoule and the chunks of the source material were essentially unaffected. The chunky source material in the ampoule has a limited surface area and, thus, should result in a low amount of residual gas. However, the large grains of the source and the low heat treatment temperature apparently did not allow for a proper adjustment of the composition toward that of the congruent sublimation condition. Figure 3.15b shows that in the second ampoule, which was heat treated using the optimized procedure, a 2.8 cm long ZnSe crystal with a convex crystal-vapor interface and a well-defined source surface has been developed.

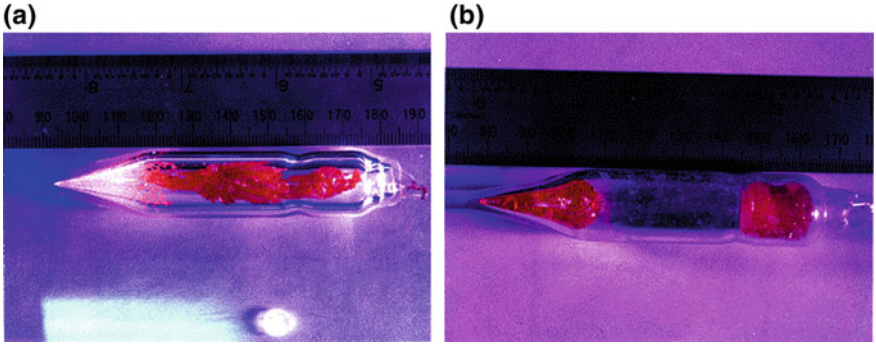

Fig. 3.15 Growth ampoules after 6 days of the growth process. In **a** the ampoule was loaded with chunk material and had a limited transport rate, while **b** contained ground sample that was heat treated using the optimized procedure. The growth resulted in a 2.8 cm long crystal and a convex crystal-vapor interface

3.3.6 Summary of Heat Treatment of Starting Material of ZnSe

The mass flux measurements confirmed that the two parameters, the partial pressure ratio over the source and the residual gas pressure are critical in determining the mass flux. Therefore, various heat treatments were conducted to control the partial pressure ratio (vapor phase stoichiometry) over the source and the effectiveness of the treatments was evaluated by partial pressure measurements. A simultaneous measurement of mass flux and partial pressure was performed and the experimentally obtained mass fluxes were compared and agreed well with those calculated, without any adjustable parameters, from a one-dimensional diffusion model which uses all the measured parameters as inputs. A hydrogen reduction treatment was established and was found to be effective in reducing the oxygen-related residual gas species. The optimum hydrogen reduction and dynamic vacuum treatment procedure was also employed for the source to maximize the mass flux in the CdTe [24] PVT process.

In summary, after conducting over one hundred vapor transport/growth experiments of ZnSe by PVT, the optimum procedures for the preparation of growth ampoule and heat treatments of starting material can be generalized as the followings:

1. Selecting fused silica with low OH content to minimize the outgassing of residual gases.
2. Modifying growth ampoule by HF etching, cleaning by distilled H_2O, methanol, acetone and distilled H_2O.
3. Inserting the cleaned ampoule inside another larger diameter fused silica tube coaxially and connecting the two-tube assembly to a vacuum pump to outgas the ampoule from its inner and outer walls in the temperature range of 1050–1100 °C for at least 16 h.
4. Loading the starting materials of ZnSe in powder form into the baked ampoule.
5. Evacuating the loaded ampoule to a vacuum level lower than 10^{-5} Torr.
6. Back-filling the ampoule with high purity H_2 gas to a pressure level of about 0.5 atm and baking the starting material in the closed ampoule at 1050 ± 20 °C for 30 min to reduce the oxide.
7. Evacuating the H_2 gas before baking the starting material under dynamic vacuum lower than 10^{-4} Torr in the 1050 ± 20 °C range for 10 min to adjust its stoichiometry.
8. Continuing evacuating the ampoule at room temperature until the vacuum level reaching lower than 5×10^{-6} Torr before sealing off the growth ampoule by H_2–O_2 torch.

The important strategy in the heat treatment is that once ZnSe starting material is loaded inside growth ampoule and connected to vacuum pump, it shall not be exposed to the atmospheric environment until the growth process is completed. It should be noted that the duration of 20 min baking under dynamic vacuum was optimized for ampoules with 6–8 mm I.D. tubing connecting to a turbo-molecular vacuum pump. The optimum baking durations depend on the pumping capability

and can be adjusted for various I.D. sizes of the tubing. Also, to make it easier to the sealing of the ampoule by H_2–O_2 torch, some researchers use fused silica cup or rod to place inside the ampoule in the seal-off location and apply the torch to fuse the ampoule tube around the cup/rod. The location of the cup/rod needs to be carefully selected so that the interior surface of the cup/rod will not recollect the condensation of the vapor phase which was intentionally sublimed to adjust the stoichiometry of the source material.

3.4 Mass Fluxes in ZnSe-Related Ternary Systems

The heat treatment of the starting material for a ternary system is also critical but more complicated than that of a binary system. Two methods are regularly practiced at our facility. The first method is simply baking out the starting ternary material of a known composition under dynamic vacuum. In general, for a ternary system the congruent sublimation composition does not necessarily exist inside the homogeneity range of the solid solution. The bake-out process will shift the composition of the starting material continuously towards a value corresponding to a higher transport rate and eventually all the material will sublime. The second method is to mix certain amounts of two binary compounds of known pressure ratios, α [35, 45]. The ternary starting material prepared by this method has a well-defined and reproducible stoichiometry although the pressure ratios after the homogenization of the ternary system are not known.

3.4.1 One-Dimensional Diffusion Model for Ternary Case

When two II–VI compounds form a ternary solid solution, such as $A^{II}B^{VI}_{1-x}C^{VI}_{x}$ or $A^{II}_{1-x}B^{II}_{x}C^{VI}$, the vapor phase contains three transport species governed by the two reactions with the proper ratio (1−x)/x. In the first case, they are:

$$AB(s) \rightarrow A(g) + \frac{1}{2}B_2(g) \tag{3.36}$$

and

$$AC(s) \rightarrow A(g) + \frac{1}{2}C_2(g) \tag{3.37}$$

If the residual gas is considered as the fourth, stagnant component, four Maxwell equations need to be solved. The fourth one can still be decoupled and integrated using $J_Z = 0$ which results in an equation similar to Eq. (2.22):

$$\frac{J_A}{D_{AZ}} + \frac{J_B}{D_{BZ}} + \frac{J_C}{D_{CZ}} = \frac{P}{RT(L-y)} \ln\left(\frac{P_Z(y)}{P_Z(L)}\right) \tag{3.38}$$

where the subscripts B and C stand for B_2 and C_2. The other three equations, unfortunately, cannot be solved practically to give three analytical equations. Therefore, numerical method has to be used. Using the argument similar to that in a binary case a relation among the individual flux can be established, which is:

$$J_A = 2(J_B + J_C) \text{ or } J_A + J_B = 2J_C \tag{3.39}$$

depending upon the combination of the compound. If the grown crystal has only one phase, its composition, x in $A^{II}B^{VI}_{1-x}C^{VI}_{x}$, can be significantly different from that of the source and is given by:

$$x(0) = \frac{J_C}{J_B + J_C} \tag{3.40}$$

in the first case. From reactions Eqs. (3.36) and (3.37), we have

$$\frac{P_A P_{B2}^{1/2}}{(1-x)\Gamma_{AB}(T)} = K_{AB}(T) \tag{3.41}$$

and

$$\frac{P_A P_{C2}^{1/2}}{x\Gamma_{AC}(T)} = K_{AC}(T) \tag{3.42}$$

respectively, where $\Gamma_i(T)$ is the activity coefficient of the binary compound, i, in the ternary solid solution. To perform the calculation, T(L), T(0), $P_Z(L)$, and a relation describing the stoichiometry of the source material (such as $\alpha(L) \equiv P_A(L)/P_B(L)$ have to be given. With the relation given above, Eqs. (3.41) and (3.42), $P_A(L)$, $P_{B2}(L)$, and $P_{C2}(L)$ can be calculated. Then, with three Maxwell's equations, Eqs. (3.38)–(3.42) are used simultaneously to solve J_A, J_B, J_C, $P_A(0)$, $P_{B2}(0)$, $P_{C2}(0)$, $P_Z(0)$, and x(0). Without any information on the thermodynamic properties of the ternary systems studied here, an ideal solution was assumed for these ternary solid solutions, i.e. $\Gamma(T) = 1$.

3.4.2 Mass Flux of PVT for $ZnSe_{1-x}Te_x$ System

3.4.2.1 Mass Flux of ZnSeTe from One-Dimensional Diffusion Model

Figure 3.16 shows the calculated mass flux as a function of $\alpha \equiv P_{Zn}(L)/P_{Se2}(L)$ under the conditions of T(L) = 1150 °C, T(0) = 1130 °C, and $P_Z(L) = 0.008$ atm for

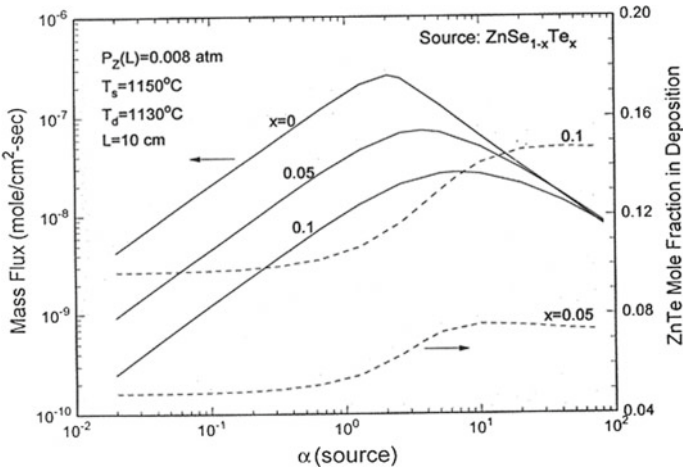

Fig. 3.16 Calculated mass flux as a function of $\alpha \equiv P_{Zn}(L)/P_{Se2}(L)$ under the conditions of T(L) = 1150 °C and T(0) = 1130 °C, and $P_Z(L) = 0.008$ atm for three $ZnSe_{1-x}Te_x$ source materials with x(L) = 0, 0.05, 0.1. The calculated compositions of the grown crystal, x(0), with its dependence on α, are also shown. The x values given for each curve are the compositions of the source. The composition of the residual gas for all the calculation is 36% CO_2, 26% each for CO and N_2, and 12% H_2 (taken from Fig. 1 of Ref. [45])

$ZnSe_{1-x}Te_x$ source materials with x(L) = 0, 0.05, 0.1. The calculated compositions of the grown crystal, x(0), as functions of α are also shown in Fig. 3.16 with reference to the right scale. There are three noteworthy points. (1) The mass fluxes decrease when ZnTe is introduced into the ZnSe system, (2) the maximum mass flux in the ternary system does not necessarily occur at $\alpha(L) = 2.0$, and (3) the composition of the grown crystal is usually not equal to that of the source, and depends strongly on the α values of the source material. For instance, in the case of x(L) = 0.1, the grown crystal composition, x(0), varies from 0.147 to 0.105 when α varies from 15 to 1.

3.4.2.2 Experimental Results from Mass Flux Measurements on ZnSeTe

The mass flux during PVT of $ZnSe_{1-x}Te_x$ was measured. The ZnSe binary starting material was treated by distilling under vacuum whereas the ZnTe starting material was baked under vacuum at 1000 °C for 10 min. The two compounds were weighted, ground into powder, mixed together and baked under vacuum with an H_2–O_2 torch for 3 min before sealing.

One transport ampoule, ZSTT-1, was prepared with x = 0.07 for the source material and the mass fluxes were measured using the in-situ described in Sect. 3.3.1 and the results of the mass flux are plotted in Fig. 3.17 as a function of the reciprocal source temperature. The ΔT values used were between 17 and 21 °C. Three theoretical curves calculated with α(L) = 7, 26, and 40 are displayed in the figure. The first

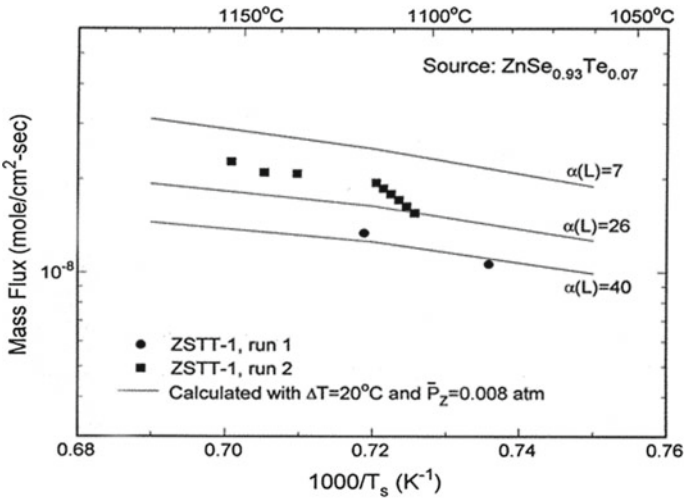

Fig. 3.17 Mass flux of $ZnSe_{0.93}Te_{0.07}$ as a function of reciprocal source temperature. ΔT is between 17 and 21 °C. The theoretical curves calculated using α(L) = 7, 26, and 40 are displayed. α = 7 corresponds to the maximum flux achievable under the given conditions while α = 26 was derived experimentally from the results of first deposition and the improvement in stoichiometric condition with increasing temperature gives higher measured fluxes (taken from Fig. 7 of Ref. [45])

curve corresponds to the maximum mass flux achievable under the given conditions. The α value for the second curve was derived by comparing the initial segment of the ZSTT-1 (run 2) data with the calculated mass flux. The stoichiometric condition of the vapor improved with increasing temperature giving somewhat higher mass fluxes.

In Fig. 3.18, the calculated mass flux and composition of the deposition using the experimental condition for the initial segment of the ZSST-1 run 2 are plotted. As shown in the figure, the α value was estimated from the experimental mass flux data from the initial segment (shown as solid circle) which indicates a value of about 26 for the source material. From the theoretical curves, shown in the same figure, a deposition composition of 0.105 was obtained by setting $\alpha = 26$. Experimentally, the average composition for the first deposited surface mapped by wavelength dispersive X-ray spectroscopy (WDS) was 0.106 (open circle).

3.4.3 Mass Flux of PVT for $ZnSe_{1-x}S_x$ System

3.4.3.1 Mass Flux of ZnSeS from One-Dimensional Diffusion Model

Similar calculations were performed for ternary $ZnSe_{1-x}S_x$ and the results are shown in Fig. 3.19. Observations similar to the ZnSeTe case can be made with variations

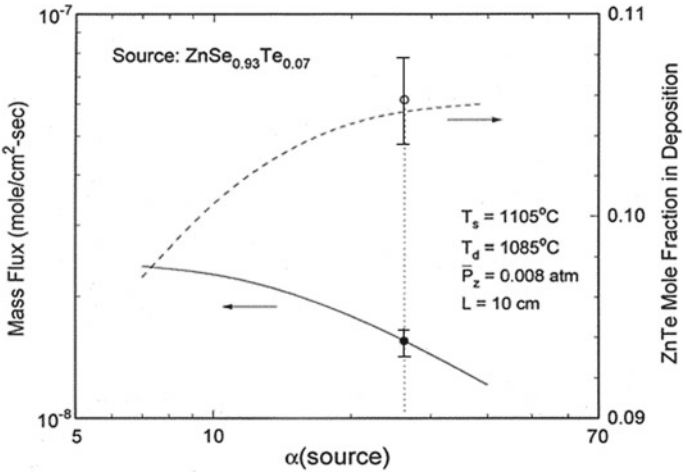

Fig. 3.18 Comparison between experimental and theoretical results for the flux measurements of $ZnSe_{0.93}Te_{0.07}$. α(source) = 26 was obtained by comparing the first flux data with the theoretical curve. Alloy composition mapping on the surface of the first deposited crystal by WDS averaged to be 0.106. By setting α = 26, a deposition composition of 0.105 was determined from theoretical curves (taken from Fig. 8 of Ref. [45])

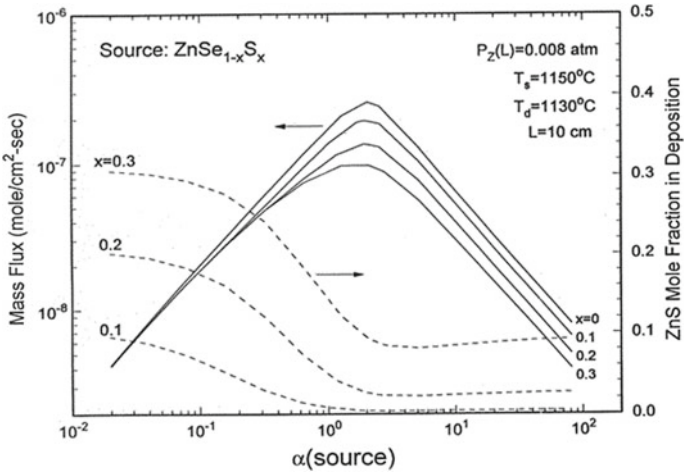

Fig. 3.19 Calculated mass flux as a function of $\alpha \equiv P_{Zn}(L)/P_{Se2}(L)$ under the conditions of T(L) = 1150 °C and T(0) = 1130 °C, and $P_Z(L) = 0.008$ atm for $ZnSe_{1-x}S_x$ source materials (taken from Fig. 3 of Ref. [45])

such as the opposite dependence of the composition of the grown crystal on the α-value. The variation is caused by the fact that the partial pressure of S_2 in this case is much smaller than that of Se_2, whereas in the $ZnSe_{1-x}Te_x$ system, the partial pressure of Te_2 is always greater than that of Se_2.

3.4.3.2 Experimental Results from Mass Flux Measurements on ZnSeS

For the preparations of starting materials, both ZnSe and ZnS powdered compounds were heat treated by H_2 reduction at 900 °C for 30 min and then baked at 1010 °C for 8 min before mixing. The mixed ternary compound was H_2 treated for 8 min and baked under vacuum for 2 min at 930 °C prior to sealing the ampoule. Transport ampoules were prepared for x = 0.2 (ZSST-1) and x = 0.3 (ZSST-2) and the measured mass fluxes are plotted in Fig. 3.20. The ΔT values applied ranged from 15 to 19 °C. The residual gas pressure was measured for ampoule ZSST-1 after the transport experiment. The total residual pressure measured was 2.4×10^{-3} atm at room temperature and four different species were found, H_2, CO, N_2, CO_2. The majority species are CO and N_2, being indistinguishable by the measuring method. CO and N_2 together contribute 53% of the total, CO_2 contributes 10% and H_2 accounts for the remaining 37% of the residual gas. For x = 0.2, a theoretical curve (solid line), calculated with $\alpha(L) = 0.4$, $\Delta T = 17$ °C and $P_z = 0.011$ atm, is also plotted in Fig. 3.20. The α-value for the curve, 0.4, was obtained by matching the experimental mass flux and the composition measured for the first deposition of ZSST-1 with

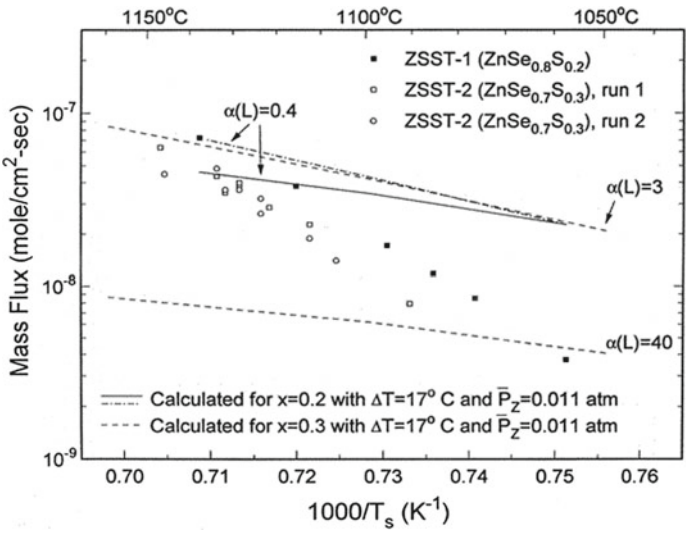

Fig. 3.20 Measured mass flux of $ZnSe_{0.8}S_{0.2}$ and $ZnSe_{0.7}S_{0.3}$ as functions of reciprocal source temperature with x = 0.2 and 0.3. The ΔT values range from 15 to 19 °C. For x = 0.3, curves are plotted for α(L) = 3 and 40 (taken from Fig. 5 of Ref. [45])

the theoretical results (see below). The pressure (0.011 atm at 1100 °C, the average processing temperature, corresponding to 2.4×10^{-3} atm at room temperature) and composition of the residual gas measured from ampoule ZSST-1 were used in the calculation. Another curve (chain line) was calculated using 20% of the total residual pressure measured above at the high-temperature end. The agreement between the experimental and theoretical results is good at the high-temperature end. With decreasing temperature, the composition of the source material may shift and cause the mass flux to decrease more rapidly. For $x = 0.3$, two curves calculated with $\alpha(L) = 3$ and 40 are plotted in Fig. 3.19 (dashed lines). The upper curve represents the mass flux near its maximum under the given conditions. All experimental data fall between these two theoretical curves. The stronger temperature dependence of the measured mass flux again indicates a progressive shift of the source composition towards the congruent sublimation condition with increasing source temperature, which is consistent with the earlier observation in the ZnSe PVT system.

Alloy composition mapping was performed on the flat surface of the first deposited crystal of the ZSST-1 sample by WDS. The surface was against the flat end of the ampoule and was perpendicular to the transport direction. The ZnS mole fraction, x, with a slight variation, was averaged to be 0.14. In Fig. 3.21, the calculated mass flux and composition of the deposition using the experimental conditions for the first segment of the transport (corresponding to the experimental data at the highest temperature for ZSST-1 in Fig. 3.20) are plotted. Since the experimental conditions were at the earliest stage of the run, the residual gas pressure used for the calculation was assumed to be 20% of the measured value. The α-value for the source material during the first mass flux measurement of the run can be obtained by matching the

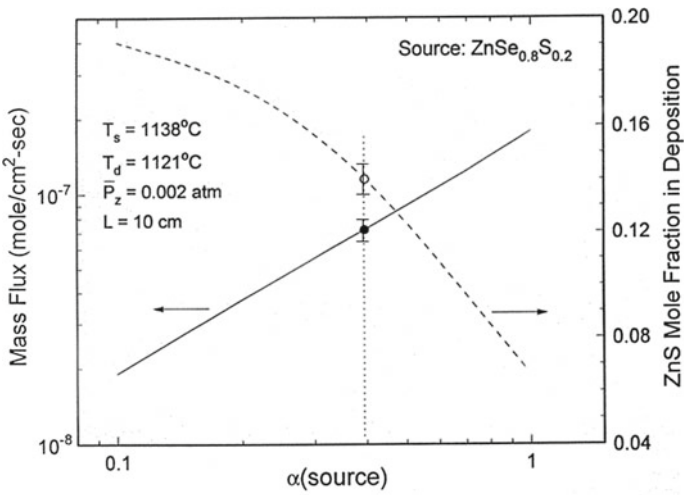

Fig. 3.21 Calculated mass flux (solid line) and deposition composition (dashed line) of $ZnSe_{0.8}S_{0.2}$ as a function of α(source) and the corresponding experimental results from the first measurements for sample ZSST-1 (taken from Fig. 6 of Ref. [45])

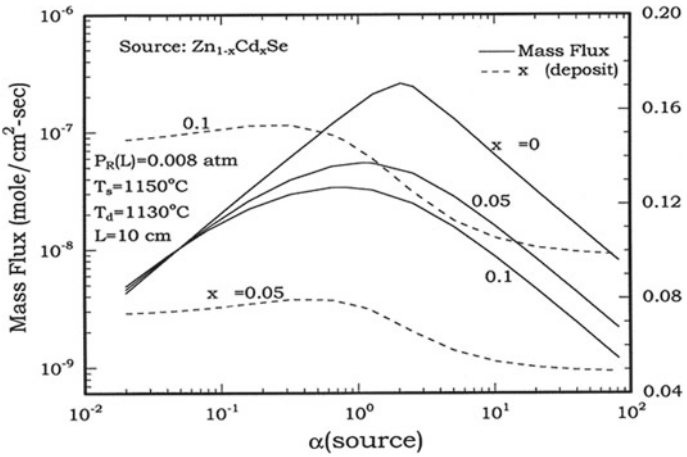

Fig. 3.22 Calculated mass flux (solid lines) and deposition composition (dashed lines) for $Zn_{1-x}Cd_xSe$ as functions of α(source) = P_{Zn}/P_{Se_2}

mass flux data (solid circle in Fig. 3.21) with the theoretical curve which turns out to be about 0.4. Then, the theoretical composition of the deposition can be determined by intersecting the vertical line and the dashed curve. The measured composition of the theoretical value agrees well with the first deposited material, 0.14 (open circle).

3.4.4 *Mass Flux of $Zn_{1-x}Cd_xSe$ System from One-Dimensional Diffusion Model*

The theoretical results of the one-dimensional diffusion model for the ZnCdSe system are given in Fig. 3.22 which shows the calculated mass flux and deposition composition as functions of α(L) for x(L) = 0, 0.05 and 0.1. The results predict trends similar to those for the ZnSeS system.

3.4.5 *Summary of Mass Flux of ZnSe-Related Ternary Systems*

One dimensional diffusion analysis performed on ZnSeTe, ZnSeS and ZnCdSe systems predicts the following:

(1) The mass flux is lower than that for ZnSe.
(2) The flux maximum is not necessarily at α(L) = P_{Zn}/P_{Se_2} = 2.0.
(3) The composition of the grown crystal depends strongly on α and ΔT.

The mass fluxes for three samples, $ZnSe_{0.93}Te_{0.03}$, $ZnSe_{0.80}S_{0.20}$ and $ZnSe_{0.70}S_{0.30}$ were measured using the in-situ dynamic technique with the starting binary materials heat treated to obtain near-congruent sublimation compositions. Reasonable agreement between the experimental and theoretical results was observed.

References

1. M. Zha, M. Piechotka, E. Kaldis, J. Cryst. Growth **115**, 43 (1991)
2. E. Kaldis, M. Piechotka, *Handbook of Crystal Growth*, vol. 2, Ch. 11 (Elsevier Science, North-Holland, 1994)
3. J.A. Zoutendyk, W.M. Akutagawa, *Material Processing in the Reduced Gravity Environment of Space*, ed. by G. E. Rindone (Elsevier Science, 1982), p. 449
4. Su Ching-Hua, J. Cryst. Growth **80**, 333 (1987)
5. H. Wiedemeier, D. Chandra, F.C. Klaessic, J. Cryst. Growth **51**, 345 (1981)
6. W. Palosz, H. Wiedemeier, J. Cryst. Growth **129**, 653 (1993)
7. K. Igaki, N. Ohashi, K. Mochizuki, Jap. J. Appl. Phys. **15**, 1429 (1976)
8. K. Igaki, K. Mochizuki, J. Cryst. Growth **24**(25), 162 (1974)
9. K. Mochizuki, J. Cryst. Growth **51**, 453 (1981)
10. K. Mochizuki, J. Cryst. Growth **53**, 355 (1981)
11. T. Kiyosawa, K. Igaki, N. Ohashi, Trans. Jap. Inst. Met. **13**, 248 (1972)
12. K. Mochizuki, K. Igaki, J. Cryst. Growth **45**, 218 (1978)
13. K. Mochizuki, J. Cryst. Growth **58**, 87 (1982)
14. Y.-G. Sha, C.-H. Su, W. Palosz, M.P. Volz, D.C. Gillies, F.R. Szofran, S.L. Lehoczky, H.-C. Liu, R.F. Brebrick, J. Cryst. Growth **146**, 42 (1995)
15. C.-H. Su, Y-G. Sha, K. Mazuruk, S.L. Lehoczky, H.-C. Liu, R. Fang, R.F. Brebrick, J. Cryst. Growth **166**, 736 (1996)
16. D.M. Shteingradt, V.E. Lyusternik, Russ. J. Phys. Chem. **56**, 1379 (1982)
17. R.C. Reid, J.M. Prausnitx, T.K. Sherwood, *The Properties of Gasses and Liquids*, 3rd edn. (McGraw-Hill, New York, 1977), p. 113
18. P.D. Fochs, W. George, P.D. Augustus, J. Cryst. Growth ¾, 122 (1968)
19. T. Tuguchi, J. Shirafuji, Y. Inuishi, Jap. J. Appl. Phys. **17**, 1331 (1978)
20. J. Morimoto, T. Ito, T. Yoshioka, T. Miyakawa, J. Cryst. growth **57**, 362 (1982)
21. G.J. Russell, N.F. Thompson, J. Woods, J. Cryst. Growth **71**, 621 (1985)
22. C.-H. Su, S.L. Lehoczky, F.R. Szofran, J. Appl. Phys. **60**, 3777 (1986)
23. C.-H. Su, Submitted to Crystal Res. Technol.
24. C.-H. Su, Y.-G. Sha, S.L. Lehoczky, H.-C. Liu, R. Fang, R.F. Brebrick, J. Cryst. Growth **183**, 519 (1998)
25. R.F. Brebrick, C.-H. Su, P.-K. Liao, *Semiconductors and Semimetals*, vol. 19, Ch. 3 (Academic Press, New York, 1983)
26. C.-H. Su, P.-K. Liao, R.F. Brebrick, J. Electrochem. Soc. **132**, 942 (1985)
27. R.F. Brebrick, A.J. Strauss, J. Phys. Chem. Solids **25**, 1441 (1964)
28. R. Fang, R.F. Brebrick, J. Phys. Chem. Solids **57**, 443 (1996)
29. R.F. Brebrick, R. Fang, J. Phys. Chem. Solids **57**, 451 (1996)
30. M. Brown, A.F.W. Willoughby, J. Cryst. Growth **59**, 27 (1982)
31. B.M. Bulakh, J. Cryst. Growth **5**, 243 (1969)
32. C. Paorici, C. Pelosi, J. Cryst. Growth **35**, 65 (1976)
33. D.W.G. Ballentyne, S. Wetwatana, E.A.D. White, J. Cryst. Growth **7**, 79 (1970)
34. W. Palosz, H. Wiedemeier, J. Cryst. Growth **131**, 193 (1993)
35. W. Palosz, F.R. Szofran, S.L. Lehoczky, J. Cryst. Growth **142**, 215 (1994)

36. W. Palosz, Material research in low gravity, in *Proceedings of SPIE*, vol. 3123, ed. by N. Ramachandran (The International Society for Optical Engineering, Bellingham, WA, 1997), p. 34
37. W. Palosz, J. Cryst. Growth **267**, 484 (2004)
38. G.J. Russell, J. Woods, J. Cryst. Growth **46**, 323 (1979)
39. G. Schmidt, R. Gruehn, J. Cryst. Growth **57**, 585 (1982)
40. Y. Morimoto, T. Igarashi, H. Sugahara, S. Nasu, J. Non-Cryst. Solids **139**, 35 (1992)
41. J.J. Murray, R.F. Pottie, R.L. Sander, J. Mater. Sci. **8**, 37 (1973)
42. C.-H. Su, Material research in low gravity, in *Proceedings of SPIE*, vol. 3123, ed. by N. Ramachandran (The International Society for Optical Engineering, Bellingham, WA, 1997), p. 7
43. H. Liu, Ph.D. Dissertation, Marquette University, March 1995; High Temp. Mater. Sci. **35**, 215 (1996)
44. C.-H. Su, W. Palosz, S. Feth, S.L. Lehoczky, J. Cryst Growth **192**, 386 (1998)
45. Y.-G. Sha, C.-H. Su, S.L. Lehoczky, J. Cryst Growth **171**, 516 (1997)

Chapter 4
Crystal Growth

Abstract After the optimum heat treatments on the growth ampoules and the source materials, the sealed ampoules were processed in a thermal profile by a three-zone furnace (left cold zone, central booster zone and right hot zone) with an adiabatic zone inserted between the central booster heater and the cold zone. During the growth, the thermal profile moved toward the hot end, through translation of either furnace or ampoule, with a rate carefully selected from the results of transport rate measurements. Relative to the gravitational direction, three different growth configurations, i.e., horizontal, vertical stabilized (hot end on top) and vertical destabilized (cold end on top), were practiced. For each configuration, the growth ampoule was designed for either self-seeded or seeded growth. The PVT growth experiments were performed on the systems of ZnSe, ZnSe doped with transition metal (Cr and Fe), ZnSeTe, CdTe, CdS and ZnTe. During the growth of ZnSe, in-situ real time optical methods were performed to monitor the growth. The methods included in-situ visual observation of the growing crystal, in-situ optical absorption to measure the partial pressures along the growth ampoule and optical interferometry to map the morphology of growing surface. Lastly, a recent advancement to enhance the transport rate of PVT was developed by installing an extra out-layer of evacuated closed tube around the growth ampoule to reduce the vapor pressure diffusing into the growth ampoule.

Keywords Seeded growth · Self-seeded growth · Horizontal growth · Vertical stabilized growth · Vertical destabilized growth · In-situ real time monitoring

4.1 Growth Ampoule Preparations

The growth activities discussed here will be focused on the translational PVT growth in a closed system with seeded as well as self-seeded growth. The simple crystal growth setup consists of a three-zone tubular furnace which provides the thermal profile of a hot, a cold and a booster zone in between. There are three different furnace configurations, i.e., the horizontal, the stabilized vertical (hot zone on top) and the de-stabilized vertical (hot zone at bottom). The samples were sealed inside fused silica ampoules which were placed inside the furnace with specific initial positions. The crystal growth proceeds when the relative movement between the

© Springer Nature Switzerland AG 2020

C.-H. Su, *Vapor Crystal Growth and Characterization*,
https://doi.org/10.1007/978-3-030-39655-8_4

ampoule and the thermal profile starts. If the relative translational rate exceeds the vapor transport rate and the mass flux cannot keep up with the driving force from ΔT, then the growing crystal surface becomes unstable. Therefore, careful preparation of the growth ampoule will be needed to maximize the mass flux. As discussed earlier, the residual gas released from the fused silica ampoule and the sample material during long duration growth at high temperature can severely reduce the vapor transport rate. Hence, the preparation of the growth ampoules is important.

During the processing of these compound semiconductors at elevated temperature, some surface sections of the processed sample interact with the fused silica container and form chemical bonding, the so-called "wetting", which makes these surface sections attaching to the ampoule wall. When the sample is cooled down to room temperature after the processing, as the bulk of the sample goes through larger thermal contraction than the fused silica crucible, the wetted sample area remains attaching to the fused silica wall and, consequently, causes the sample to separate apart which causes internal cracks and other structural defects. These defects are detrimental to the electronic/optic performance of materials, especially for the high-quality compound semiconductors. For the crystal growth of these semiconductors, there have been efforts to prevent or to reduce the interaction between fused silica ampoule and samples, such as carbon coating the inner wall of ampoule. However, the coating contributes to the undesired incorporation of carbon to the grown materials and, the thin carbon film sometimes disappears from the reduction by the oxide impurities during the growth and increases the undesirable residual gas pressures of CO and CO_2. During the low-gravity experiment [1] of melt growth of CdZnTe on Space Shuttle, the flight samples have much higher structural perfection than the ground samples processed in otherwise identical growth conditions. The dislocation density was reduced from 50,000 to 100,000 cm^{-2} in the ground samples, to 500–2500 cm^{-2} in the flight samples. It was thought to have resulted from near absence of hydrostatic pressure in micro-gravity, which allowed the melt to solidify with minimum or no wall contact. It will be discussed later in Chap. 5 that some of the horizontally grown ZnSe crystals show the tendency to grow completely away from the ampoule wall without any contact [2]. This phenomenon was interpreted by employing one-dimensional diffusion model which shows that the thermal profile measured inside the empty furnace bore in the region of contactless growth was very close to the calculated thermal profile for super-saturation. However, in an effort to produce cylindrical single crystals without much interaction between grown crystal and ampoule inner wall, a simple and practical method has been demonstrated to reduce the "wetting" of ampoule wall.

The severity of the chemical interaction between the sample and fused silica inner-wall depends on several factors: (1) the chemical activity of the sample and the fused silica, (2) the processing temperature, (3) the duration at the temperature and (4) the contact area of the interaction. For example, the heating schedule in the homogenization of HgCdTe was designed to reduce the chemical activity of Cd by annealing at lower temperature to eliminate the wetting [3]. However, the first three of these factors are case-dependent, i.e., they are different for various material systems as well as different processing conditions. To find a general solution for each

different case, it is desired to focus on the fourth factor, i.e., to reduce the contact area between the sample and the container. The total area that the grown crystal contacting the container depends on the surface features of the inner-wall. A very flat and smooth surface provides a large contact area whereas a rough surface, with peaks and valleys, limits the contact area to the peaks due to the surface tension of the crystal. With this concept, a simple method to modify the surface morphology of the fused silica inner-wall was developed by etching it with hydrofluoric acid (HF) before any crystal growth activity. The HF acid, with its unique etching effects on glassware, is usually stored in plastic bottle. Typically, the HF rinse of 30 s to 2 min has been widely adopted in the cleaning of the surface of fused silica inner-tubing before any processing activities. However, the long-time HF etching of 30 min can modify the surface features of fused silica and affect the interaction between the sample and its container. The method is applicable to all processes involving interaction between materials and fused silica at elevated temperature. The effects of the 30 min HF etching have been tested and will be presented later.

The typical growth ampoules were made of 18 mm O.D., 15 mm I.D. fused silica tubing with low OH content to minimize the outgassing of residual gases. The ampoules were filled vertically with 48–51% HF and etched at room temperature for 30 min and rinsed repeatedly with acetone, methanol and distilled water. The empty ampoule was then loaded inside a larger diameter fused silica tubing which was placed coaxially in a tubular furnace to be outgassed at 1050–1100 °C under dynamic vacuum for over 16 h. The arrangement will expedite the outgassing processing by maintaining vacuum environment both inside and outside the ampoule. The amounts and composition of residual gases formed in empty sealed silica glass ampoules had been investigated [4–7] to determine the effects of the silica brand, outgassing and annealing conditions, system geometry, and presence of graphite. The findings can be generalized as the followings.

1. The dominant component of the residual gas coming from silica glass is hydrogen with the species of H_2O as the second largest component, which constitutes usually less than 10% of the gas.
2. The presence of carbon in the system converts (at higher temperatures) H_2O into hydrogen and carbon monoxide.
3. The temperature of outgassing has a strong effect on the amount of gas accumulated in the ampoule. Outgassing at 1000 °C for 16 h is sufficient to limit the pressure of residual gas in the ampoule upon annealing to 0.3–0.4 Torr at high temperatures and extended outgassing (more than a day) has a limited effect on the gas pressure [4, 5].

4.2 Heat Treatments of Starting Materials

The optimum procedures for the preparation of growth ampoule and heat treatments of starting material have been developed for each compound semiconductor. The

specific case for ZnSe was presented in Chap. 3 and will be described here again and the schedules for other II–VI compounds will be presented later.

The standard procedures can be generalized as the followings:

1. Selecting fused silica with low OH content to minimize the outgassing of residual gases.
2. Modifying growth ampoule by HF etching, cleaning by distilled H_2O, methanol, acetone and distilled H_2O.
3. Inserting the cleaned ampoule inside another larger diameter fused silica tube coaxially and connecting the two-tube assembly to a vacuum pump to outgas the ampoule from its inner and outer walls in the temperature range of 1050–1100 °C for at least 16 h.
4. Loading the starting materials of ZnSe in powder form into the baked ampoule.
5. Evacuating the loaded ampoule to a vacuum level lower than 10^{-5} Torr.
6. Back-filling the ampoule with high purity H_2 gas to a pressure level of about 0.5 atm and baking the starting material in the closed ampoule at 1050 ± 20 °C for 30 min to reduce the oxide.
7. Evacuating the H_2 gas before baking the starting material under dynamic vacuum lower than 10^{-5} Torr in the 1050 ± 20 °C range for 20 min to adjust its stoichiometry.
8. Continuing evacuating the ampoule at room temperature until the vacuum level reaching lower than 5×10^{-5} Torr before sealing off the growth ampoule by H_2–O_2 torch.

The important strategy in the heat treatment procedures is that once ZnSe starting material is loaded inside growth ampoule and connected to vacuum pump, it shall not be exposed to the atmospheric environment until the growth process is completed. It should be noted that the duration of 0 min baking under dynamic vacuum was optimized for ampoules with 6–10 mm I.D. tubing connecting to a turbo-molecular vacuum pump. The optimum baking durations depend on the pumping capability and can be adjusted for various I.D. sizes of the tubing. Also, to make it easier to the sealing of the ampoule by H_2–O_2 torch, some researchers use fused silica cup or rod to place inside the ampoule in the seal-off location and apply the torch to fuse the ampoule tube around the cup/rod. The location of the cup/rod needs to be carefully selected so that the interior surface of the cup/rod will not recollect the condensation of the vapor phase which was intentionally sublimed to adjust the stoichiometry of the source material.

4.3 Crystal Growth Environments

4.3.1 Temperature Profile

After the heat treatment procedure for the starting material was optimized the crystal growths were conducted with judicious choices of the growth parameters. Usually, the heat treatment technique which resulted in the highest transport rate was adopted. The furnace translation rate was carefully selected from the results of transport rate measurements. Figure 4.1 illustrates schematics of the temperature profile and the initial ampoule positions for both self-seeded and seeded growth conditions for a growth run [8–11]. The profile can be easily provided by a three-zone furnace (left cold zone, central booster zone and right hot zone) with an adiabatic zone inserted between the central booster heater and the cold zone. For the self-seeded situation, the crystal starts to nucleate when the ampoule tip is at a temperature lower than the thermal supersaturation as shown in Fig. 4.1. In the case of the seeded growth, the initial ampoule position needs to be carefully adjusted such that the middle section of the seed is positioned at the supersaturation position. Under such condition, part of the seed sublimes first, i.e. thermally etched, and then the grown crystal nucleates and grows on top of the seed. The ampoule was positioned inside the furnace at room

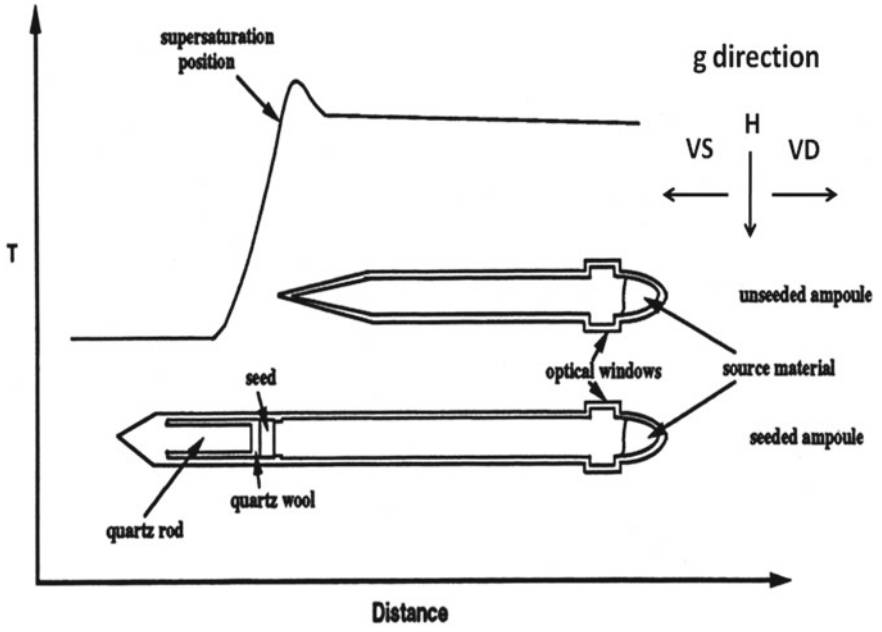

Fig. 4.1 Typical temperature profile and initial ampoule positions for seeded and unseeded growth conditions. The three gravity directions present the growth configurations: H for horizontal, VS for vertical stabilized and VD for vertical destabilized

temperature before the thermal profile was programmed to heat rigidly to the final settings. The temperature profile translates to the source end during the growth. For several growth runs, the partial pressures over the source materials were measured in-situ during the growth. The drawings in Fig. 4.1 show the designs and locations of the optical windows for both self-seeded and seeded configurations.

The advantages of the temperature profile used here for crystal growth are the following [12]:

1. The peak in the thermal profile provides confinement of the supersaturation position to a narrow region because of the high temperature gradient at the growing surface.
2. The peak in the profile also eliminates possible secondary nucleation sites by desorbing inadvertently deposited material from the ampoule wall just ahead of the crystal/vapor growth interface.
3. The use of furnace (or ampoule) translation enables the self-adjustment on the degree of supersaturation, or ΔT, to match the mass flux with the crystal growth rate throughout the growth run.
4. The use of the insulation (or adiabatic) zone allows for precise control of the growth interface shape which promotes favorable crystalline grain selection, eliminates the nucleation of undesirable secondary grains, causes existing extended defects to grow toward the container wall and be eliminated.

The generation of crystal defects usually results from the low yield strength at the high growth temperatures. In general, the yield strengths of materials rapidly increase with decreasing temperature. With the heat treatment methods and the growth apparatus described here, growth can be accomplished at temperatures lower than commonly used. This allows the production of crystals with a higher degree of perfection because of the increased crystal yield strength. Using this method, large crystals of CdS [8], PbSe, CdTe, ZnTe [9], and ZnSe [12] have been grown consistently.

4.3.2 Growth Configurations

Three different growth configurations have been practiced to study the gravity effects on grown crystals. In the figure, the horizontal, vertical stabilized (hot zone on top) and vertical stabilized (cold zone on top) configuration is shown with the respective gravity direction. For most of the horizontal and vertical destabilized self-seeded growth runs, the ampoule is ready to grow by simply shifting the powder to the source end by hands. Figure 4.2a shows a typical self-seeded ampoule before it was positioned inside the growth furnace. The thermal peak will drive the source powder near the growth tip toward the source end before the ampoule tip reaching the supersaturation position where nucleation will start to form.

In the vertical stabilized and any seeded growth configurations, the source powder needs to sinter in the source end which can be accomplished by placing the ampoule in the reverse direction of the thermal profile, i.e., the source end in the cold zone,

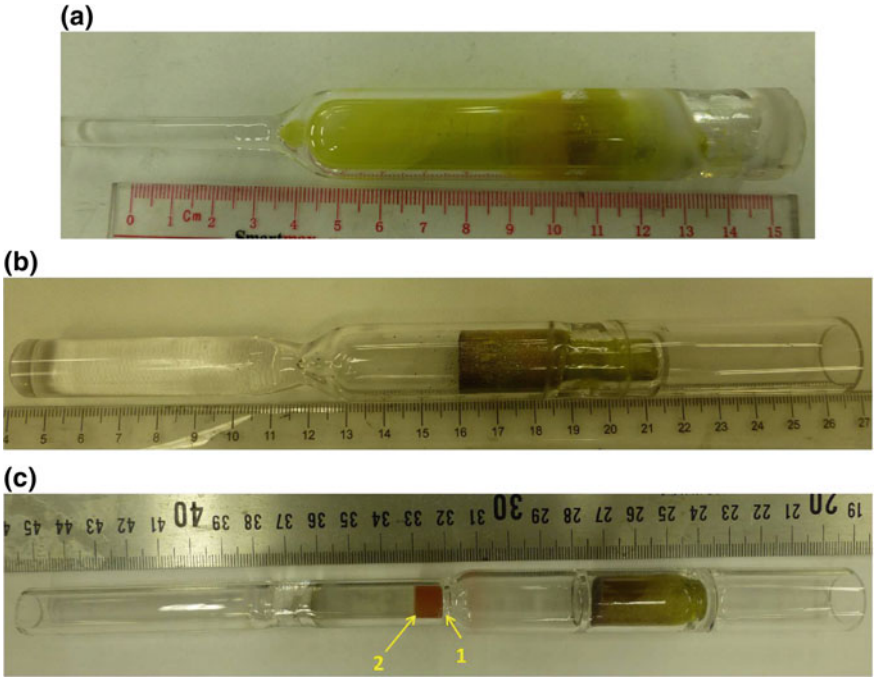

Fig. 4.2 Photos of ZnSe growth ampoules. **a** Self-seeded ampoule. **b** Sintered self-seeded ampoule **c** Seeded ampoule

and annealed under the thermal profile as shown in Fig. 4.1 to back transport the source for 12–16 h. A typical self-seeded sintered ampoule is shown in Fig. 4.2b. The seeded ampoule was made by fusing 20 × 16 mm and 15 × 11 mm silica tubing with a 9 mm diameter ring in between as a seed restriction (marked as 1 in a seeded ampoule shown in Fig. 4.2c. After completing the back-transport, the ampoule will be opened on the seeded end and a cylindrical single crystal seed, 10 mm diameter, 8 mm long, can be secured by pushing it with a fused silica rod on top of a thin layer of baked quartz wool (for the thermal expansion of the seed during heating; marked as 2) then seal it around the rod under vacuum condition.

In the case of the seeded growth, the initial position of the seed surface, which dictates its temperature, is very critical in that (a) spontaneous nucleation occurs if it's lower than the supersaturation temperature, T_{Sup} and (b) seed completely sublimes if the temperature is much higher than T_{Sup}. To verify this approach, a simulation test was conducted by positioning a seeded ampoule, except without the planned 3 mm thick seed, at the supersaturation position for 64 h and then rapidly cooled to study the thermal field. As shown in Fig. 4.3, the deposition from the source formed a 3 mm thick condensation with a convex interface shape that agrees with the results from the numerical simulation to be discussed later.

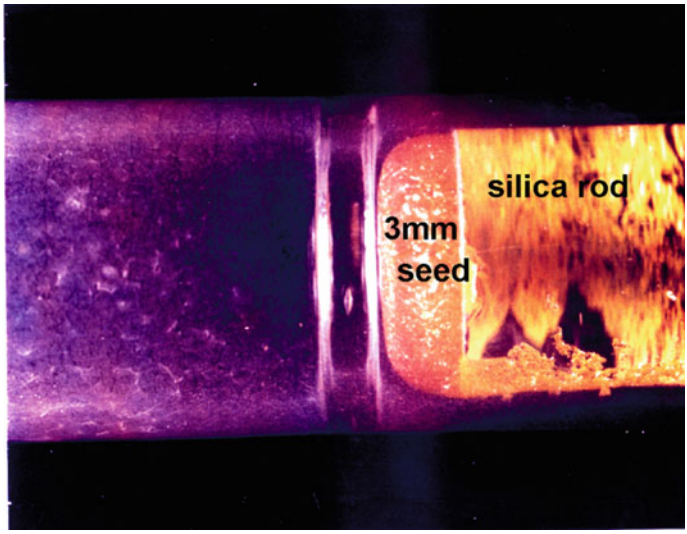

Fig. 4.3 The simulation of a seeded growth by placing the ampoule with the seed surface at the supersaturation position for 64 h

4.3.3 Crystal Growth of ZnSe by PVT

A total of more than 50 crystal growth experiments, including self-seeded and seeded; horizontal, vertical stabilized and destabilized configurations have been conducted on the PVT of ZnSe. The source materials for ZnSe were provided by five vendors: Cleveland Crystals, Eagle-Picher, Inc., Furukawa Co. Ltd, Yamanaka Hutech Corp. and Alfa Aesar. Three different heat treatments were employed for the source: (1) baking under vacuum, (2) distillation under vacuum and (3) H_2 reduction and baking under vacuum (the optimum procedure). The seed crystals were provided by Eagle-Picher, and (100), (110) and (111) orientations were selected. A wide range of growth conditions were studied. The source temperature varied from 1070 to 1160 °C and the furnace translation rate from 3 to 15 mm/day. After crystal growth the furnace was cooled down from the growth temperature to room temperature in 12–96 h.

Table 4.1 lists the information of some selected horizontal growths, including the vendors of source materials, the amounts of ZnSe loaded and the conditions for H_2 and vacuum baking heat treatments for the growth runs. Table 4.2 lists the thermal profile, the furnace translation rate, the degree of supersaturation and the measured residual gas pressure (at room temperature) for each growth run. The thermal gradient was measured at the supersaturation location. From the measured thermal profile, the degree of supersaturation, ΔT, was calculated after the growth from the temperature at the grown crystal surface and the supersaturation temperature. As the furnace translation rate increased, the degree of supersaturation also increased because higher ΔT is needed to provide larger mass flux to catch the furnace translation until mass

Table 4.1 The vendor of source material, the amount of ZnSe loaded and the condition of H_2 and vacuum baking heat treatments for selected horizontal growth runs

Growth number	Vendor[a]	Mass loaded (g)	H_2 pressure and temperature[b]	Baking temperature and duration
ZnSe-34	1	14.01	0.59 atm, 1010 °C	1010 °C, 12 min
ZnSe-39	1	15.20	0.63 atm, 1000 °C	1000 °C, 12 min
ZnSe-40	1	14.77	0.53 atm, 1000 °C	1000 °C, 12 min
ZnSe-42	2	16.20	0.54 atm, 1015 °C	1045 °C, 20 min
ZnSe-43	2	19.26	0.56 atm, 1030 °C	1045 °C, 10 min
ZnSe-44	2	15.75	0.51 atm, 1035 °C	1035 °C, 20 min
ZnSe-45	3	15.52	0.55 atm, 1035 °C	1050 °C, 20 min
ZnSe-46	1	13.55	0.56 atm, 1035 °C	1050 °C, 20 min
ZnSe-47	1	13.72	0.52 atm, 1035 °C	1035 °C, 22 min

[a]Vendors: 1—Eagle Picher, Inc. (high purity grade), 2—Furukawa Co. Ltd. (99.9999%) and 3—Cleveland Crystals (99.995% purity)
[b]The duration of H_2 treatment was 30 min

Table 4.2 The source temperature, T_H, the thermal gradient, the furnace translation rate, the degree of supersaturation and the measured residual gas pressure (at room temperature) for selected horizontal growth runs

Growth run	T_H (°C)	Thermal gradient (°C/cm)	Translation rate (mm/day)	Super-saturation (°C)	Residual gas pressure (10^{-3} atm)
ZnSe-34	1133	12	6.76	17	–
ZnSe-39	1155	12	5.00	2	–
ZnSe-40	1140	12	4.90	13	–
ZnSe-42	1140	14	4.95	3	1.18
ZnSe-43	1045	10	4.78	2	–
ZnSe-44	1138	10	4.96	–	1.15
ZnSe-45	1138	10	5.00	13	0.875
ZnSe-46	1147	11	2.44	3	1.26
ZnSe-47	1147	11	7.45	16	1.08

flux flattened out with increasing ΔT. The loss of source material during baking under vacuum process was measured after the growth runs and, in a typical case, e.g. ZnSe-42; it was 0.96 g, or 6%.

Table 4.3 lists the growth information on selected growth runs in vertical configuration where the growth number ended with VD, for vertical destabilized, and VS, for vertical stabilized. All of the ampoules were loaded with starting materials from Eagle Picher, Inc. (high purity grade) except Furukawa Co. Ltd. (99.9999%) for the ZnSe-48VS run. The H_2 heat treatment duration was 30 min except 40 min for ZnSe-31VD.

Table 4.3 The starting material mass, heat treatments of H_2 and dynamic vacuum baking conditions, the source temperature, T_H, and the furnace translation rate for selected growth runs in vertical configuration

Growth[a] number	Mass loaded (g)	H_2 pressure and temperature	Baking temperature and duration	T_H (°C)	Translation rate (mm/day)
ZnSe-31VD	12.06	0.52 atm, 870 °C	950 °C, 12 min	1150	4.98
ZnSe-32VS	12.18	0.53 atm, 1010 °C	1010 °C, 15 min	1149	3.80
ZnSe-35VS	13.96	0.61 atm, 1000 °C	1000 °C, 12 min	1153	11.45
ZnSe-48VS	15.00	0.56 atm, 1035 °C	1035 °C, 22 min	1143	3.81

[a]VD—vertical destabilized configuration; VS—vertical stabilized configuration

4.3.4 *Crystal Growth of ZnSe Doped with Transition Metals by PVT*

Transition metal (TM)-doped II–VI semiconductors have been studied as the front candidate for the development of near-to-mid infrared tunable solid-state lasers, covering the spectral region from 2 to 4.5 μm [13–17], which has applications of particular importance for environmental monitoring, military countermeasures, medical applications and remote sensing [19]. TM ions such as Cr^{2+}, Ni^{2+}, Co^{2+} and Fe^{2+} have been investigated as potential lasing ions in ZnSe, ZnS, ZnTe [13, 14], CdSe [15], and host crystals. Cr-doped chalcogenides, and particularly Cr^{2+} doped ZnSe, have been demonstrated to be extremely attractive for room-temperature laser operation.

Self-seeded growths of Cr- and Fe-doped ZnSe were performed in the horizontal and vertical (stabilized) configuration. The source for the Cr-doped ZnSe growths was a mixture of ZnSe from Eagle-Picher, Inc. or Furukawa Co. and CrSe (99.5%) from Alfa Aesar Inc. To homogenize the starting material, the ampoules were intentionally positioned toward the hot zone for a period time before the tip reaching supersaturation position during the growth. The amount of time for this pre-growth annealing was estimated for each run. In the horizontal growth of ZnSe-36H, 8.5 g of $(Zn_{0.963}Cr_{0.037})Se$, or $[Cr] = 8.1 \times 10^{20}$ cm^{-3}, and in the vertical growth of ZnSe-38V, 8.93 g of $(Zn_{0.962}Cr_{0.038})Se$, or $[Cr] = 8.4 \times 10^{20}$ cm^{-3}, was loaded into the growth ampoule. Both ampoules were reduced with 0.55 atm H_2 at 1000 °C for 30 min and then baked under vacuum at 1000 °C for 12 min. The growth parameters were almost identical for the two growths. The growth temperature for ZnSe-36H was 1140 °C, with a gradient $\Delta T/\Delta x = 13.5$ °C/cm and the furnace translation rate was 2.17 mm/day. The growth temperature for ZnSe-38V was 1150 °C, with $\Delta T/\Delta x = 14.0$ °C/cm and translation rate was 1.87 mm/day.

Table 4.4 A list of Cr-doped ZnSe growth runs with growth configuration, starting material, heat treatment and furnace translation rate

Run	Starting material	H_2 reduction	Dynamic vacuum	Translation rate (mm/day)	Annealing time (h)
ZnSe-36H (horizontal)	8.52 g $(Zn_{0.963}Cr_{0.037})Se$	0.55 atm at 1000 °C for 30 min	1000 °C for 12 min	2.17	101
ZnSe-37H (horizontal)	8.63 g $(Zn_{0.979}Cr_{0.021})Se$	0.55 atm at 1000 °C for 30 min	1000 °C for 12 min	1.87	199
ZnSe-38V (vertical)	8.93 g $(Zn_{0.962}Cr_{0.038})Se$	0.55 atm at 1000 °C for 30 min	1000 °C for 12 min	1.87	226
Cr–ZnSe #1 (horizontal)	19.31 g $(Zn_{0.987}Cr_{0.013})Se$	0.55 atm at 1050 °C for 30 min	1050 °C for 10 min	3.60	80
Cr–ZnSe #2 (horizontal)	27.12 g $(Zn_{0.984}Cr_{0.016})Se$	0.55 atm at 1050 °C for 30 min	1050 °C for 10 min	3.62	80

After the growth the furnace was cooled down from growth temperature to 400 °C in 72 h and from 400 to 25 °C in 24 h. The detailed information on these growth runs of Cr-doped ZnSe is listed in Table 4.4.

The starting material for Fe-doped ZnSe was prepared by grinding ZnSe (Furukawa Co. 99.9999% purity) and FeSe (Alfa Aesar 99.9%) in mortar. Because the low melting point of 965 °C for FeSe, the mixture was baked under dynamic vacuum at 920 °C for 30 min. For the growth of Fe–ZnSe #1, the source was annealed at 920 °C for 72 h before it was raised to 1130 °C when the furnace translation started. The starting material for the Fe-ZnSe #2 and #3 was annealed as a batch. Firstly, 52.591 g of ZnSe and 1.007 g of FeSe was mixed and loaded into a 16 mm I.D., 20 mm O.D. ampoule before it was connected to vacuum pump. The ampoule was sealed after baking under dynamic vacuum at 920 °C for 30 min and then annealed at 920 °C for 115 h. The retrieved sample provided the source materials for the growth of Fe–ZnSe #2 and #3. For each run, the loaded ampoule was prepared with the heat treatment of H_2 reduction and then dynamic vacuum as given in Table 4.5. The growth of Fe–ZnSe #3 was conducted in a vertical stabilized configuration, i.e., hot source on the top.

4.3.5 Crystal Growth of ZnSeTe by PVT

Several crystal growth experiments of the ternary compound of ZnSeTe were performed [18]. The $ZnSe_{1-x}Te_x$ source materials were prepared for three compositions,

Table 4.5 A list of Fe-doped ZnSe growth runs with growth configuration, starting material, heat treatment and furnace translation rate

Run	Starting material	H_2 reduction	Dynamic vacuum	Translation rate (mm/day)
Fe–ZnSe #1 (horizontal)	21.97 g $(Zn_{0.960}Fe_{0.040})Se$	None	920 °C for 30 min	2.79
Fe–ZnSe #2 (horizontal)	22.20 g $(Zn_{0.980}Fe_{0.020})Se$	0.55 atm at 920 °C for 30 min	920 °C for 30 min	3.62
Fe–ZnSe #3 (vertical)	22.02 g $(Zn_{0.980}Fe_{0.020})Se$	0.55 atm at 920 °C for 30 min	920 °C for 30 min	5.03
Fe–ZnSe #4 (horizontal)	22.32 g $(Zn_{0.979}Fe_{0.021})Se$	0.61 atm at 920 °C for 30 min	920 °C for 30 min	5.04

x = 0.10, 0.20 and 0.30, and for each composition two PVT runs, self-seeded growth under horizontal and vertical stabilized configurations, were performed. In the cases of x = 0.10 and 0.30, ZnSeTe batches were prepared by mixing heat treated ZnSe and ZnTe starting materials and then homogenizing the mixtures at elevated temperatures in vacuum-sealed fused silica ampoules. The ampoules were opened and the homogenized batches were used as source materials for the growth ampoules. In the case of $ZnSe_{0.90}Te_{0.10}$, the ZnSe starting material from Eagle Picher, Inc. was first reduced under 0.58 atm H_2 pressure at 1000 °C for 20 min, followed by baking under vacuum at 1000 °C for 12 min. The ZnTe starting material was synthesized in-house from pure Zn and Te elements provided by Johnson Matthey (99.9999% purity) and then purified by vacuum distillation. The $ZnSe_{0.90}Te_{0.10}$ batch was made from 29.696 g of the heat-treated ZnSe and 4.411 g of the synthesized ZnTe. The binary compounds were ground, mixed and loaded into a previously outgassed fused silica ampoule and then heat treated by H_2 reduction (0.57 atm at 1000 °C for 25 min) and baking under vacuum (1000 °C for 3 min). The sealed ampoule was soaked at 1140 °C for 144 h to homogenize the solid solution and then cooled to 30 °C in 12 h. The ampoule was opened and 10.6 g of the homogenized sample was loaded into each of the ZST-6V and -7H growth ampoules. Prior to seal-off the ampoules were also heat treated by hydrogen reduction (0.53 atm at 1020 °C for 30 min) and baking at 1020 °C under vacuum for 3 min. The sample preparation procedure for $ZnSe_{0.70}Te_{0.30}$ was similar to that of $ZnSe_{0.90}Te_{0.10}$. The ZnSe starting material (Eagle Picher, Inc.) was first reduced under 0.60 atm H_2 pressure at 1010 °C for 20 min and followed by baking under vacuum at 1000 °C for 5 min. The $ZnSe_{0.70}Te_{0.30}$ batch was made from 28.302 g of the heat-treated ZnSe and 16.154 g of the in-house synthesized ZnTe. The mixture of the binary compounds was then heat treated by H_2 reduction (0.56 atm at 950 °C for 35 min) and baking under vacuum (950 °C for 5 min). The sealed ampoule was soaked at 1050 °C for 77 h and cooled to 30 °C in 24 h. Then, 10.5 and 11.5 g of the homogenized sample were loaded into the previously out-gassed ZST-3H and -5V

growth ampoules, respectively. The loaded ampoules were heat treated by hydrogen reduction (0.57 atm at 950 °C for 10 min) and baking at 950 °C under vacuum for 3 min prior to seal-off.

In the case of $ZnSe_{0.80}Te_{0.20}$, the heat-treated ZnSe and ZnTe materials were loaded directly into the growth ampoules as source materials. The starting material of ZnSe (high-purity grade) provided by EaglePicher, Inc. was ground and loaded into a previously outgassed fused silica ampoule. After evacuating to a pressure lower than 10^{-6} Torr the loaded ZnSe was heat treated by annealing at 1000 °C under 0.57 atm pressure of hydrogen for 30 min to remove the oxide in the starting material followed by baking under dynamic vacuum for 7 min at 1000 °C to adjust the source composition toward that of congruent sublimation. The ZnTe starting material (99.999% purity) was provided by Cleveland Crystals, Inc. A total amount of 25.96 g of ground ZnTe was annealed at 1070 °C under 0.66 atm pressure of hydrogen for 45 min, baked under vacuum at 1070 °C for 10 min, then distilled under vacuum at 1070 °C for 3.5 h. The distilled ZnTe, about 6.77 g, was retrieved and heat treated again by hydrogen reduction at 870 °C for 35 min and baking under vacuum at 870 °C for 4 min. The heat-treated ZnSe and ZnTe were ground, mixed and loaded into two growth ampoules, ZST-1V and -2H (V-vertical and H-horizontal). The loaded ampoules were further heat treated by hydrogen reduction (0.56 atm at 890 °C for 10 min) and baking at 890 °C under vacuum for 3 min before sealing under vacuum. The amount of source material and the sample composition for each growth ampoule are listed in Table 4.6.

Two identical three-zone translational furnaces were used for the horizontal and vertical PVT growth experiments. The central zone provided a thermal maximum with a peak at T_P, which was maintained at 1150–1170 °C, about 7–20 °C higher than the source temperature, T_S, while the isothermal cold zone, equipped with heat pipe liner, was controlled at about 1020 °C. Efforts were made to provide a similar thermal profile for the horizontal and vertical growth configurations. Initially, the source was positioned in the source zone with the conical tip of the ampoule in the

Table 4.6 Growth ampoules, masses and compositions of source materials, source temperature T_S, central peak temperature T_P, and furnace translation rates for the ZnSeTe growth runs

Source composition		x = 0.10		x = 0.20		x = 0.30	
Growth run		ZST-6V	ZST-7H	ZST-1V	ZST-2H	ZST-3H	ZST-5V
Starting material	ZnSe	–	–	9.8734 g	9.9205 g	–	–
	ZnTe	–	–	3.3127 g	3.3298 g	–	–
	$ZnSe_{1-x}Te_x$	10.5738 g	10.5823 g	–	–	10.4855 g	11.4743 g
	x	0.09998	0.09998	0.2006	0.2007	0.2992	0.2992
Growth parameters	T_S (°C)	1146	1145	1147	1152	1138	1145
	T_P (°C)	1153	1155	1170	1166	1150	1163
	Furnace translation rate (mm/day)	2.64	2.75	1.96	2.11	2.30	2.30

central zone region. The furnace translated toward the source end and the crystal started to nucleate when the conical tip moved into the cold zone and reached the condition of supersaturation. The annealing time for the source materials at T_S before the onset of nucleation was estimated to be 7.5 days for the ZST-6V and -7H runs and 2 days for the other growth runs. After the furnace has translated 3.3–4.1 cm (4.9 cm for ZST-6V and 6.1 cm for ZST-7H) the growth was terminated by stopping the furnace translation, lowering the source temperature by 10 °C (to prevent further deposition on the growing surface) and then, except for ZST-2H, cooling the settings of three thermal zones at the same rate. The cooling rate was roughly 20 °C/h for ZST-1V and was 10 °C/h for ZST-3H and -5V. For ZST-6V and -7H the furnaces were cooled from 1150 to 400 °C in 72 h and then from 400 to 30 °C in 24 h. During the ZST-2H run the central zone burned out after the furnace had translated 2.4 cm and the furnace was cooled down passively. In addition to the amounts and compositions of source materials, Table 4.6 also lists the source temperature, T_S, the central zone peak temperature, T_P, and the furnace translation rate.

4.3.6 Crystal Growth of CdTe by PVT

High-resistivity CdTe crystals with high mobility-lifetime product are needed for room temperature nuclear radiation detectors [19–22]. The desired high resistivity in CdTe is usually accomplished by the introduction of dopants, such as halogens [23, 24], to compensate for the native defect centers, which are generally thought to be related to Cd vacancies. The requirement of a high mobility-lifetime product means that the crystal needs to show good crystalline quality and have a low concentration of defects, including native or impurity point defects as well as the two- and three-dimensional structural defects such as grain boundaries and Te inclusions or precipitates. The main method used to grow detector grade CdTe material was the traveling heater method (THM) from Te-rich solvent [20, 25, 26]. This low-temperature technique has some advantages over the other high-temperature growth methods in that it results in less thermal strain in the grown crystals and it extracted impurities. The disadvantage of this non-stoichiometric (Te-rich) growth condition is the introduction of Te inclusions and precipitates as well as the native defects such as Cd vacancies which needs a post-growth annealing to mend. Vapor growth techniques offer similar advantages as the THM in that the growth temperature is considerably lower than the melting point. In principle, with accurate control of the stoichiometry during the PVT growth process one should grow CdTe crystal with high resistivity. However, it is difficult to reproducibly grow CdTe crystals with the desired electrical properties and free from Te-precipitates when the partial pressures of the predominant vapor species, Cd and Te_2, vary over orders of magnitude at the growth temperature due to deviations from stoichiometry of the source materials. With the demonstration of heat treatment to consistently drive the source material of CdTe toward congruently sublimation as discussed above, the PVT growth of CdTe has been performed horizontally [27] for self-seeded and seeded configurations.

The starting elements were QZR or double zone refined, 99.9999% purity, Cd rods and QZR, six-nine grade Te bars from Johnson Matthey, Inc. The elements were weighed to the accuracy of 0.1 mg. For different batches, total amounts of 100–220 g of the pure elements were loaded into each ampoule with the nominal Te content ranging from 0.50001 to 0.50006. The sealed ampoules were heated slowly from room temperature to the homogenization temperature of 990 °C and maintained at the temperature for 35–50 h before slow cooling to room temperature. The ampoules were opened and the reacted sponge-like CdTe was crushed and ground into particles with diameter of less than 0.5 mm. The typical heat treatment used to adjust the stoichiometry of the starting materials towards that of the congruent sublimation condition [28] was performed by baking the loaded ampoule at 870 ± 10 °C under dynamic vacuum for 5–10 min. For the seeded growth, the CdTe seeds, provided by Keystone Crystal Corp., were 7 mm dia., 2 cm long (111) or (211) orientation twin-free single crystals. The typical thermal profile for the growth was: source temperature at 840 ± 15 °C with a central maximum of 10–15 °C higher than the source and a cold zone of 780 ± 20 °C. The thermal gradient at the crystal interface was about 22 ± 8 °C/cm. The furnace translation was 3.3 to 3.9 mm/day and the crystal was cooled at a rate of 15 ± 5 °C/h to room temperature. Tables 4.7 and 4.8 list the growth parameters of the experimental runs for self-seeded and seeded growth, respectively. The information includes the baking under dynamic vacuum, the growth temperatures (cold; peak; hot), the furnace translation rate, and the specific comment on the runs.

Table 4.7 Growth parameters for the experimental self-seeded runs for CdTe

Run	Bake condition temperature (°C); min.	Growth temperature (°C)	Translation rate (mm/day)	Comments
CdTe-8	865; 10	680; 875; 865	3.91	All material transported
CdTe-11	880; 4	680; 887; 872	3.75	–
CdTe-13	880; 5	740; 890; 883	3.13	–
CdTe-16	880; 5	735; 896; 880	3.22	Flat and facet growing surface
CdTe-17	880; 7	735; 893; 875	3.96	Flat and facet growing surface
CdTe-18	880; 5	735; 893; 875	4.25	Flat and facet growing surface; all material transported

Table 4.8 Growth parameters for the experimental seeded runs for CdTe

Run[a]	Bake condition temperature (°C); min.	Growth temperature (°C)	Translation rate (mm/day)	Comments
CdTe(s)-1	870; 10	710; 862; 853	3.79	1.4 cm grown on top of seed
CdTe(s)-4	860; 8	730; 874; 863	3.74	2.0 cm grown on top of seed
CdTe(s)-6	860; 8	730; 874; 863	3.67	All the material transported
CdTe(s)-7	865; 8	730; 874; 863	3.87	Convex growing surface
CdTe(s)-9	860; 8	715; 844; 826	3.33	Convex growing surface
CdTe(s)-10	825; 10	715; 844; 826	3.85	–
CdTe(s)-14	798; 12	715; 844; 826	4.26	1.6 cm grown on top of seed
CdTe(s)-20	825; 10	705; 868; 846	3.89	1.6 cm grown on top of seed
CdTe(s)-22	1000; 7	800; 863; 852	3.87	Growth direction: 10° off (211)

[a]All runs were grown on top of (111) seed except CdTe(s)-20 and -22 on (211) seed

4.3.7 Crystal Growth of CdS by PVT

Growth of CdS by PVT has been investigated for many years [29–39]. In most cases, the growth was accomplished by simply establishing a temperature difference between the starting material and the cold end of the ampoule where the crystal was grown. Furnace translation was used in few cases. However, poor reproducibility of these methods resulted in low yield.

In our studies [8], the CdS starting materials were supplied by Cleveland Crystals, Inc., and were either 99.99 or 99.995% purity. The amount of starting material loaded into the growth ampoule varied from 8 to 39 g. The growth ampoules were typically 20 mm I.D. and 24 mm O.D. For self-seeded growth, one end of the ampoule was tapered to a point. For seeded growth, a section of a 10 mm I.D. silica tube was connected to the tapered end and a CdS seed crystal of diameter slightly less than 10 mm was placed in the tube and was held in position by a fused silica rod. The ampoules were evacuated by a turbo-molecular pump after the starting materials were loaded. When the vacuum had reached 3×10^{-6} Torr, a sliding tubular furnace moved into bake out the sample at temperature between 950 to 1030 °C for 7 to 15 min and the vacuum level stabilized below 1×10^{-5} Torr. The thermal profile for the crystal growth was: 930–985 °C for the hot zone with the thermal peak 15–20 °C higher than the hot zone and 620 °C for the cold zone. The furnace translated with a rate between 2.7 and 4.9 mm/day. To study the effects of heat treatment, the source

material for two self-seeded runs were baked under dynamic vacuum at 1050 °C for 15 and 32 min. After the growth with furnace translation rate of 3.8–4.0 mm/day, the entire source has transported. However, the measured masses of the two grown crystals were 56 and 37% of that of the loaded source materials, respectively, for the 15 and 32 min treatment under dynamic vacuum.

4.3.8 Crystal Growth of ZnTe by PVT

The growth process of PVT has been employed [40–42] to produce ZnTe crystals of high purity and good crystalline quality for various electro-optic devices. In our study [9, 43], the starting material of ZnTe was synthesized by weighing the stoichiometric amount of six-nines grade Zn and Te, provided by Johnson Matthey, loading and sealing them in a fused silica ampoule under vacuum. The homogenization was accomplished by annealing the ampoule at 1020 °C for 14 days and then at 1100 °C for 8 days. The interior of the fused silica growth ampoules were graphitized (carbon-coated) by maintaining it at about 1000 °C while a mixture of 90% Ar and 10% methane was flowing inside. Two crystal growths by the horizontal PVT, ZnTe-1 and ZnTe-2, were performed. After the ampoules were cleaned, baked and graphitized, ZnTe starting material synthesized from the same batch were loaded. For ZnTe-1, 27.1 g source material was baked out at 1000 °C for 8 min under dynamic vacuum condition whereas, for ZnTe-2, 28.9 g of ZnTe was baked at 876 °C for 10 min. During the growth of ZnTe-1, the hot zone was at 1010 °C with a maximum of 1022 °C at the booster heater and a cold zone of 860 °C. The furnace translated for a distance of 5.8 cm with the rate of 3.38 mm/day and all of the source material was transported. The first run for ZnTe-2 was conducted at lower temperatures with the hot zone at 870 °C, a maximum of 883 °C and a cold zone of 675 °C with a translation rate of 3.2 mm/day for 5.0 cm. There was very small amount of material with a 5 mm long shape of cone formed at the growth tip. The ampoule was grown again using the same thermal profile as ZnTe-1. After a translation distance of 5.4 cm with a rate of 3.30 mm/day, all of the source material was transported. Comparing the mass of the grown crystal, 27.9 g to the initial load of 28.9 g, 3.5% of the starting material was lost during the baking under dynamic vacuum.

4.4 In-situ Real Time Optical Monitoring During Growth

As discussed early, two of the three processes of PVT: transport of vapor species and condensation of vapor species to form crystal can be affected by the convective flow in the vapor phase. To have a better understanding of the vapor transport and condensation process, i.e., the partial pressures and growth kinetics on the growing surface, a series of in-situ real time optical monitoring techniques were employed.

4.4.1 Optical Absorption Measurements

Figure 4.4 is a schematic of the in-situ monitoring furnace developed in our laboratory. A 20 cm × 1 cm quartz window is positioned on either side of the furnace to allow optical absorption measurements as well as visual monitoring. Because the window splits the furnace in half, and because of the heavy thermal losses at the window, several guard elements were installed around the windows. A total of 15 heating elements were independently controlled by 8 controllers. The instrument for the in-situ optical absorption measurements is essentially the same as that for the partial pressure measurements described in Sect. 2.1.3. Briefly, the optical absorption portion of the in-situ monitoring furnace is a two beam system. It consists of lamp housing with an ultra violet deuterium lamp and a visible xenon lamp as the excitation sources and a monochromator/spectrometer as an analysis device. The lamp housing and monochromator/spectrometer move in tandem so that optical absorption measurements may be taken at any location along the 20 cm length of the window. This allows the vapor species to be determined at any position along the length of the ampoule. The optical absorption apparatus can also be moved completely away from the window, allowing visual monitoring of the crystal from a side view. Figure 4.4 shows the location of the video camcorder, (as a cross-hatched box), when the optical absorption apparatus is moved away.

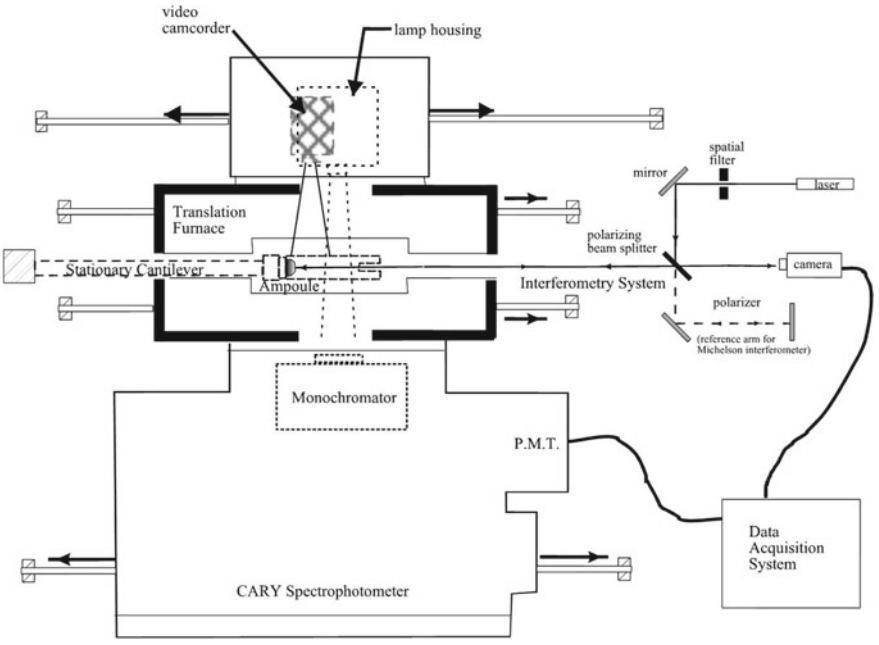

Fig. 4.4 Schematic of the in-situ monitoring furnace and optical instruments; top view (taken from Fig. 3 of Ref. [44])

4.4.1.1 In-situ Optical Absorption for Partial Pressure Measurements

In-situ optical absorption was measured [44] along the length of the growth ampoule at the square tubing section during the growth. The operation was automated such that measurements at specific positions and times over a specified wavelength range were made following a script file. Figure 4.5 shows the partial pressures of Se_2 measured as a function of experimental time at three positions along the ampoule during the ZnSe(IS)-5 run. The source to seed distance was 8 cm and the measurements were made at 3.2, 4.2 and 5.2 cm from the seed. From the beginning of the run when furnace heating was initiated to 20 h into the run, the measured P_{Se_2} were about the same, 2×10^{-3} atm, at these three locations. For the rest of the run, i.e. from 20 to 140 h, the measured P_{Se_2} at 3.2 and 5.2 cm were about the same. Their values stayed constant at about 2×10^{-3} atm until 30 h into the run where the onset of crystal growth was observed by visual observation described in the later Sect. 4.4.1.2. After that the measured P_{Se_2} kept on increasing to about 6×10^{-3} atm at the end of the run. The P_{Se_2} measured at the middle position, 4.2 cm from the seed, however, varied from about 2 times higher than that measured at the 3.2 and 5.2 cm at 30–50 h into the run to about one half of the values at the two end positions between 70 and 135 h into the run. The error associated with the experimental measurements on the partial pressures of Se_2 is estimated to be 15–20%.

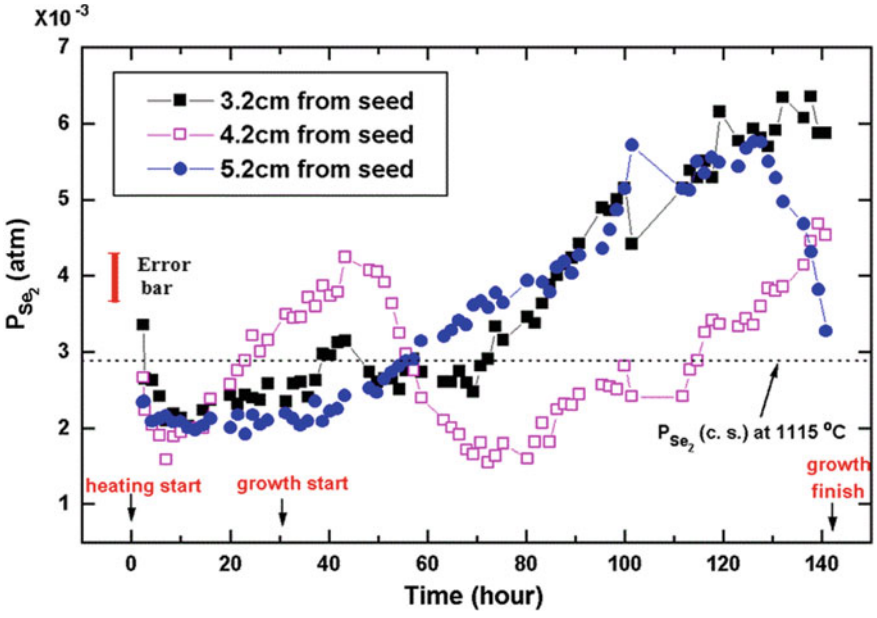

Fig. 4.5 Partial pressures of Se_2 measured as a function of experimental time at three positions along the ampoule during the ZnSe(IS)-5 run (taken from Fig. 4 of Ref. [44])

The increase in the P_{Se_2} for the end positions implies that the growing ZnSe crystal was more Zn-rich than the source and thus the source composition kept shifting toward Se-rich. The large difference in the P_{Se_2} measured at the middle and end sections of the ampoule is not consistent with the results of a one dimension diffusion model which predicts a monotonic variation in the partial pressure profile from source to crystal.

4.4.1.2 In-situ Visual Observation

The imagines of growing crystal were taken in-situ over duration of 10–20 s via a camcorder every 6–8 h [12]. The furnace was hot enough that no illumination source was necessary, although a neutral density filter was used to avoid saturation of the camera. A series of pictures was created which shows the progress of the growing crystal (see Fig. 4.6). As intended, the seed crystal first etched back, with greater thermal etching occurring along the edges of the seed crystal. Once growth started, the crystal grew in a predominately non-contact mode and facets were evident during growth. The crystal did not grow symmetrically, which is believed to be due to the unintentional asymmetry of the radial thermal profile in the furnace. The fact that the top of the crystal continued to etch back, while the bottom grew again indicates an asymmetry in the thermal profile.

4.4.2 Optical Interferometry Measurements

The optical interferometer looks into the central bore of the furnace, and through the window of a specially designed ampoule as shown schematically in Fig. 4.7. The interferometer can be used to monitor in real-time the evolution of growing surface morphology and crystal growth rate. The measurements can be set up in one of two configurations. The first set-up is a standard Michelson interferometer, as shown in Fig. 4.8a, using a polarized laser and polarizing beam splitter to allow more optical power to be imaged on the crystal surface where losses are higher than at the surface reflecting mirror used in the reference arm. The second set-up is a Fabry–Perot type set-up as shown schematically in Fig. 4.8b. In this case the reference arm of the Michelson interferometer is blocked, and the Fabry–Perot interference is formed between the lights partially reflected from the front surface and the light reflected at the back surface of the crystal. The advantages of Fabry–Perot interferometry are (1) it does not need a calibration standard and (2) it only measures the relative spatial displacement of the front and back surfaces without any influence from the external environment.

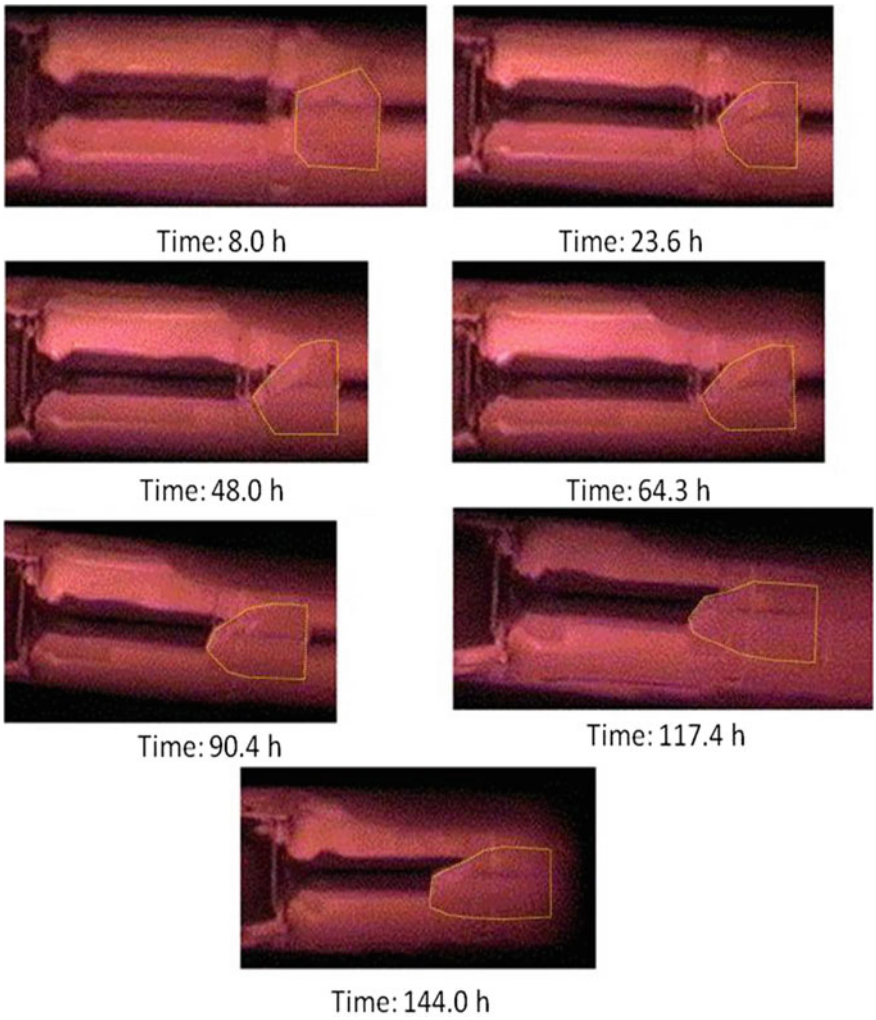

Fig. 4.6 Series of pictures from video photographs taken during growth. The seed crystal first etched back, with greater thermal etching occurring along the top edges of the seed crystal. Once furnace translation started, the crystal grew in a predominately non-contact mode and growth facets are evident during growth. The dashed line is intended as viewing guide to delineate the contour of the growing crystal

4.4.2.1 Thermal Expansion Coefficient

One of the by-products from the in-situ real time optical monitoring during crystal growth is the thermal expansion of ZnSe which was measured by Fabry–Perot interferometry from 17 to 1080 °C during the heat-up of a seeded crystal growth experiment [45]. The ZnSe sample was a single crystal, in the shape of a 10 mm

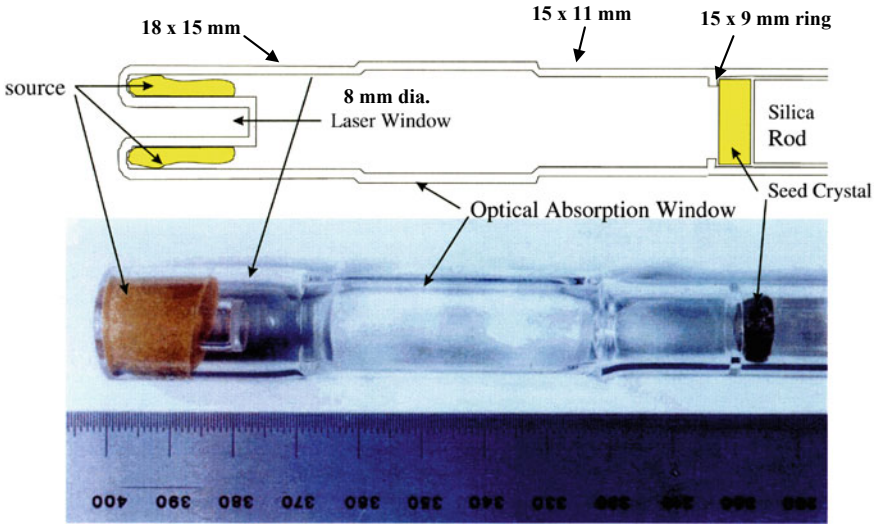

Fig. 4.7 Schematic (top) and photograph (bottom) of the specially designed ampoule for in-situ optical monitoring of surface morphology and growth rate (taken from Fig. 1 of Ref. [45])

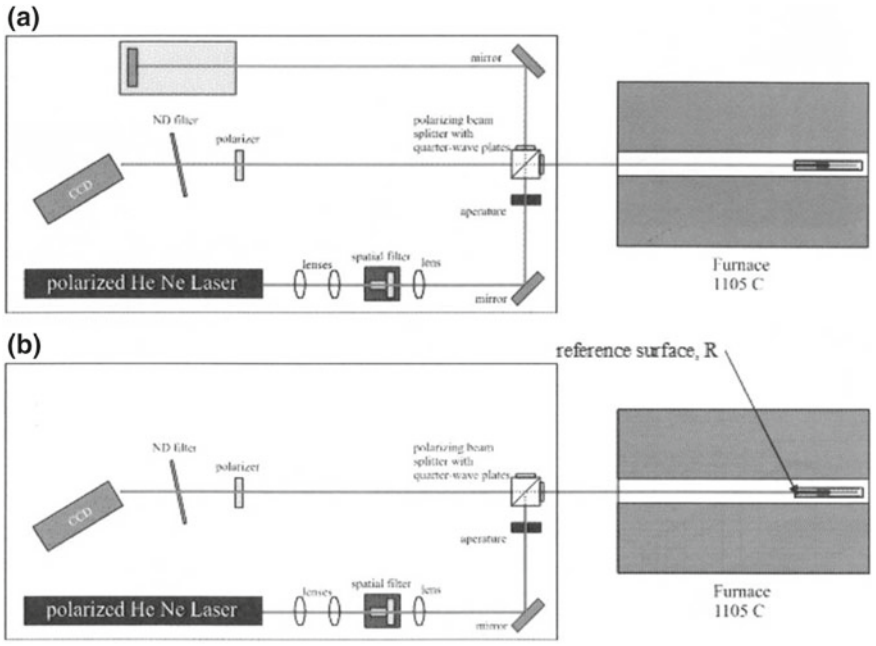

Fig. 4.8 Optical interferometric set-ups for the **a** Michelson configuration. **b** The Fabry–Perot configuration for monitoring crystal surface morphology and growth rate

dia. cylindrical disk with polished (110) surfaces, provided by Eagle-Picher, Inc. The thickness was measured to be 4.48 mm by an Ono Sokki precision linear gauge GS-112/DG-3610. The light source, a polarized He–Ne laser, was reflected through a beam splitter, located at about 60 cm outside the furnace, and directed on the ZnSe seed crystal inside the optical ampoule, which was positioned coaxially inside the tubular furnace. Since the ZnSe crystal is partially transparent to the He–Ne red laser (wavelength 632.8 nm), the reflecting light from the front and back surfaces of the ZnSe disc formed a Fabry–Perot interference pattern, which was recorded on a CCD camera.

A two-step heat-up of the furnace was performed with the initial settings of all the zones at 830 °C, and later raised to 1080 °C. About 20 min after the initial heat-up, the furnace reached 830 °C and was equilibrated at that temperature for about 40 min before heating up to the final settings of 1080 °C with the following equilibrating time of about 15 min. The readings of the two thermocouples were recorded as a function of time. The readings of the thermocouples near the crystal are plotted as a function of time in Fig. 4.9.

As the sample expanded during heating, the fringe pattern was recorded continuously as a function of time. After the heating was completed, the video of the interference fringe pattern, showing movement in the upward direction in this case, was reviewed and the accumulated number of fringes passing through the center of the screen was recorded as a function of time. The sample expansion can be calculated using the equation $\Delta L = n(\lambda/2)$, where ΔL is the change in sample thickness, n the accumulated number of fringes, and λ the wavelength of the light source. Using λ of 632.8 nm for the He–Ne laser, the thermal expansion, ΔL, was calculated. Figure 4.9

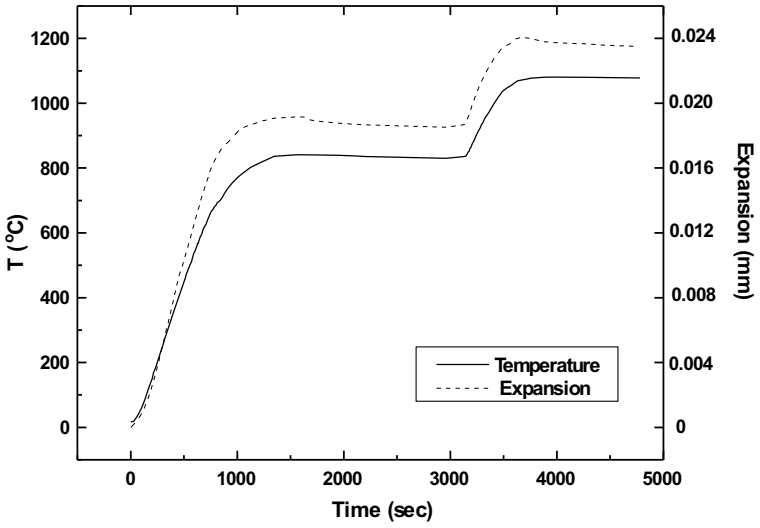

Fig. 4.9 The synchronized plots of sample temperature (left ordinate) and the measured thermal expansion (right ordinate) (taken from Fig. 2 of Ref. [45])

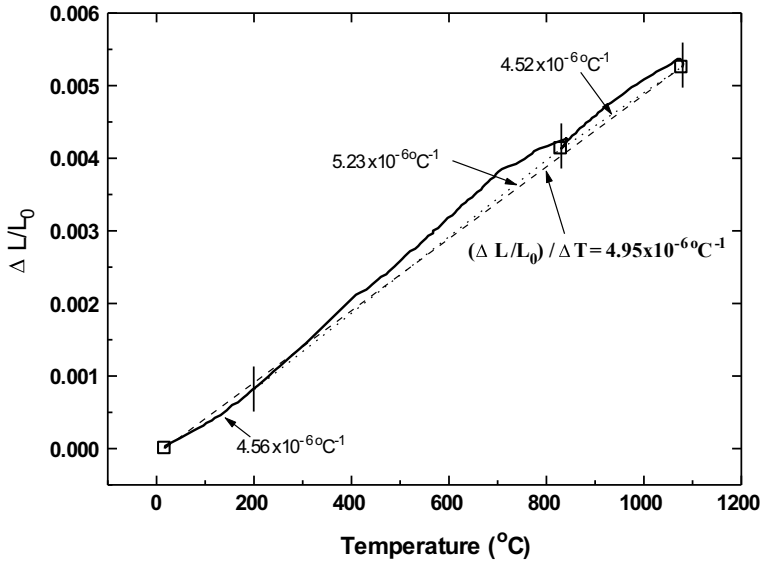

Fig. 4.10 The measured $\Delta L/L_0$ (the solid curve) plotted as a function of temperature. The interpolation between the data at 17 and 1080 °C gives the thermal expansion coefficient, α, of 4.95 × 10^{-6} °C^{-1}, whereas the three piece-wise linear interpolations give α values of 4.56, 5.23, and 4.52 × 10^{-6} °C^{-1} (taken from Fig. 3 of Ref. [45])

plots the sample temperature and thermal expansion as a function of time, which was synchronized to the onset of furnace heat-up as time zero. The thermal expansion, shown in Fig. 4.9 follows the two-step heating schedule very well. It also shows that the sample was slightly overheated at the end of both the initial and final heating, as indicated by the small contraction (fringe moving in opposite direction, i.e., downward) during the subsequent equilibration time.

To determine the linear thermal expansion coefficient, α, which is defined as $\alpha = \frac{\Delta L/L_0}{\Delta T}$, $\Delta L/L_0$ is plotted against temperature, T, in Fig. 4.10 using the initial sample thickness $L_0 = 4.48$ mm. Taking the value of zero for ΔL at 17 °C and the final thermal equilibrated point for $\Delta L/L = 0.00526$ at 1080 °C, the single linear interpolation, shown as dashed line in Fig. 4.10 gives a value of α as 4.95 × 10^{-6} °C^{-1}. The estimated errors associated with α gives its range of 4.60 to 4.99 × 10^{-6} °C^{-1}.

4.4.2.2 Growing Surface Morphology Mapping by Interferometer

Video of the fringes from the optical interferometer was recorded continuously over the entire crystal growth run. The interferometer was aligned initially at room temperature and realigned several times during the growth as the advancing surface moves out of the focused range of the optical set-up. The system can be realigned by either

changing the position of the camera, changing the position of the optical breadboard table the interferometer is mounted to or by changing the position of the ampoule containing the growing crystal. Since the latter adjustment also slightly changes the thermal profile around the growing crystal, this is done only when necessary. On the left of Fig. 4.11 shows an interferogram taken from the surface of the ZnSe seed crystal at room temperature. The size of the image correlates to an area on the seed crystal of roughly 2.8 mm by 3.7 mm. On the right of Fig. 4.11 shows the results of fringe analysis obtained for this interferogram using Fast/Vai software. Although Fast/Vai is a relatively simple fringe analysis program, it is evident that reasonable data can be obtained. Figure 4.12 shows the results from a more sophisticated fringe analysis technique which allows background subtraction, among other things [46]. These preliminary results show the feasibility of using a system such as the one

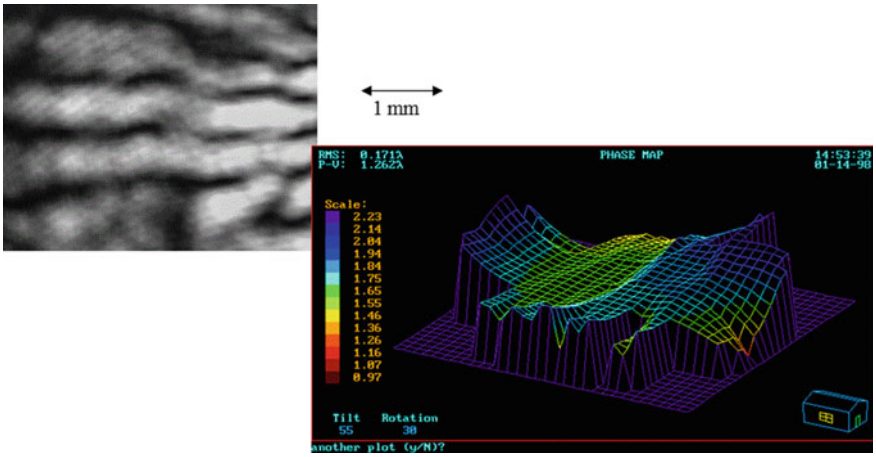

Fig. 4.11 (Left) Interferogram taken on the surface of the ZnSe seed crystal at room temperature, and (right) the results of fringe analysis obtained for this interferogram using the Fast/Vai program. The size of the image correlates to an area on the seed crystal of roughly 2.8 mm by 3.7 mm

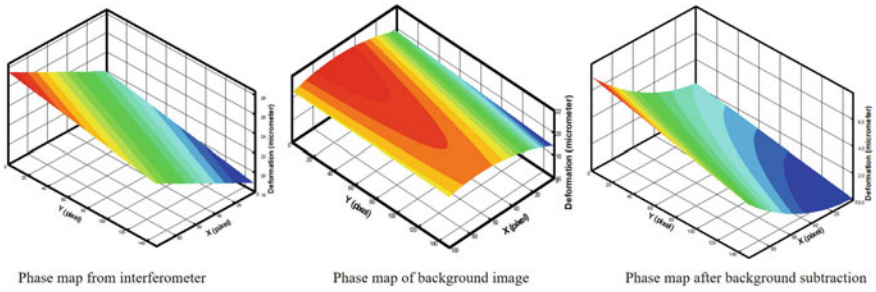

Fig. 4.12 Results using a more sophisticated fringe analysis technique that allows background subtraction

described here to measure the instantaneous growth rates and the evolution of the growing surface morphology. Both Michelson and Fabry–Perot interferometers were set up to perform in-situ monitoring of the growing surface. Each has specific advantages. The Michelson set-up was flexible, i.e. the optics was easy to adjust before and during growth, but the fringe patterns were noisy because of the changes in the surrounding thermal environment. The Fabry–Perot set-up provided good quality fringe patterns but the optics was rigid and difficult to adjust through the run.

The noise could be significantly suppressed by using a Michelson interferometer with a modified in-situ monitoring growth ampoule as shown in Fig. 4.13 to reduce the effects of thermal disturbance. Similar to the triple cell described in Sect. 2.1.3 for the partial pressure measurements by optical absorption, an evacuated dummy tube was attached to the source end of the in-situ monitoring ampoule to eliminate the thermal disturbance from the air along the path of the laser beam. The ampoule, ZnSe(IS)-7, was placed inside the furnace and was aligned for the Michelson interferometer setup. The interference images were recorded by the camera during the heat-up of the furnace from 25 to 1120 °C. As a result of the modification, highly stable as well as good quality fringe patterns were observed during the entire heat-up period and Fig. 4.14 shows the results of fringe analysis obtained from an interferogram taken at 1120 °C.. The test confirms that the noise observed earlier in the Michelson interferograms was caused by thermal convection of the air along the laser path. As the thermal etching of the seed progressed, the fringe patterns started to become fuzzy and eventually disappeared as the planar growing surface evolved into curved surface with facets which was evident in the discussions of in-situ visual observation.

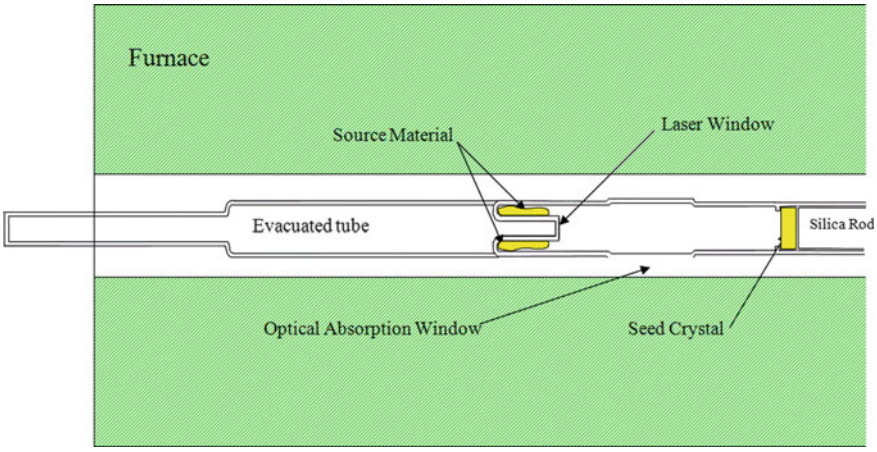

Fig. 4.13 Modified in-situ monitoring growth ampoule. This set-up allows the use of the Michelson configuration even at high temperature

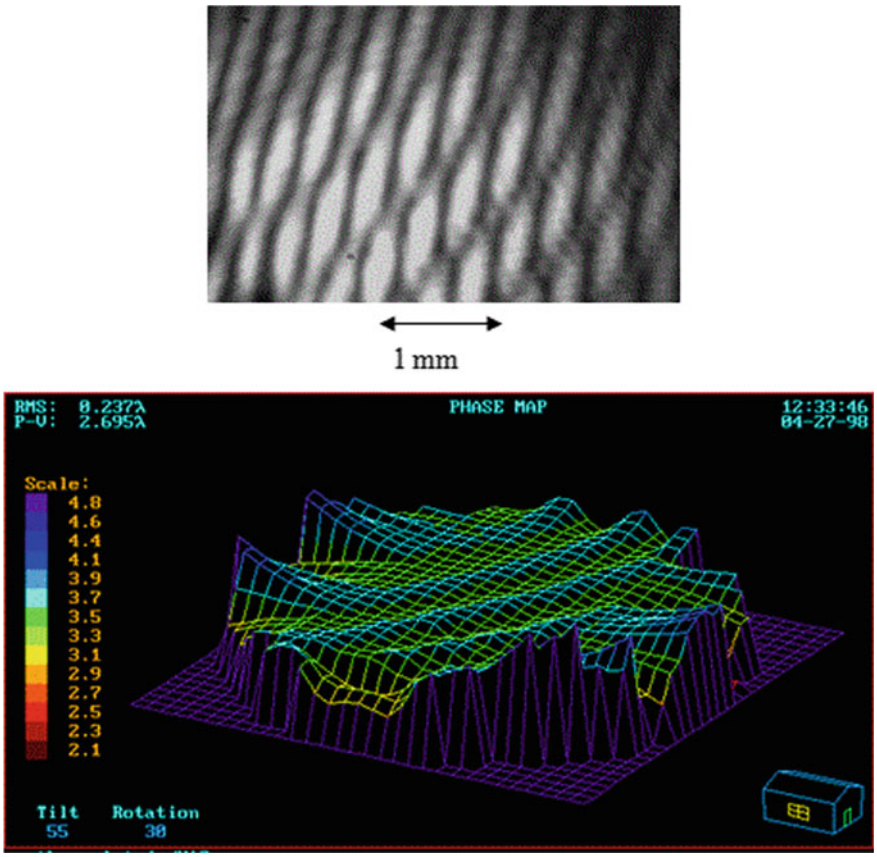

Fig. 4.14 Results of fringe analysis (bottom) obtained from an interferogram (top) using the modified ampoule shown in Fig. 4.13 taken at 1120 °C

4.5 Recent Advancement on the Enhancement of Transport Rate by PVT

Some of the results reported above were obtained before 2013. Then, the crystal growth laboratory was moved into a new building. After the growth facility was set up in the new laboratory, it was found that the mass flux during the PVT process of ZnSe was much lower than that in the old building. In the reviewing of the PVT process, it has been reminded that during the homogenization of CdZnTe, after the pure elements of Cd, Zn, and Te were sealed inside a fused silica ampoule under vacuum and heated up to 1160 °C for 3–5 h to mix and homogenize the melt, significant contaminations of Cu, C, and O were observed [47]. By processing the loaded ampoules inside a larger diameter fused-silica tube, which was evacuated to 1×10^{-3} Torr during the high temperature homogenization, the contamination was minimized. The mass diffusion

of O_2 through quartz has been studied in the temperature range of 450–700 °C [48] which showed a good correlation of the diffusion coefficient with water fugacity. The result suggests that the oxygen-bearing species responsible for the rapid transport of oxygen is molecular water. The rate controlling step for oxygen diffusion may be either the rate of migration of water molecules, or the rate of oxygen exchange between the water molecules and the fused silica structure. Hence, it is postulated that the diffusion rate of O-based vapor species from the atmosphere through the fused-silica wall at elevated temperature depends on the external atmospheric environment which may cause the high level of residual gas pressure and slow the mass flux of the PVT process. Therefore, an extra out-layer of evacuated closed tube will reduce the vapor pressure diffusing into the growth ampoule and can enhance the crystal growth rate. The testing of the hypothesis was conducted on the horizontal self-seeded growth of ZnSe [49].

The setup of the horizontal growth furnace is shown in Fig. 4.15. As reported in Sect. 4.3.1, it consists of three independently controlled electric-resistivity tubular heating zones, two long zones on the sides and a short central booster heater in the middle. A 29 mm O.D., 26 mm I.D., 8-foot long fused silica tubing, with the right end closed and the left end connected to a mechanical pump, was hanging coaxially inside the tubular heaters by two holders outside the furnace. The furnace assembly was provided with stepping motor for translational mechanism while the hanging tubing with the growth ampoule inside, remains stationary. The 20 mm O.D., 16 mm I.D. fused silica growth ampoule, with a silica rod connected to the tapered tip at the left and source material at the right end, was initially placed inside the tubing at a prescribed location relative to the thermal profile as shown schematically in Fig. 4.16.

The initial testing consists of two growth runs. Both runs were processed with the same procedures except the run, ZnSe-1, was processed with the growth ampoule in the fused silica tubing under the environment of normal atmosphere, whereas ZnSe-2 was processed inside the tubing with a vacuum level of 1×10^{-3} Torr provided by a mechanical pump. The detailed procedures are presented below with the growth parameters given in Table 4.9. The growth ampoules were cleaned and baked at 1080 °C under vacuum for 16 h. About 29.7 g (99.999%) ZnSe powder, provided

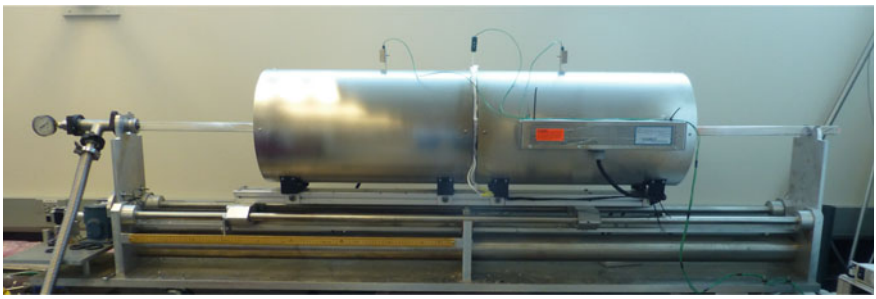

Fig. 4.15 The three-zone horizontal growth furnace with a fused silica tubing containing the growth ampoule

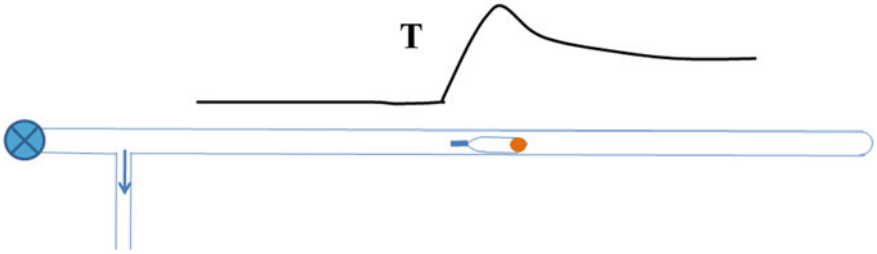

Fig. 4.16 Schematics of the assembly of closed-end fused silica tubing and the initial position of the growth ampoule relative to the thermal profile

Table 4.9 Initial mass loaded, processing time, furnace translational rate, and mass of grown crystals

Growth run	Mass of starting ZnSe (g)	Processing time (h)	Translational rate (mm/day)	Mass of grown crystal (g)
ZnSe-1	29.698	212.75	4.92	4.195
ZnSe-2	29.685	210.50	5.03	29.239
ZnSe-3	29.672	107.78	9.82	24.025

by Alfa Aesar, were loaded inside ampoules and evacuated to 2×10^{-5} Torr. The loaded ampoules were then back filled with 0.55 atm of high purity H_2 and baked at 1050 °C for 30 min to reduce the oxides. After the reduction, the ampoules were re-opened to the vacuum pump, without exposing to the atmosphere, and the samples were baked at 1050 °C under dynamic vacuum of 2×10^{-5} Torr for 10 min. Then the loaded ampoules were evacuated at room temperature and sealed under a vacuum of 1×10^{-5} Torr. The growths by PVT were processed horizontally inside the tubular furnaces shown in Fig. 4.15 with the sources at the temperature range of 1100–1130 °C for about 210 h as the furnace translated with a speed of roughly 5 mm/day. After the growth, the furnace was cooled down, at a rate of 1 °C/min from 1130 to 1000 °C, about 3.5 °C/min from 1000 to 400 °C.

The growth ampoules were retrieved and photographs were taken. In the case of ZnSe-1, Fig. 4.17a shows that only a few crystalline specks, with enlarged view shown in Fig. 4.17b, were formed at the left tip with a large amount of starting material remaining un-transported at the right end. The fact that there was no stable crystal growing front indicates that the mass flux, even under large ΔT, could not catch up with the furnace translation rate of 4.92 mm/day.

The growth ampoule of ZnSe-2, the run processed under the vacuum environment, is given in Fig. 4.18a, which shows that all of the starting material had transported with small amount of residual impurities left behind in the form of black powder. Figure 4.18b shows the photograph of the 3.5 cm long grown crystal. The measured mass of the grown crystal indicates more than 98% yield from the starting ZnSe material with, probably, most of the waste lost during baking under vacuum.

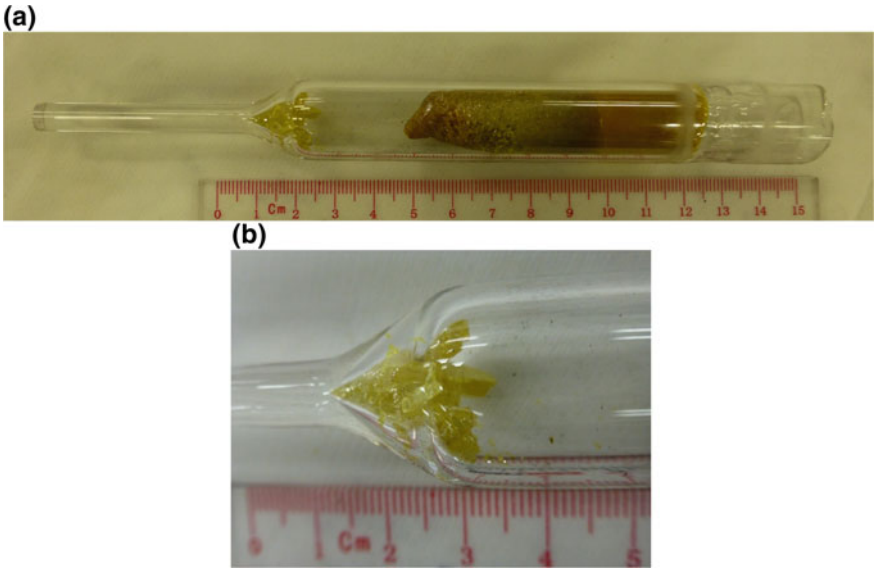

Fig. 4.17 **a** Grown ampoule of ZnSe-1. **b** Enlarged view of the grown section

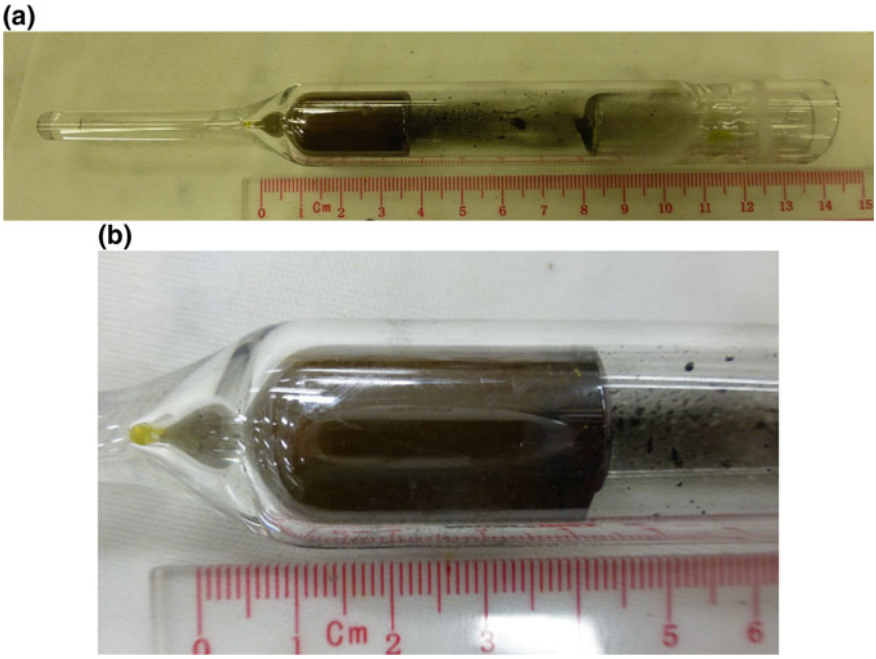

Fig. 4.18 **a** Grown ampoule of ZnSe-2. **b** Enlarged view of the grown section

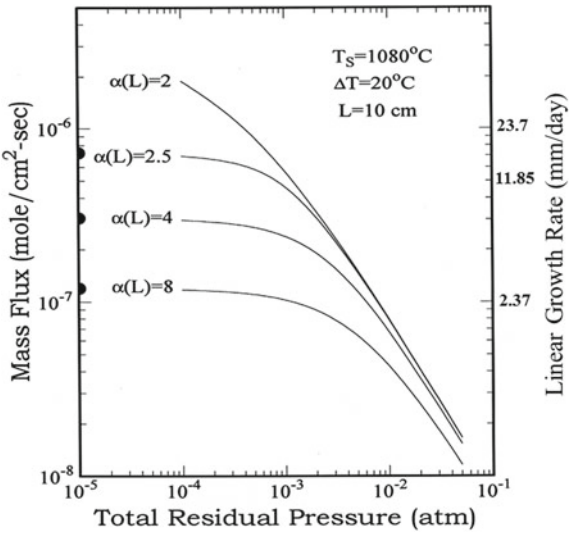

Fig. 4.19 Calculated mass flux of ZnSe as a function of total residual pressure, for source temperature at 1080 °C and different values of α(L). The right scale gives the corresponding linear growth rate in mm/day (taken from Fig. 3 of Ref. [50])

The fact that the starting material has transported completely indicates that the mass flux during the growth process is higher than the furnace translational rate of 5.03 mm/day. The calculated results on the mass flux of ZnSe from Chap. 2 and Ref. [50], as shown in Fig. 4.19, predicts that, for the growth conditions of the run, i.e., an estimated starting material of $\alpha(L) = 2.5$ and a residual gas pressure of less than 10^{-3} atm, the linear growth rate should be higher than 12 mm/day. Therefore, another test run, ZnSe-3, was performed which was processed under the similar procedures as ZnSe-2 except the furnace translational rate was 9.82 mm/day, about twice faster than that for ZnSe-2. The growth ampoule, given in Fig. 4.20a, shows that all of the starting material has transported to the left end and the grown crystal is about 3.2 cm long, as shown in Fig. 4.20b.

The results of the tests prove that, with the processed ampoule under the environment of vacuum, the production yield of PVT growth can be greatly enhanced in terms of (a) much less waste of starting material and (b) much higher throughput of the grown crystals from the faster growth rate. The setup of a vacuum environment for the growth ampoule is rather simple, especially for the horizontal growth configuration, and the outer fused silica tubing can be much shorter in length than the 8 feet used here with two closer stands and shorter furnace assembly.

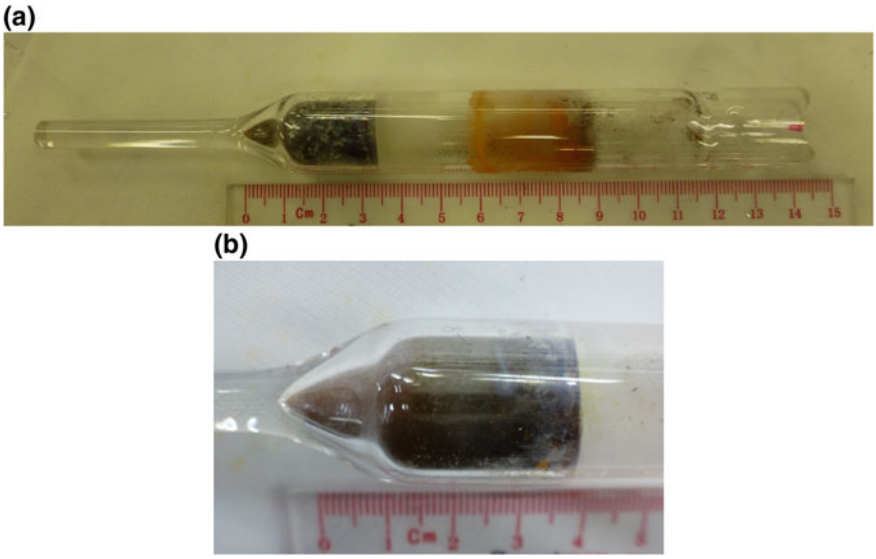

Fig. 4.20 **a** Grown ampoule of ZnSe-3. **b** Enlarged view of the grown section

References

1. D.J. Lawson, Jr., J.I.D. Alexander, D. Gillies, F.M. Carlson, J. Wu, D. Black, Joint Launch + One Year Science Review of USML-1, in *NASA Conference Publication* 3272, vol. 1 (1994), pp. 129
2. C.-H. Su, M.A. George, W. Palosz, S. Feth, S.L. Lehoczky, J. Cryst. Growth **213** (2000), 267
3. C.-H. Su, S.L. Lehoczky, F.R. Szofran, J. Appl. Phys. **60** (1986), 3777
4. W. Palosz, H. Wiedemeier, J. Cryst. Growth **131**, 193 (1993)
5. W. Palosz, F.R. Szofran, S.L. Lehoczky, J. Cryst. Growth **142**, 215 (1994)
6. W. Palosz, J. Cryst. Growth **191**, 897 (1998)
7. W. Palosz, J. Cryst. Growth **267**, 475 (2004)
8. C.-H. Su, S.L. Lehoczky, F.R. Szofran, J. Cryst. Growth **101** (1990), 221
9. C.-H. Su, M.P. Volz, D.C. Gillies, F.R. Szofran, S.L. Lehoczky, M. Dudley, G.-D. Yao, W. Zhou, J. Cryst. Growth **128**, 627 (1993)
10. C.-H. Su, Y.-G. Sha, M.P. Volz, D.C. Gillies, F.R. Szofran, S.L. Lehoczky, W. Zhou, M. Dudley, H.-C. Liu, R.F. Brebrick, J.C. Wang, Proc. AIAA 32nd Aerospace Sciences Meeting (1994), paper 94-0564
11. C.-H. Su, Y.-G. Sha, *Current Topics in Crystal Growth Research*, vol. 2 (1995), p. 401
12. C.-H. Su, Y.-G. Sha, K. Mazuruk, S.L. Lehoczky, H.-C. Liu, R. Fang, R.F. Brebrick, J. Cryst. Growth **166**, 736 (1996)
13. L.D. DeLoach, R.H. Page, G.D. Wilke, S.A. Payne, W.F. Krupke, IEEE J. Quantum Electron. **32**, 885 (1996)
14. R.H. Page, K.I. Schaffers, L.D. Deloach, G.D. Wilke, F.D. Patel, J.B. Tassano Jr., S.A. Payne, W.F. Krupke, K.-T. Chen, A. Burger, IEEE J. Quantum Electron. **33**, 609 (1997)
15. J. McKay, K.L. Schepler, G. Catella, OSA TOPS **26**, 420 (1999)
16. R.H. Page, J.A. Skidmore, K.I. Schaffers, R.J. Beach, S.A. Payne, W.F. Krupke, in *OSA, Trends in Optics and Photonics*, ed. by C. R. Pollock, W. R. Bosenberg, vol. 10 (OSA, Washington, DC, 1997), p. 208
17. M. Seiter, D. Keller, M.W. Sigrist, Appl. Phys. B **67**, 351 (1998)

18. C.-H. Su, Y.-G. Sha, M.P. Volz, P. Carpenter, S.L. Lehoczky, J. Cryst. Growth **216**, 104 (2000)
19. K. Zanio, W. Akutagawa, J.W. Mayer, Appl. Phys. Lett. **11**, 5 (1967)
20. T. Taguchi, J. Shirafuji, Y. Inuishi, Jpn. J. Appl. Phys. **13**, 1169 (1974)
21. P. Siffert, A. Cornet, R. Stuck, R. Triboulet, Y. Marfaing, IEEE Trans. Nucl. Sci. NS **22**, 211 (1975)
22. J.C. Tranchart, P. Bach, J. Crystal Growth **32**, 8 (1976)
23. R.O. Bell, F.V. Wald, C. Canali, F. Nava, G. Ottaviani, IEEE Trans. Nucl. Sci. NS **21**, 331 (1974)
24. C. Eiche, W. Joerger, M. Fiederle, D. Ebling, R. Schwarz, K.W. Benz, J. Cryst. Growth **146**, 98 (1995)
25. H. Chen, S.A. Awadalla, K. Iniewski, P.H. Lu, F. Harris, J. Mackenzie, T. Hasanen, W. Chen, R. Redden, G. Bindley, I. Kuvvetli, C. Budtz-Jørgensen, P. Luke, M. Amman, J.S. Lee, A.E. Bolotnikov, G.S. Camarda, Y. Cui, A. Hossain, R.B. James, J. Appl. Phys. **103**, 014903 (2008)
26. S.A. Awadalla, J. Mackenzie, H. Chen, B. Redden, G. Bindley, M.C. Duff, A. Burger, M. Groza, V. Buliga, J.P. Bradley, Z.R. Dai, N. Teslich, D.R. Black, J. Cryst. Growth **312**, 507 (2010)
27. K. Chattopadhyay, S. Feth, H. Chen, A. Burger, C.-H. Su, J. Crystal growth **191**, 377 (1998)
28. C.-H. Su, Y.-G. Sha, S.L. Lehoczky, H.-C. Liu, R. Fang, R.F. Brebrick, J. Cryst. Growth **183**, 519 (1998)
29. D.C. Reynolds, L.C. Green, J. Appl. Phys. **29**, 559 (1958)
30. L.C. Green, D.C. Reynolds, S.J. Czyzak, W.M. Baker, J. Chem. Phys. **29**, 1375 (1958)
31. D.R. Boyd, Y.T. Sihvonen, J. Appl. Phys. **30**, 176 (1959)
32. W.W. Piper, S.J. Polich, J. Appl. Phys. **32**, 1278 (1961)
33. N. Henimat, M. Weinstein, J. Electrochem. Soc. **114**, 851 (1967)
34. P.D. Fochs, W. George, P.D. Augustus, J. Cryst. Growth **3**(4), 122 (1968)
35. L. Clark, J. Woods, J. Cryst. Growth **3**(4), 127 (1968)
36. L.M. Rouse, E.A.D. White, J. Cryst. Growth **17**, 117 (1972)
37. R. Takahashi, Japan. J. Appl. Phys. **17**, 1275 (1978)
38. G.H. Dierssen, T. Gabor, J. Cryst. Growth **43**, 572 (1978)
39. G.J. Russell, J. Woods, J. Cryst. Growth **46**, 323 (1979)
40. M. Aven, B. Segall, Phys. Rev. **150**, 541 (1966)
41. M. Aven, J. Appl. Phys. **38**, 4421 (1967)
42. A.S. Jordan, L. Derick, J. Electrochem. Soc. **116**, 1424 (1969)
43. W. Zhou, J. Wu, M. Dudley, C.-H. Su, M.P. Volz, D.C. Gillies, F.R. Szofran, S.L. Lehoczky, Infrared detectors—materials, processing, and devices, in *Materials Research Society Symposium Proceedings*, ed. by A. Applebaum, L.R. Dawson, vol. 299 (1994), p. 203
44. C.-H. Su, S. Feth, S.L. Lehoczky, J. Cryst. Growth **209**, 687 (2000)
45. C.-H. Su, S. Feth, S.L. Lehoczky, Mater. Lett. **63**, 1475 (2009)
46. S.-Y. Cha, Private communication
47. C.-H. Su, S.L. Lehoczky, J. Cryst. Growth **319**, 4 (2011)
48. J.R. Farver, R.A. Yund, Chem. Geol. **90**, 55 (1991)
49. C.-H. Su, Submitted to Crystal Res. Technol.
50. Y.-G. Sha, C.-H. Su, W. Palosz, M.P. Volz, D.C. Gillies, F.R. Szofran, S.L. Lehoczky, H.-C. Liu, R.F. Brebrick, J. Cryst. Growth **146**, 42 (1995)

Chapter 5
Residual Gas Measurements and Morphology Characterization on Grown Crystals

Abstract After the growth of the crystals, the samples have been evaluated through a comprehensive characterization plan. The first part of characterizations, which included the residual gas measurements on selected ampoules and the studies on the morphology of the grown crystals, are presented in this chapter. The residual gas pressures and compositions measured after growths with the source materials from different vendors suggested that the H_2 reduction and dynamic baking heat treatment are essential in providing a reproducible environment of low residual gas pressure during each growth. On the morphology of the grown ZnSe crystals, although in the vertical configuration, the crystals grew in full contact with the wall to the full diameter of the ampoule, but, frequently, the crystals grown in the horizontal configuration grew away from the ampoule wall without any contact. From the observations under scanning electron microscope (SEM) and atomic force microscope (AFM), the growing surface of a horizontal grown crystal, consists of terraces of the orientation of (110) with numerous steps between the terraces and the crystal grew by the extending of these steps. However, from the microscopy on the as-grown surface of vertical grown crystals, the growth mechanism can be viewed as island mode with nucleation of islands in the order of 10 nm in height. The morphologies by visual observation and the micro-morphology of grown surface by SEM and AFM have been examined for the growths of self-seeded and seeded ZnSe and CdTe, self-seeded ZnSe doped with transition metals, self-seeded ZnSeTe, CdS and ZnTe.

Keywords Residual gases measurement · Contactless growth · Step growth mechanism · ZnSe doped with transition metals

Various techniques were applied to characterize the crystal morphology, crystalline structural properties, impurity and defects distributions as well as other electrical and optical properties of the grown crystals [1]. The studies on structural defects, such as impurities, voids, precipitates, dislocations, slip bands, small angle grain boundaries, twins and compositional variation, were accomplished by different techniques including spectroscopy such as atomic absorption spectroscopy, glow discharge mass spectroscopy, spark source mass spectroscopy, energy and wavelength dispersive X-ray spectroscopy, photoluminescence spectroscopy and secondary ion mass spectroscopy (SIMS), X-ray diffraction (Laue reflection and rocking curve), synchrotron

© Springer Nature Switzerland AG 2020

C.-H. Su, *Vapor Crystal Growth and Characterization*,
https://doi.org/10.1007/978-3-030-39655-8_5

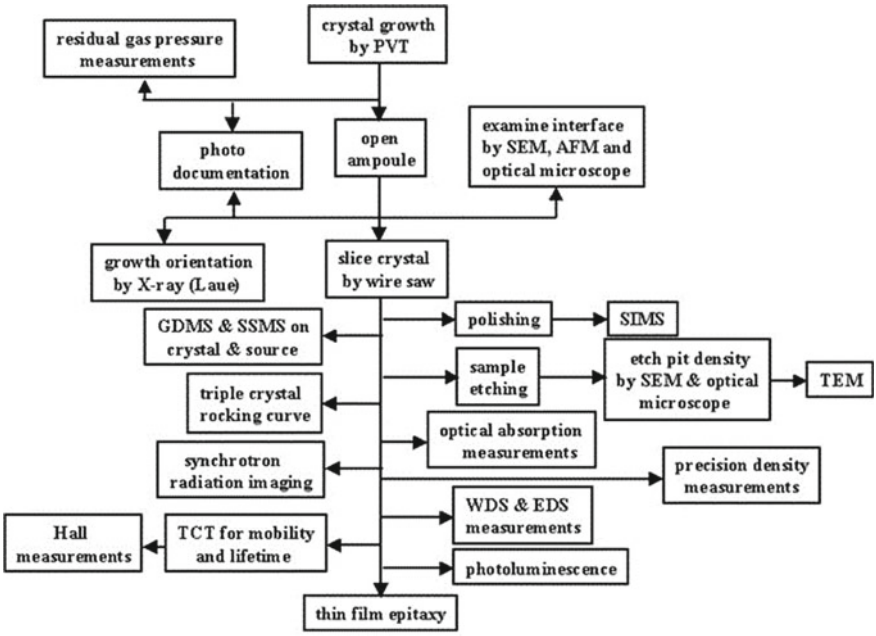

Fig. 5.1 Flow chart of sample preparation and characterization plan

white beam X-ray topography (reflection and transmission), microscopy (optical, electron, and atomic force), precision density measurements, and optical transmission measurements. The electrical and optical characterizations were performed by optical absorption and I–V measurements. Figure 5.1 shows the flow chart of the characterization plan.

5.1 Residual Gas Measurements

After the completion of the growth experiments, the cooling of the furnace and the photography documentation of the grown ampoule, several ampoules were selected to be tested with the measurements of residual gas using the technique reported in Sect. 3.3.2. Table 5.1 gives the measured residual total pressures and their compositions on selected growth runs together with vendors of the source material, the heat treatment employed, the growth duration. The total residual gas pressures, as shown in Table 5.1, tend to separate into two groups. The first 4 ampoules have the higher pressure from 2.5 to about 4×10^{-3} atm at room temperature whereas the last 5 ampoules ranged from 0.9 to 1.2×10^{-3} atm. From the results of the last two ampoules, the Eagle-Picher source material seems not to be the cause for the higher values. With similar heat treatment procedure, the measured results from the last 5

Table 5.1 The vendor of the source material, the heat treatment employed, the growth duration, the measured total residual total pressures (at room temperature) and their compositions on selected growth runs

Growth run	Sample mass (g)	H_2^+ treatment (°C)	Baking treatment (°C; min)	Growth duration (h)	P(10^{-3} atm) at R.T.	Composition (vol. %)				
						CO	H_2	CO_2^*	N_2	He
14[1]	13.70	–	1050; 15	258	2.97	95	2.7			2.2
15[1]	12.16	–	1062; 10	306	2.50	92.5	5.5			2.1
28[1]	12.44	870	970; 15	238	3.84	95.5	0.9	2.2	0.2	1.3
41[1]	8.57	1020	1020; 12	143	3.28	97	2.0			1.1
42[2]	16.20	1015	1045; 20	165	1.18	89	5.5		1.1	3.8
44[2]	15.57	1035	1035; 20	168	1.15	83	6.5	0.5		9.5
45[3]	15.52	1035	1050; 20	197	0.875	76	21			2.8
46[1]	13.55	1035	1050; 20	403	1.26	95.5	2.0	1.0		1.5
47[1]	13.72	1035	1050; 22	164	1.08	92	5.5	0.3		2.0

*Vendors: 1—Eagle Picher, Inc. (high purity grade), 2—Furukawa Co. Ltd. (99.9999%) and 3—Cleveland Crystals (99.995% purity)
+Typical H_2 reduction duration was 20−30 min
*The presence of CO_2 indicates absence of graphite in the system

runs reported the residual gas pressure of 0.875×10^{-3} atm (76% CO, 21% H_2 and 3% He) for Cleveland Crystals, about 1.16×10^{-3} atm (86% CO, 6% H_2 and 7% He) for Furukawa Co. and 1.26×10^{-3} atm (96% CO, 2% H_2 and 1.5% He) for Eagle-Picher Inc. source material. The comparable residual gas pressures and compositions measured among the source materials from different vendors suggested that the H_2 reduction and dynamic baking heat treatment are essential in providing a reproducible environment of low residual gas pressure during each growth. It is noteworthy that an extra long crystal growth run of 403 h on #46 didn't affect the residual gas pressure much. The comparison of the residual gas pressures between the ZnSe processed ampoules and the ampoule processed under similar conditions but without the presence of ZnSe, i.e., 0.23×10^{-3} atm at room temperature [2] indicates that the lowest residual pressures in the processed ZnSe ampoules are 4 to 5 times higher.

5.2 Morphology of the Grown Crystals

5.2.1 Self-seeded Grown Crystals of ZnSe in Horizontal Configuration

5.2.1.1 Contactless Growth of ZnSe Crystals

The crystal growth of ZnSe showed an interesting phenomenon of contactless growth. Although in the vertical configuration, the crystals grew in full contact with the wall to the full diameter of the ampoule, but, frequently, the crystals grown in the horizontal configuration grew away from the ampoule wall without any contact [3]. Contactless growth, i.e. growth with no contact between crystal and ampoule wall, has the advantages in (1) no parasitic nucleation from ampoule wall, (2) no stress applied to crystal from ampoule wall during post-growth cooling and (3) minimal contamination from ampoule due to the interaction between crystal and ampoule. Experimentally, contactless growth was reported earlier [4] on the vapor growth of CdS and recently on the growth of CdTe [5], PbSnTe [6, 7] and CdZnTe [8].

The thermal profile of these contactless growth was similar to most of the growths, i.e., the central zone provided a thermal maximum which was maintained at about 10 °C higher than the hot zone temperature T_H while the isothermal cold zone, equipped with heat pipe liner, was controlled at about 1015 °C. In an effort to preserve the growing surface morphology, after the furnace has translated 3.3 to 4.1 cm, all of the growths (except ZnSe-40) were terminated by stopping the furnace translation, lowering the source temperature by 10 °C (to prevent further deposition on the growing surface) and then, cooling the thermal profile rigidly from the growth temperatures to 550 °C in 72 h and from 550 to 30 °C in 24 h. At the end of the ZnSe-40 run the ampoule was directionally cooled (crystal end first) to room-temperature environment in 2 min by moving the furnace. Table 4.2 of Chap. 4 lists

the source temperature, T_H, the thermal gradient, the furnace translation rate, the degree of supersaturation and the measured residual gas pressure (at room temperature) for selected horizontal growth runs. The thermal gradient was determined at the supersaturation position using the thermocouple data measured along the empty furnace bore prior to each run. After the growth run the degree of supersaturation was calculated from the temperature difference between TH and the highest temperature of the grown crystal interface using the one−dimensional thermal profile measured inside the empty furnace bore. In most of the cases, the degree of supersaturation is small, i.e. in the order of 1 to 3 °C. The high degree of supersaturation, 17 and 16 °C, respectively, for ZnSe-34 and ZnSe-47 was caused by the high growth rate—a larger temperature difference between the source and crystal is needed to maintain a higher mass flux.

Figure 5.2 shows photographs of the horizontal grown ZnSe crystals inside the conical shape self-seeded growth ampoules. The gravitational direction is either in or out of paper. The crystals started to grow away from the wall just prior to the beginning of full ampoule diameter with large (110) facets, as determined by Laue X-ray diffraction photographs, tend to align parallel to the gravity direction. This is evidenced in the ZnSe-45 grown crystal as shown in Fig. 5.2e, f where two large (110) facets formed parallel to the gravity direction on both sides of the crystals.

5.2.1.2 Surface Morphology by Scanning Electron and Atomic Force Microscopy

The as-grown surface morphology was studied by a Zeiss DSM960 digital scanning electron microscope (SEM) and by a Digital Instrument Dimension 3000 atomic force microscope (AFM) operating in tapping mode [3]. The SEM micrographs and the AFM images on the facets of ZnSe-40, given in Figs. 5.3 and 5.4, respectively, show that large terraces, identified to be (110) planes by electron back scatter patterns, and steps dominate the as-grown surfaces. An AFM height image on the as-grown facet of ZnSe-39 is illustrated in Fig. 5.5a with a close-up three-dimension image given in Fig. 5.5b. The surface features consist of large terraces (up to 0.5 mm wide) and close-spaced stair-shaped steps. The AFM section analysis indicated that the height difference between the adjacent terraces is 20–60 nm. Smaller step heights, as low as 3 nm, were also observed on other areas of the ZnSe-39 as-grown facets. The surface characteristics shown here is a representation of the grown surface after a long duration post-growth cooling when the surface was in equilibrium with the vapor phase. However, because of the contactless nature of the growth process the (110) facets on the crystal sides should be in equilibrium with the vapor phase during the growth and the as-grown surface of the rapidly cooled ZnSe-40 crystal showed similar features as described above. Hence, the observed post-growth surface features may resemble the in-situ facet surfaces.

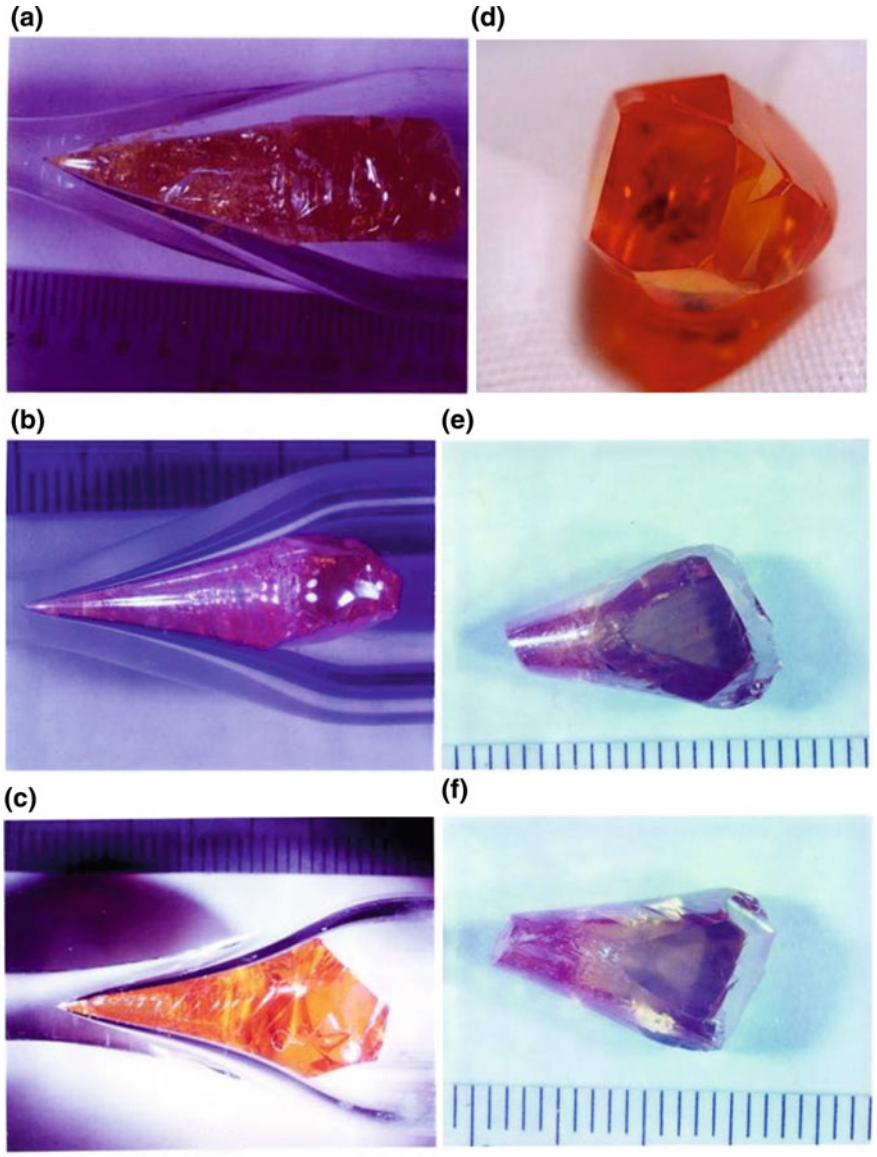

Fig. 5.2 Contactless growths of the as-grown crystals: **a** ZnSe-39, **b** ZnSe-43, **c**, **d** ZnSe-44 (note: gravity vector out of paper for (**a**) and into paper for (**b**) and (**c**)); **e**, **f** are side views of ZnSe-45 crystal (*note*: gravity vector upward for (**e**) and downward for (**f**))

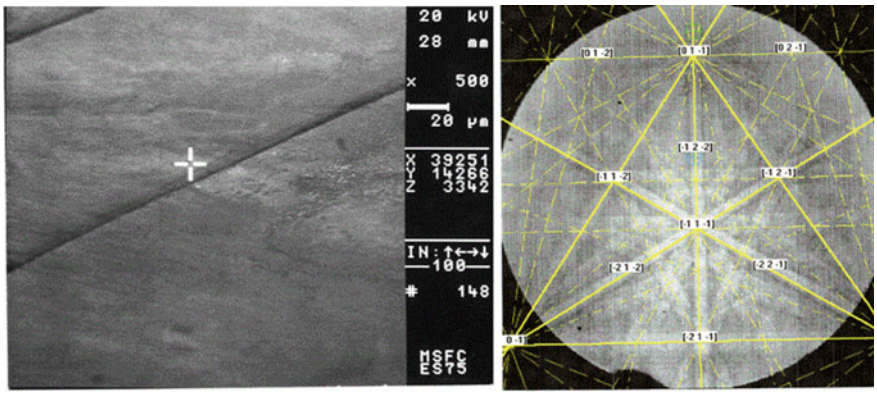

Fig. 5.3 SEM micrograph of the as-grown surface of a horizontally grown ZnSe crystal, ZnSe-40

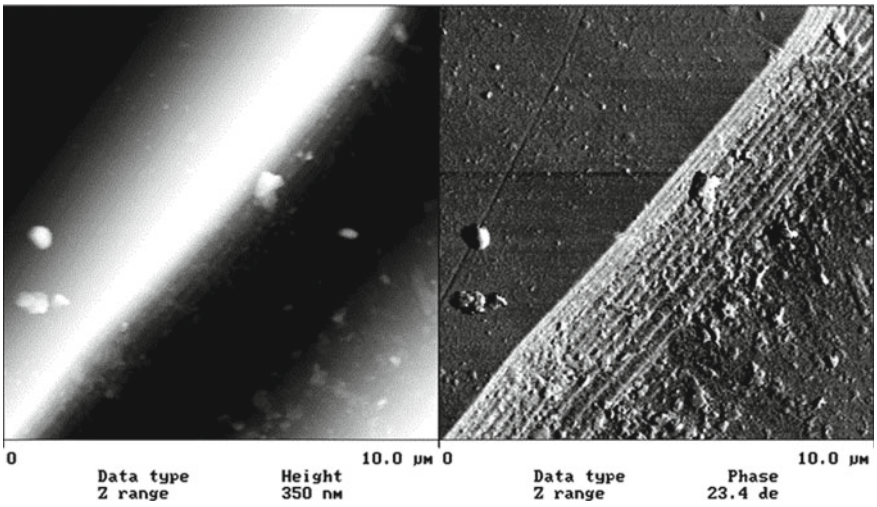

Fig. 5.4 AFM image of the as-grown surface of the horizontally grown ZnSe-40 crystal

5.2.2 Self-seeded Grown Crystals of ZnSe in Vertical Configuration

5.2.2.1 Morphologies of Self-seeded Grown Crystals

The pictures of the grown surface and the morphology of self-seeded grown ZnSe-31VD crystals in vertically destabilized configuration are given in Fig. 5.6. No crystalline facets growing away from the wall were observed. Figure 5.7, shows the crystals, (a) ZnSe-35VS and (b) ZnSe-32VS, grown in the vertical stabilized configuration. With a fast furnace translation rate of 11.45 mm/day, the growing surface of

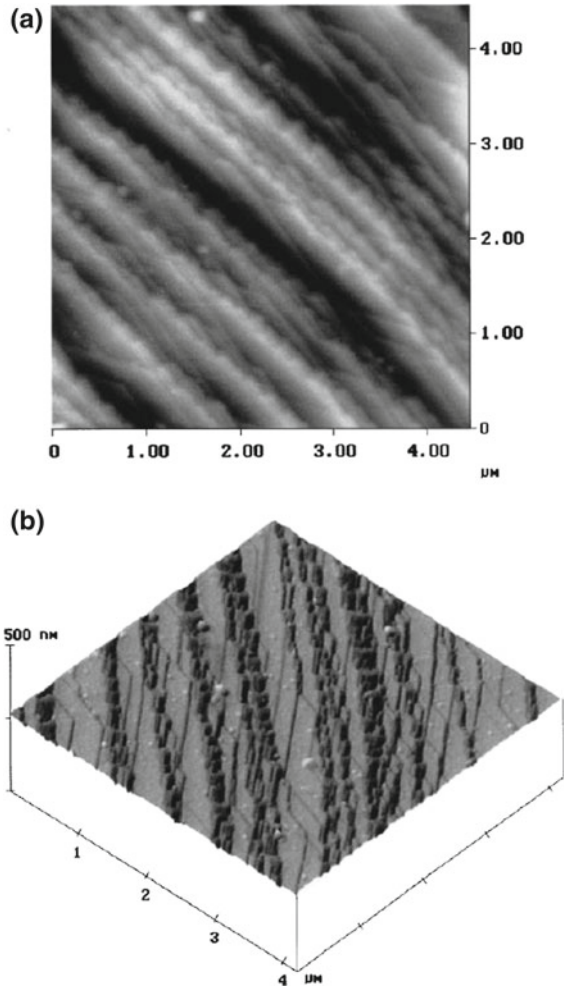

Fig. 5.5 AFM height image (**a**) and three-dimensional image (**b**) on the as-grown (110) facet of ZnSe-39 crystal (taken from Fig. 3 of Ref. [3])

ZnSe-35VS showed many lumps and the interface grew toward one side of ampoule, probably caused by the asymmetric thermal profile. Figure 5.8 presents photographs of other self-seeded ZnSe crystals grown in the vertical configurations. On the contrary to the horizontal configuration, the crystals grew in contact with the wall to the full diameter of the ampoule. Hence, the contactless growth was rarely observed in the vertical configuration.

It is interesting to note that when furnace translation rates were set higher than mass flux the growing crystals respond differently in the horizontal and vertical configurations. As shown in Fig. 5.9a, in the horizontal growth of ZnSe-47H, with furnace translation rate of 7.50 mm/day, the crystal maintained the growth surface

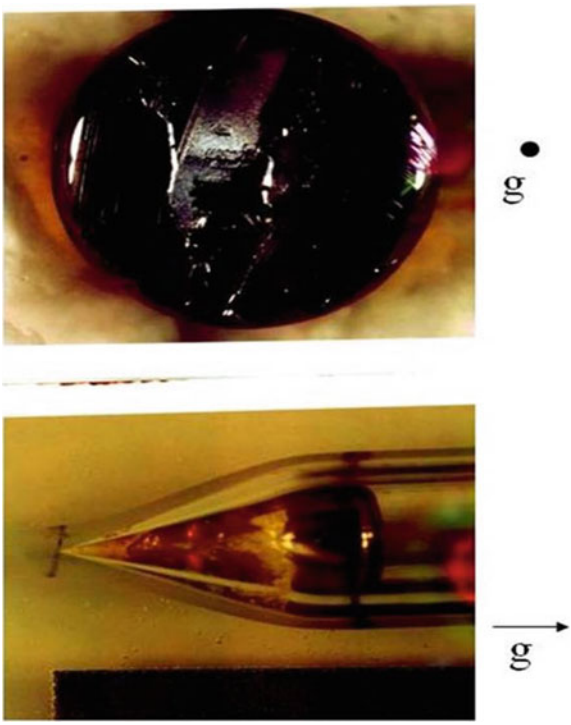

Fig. 5.6 Morphologies of self-seeded grown ZnSe-31VD crystals in vertically destabilized configuration

morphological stability by (1) self-adjusting the degree of supersaturation to increase the mass flux or/and (2) by reducing the cross section area of the grown crystal. However, during the vertical growth of ZnSe-35VS, with furnace translation rate at 11.4 mm/day, the crystal growth surface became morphologically unstable. The 2.5 cm long of the last grown crystal was sliced axially along the growth direction and, as shown in Fig. 5.9b, it was embedded with voids and pipes.

5.2.2.2 Surface Morphology by SEM and AFM

The SEM micrographs and AFM images of vertically grown ZnSe crystals are shown in Figs. 5.10 and 5.11, respectively. The surface was dominated by granular structures with tubular structures on top as shown in Fig. 5.11. From the AFM section analysis as shown in Fig. 5.12, the tubular structures were about 200 nm O.D., 75 nm I.D. and 25 nm in height.

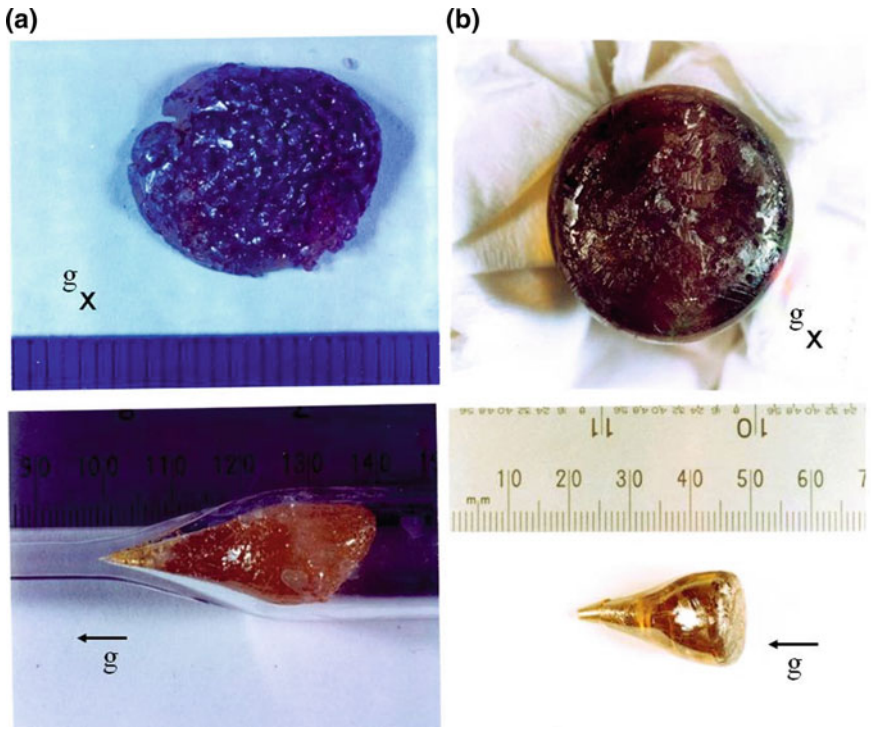

Fig. 5.7 Morphologies of self-seeded grown ZnSe crystals in vertically stabilized configuration **a** ZnSe-35VS and **b** ZnSe-32VS

5.2.3 Seeded Grown Crystals of ZnSe

Similar characteristics, i.e., crystals grew in full contact with the wall of the ampoule in the vertical configuration (Fig. 5.13) and grew away from the ampoule wall in horizontal configuration (Fig. 5.14) were observed for the as-grown seeded crystals.

5.2.4 Analysis on Contactless Growth

In the analysis given by Markov and Davydov [4] on the contactless growth of CdS it was assumed that the equilibrium state corresponding to contactless growth is when the distribution of partial pressure due to diffusion coincides with the distribution of equilibrium vapor pressure from the temperature gradient. However, only one partial pressure gradient is assumed in their analysis. This assumption is not applicable to most of the II–VI semiconducting compounds as the partial pressures in equilibrium with the compounds were well established experimentally which showed the predominant vapor species of the group II atom and the group VI diatomic molecule. Therefore, a one-dimensional diffusion model on the mass

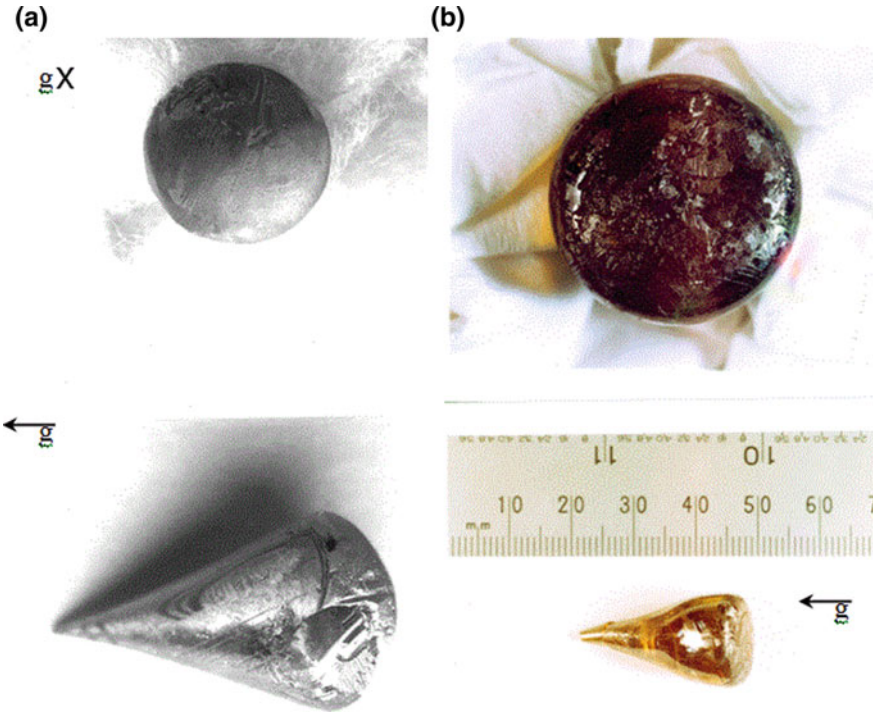

Fig. 5.8 Photographs of the self-seeded ZnSe crystals grown in the vertical configuration with the marked gravity direction

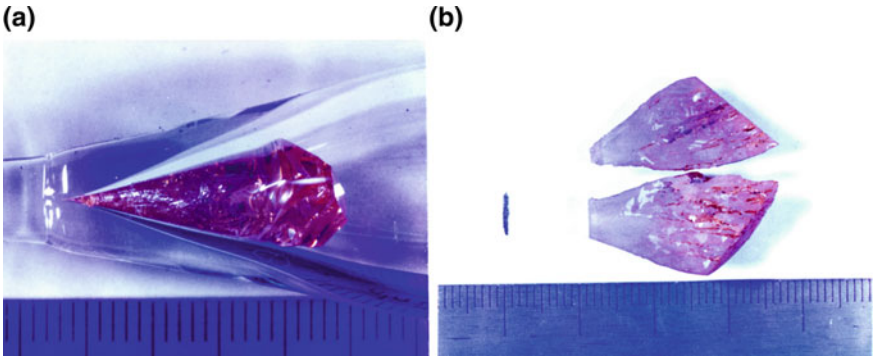

Fig. 5.9 **a** The horizontal grown crystal of ZnSe-47, with furnace translation rate of 7.50 mm/day and **b** the slices of the last 2.5 cm grown crystal of ZnSe-35VS, with furnace translation rate at 11.4 mm/day

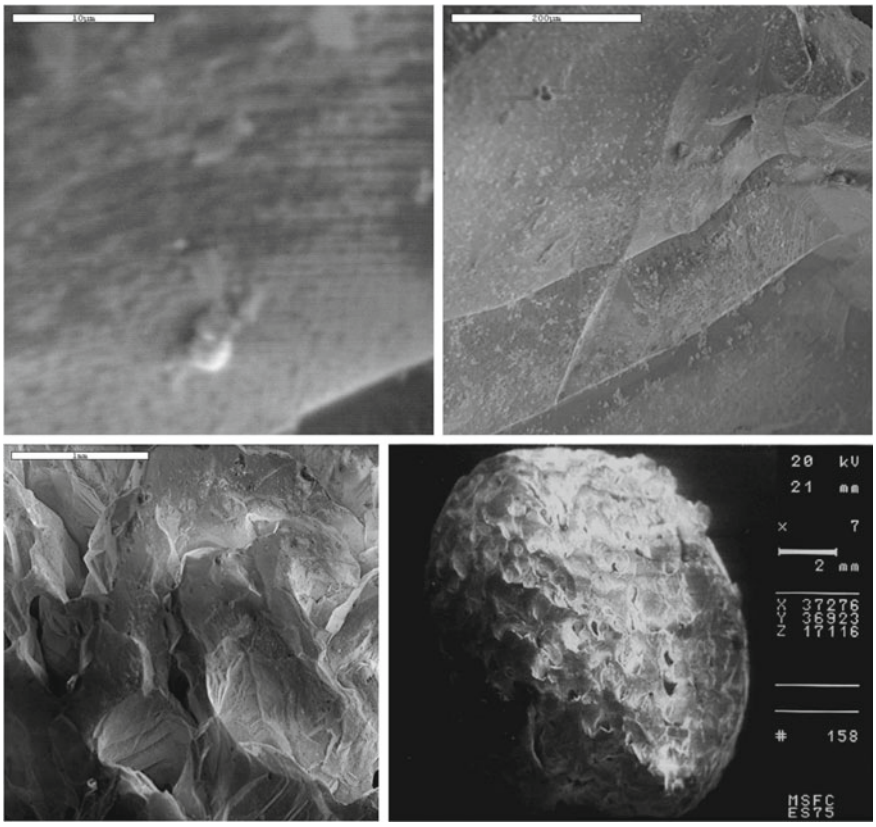

Fig. 5.10 SEM micrographs of the surface of a vertically grown ZnSe crystal, ZnSe-35 V (the scale on the top of each image is, respectively, 10 μm for upper-left image, 200 μm for upper-right and 1 mm for lower-left)

flux of a multi-species PVT system was employed to analyze the conditions for contactless growth. The model has been well established [9, 10] and, essentially, there are four parameters which determine the mass flux: temperatures at the source (T_S) and the crystal (T_C), the vapor stoichiometry at the source and the residual gas pressure and composition. From the partial pressure measurements [11] the typical stoichiometry of the vapor phase in equilibrium with the starting material after the heat treatments of H_2 reduction and vacuum baking corresponds to a value of α (defined as P_{Zn}/P_{Se_2}) = 2.9. The growth condition for ZnSe-42 was adopted for the analysis. The thermal profile measured along the empty furnace bore and the final position of the ampoule are given schematically in Fig. 5.15. The crystal started to grow away from the ampoule wall at 78.6 cm which corresponded to a temperature of 1131 °C from the thermal profile. The highest temperature along the convex growth interface was 1142 °C at 79.3 cm and the source surface temperature was 1145 °C at 82.8 cm. Two setf alculations were performed to establish the partial pressure profiles along the growth direction inside the ampoule. For the first set of calculation

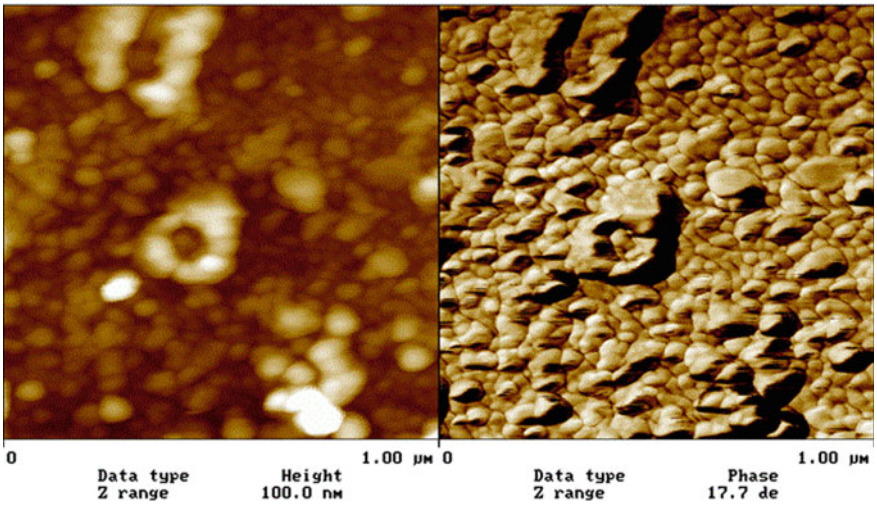

Fig. 5.11 AFM image of the surface of a vertically grown ZnSe crystal, ZnSe-25V. Note the granular structure with tubular features on the top

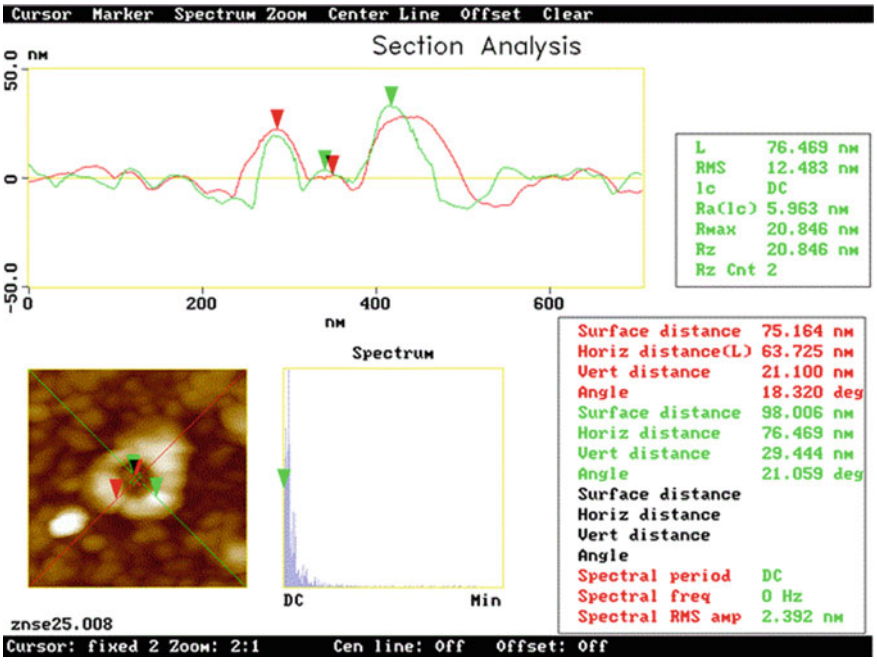

Fig. 5.12 AFM sectional analysis of ZnSe-25V. The tube was about 200 nm OD, 75 nm ID and 25 nm in height

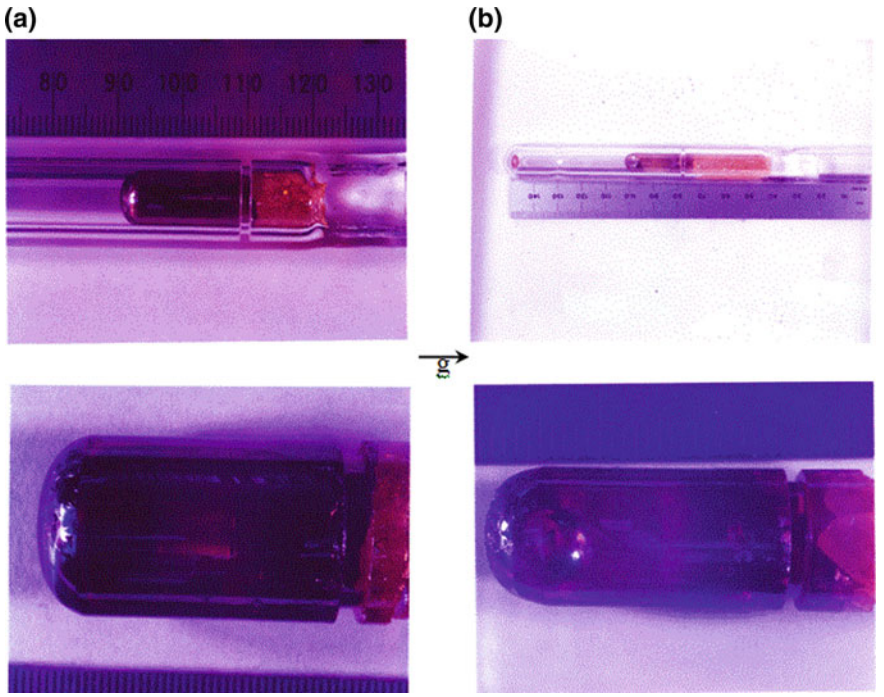

Fig. 5.13 Photograph of the seeded ZnSe crystal grown in the vertical stabilized configuration

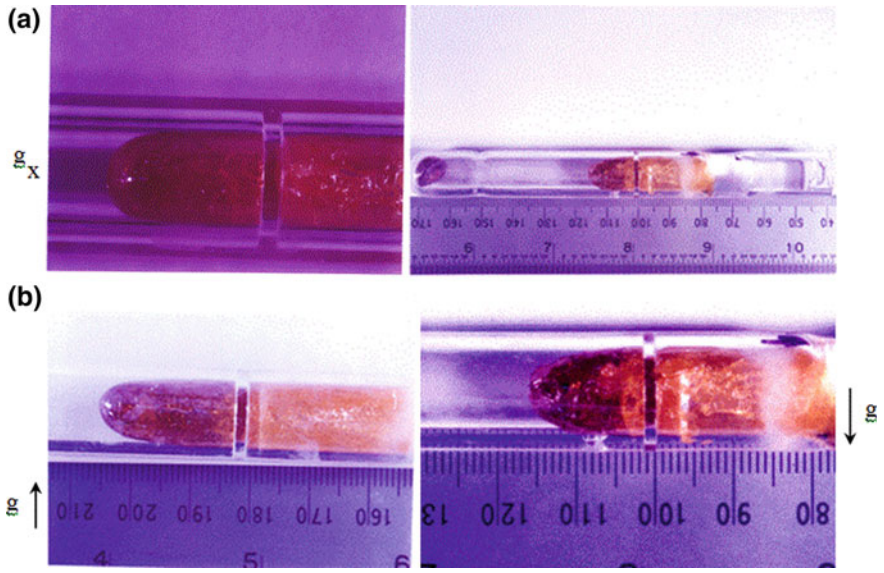

Fig. 5.14 Photograph of the seeded ZnSe crystal grown in the horizontal configuration

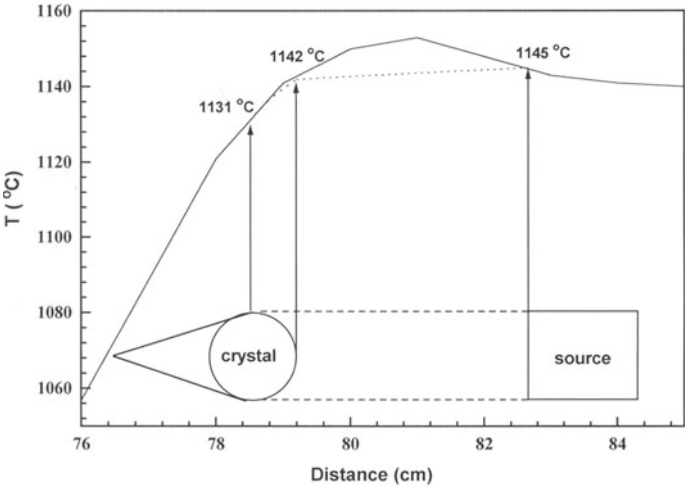

Fig. 5.15 The measured thermal profile (solid curve) and the calculated T_{sup} pro-file (dotted curve) at the end of the ZnSe-42 run (taken from Fig. 6 of Ref. [3])

the input parameters were: L (transport length) = 3.5 cm, T_S = 1145 °C, T_C = 1142 °C, α(source) = 2.9 and the measured residual gas pressure and composition given in Table 5.1. The calculated results included: (1) the partial pressure profiles of Zn and Se_2 from the source surface to the convex interface position, i.e. at 79.3 cm, (2) a calculated mass flux of 2.2×10^{-7} mole/cm^2 s, or 5.2 mm/day, which agrees well with the experimental growth rate of 4.95 mm/day and (3) a value of $\alpha = 3.178$ for the vapor phase in equilibrium with the crystal at the convex position (at 79.3 cm). The second set of calculation considers the grown crystal re-distributed itself by assuming crystal at the convex position as the source and the location where the crystal started to grow away from the wall as the crystal surface. The input parameters were L = 0.7 cm, T_S = 1142 °C, T_C = 1131 °C, α(source) = 3.178 and the same residual gas pressure and composition as the first set of calculation. As the results of the calculation the partial pressure profiles of Zn and Se_2 from the convex interface position (at 79.3 cm) to the position of the onset of contactless growth (at 78.6 cm) were established. Using the partial pressure profiles from the two sets of calculations the temperature profile for supersaturation, T_{sup}, was solved from Eq. (2.9) in Chap. 2

$$RTln\left(P_{Zn}P_{Se_2}^{1/2}\right) = \Delta G_f = -361,807 + 191.485\text{T(J/mole)} \qquad (5.9)$$

where ΔG_f is the Gibbs energy of formation for ZnSe(s) from the vapor phase. Showing as two dotted lines in Fig. 5.15, T_{sup} is the boundary between sublimation and condensation in the sense that if the local temperature is below T_{sup} the solid phase is more stable than the vapor phase and reaction of condensation should proceed and, on the other hand, if the local temperature is above Tsup the vapor phase should be stable. The measured thermal profile between the convex position of the interface and the source material (79.3–82.8 cm) shown in Fig. 5.15 is much higher than the profile for Tsup and, hence, the vapor phase is stable and no condensation

should be formed. However, the measured thermal profile between the onset of contactless growth and the convex position along the interface (78.6–79.3 cm) is just a few tenths of 1 °C higher than the T_{sup} profile. The real thermal profile inside the ampoule can be flattened to approach the Tsup profile due to the introduction of the ampoule/crystal thermal configuration as well as the possible convection in the vapor phase. In fact, the grown crystal morphology is the experimental evidence of this modification of thermal profile inside the ampoule because the as-grown interface is the boundary where the partial pressures adjacent to the interface should satisfy the above equation with T in the equation as local temperature.

In the simple calculation above, only one-dimensional diffusion partial pressure and temperature profiles as well as bulk properties of ZnSe solid were taken into consideration. Under the realistic growth conditions the convection in the vapor phase caused by thermal/solutal density gradient will result in a three-dimensional partial pressure profiles inside the ampoule. This convection and the ampoule/crystal thermal configuration will also alter the assumed one-dimensional thermal profile to a three-dimensional one. The effects of convective flows were observed experimentally during the PVT growth of ZnSe in the vertical (stabilized and destabilized) configuration under otherwise similar growth conditions as the horizontal configuration described. As shown in the results, for most of the growths in the vertical configuration the crystals grew to the full diameter of the ampoule and the as-grown interfaces were dominated by granular structures instead of terraces and steps. When the growth kinetics and the anisotropy of the surface energy are taken into consideration the Gibbs energy of formation for ZnSe(s) used in the calculation needs to be modified and this might have resulted in the predominant appearance of (110) facets on the as-grown surfaces.

5.2.5 Growth Kinetics

In 1951, Burton, Cabrera and Frank (BCF) presented the theory of growth kinetics on the crystal surface during vapor/melt growth process [12] that the adsorption of molecules at the terraces with subsequent surface diffusion to attach to the step if the conditions favor the lowering of the free energy. The BCF model [13] is based on the assumption of the incorporation of the molecules at the steps and no growth at the terraces. Also, at some distance from the interface, the distribution of the species in the vapor/liquid phase is assumed to be homogeneous which is separated by a boundary layer from the growing interface and diffusion takes place within this layer.

It is speculated that the difference in the morphology of the growing surface between horizontal and vertical configurations is caused by the different growth kinetics. The Zn atom and Se_2 molecules sublime from the source, transport through the vapor phase and approach the growing surface of crystal by diffusion and convection. In the ideal vertical stabilized configuration, i.e., no radial thermal asymmetry along the vertical length of the ampoule, the transport mode can be treated as one-dimensional diffusion. It means that all of the atoms and molecules transport vertically in the downward direction. When they approach the horizontally flat crystal surface, the growth was initiated with individual spontaneous nucleation. However, these nuclei cannot grow very far because their growing tips are getting

into hotter thermal field and the condition of lower energy disappears. Consequently, other nucleation starts to commence in different area. The growth mechanism can be viewed as island mode with nucleation of islands in the order of 10 nm in height. On the other hand, as discussed early in the section of convective transport, if there is a positive thermal gradient perpendicular to the gravitational field, i.e., in the horizontal configuration, then thermal convective flow with a component parallel to the growing crystal surface will occur. This component can move atoms and molecules across the growing surface. The growing surface of a horizontal grown crystal, as shown in Fig. 5.16, consists of terraces of the orientation of (110) with numerous steps between the terraces. Although the post-growth morphology of the surface was the result of the re-arrangement by atomic surface diffusion from the real-time growing surface during long-duration of cooling, it still has retained the major features of the growing surface. A schematic of the growing surface can be viewed in Fig. 5.17, which contains the irregular structures of terraces (T), steps (S) and kinks (K). The crystal growth process is a discrete process that Zn and Se_2 species reach the surface to form adsorbed atoms (adatoms) that can migrate on the surface by diffusion. A kink, K, can make it a favorable site for the formation and attachment of adatom where it is incorporated as a part of the crystal. As the kink being filled to the edge of the surface, one step, S, is grown and the terrace extends one step to the right. When the terrace, T, fills up the whole growing surface, the crystal grows upward by the length of the step height. The crystal growth velocity, R, can be calculated by: $R = dv/l$ where d is the step height; l is the distance between steps; v is the growth velocity of the step. From the typical experimental values: R is 3 to 5 mm/day, assuming $d = 10$ nm and $l = 10$ μm, v is estimated to be 0.05 mm/s or 50 μm/s.

The lower energy favorable for the step growth includes not only the consideration of Gibbs energy of formation of ZnSe(s) to be lower than that of the vapor phase but also the chemical bonding between the adatom and growing surface of crystal which lowers the surface energy. This driving force may have resulted in the contactless

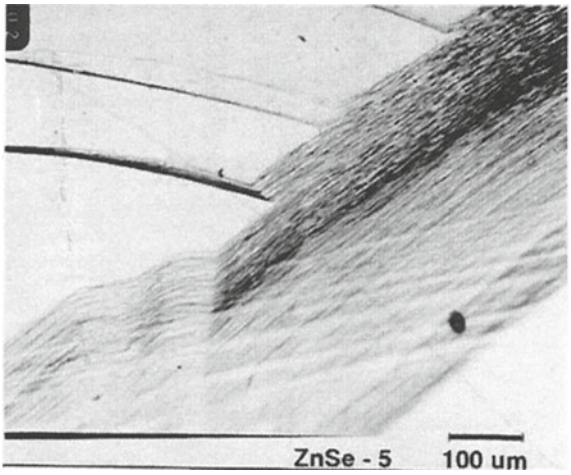

Fig. 5.16 SEM micrograph of the surface of the as-grown ZnSe-5 crystal

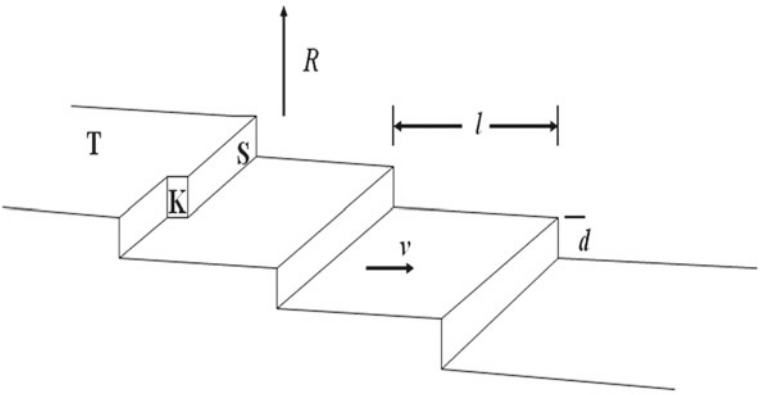

Fig. 5.17 Schematics of the step growth mechanism on a growing surface with terrace (T), kink (K) and step (S)

growth of the horizontal configuration as the crystal overcomes the growth into the hotter thermal field but also with higher nutrient contents.

5.2.6 Growth Direction from X-ray Diffraction

The growth direction was determined by Laue X-ray diffraction [3]. All of the self-seeded grown boules were determined to be single crystal by X-ray diffraction techniques. The growth direction of each crystal was determined by Laue diffraction and is shown in Fig. 5.18. The growth directions of several crystals were found in the

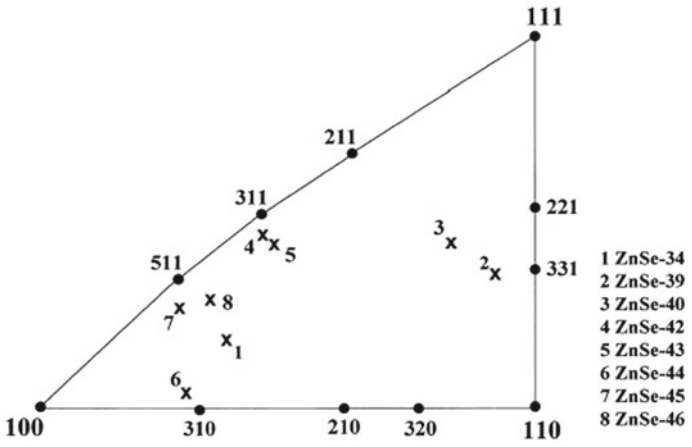

Fig. 5.18 Growth directions of the self-seeded grown crystals by Laue X-ray diffraction (taken from Fig. 5 of Ref. [3])

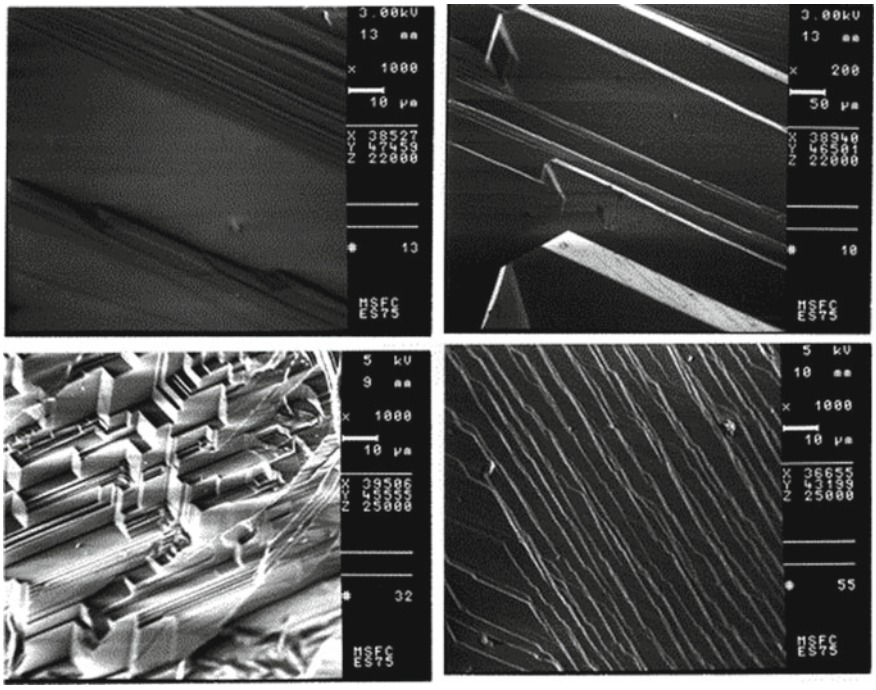

Fig. 5.19 SEM micrograph of the surface of a horizontally grown Cr-doped ZnSe crystal, ZnSe-36H

neighborhood of [511] and [311] directions which are consistent with the observation that (110) facets tend to grow parallel to the gravity direction in that the angle between the directions of [511] and [311] and that of [110] is 90°.

5.2.7 Transition Metal Doped Crystals of ZnSe

5.2.7.1 Morphology of Cr-Doped ZnSe

Similar to the as-grown surface of horizontally grown ZnSe crystals, the surface of the horizontally as-grown Cr-doped ZnSe crystal, shown in Fig. 5.19, exhibits facets and steps on the grown surface. On the growing surface of a vertically grown Cr-doped ZnSe-38V crystals, the SEM micrographs in Fig. 5.20 show a network of high plateaus. The AFM image for ZnSe-38V in Fig. 5.21 shows a plateau in the shape of an island with 30–70 μm in diameter and 3.5 μm in height. Numerous nuclei with diameters of 20–50 nm and heights of 1–nm were observed on top of these islands as shown in the AFM images of the plateaus on ZnSe-38V in Fig. 5.22.

5.2.7.2 Morphology of Fe-Doped ZnSe [14]

The as-grown crystal boules of Fe-ZnSe #1 and #3 are shown in Fig. 5.23. The Fe-ZnSe #1, shown in Fig. 5.23a, was cleaved along the (110) plane in the growing tip region through the whole cross section area, implying a single crystal. The photo of

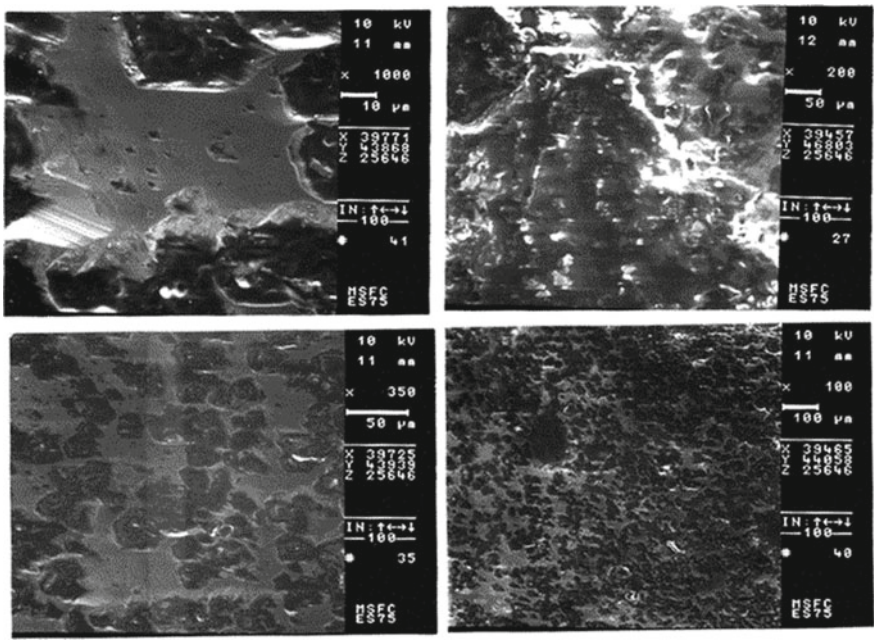

Fig. 5.20 SEM micrograph of the surface of a vertically grown Cr-doped ZnSe crystal, ZnSe-38V. Note the network of high plateaus

the 3.5 cm long Fe–ZnSe #3 crystal, taken on a light table (Fig. 5.23b), shows very few macro structural defects.

The Fe-ZnSe #1 boule was sliced by wire sew into 5 sections, labeled from A to E, along the (110) plane as shown in Fig. 5.24. The slices B and D, with thickness 1.5 mm and 1.8 mm, respectively, were polished with 0.5 μm particles of silicon carbide slurry and then cleaned with glycol are shown in Fig. 5.25a–c without and with wire mesh in the background. Bulk inhomogeneity, inclusions, precipitates and distortion within the disc were further studied by illumination of the polished crystals and, as shown in Fig. 5.25b, c, there was no bulk optical distortion due to inhomogeneity or macro defects.

5.2.8 Morphology of Grown Crystals of ZnSeTe

The as grown crystals of $ZnSe_{1-x}Te_x$ with x = 0.10, 0.20 and 0.30 are shown in Fig. 5.26, 5.27 and 5.28 with the name ended "H" for horizontal and "V" for vertically stabilized configuration. When x is greater than 0.10, the crystals showed multiple twins. A picture of the ZST-3H as-grown boule, given in Fig. 5.28, shows that multiple (111) twins run almost axially throughout the crystal with cleaves near the tip of the boule. To determine the axial growth direction, Laue X-ray diffraction patterns were

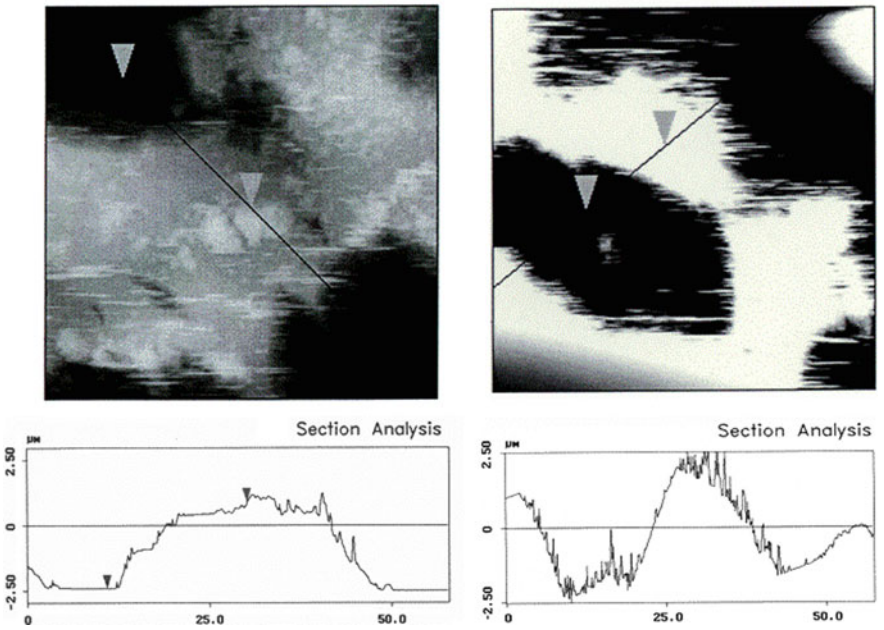

Fig. 5.21 AFM image of ZnSe-38V. Note the plateau in the shape of an island is 30–70 μm in diameter and 3.5 μm in height

taken on the cleaved surfaces near the first-grown region as well as across the as-grown surfaces of the grown crystals. The cleaved surface was identified to be (110). All of the grown boules were single crystal at the beginning of the growth and then, except for ZST-6V and -3H, developed into 2–4 grains at the end of growth. For ZST-6V and -3H the whole grown boule was single crystal. The axial growth direction was [511] for ZST-6V and 6° off [211], 7° off [321] and 8° off [311] for ZST-3H (Fig. 5.27).

5.2.9 Morphology of Grown Crystals of CdTe

In the self-seeded crystal growth of CdTe, various ampoule designs were employed to try to make the growth of single grain after the initial nucleation as shown in Fig. 5.29. The growth preparation and parameters are given in the Sect. 4.3.6 and listed in Table 4.7 in Chap. 4. With a long and sharp tapered ampoule, the growth of CdTe-16 resulted in two large grains at the final growth surface. The design of "crookneck" ampoule of CdTe-17 ampoule resulted in a single crystal with facets around the edge at the end of growth. A seeded ampoule, CdTe(s)-20, is shown on the left of Fig. 5.30 where the (111) orientation single crystal seed was pushed by a fused silica rod against a restricted ring. After the process of crystal growth

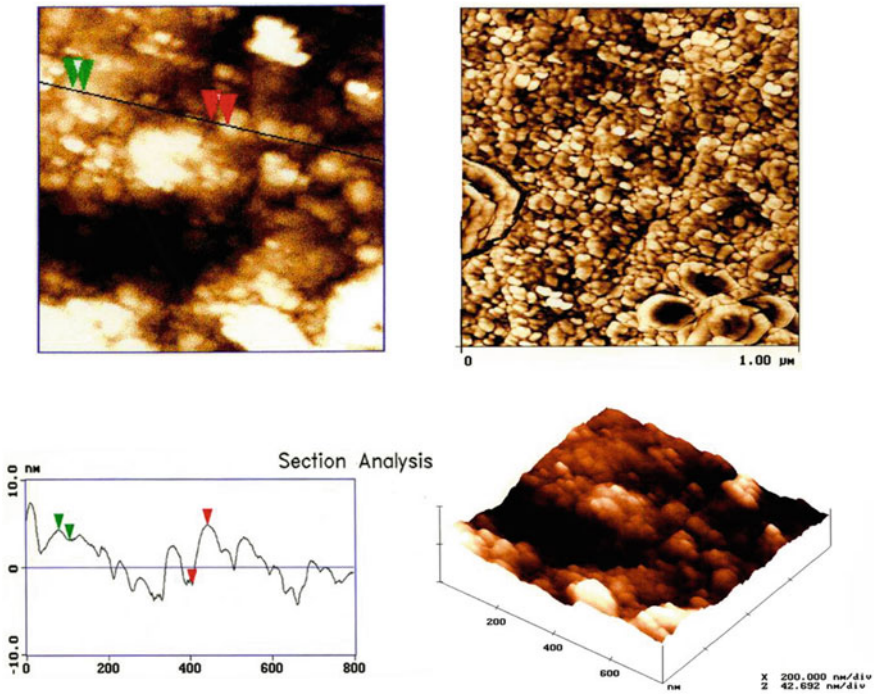

Fig. 5.22 AFM images on the plateau of ZnSe-38 V, as-grown surface. Nuclei with diameter of 20–50 nm and height of 1–7 nm were observed on the plateau region

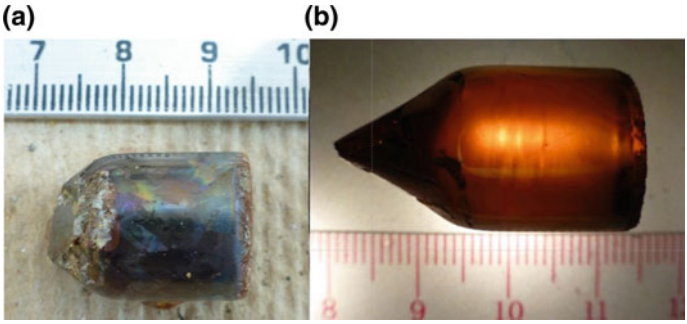

Fig. 5.23 **a** The as-grown crystals of Fe-ZnSe #1 and **b** Fe-ZnSe #3

the grown crystal is shown on the right. It shows the similar features as the grown crystals processed by the self-seeded configuration. A series of seeded growth has been processed with the growth information also listed in in Table 4.8 of Chap. 4. Figure 5.31 shows the photographs of several as-grown seeded ampoules.

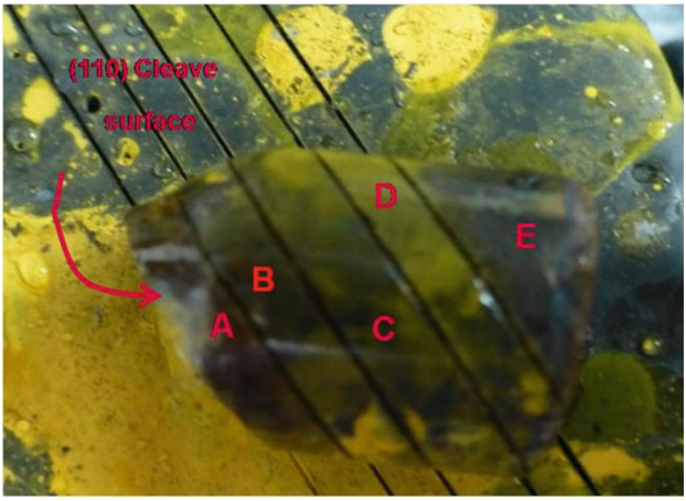

Fig. 5.24 The Fe-ZnSe #1 boule was sliced into 5 sections labeled from A to E

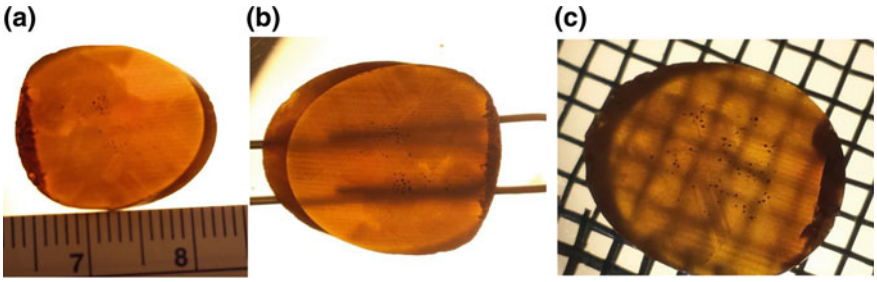

Fig. 5.25 Bulk transparency of Fe-ZnSe crystal **a** nothing in background, **b** with metal clip and **c** metal wire mesh showing no voids, bubbles and optical distortion

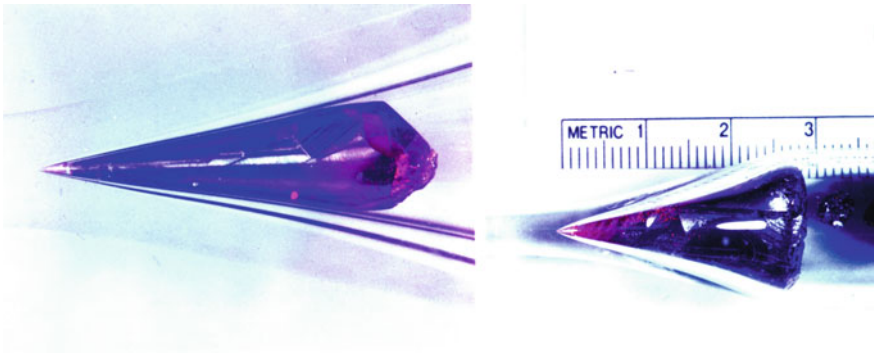

Fig. 5.26 Morphology of the $ZnSe_{0.90}Te_{0.10}$ crystals: ZnSeTe-6 V (left) and ZnSeTe-7H (right, the gravity is going down)

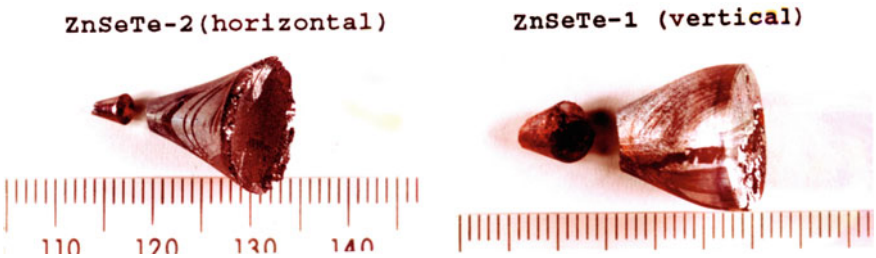

Fig. 5.27 Morphology of the $ZnSe_{0.80}Te_{0.20}$ crystals: ZnSeTe-2H (left, the gravity direction is going down) and ZnSeTe-1 V (right)

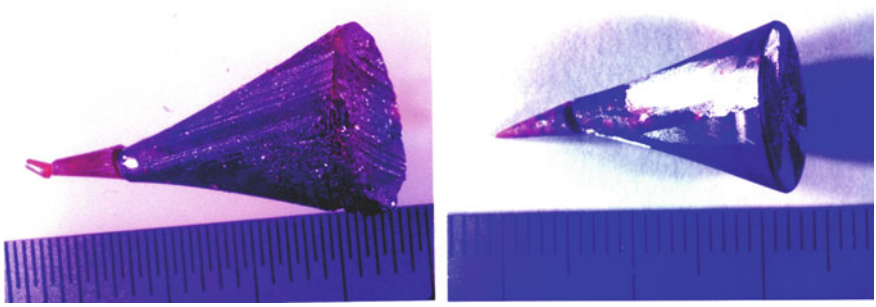

Fig. 5.28 Morphology of the $ZnSe_{0.70}Te_{0.30}$ crystals: ZnSeTe-3H (left, the gravity direction is out of paper) and ZnSeTe-5 V (right)

5.2.10 Morphology of Grown Crystals of CdS

The self-seeded and seeded grown ampoules of CdS are given in Figs. 5.32 and 5.33, respectively. The growing surface tended to be slightly convex.

Although the growth parameters were kept essentially constant, two kinds of crystals were produced: "clear" and "dark". The "clear" crystal has a typical yellow color while the "dark"-type crystal is darker and opaque. It has been shown [15] that, from the comparisons between photoluminescence spectra of samples annealed under vapor pressures of Cd and S, the color difference may have been caused by the stoichiometry of the sample and will be described in details later in Sect. 7.2.

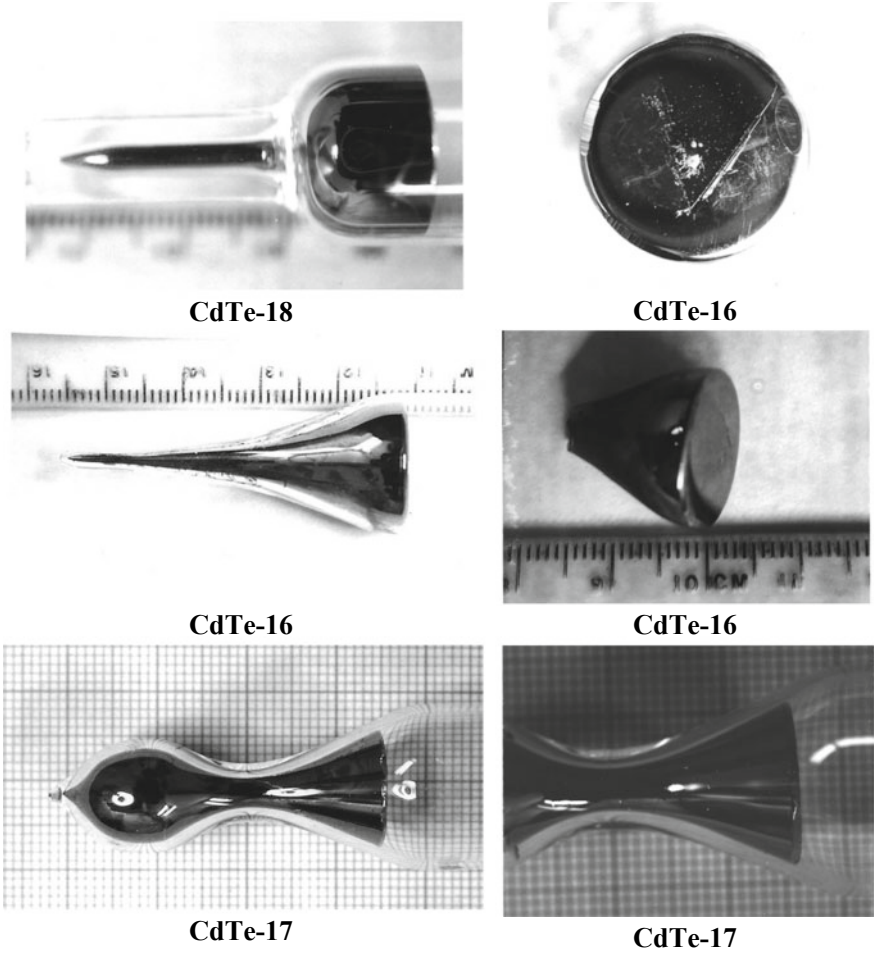

Fig. 5.29 Different ampoule designs for self-seeded growth of CdTe

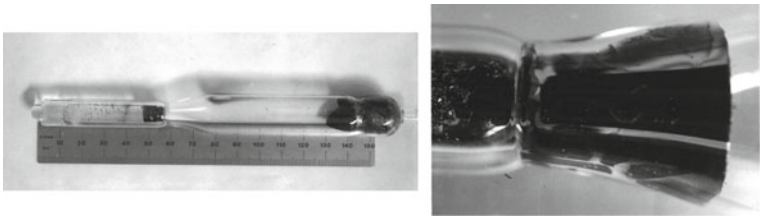

Fig. 5.30 Seeded growth of CdTe(s)-20 ampoules. Pre-growth ampoule (left) and post-growth crystal (right)

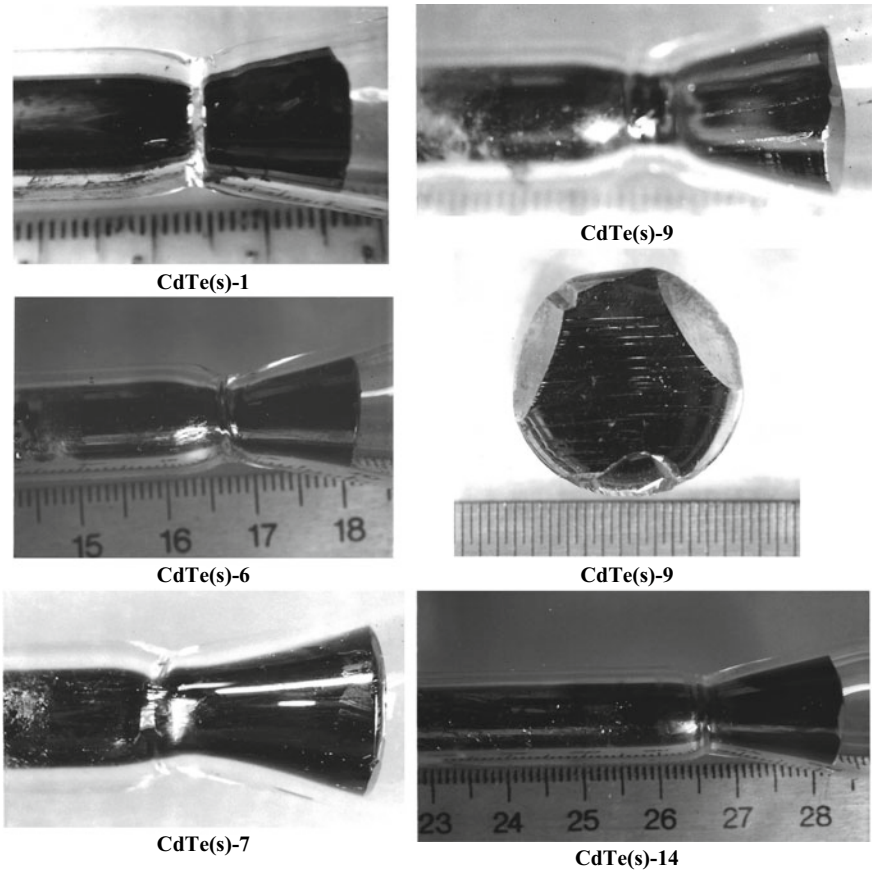

Fig. 5.31 As-grown CdTe crystals by seeded PVT

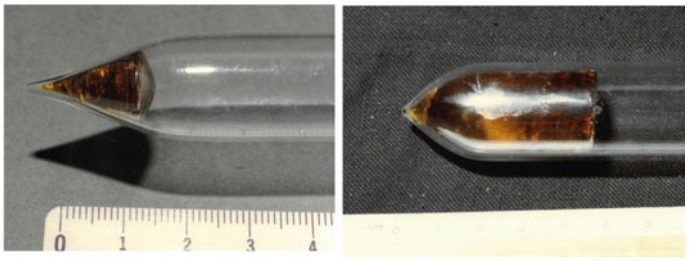

Fig. 5.32 CdS self-seeded grown ampoule (left) and another as-growth crystal (right)

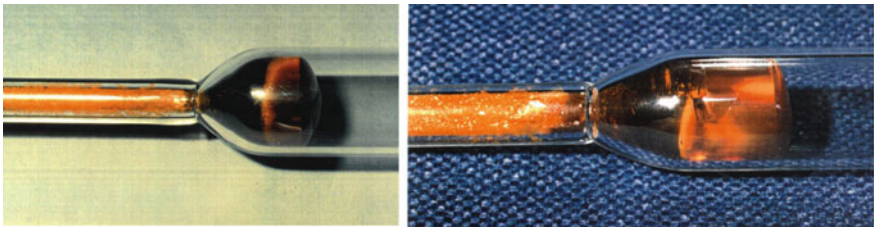

Fig. 5.33 Two seeded grown ampoules of CdS

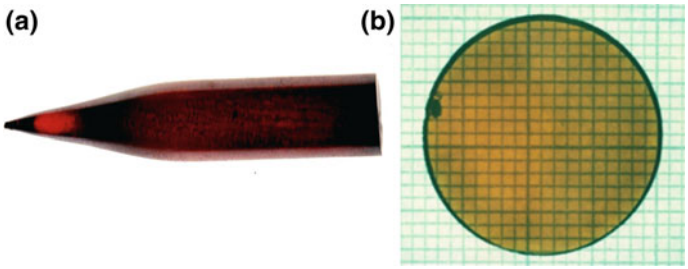

Fig. 5.34 **a** The grown crystals of ZnTe-1, 10 mm dia., and **b** the slice cut from ZnTe-2 crystal, 20 mm dia

5.2.11 Morphology of Grown Crystals of ZnTe

Figure 5.34a shows the grown crystals from the growth experiment of ZnTe-1, as described in the Sect. 4.3.8. Several (111) wafers have been sliced and polished from the as-grown boule of ZnTe-2 and one of them is shown in Fig. 5.34b.

References

1. C.-H. Su, M. Dudley, R. Matyi, S. Feth, S.L. Lehoczky, J. Crystal Growth **208**, 237 (2000)
2. W. Palosz, F.R. Szofran, S.L. Lehoczky, J. Crystal Growth **142**, 215 (1994)
3. C.-H. Su, M.A. George, W. Palosz, S. Feth, S.L. Lehoczky, J. Crystal Growth **213**, 267 (2000)
4. E.V. Markov, A.A. Davydov, Izv. Akad. Nauk SSSR Neorgan. Mater. **7**, 575 (1971)
5. K. Grasza, J. Crystal Growth **146**, 65 (1995)
6. Z. Golacki, Z. Furmanik, M. Gorska, A. Szczerbakow, W. Zahorowski, J. Crystal Growth **60**, 150 (1982)
7. Z. Golacki, M. Gorska, T. Warminski, A. Szczerbakow, J. Crystal Growth **74**, 129 (1986)
8. W. Palosz, K. Grasza, D. Gillies, G. Jerman, J. Crystal Growth **169**, 20 (1996)
9. Y.-G. Sha, C.-H. Su, W. Palosz, M.P. Volz, D.C. Gillies, F.R. Szofran, S.L. Lehoczky, H.-C. Liu, R.F. Brebrick, J. Crystal Growth **146**, 42 (1995)
10. C.-H. Su, Y.-G. Sha, K. Mazuruk, S.L. Lehoczky, H.-C. Liu, R. Fang, R.F. Brebrick, J. Crystal Growth **166**, 736 (1996)
11. C.-H. Su, W. Palosz, S. Feth, S.L. Lehoczky, J. Crystal Growth **192,** 386 (1998)

12. W.K. Burton, N. Cabrera, F.C. Frank, Philos. Trans. R. Soc. London **243**, 299 (1951)
13. G.H. Gilmer, R. Ghez, N. Cabrera, J. Crystal Growth **8**, 79 (1971)
14. N.B. Singh, C.-H. Su, B. Arnold, F.-S. Choa, B. Cullum, Stacey Sova and Christopher C. Cooper, Crys. Res. Tech. **180023**, 1 (2019)
15. K.-T. Chen, Y. Zhang, S.U. Egarievwe, M.A. George, A. Burger, C.-H. Su, Y.-G. Sha, S.L. Lehoczky, J. Crystal Growth **166**, 721 (1996)

Chapter 6
Characterizations on Crystalline Structures and Defect Distributions

Abstract The crystalline structural quality of the grown crystals were examined by synchrotron white beam X-ray topography (SWBXT), high resolution triple axis X-ray diffraction (HRTXD) analysis, cathodoluminescence (CL) imaging and chemical etching. Two modes of SWBXT have been performed: (1) the transmission mode when the images of X-ray transmitted through a thin sample slab and (2) the reflection mode from the sample surface. Detailed topographs and HRTXD analyses have been performed on self-seeded grown ZnTe and ZnSe crystals as well as seeded grown ZnSe crystals. The major structural defects revealed on these vapor grown II–VI semiconductors were twins, subgrain boundary and dislocations. Chemical etching and cathodoluminescence revealed the density and shape of the dislocations in grown crystals of ZnSe, CdTe and CdS. The concentrations of impurities and dopants in the grown crystals were examined by Secondary Ion Mass Spectroscopy (SIMS) and Glow Discharge Mass Spectroscopy (GDMS) whereas the distributions of impurities and native point defects were mapped by photoluminescence (PL). The compositional distributions in the grown crystals of ternary ZnSeTe crystals were studied by wavelength dispersive X-ray spectroscopy (WDS), optical transmission measurements and precision density measurements.

Keywords Synchrotron white beam X-ray topography (SWBXT) · High resolution triple axis X-ray diffraction (HRTXD) · Cathodoluminescence · Secondary ion mass spectroscopy (SIMS) · Glow discharge mass spectroscopy (GDMS) · Photoluminescence (PL)

The crystalline structural quality of the grown crystals were examined by synchrotron white beam X-ray topography (SWBXT), high resolution triple axis X-ray diffraction (HRTXD) analysis, cathodoluminescence (CL) imaging and chemical etching.

© Springer Nature Switzerland AG 2020

C.-H. Su, *Vapor Crystal Growth and Characterization*,
https://doi.org/10.1007/978-3-030-39655-8_6

6.1 Synchrotron White Beam X-ray Topography and High Resolution X-ray Diffraction Analysis

The setup of Synchrotron white beam X-ray topography (SWBXT) was analogous to the Laue technique except the high intensity and natural collimation of the synchrotron beam provides the following advantages: (1) the short time, in seconds, needed for imaging, (2) the spatial resolution, in principle, can be on the order of less than 1 μm, and (3) a large beam area, about 25 cm in diameter, delivered at sample location. Two modes of topography have been performed: (1) the transmission mode when the images of X-ray transmitted through a thin sample slab were taken and (2) the reflection mode from the sample surface. The wafers for the transmission topography were polished with an Al_2O_3/sodium hypochlorite solution to a thickness of about 200 μm. The major structural defects revealed by SWBXT on these vapor grown II–VI semiconductors were twins, subgrain boundary and dislocations.

6.1.1 ZnTe Crystals Grown by Self-seeded Horizontal PVT

The PVT grown crystal of ZnTe has been thoroughly studied by SWBXT [1, 2]. As illustrated in Fig. 6.1, five wafers with (111) orientation were sliced consecutively from the ZnTe-2 as-grown crystal which showed a growth direction of approximately 6° off [311] from Laue diffraction. Each wafer was about 0.1 mm thick with #1wafer closest to the first-grown tapered region of the ampoule and #5 closest to the last-grown region. The SWBXT image of wafer #3 in transmission Laue geometry with the crystal surface perpendicular to the incident beam is shown in Fig. 6.2. The image consists of two superimposed diffraction patterns. Close examination revealed that

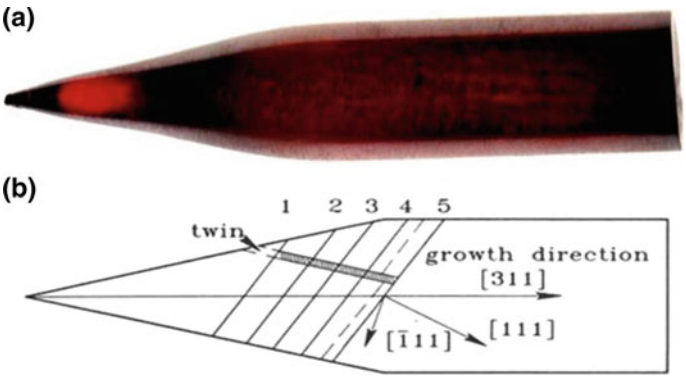

Fig. 6.1 **a** The picture of as-grown ZnTe-2 crystal and **b** the relative locations of five slices (1–5) with respect to the boule. The shaded area represents the twinned region in the boule. The broken line indicates the {111} growth interfaces

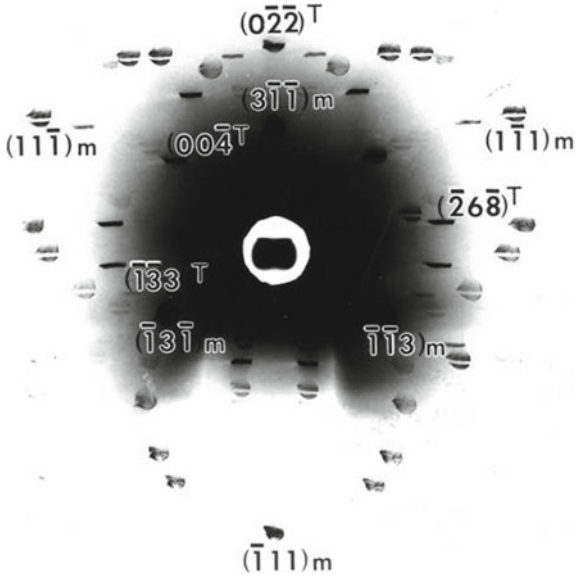

Fig. 6.2 Transmission Laue diffraction from wafer #3. Two superimposed diffraction patterns, one from the matrix region, denoted by M, and the other from twinned region, indicated by T (taken from Fig.1 of Ref. [2])

the two regions are related by a twinning operation consisting of a 180° rotation about the (111) plan normal. A part of a diffraction spot shifted to another position leaving that area with zero intensity, known as "orientation contrast", can be observed in the figure.

The evolution of the crystalline structure along the growing path can be visualized in Fig. 6.3 which shows a series of SWBXT images with diffraction vector $g = (\bar{2}\,02)$ from wafer #1 to #5. Each wafer shows the absence of twins in the mid-upper part of image due to the "orientation contrast". Part of wafer #4 was broken and the polishing strain caused some image contrasts in wafer #5. The overall twinning structure is similar for each wafer. Beside the twins, dislocations of slip bands lying in the $(11\,\bar{1})$ plane, S_1, showing the direction of upper-right to lower-left (except on wafer #1), slip dislocations lying in both the $(11\,\bar{1})$, S_1, and $(1\,\bar{1}\,1)$, S_2, planes were revealed. Between the slip bands, cellular structures of dislocations were formed as subgrain boundaries. Also, the dislocation density was the highest for wafer #1 and decreased gradually toward the end of the boule. This implies that stress concentrated near the tapered neck region and, as the diameter of the boule increased to final constant size, the strain relaxed by forming more uniformly distributed dislocation cell-structure as observed in wafer #3 and #4. To better delineate the matrix and the twin, a topograph of wafer #1 with clear contrast is given on the top of Fig. 6.4 with a schematic drawing to show the twin regions, the twin boundaries and lateral boundaries (LB).

Figure 6.5 is an example of image with an absence of "orientation contrast" which shows a transmission tomography taken on wafer #3. The image shows the slip bands, S_1, the cellular dislocation structure, C, the twin boundaries (TB), and the lattice rotational distortion, R, probably caused by the contact with the ampoule wall.

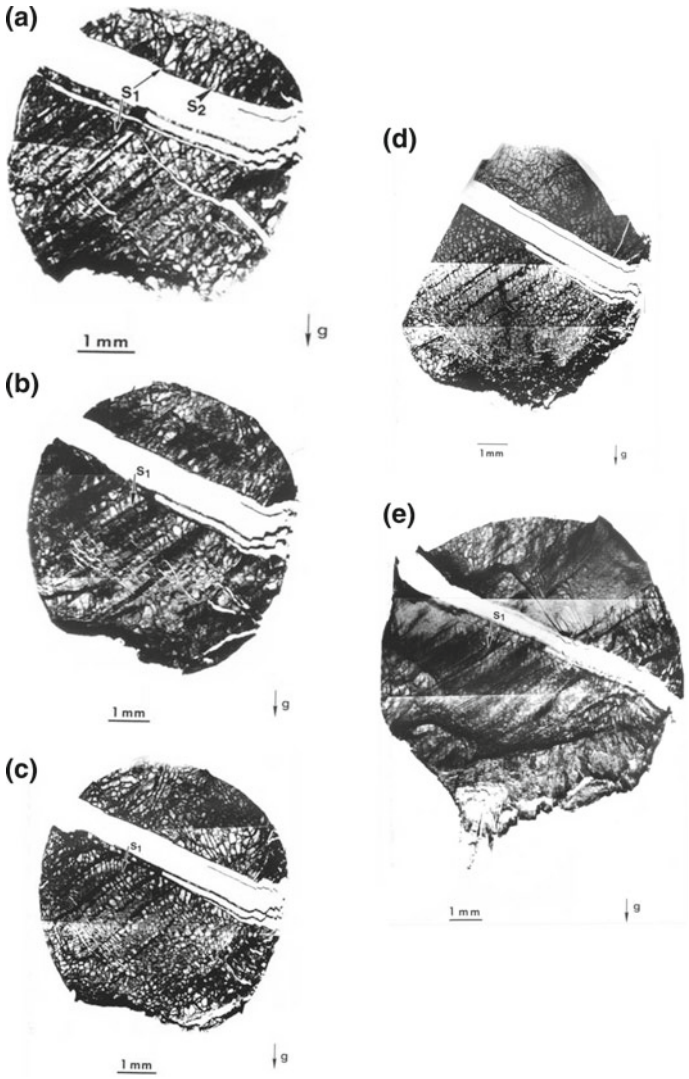

Fig. 6.3 The transmission SWBXT images for the as-grown ZnTe crystal for wafer #1(**a**)—#5(**e**)

The dislocations show a density of around 10^5–10^6 cm^{-2} in those areas comprising cellular structure and slip bands and, on the other hand, a lower dislocation density around 10^3 cm^{-2} within the subgrains.

The Burger's vector of dislocation can be resolved from the high magnification topograph of wafer #3 in the cellular structure region, C, in Fig. 6.5 where a series of topographs using different diffraction vectors are shown in Fig. 6.6. Part of the dislocation structure donated by D_1, which clearly belongs to (111) slip plane in Fig. 6.6a, disappeared on the images (b) and (c) for $g = 2\,\bar{4}\,2$ and $(\bar{1}\,3\,\bar{1})$ diffraction

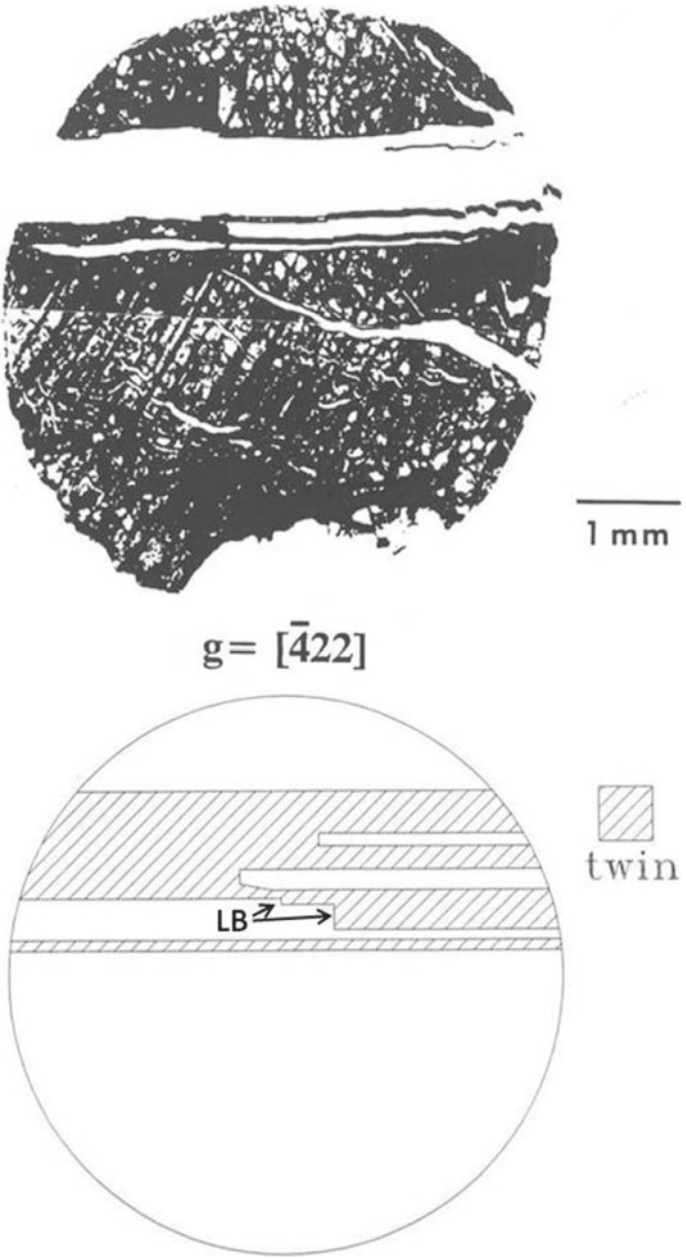

Fig. 6.4 A SWBXT image of wafer #1 (top) and the schematic drawing of twin area and lateral boundary (LB) (bottom)

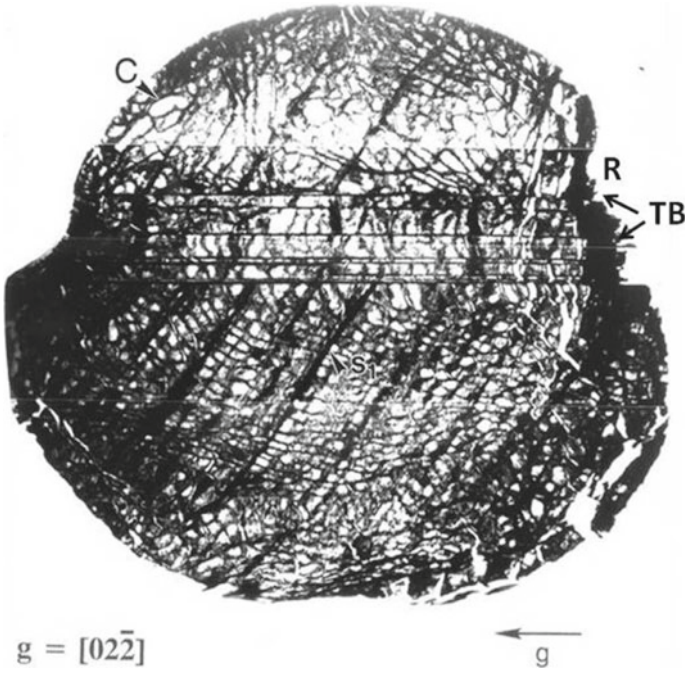

Fig. 6.5 A transmission tomography taken on wafer #3 shows the absence of "orientation contrast". The slip bands, S_1, the cellular dislocation structure, C, the lattice rotational distortion, R, and the twin boundaries (TB) were indicated

vectors, respectively, while dislocations indicating by D_2 disappeared on images (d) and (e) for g = $(\bar{1}\,\bar{1}\,3)$ and $(22\,\bar{4})$ diffractions, respectively. Applying $g \cdot B = 0$ extinction criterion, the Burger's vector for D_1 is $\pm\frac{1}{2}[10\,\bar{1}]$ and that for D_2 is $\pm\frac{1}{2}[1\,\bar{1}\,0]$. The high magnification topograph of wafer #1, shown in Fig. 6.7, revealed the generation of slip bands, S_1, was likely from the junction of twin boundary (TB) and a subgrain boundary (SGB).

ZnTe crystals grown by PVT have tendency to form [111] twin boundary due to the fact that bonds across such boundaries are relatively unstrained, leading to minimum energy. A schematic of the three-dimensional construction for the matrix and twin regions examined on this crystal is given in Fig. 6.8. The front surface (111) is the sliced and polished face of the wafers with the twin plane of $(\bar{1}\,11)$ and the lateral twin boundary planes of $(0\,\bar{1}\,1)$ and $(1\,\bar{1}\,2)$.

With the zinc blend lattice of the ZnTe crystal, a possible structure at the twin-matrix interface can be postulated as shown in Fig. 6.9 where the twin region comes down from the top, goes through the twin plane and converts into the matrix and follows the atomic layers of aαbβcγaαcγbβaα, where abc represent Te atomic planes and αβγ represent Zn atomic planes. This kind of boundary was observed in bounding long, thin lamellar twin regions in ZnTe crystals.

Figure 6.10 gives two more SWBXT on wafer #3 to have a close-up delineation

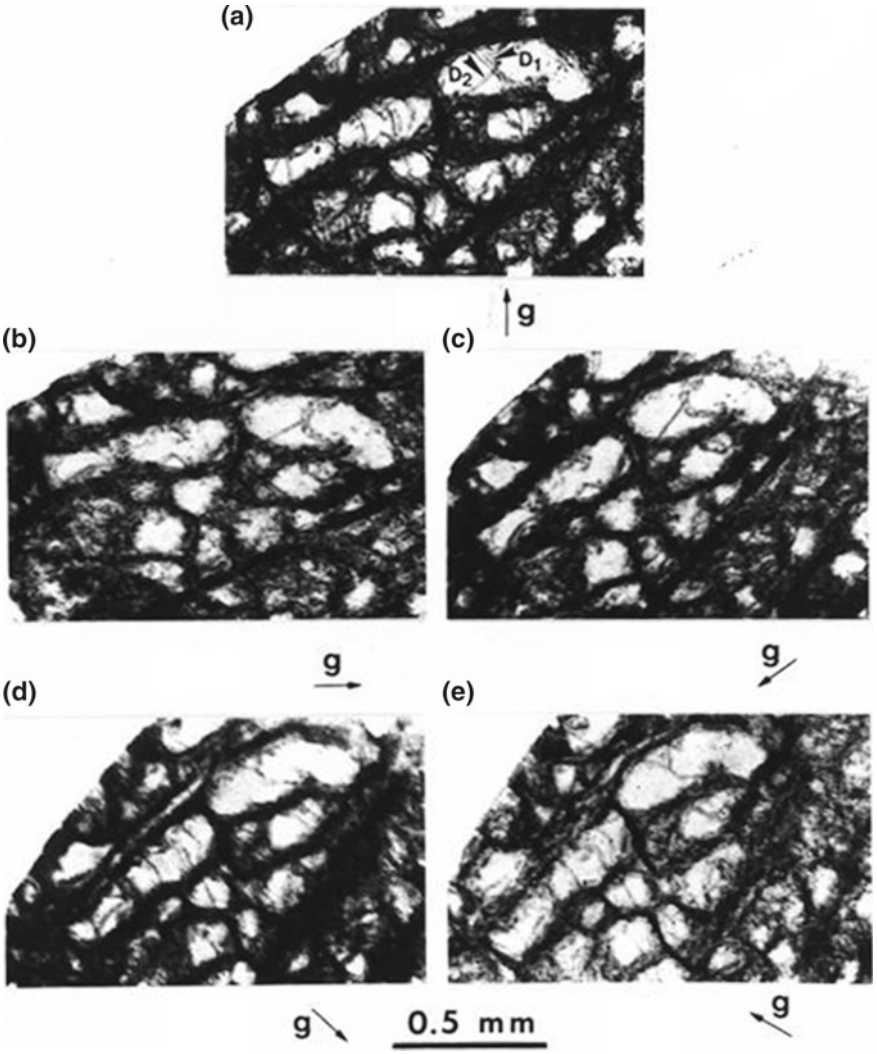

Fig. 6.6 A series of topographs taken in the same area of wafer #3 using different diffraction vectors: **a** g = $3\bar{1}\,\bar{1}$ **b** g = $2\,\bar{4}2$ **c** g = $\bar{1}3\,\bar{1}$ **d** g = $\bar{1}\,\bar{1}3$ and (e) g = $22\,\bar{4}$ (taken from Fig. 6.5 of Ref. [2])

on the structure of slip bands, cellular structure and individual dislocation. From the results of a closer examination on the various structural defects, a chronological of defect formation has been proposed. By following the trace of the major twin to its origin indicates that it may have nucleated at a position of wall contact in the tapered region early in the growth process which might involve stress relaxation. The evidence indicates that most of the slip bands tended to break up the ordered cell structure. This implies that the slip bands occurred later than the cellular structures during the

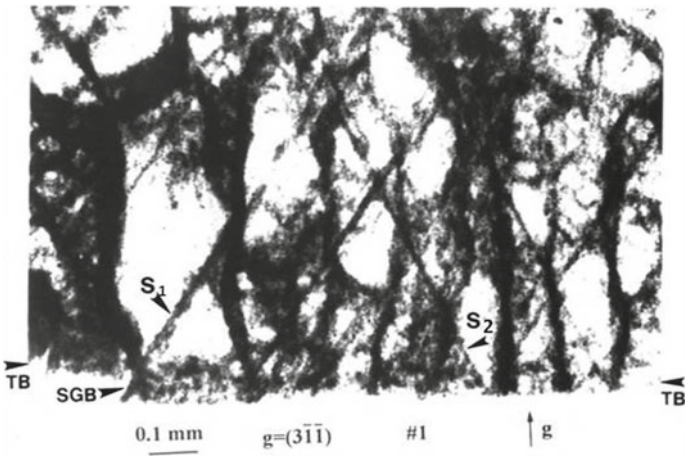

Fig. 6.7 High magnification topograph taken from wafer #1 revealed the generation of slip band, S1, from the junction of twin boundary (TB) and subgrain boundary (SGB)

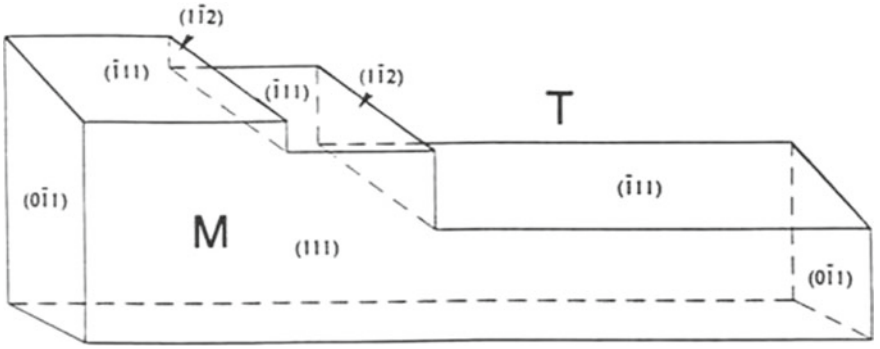

Fig. 6.8 Schematic of the three-dimensional construction of the matrix and the twin regions

growth process. Also, the slip dislocation density is much higher in the lower part of the twins than in the upper part and some of the slip dislocations originated at twin boundaries, could be an indication that twin boundaries act as barriers for the propagation of the slip dislocations and the twins formed earlier in the growth process than the generation of slip bands which might have occurred during the post-growth cooling process. Therefore, after the completion of the crystal growth process, i.e., after the furnace translation has been stopped, it is recommended that it should take at least two days for the cooling of the growth furnace to room temperature.

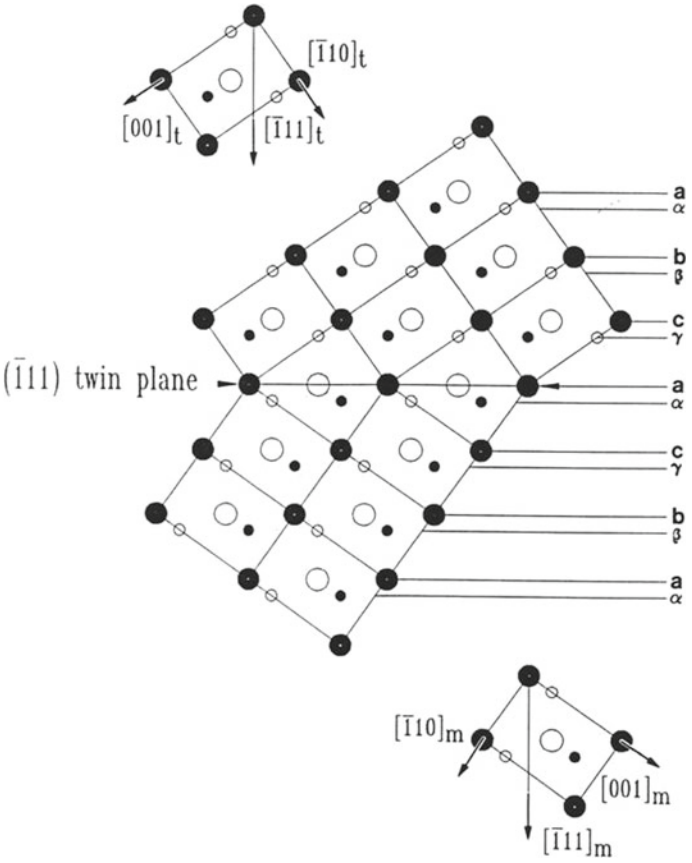

Fig. 6.9 Possible atomic structure at the twin-matrix interface where the twin region is on the top and matrix at the bottom (taken from Fig. 6.9 of Ref. [2])

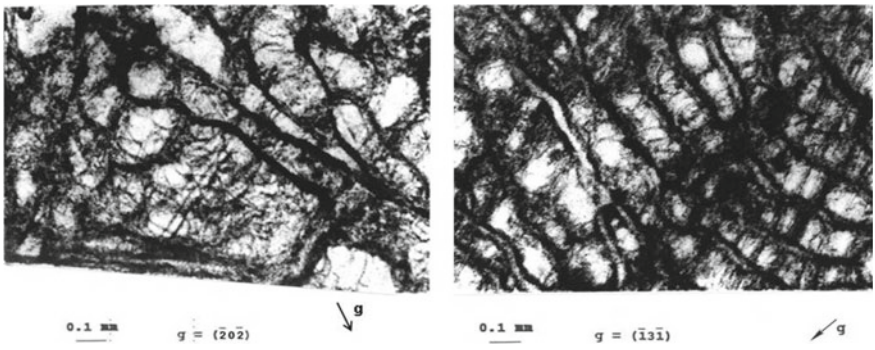

Fig. 6.10 Two close-up SWBXT images on wafer #3

6.1.2 *ZnSe Crystals Grown by Self-seeded Horizontal PVT*

Oriented wafers, sliced from several as-grown ZnSe boules, were examined by SWBXT and high resolution X-ray diffraction analysis [3]. Figure 6.11 displays the transmission SWBXT of a ZnSe-6H (110) wafer. The oriented slice was polished by Al_2O_3 powder + sodium hypochlorite to less than 0.2 mm thick. In the SWBXT images, twins (T) formed by 180° rotation about the (111) plane, slip bands (S) and cracks (C), probably introduced during polishing, were observed. Another transmission topograph, as shown in Fig. 6.12, of ZnSe-15H (111) wafer exhibits twin lamellae (TL), distortion near the ampoule wall and three sets of (111) slip band, S_1, S_2 and S_3, mostly originated from the lateral twin boundaries. It is interesting to note that the dense slip bands, subgrain boundaries and the cellular dislocation loops observed in the ZnTe crystals were absent in ZnSe.

The SWBXT in the reflection mode was performed on another ZnSe-15H (111) wafer. There was a twin on the upright section of the single crystal sample. The orientation contrast gave two images, as shown in Fig. 6.13, one for the twin (a) with

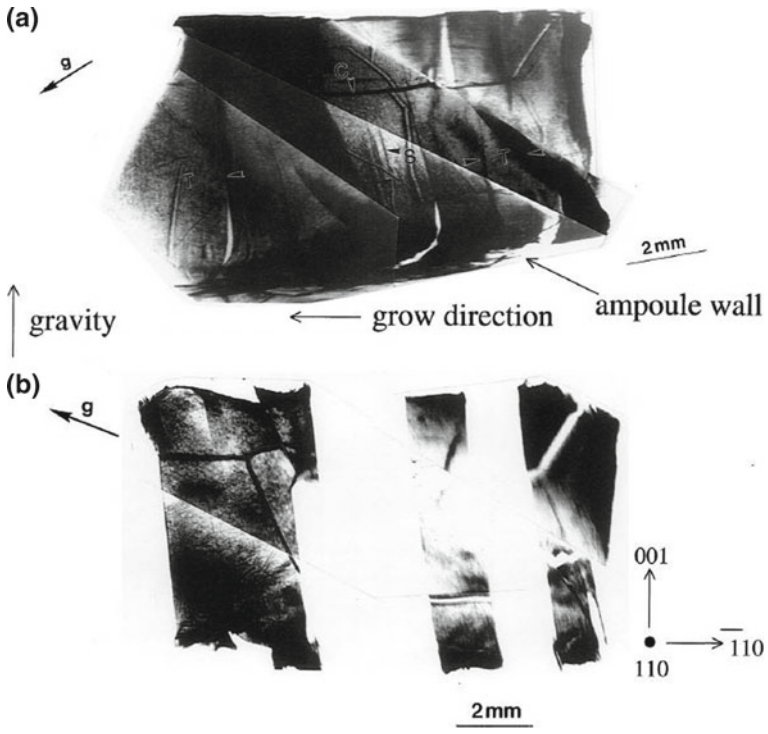

Fig. 6.11 Transmission SWBXT of a ZnSe-6H (110) wafer. **a** Structural defects such as twins (T), slip bands (S) and crack (C) are visible, g (diffraction vector) = (1 $\bar{1}$ $\bar{1}$). **b** Twins are revealed by orientation contrast, g = (1 $\bar{1}$ 1) (taken from Fig. 6.3 of Ref. [3])

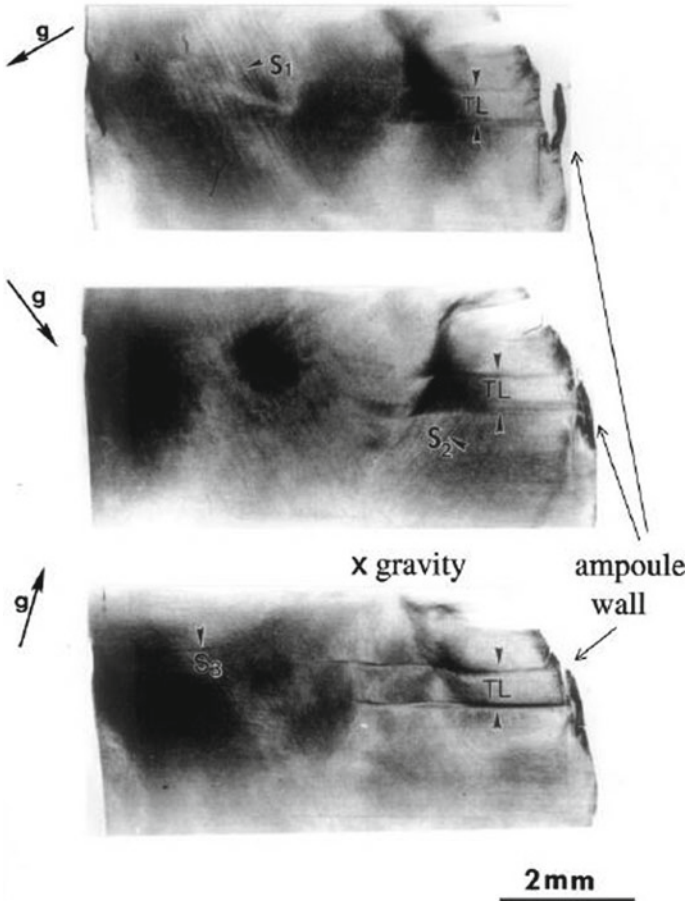

Fig. 6.12 Transmission SWBXT topograph of ZnSe-15H (111) wafer. Twins, twin lamellae (TL) and three sets of (111) slip bands (S) are visible and gravity is into the paper (taken from Fig. 6.4 of Ref. [3])

twin lamellae and slip bands and the other image for the matrix (b). The crystalline quality was quite good, especially for the matrix region. Without any sample slicing, two reflection SWBXT images were taken from one side of the as-grown ZnSe-16H boule as shown in Fig. 6.14. The whole boule is a single crystal with the initial and lower part of the boule (on the left) showing high crystalline quality and twin lamellae forming at the later stage of the growth (on the right).

A refection SWBXT on the as-grown facet of the horizontally grown ZnSe-43H crystal, shown in Fig. 6.15, exhibits areas of twins without the orientation contrast. Figure 6.16 shows the picture of the crystal (a) and a schematic mapping (b) of the matrix (in white) and twins (in brown) areas with the relevant orientations. The orientation contrast between the matrix and twins can be seen in Fig. 6.16c, d because

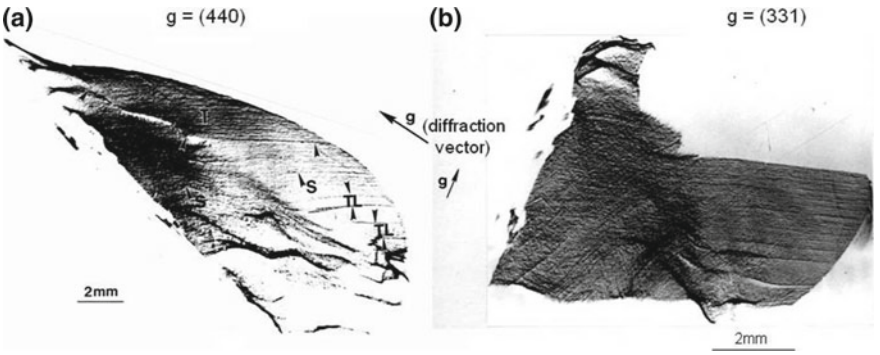

Fig. 6.13 SWBXT in the reflection mode on a ZnSe-15H wafer: **a** image of the twin with twin lamellae (TL) and (111) slip bands (S) and **b** of the matrix

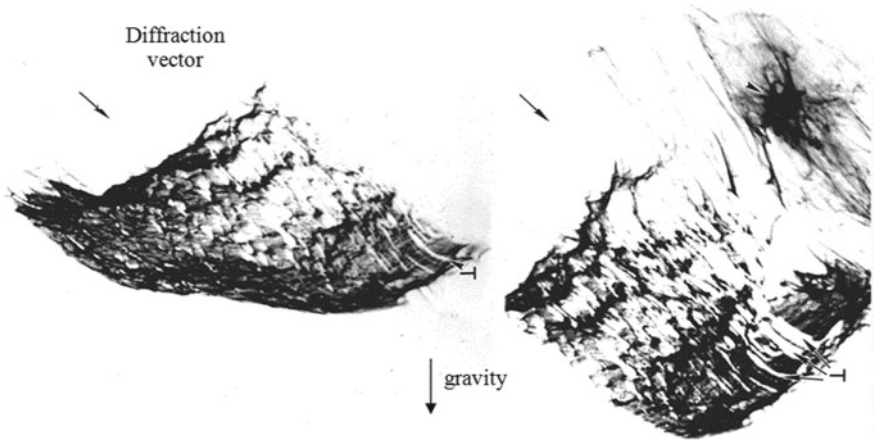

Fig. 6.14 Two reflection SWBXT images taken from one side of the as-grown ZnSe-16H boule

of the diffraction vectors of the images. The crystalline quality is generally good except the upper region just before the crystal was grown into full diameter and away from the ampoule wall.

6.1.3 High Resolution Triple X-ray Diffraction (HRTXD)

HRTXD was conducted to provide the analyses included high resolution reciprocal space mappings, transverse scans as well as rocking curves to provide supplementary structural information on specific local areas. Two diffractometers were employed for the HRTXD measurements. A Bede 150 double crystal dffractometer, modified by the addition of a two crystal, four reflection monochromator and three reflection

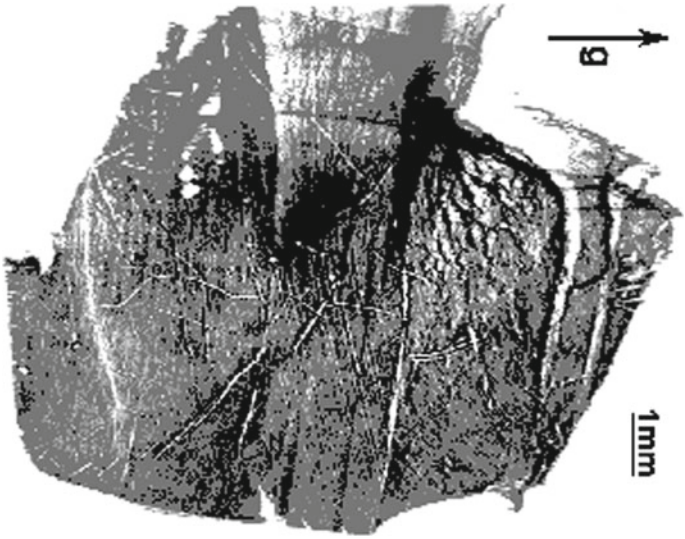

Fig. 6.15 Refection SWBXT on the as-grown facet of ZnSe-43H

analyzer, was used for the initial analyses. Later work was performed using Bede D^3 dffractometer equipped with a two crystal, four reflection monochromator and a two reflection analyzer crystal. Both diffractometers used Cu $K_{\alpha 1}$ obtained from Rigaku rotating anode generators. The X-ray footprint used was 3 mm × 0.1 mm. The sample surfaces for the X-ray analyses were either as-grown surface, as-grown (110) facets, cleaved (110) planes or wire-sawn (110) or (111) surfaces chemical-mechanically polished with an Al_2O_3/sodium hypochlorite solution.

In Fig. 6.17, nine rocking curves were performed on the same facet as in Fig. 6.15. The lower part of the facet exhibits good crystalline quality with the full width at half maximum (FWHM) in the order of 20 arc-sec. The upper part, especially in the upper region just grown away from the ampoule wall, shows FWHM generally in the 50's arc-sec range with one rocking curve showing double peaks with FWHM at 94 arc sec-taken at region straddling twin boundary.

The triple axis reciprocal lattice mappings were also performed on the facets and the correlation between the SWBXT images, the rocking curves and the reciprocal lattice mappings are shown in Fig. 6.18. At the right location, the early grown region, the reciprocal lattice mapping exhibits the double-peak feature, consistent with the rocking curve, and the diffused scattering along the $q_\perp$ direction. At the left location, a single maximum was observed along with some degree of scatter along the $q_\perp$ direction in the reciprocal lattice mapping. A surface dynamic streak along the q_{220} direction was also observed which indicates good crystalline quality of the sample and smoothness of the surface.

The effect of polishing on the crystalline quality was also studied by high resolution X-ray analysis. The (220) reciprocal space mappings were performed on two

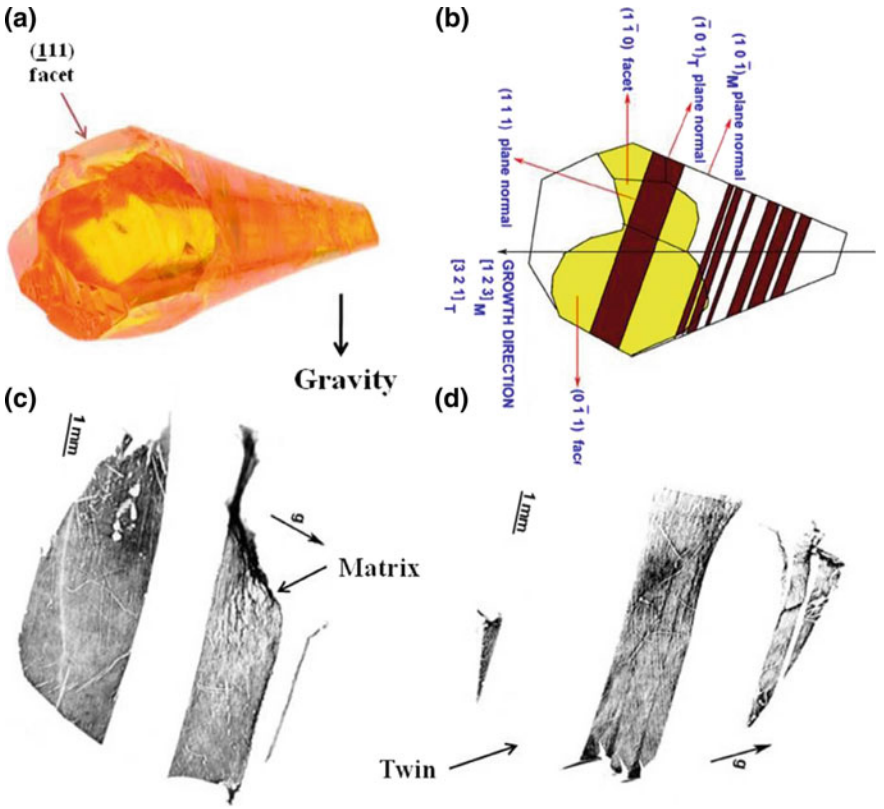

Fig. 6.16 **a** Picture of ZnSe-43H crystal. **b** Schematic mapping and relevant orientations of the matrix and twins. The contrasted SWBXT images of matrix (**c**) and twins (**d**)

samples from the ZnSe-15H crystal. One was performed on a cleaved surface and the other on the surface polished by Al_2O_3 powders in sodium hypochlorite solution. Figure 6.19a shows that the cleaved surface provided surface streak with diffuse scattering perpendicular to q_{220}—indicating good structural quality and smooth surface whereas Fig. 6.19b presents the polished surface with extensive isotropic diffuse scatter and no surface streak.

A SWBXT analysis similar o the one performed on ZnSe-43H was done on the as-grown crystal of ZnSe-45H. Figure 6.20 shows the picture of the as-grown crystal (a) and a schematic mapping (b) of the matrix (in white) and twins (in brown) with the relevant orientations. The orientation contrast between the matrix and twins can be seen in Fig. 6.20c, d. Twinning operation was observed from $(011)_T$ to $(411)_M$ to lower the energy. It is speculated that, for this particular growth direction, i.e., the 16º shoulder angle, is encouraging the formation of growing twins.

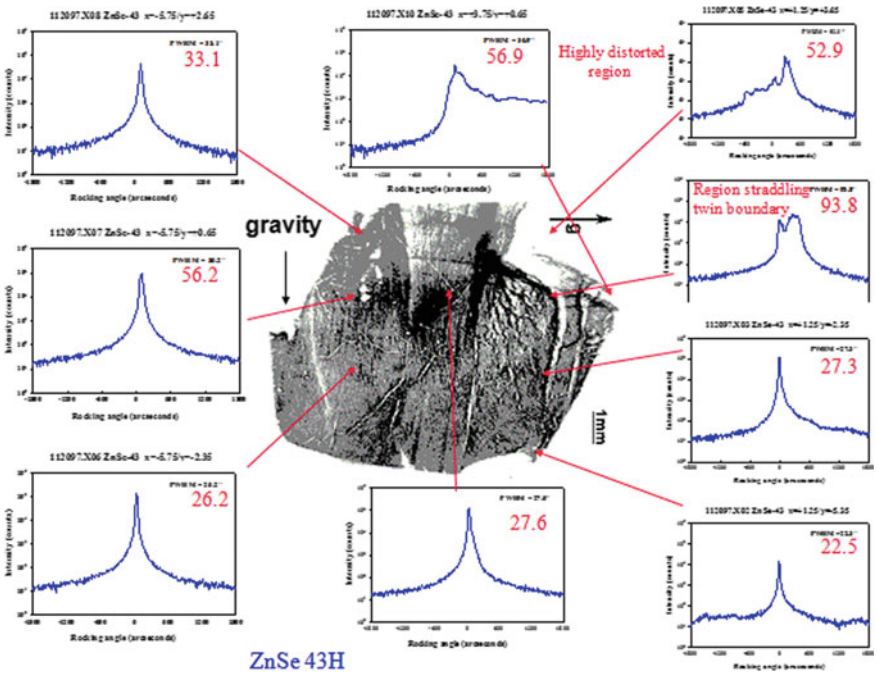

Fig. 6.17 SWBXT of ZnSe-43H with nine rocking curves (taken from Fig. 8 of Ref. [3])

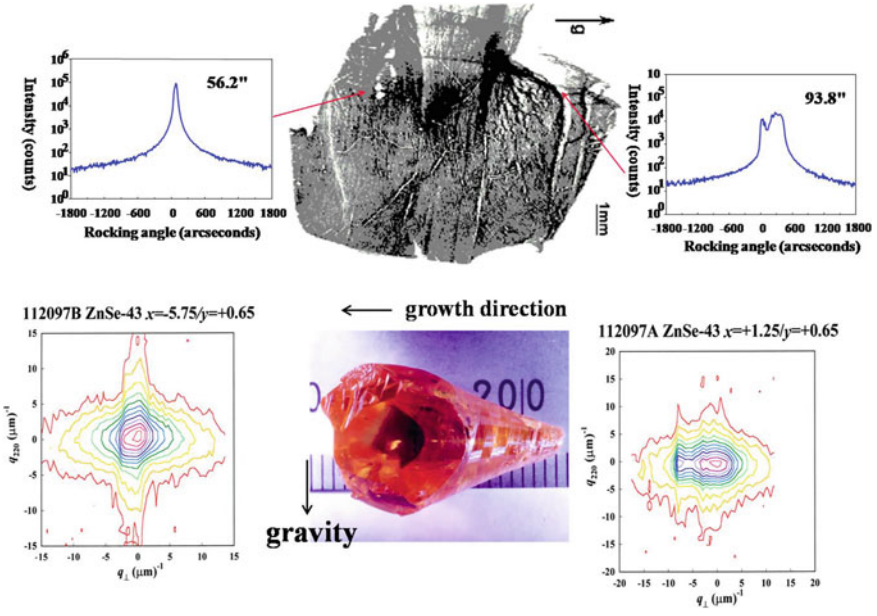

Fig. 6.18 Correlation between SWBXT, rocking curves and reciprocal space mappings for ZnSe-43H (taken from Fig.7 of Ref. [3])

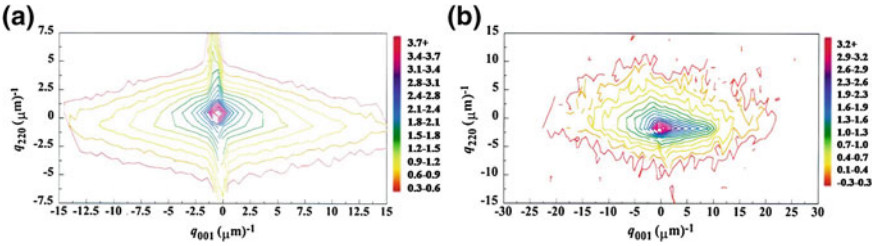

Fig. 6.19 The (220) reciprocal space mappings on two samples from the ZnSe-15H crystal. **a** The cleaved surface and **b** the surface polished by Al_2O_3 powders in sodium hypochlorite solution. The color-coded scale gives the constant diffraction intensity contours in log(intensity). (taken from Fig. 9 of Ref. [3])

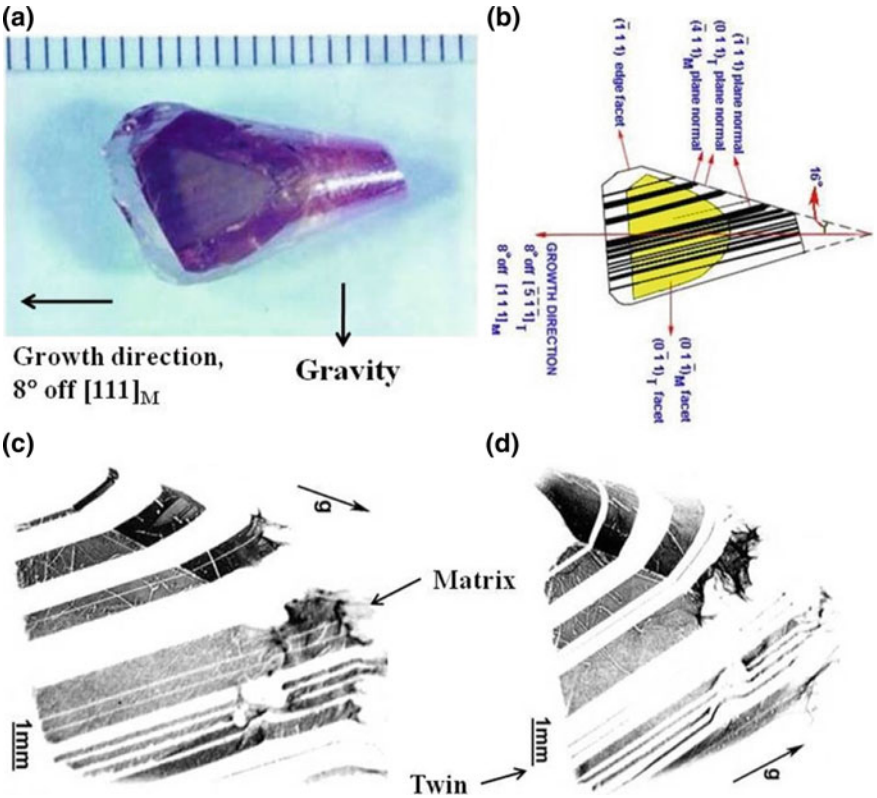

Fig. 6.20 **a** The picture of the as-grown crystal, **b** a schematic mapping of the matrix (in white) and twins (in brown) areas with the relevant orientations, **c** the orientation contrast images of the matrix and **d** the twins

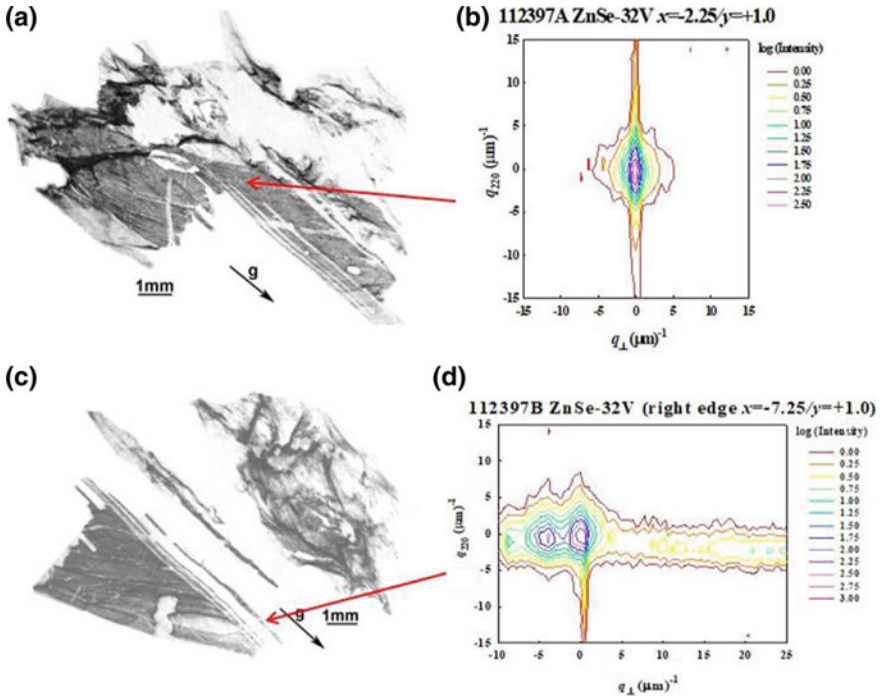

Fig. 6.21 Reflection SWBXT images taken on a cleave (110) surface from ZnSe-32VS: **a** the SWBXT image of the matrix and **c** of the twin. Triple axis reciprocal space mapping on the center of the matrix (**b**), and on the thin lamellar twin (**d**)

6.1.4 ZnSe Crystals Grown by Self-seeded Vertical PVT

On the vertical grown crystal, reflection SWBXT images were taken on a cleave (110) surface from ZnSe-32VS. As shown in Fig. 6.21, the crystal consists of matrix (a), twins and some lamellar twins (c) in the middle section of the sample. The triple axis reciprocal space mapping was performed on the low-distortion area of the matrix (shown in Fig. 6.21b and the contour plot gives a very narrow surface streak with diffuse scattering perpendicular to q_{220}—indicating a high degree of structural perfection. The mapping in Fig. 6.21d was taken in the thin lamellar twin and, thus, multiple maxima were observed.

6.1.5 ZnSe Crystals Grown by Seeded PVT

The surfaces of the seeded horizontally as-grown ZnSe boule were studied by X-ray topography in the reflection geometry. The grown crystal, ZnSe(IS)-5, was the grown crystals from one of the in situ visual and interferometric monitoring growths. The

images were recorded from the surface of the boule in the four 90° positions shown in the optical photographs in Fig. 6.22. The four positions for the X-ray images are labeled A, B, C and D as shown on the photographs.

Figure 6.23 gives a reflection topograph recorded in position A (gravity vector pointing out perpendicular to the plane of the paper) showed the presence of multiple grains. Orientation contrast from several twin bands is observed. Crystalline quality of its surface appears to be fairly good. While no definite demarcation between seed and growing crystal can be discerned, the relative positions are shown with respect to the recorded image. Figure 6.24 shows a topograph recorded in position B with the gravity vector pointing up in the image (recording geometry for the topograph was with the growth axis in the horizontal direction). Crystalline quality is fairly good. Some twin bands can be observed near the end of the grown crystal.

Figures 6.25, 6.26 and 6.27 show reflection topographs recorded with the boule in position C. The images reveal that the crystal continued to grow on top of the single

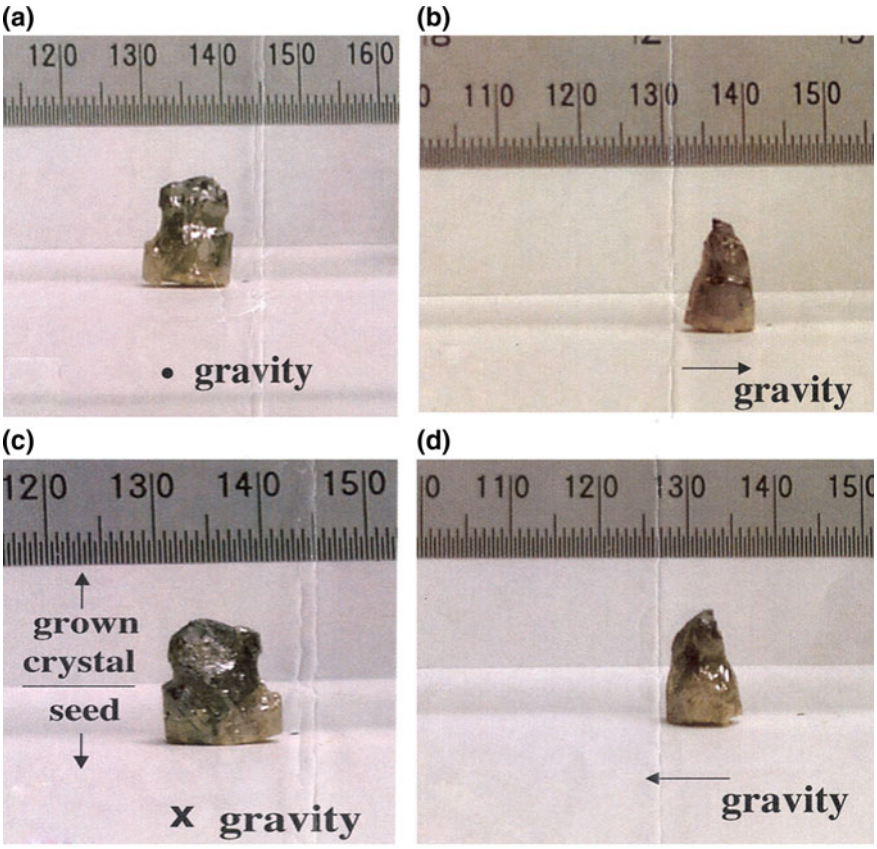

Fig. 6.22 The images of SWBXT on ZnSe(IS)-5 were recorded from the surface of the boule in the four 90° rotating positions labeled as (**a**–**d**)

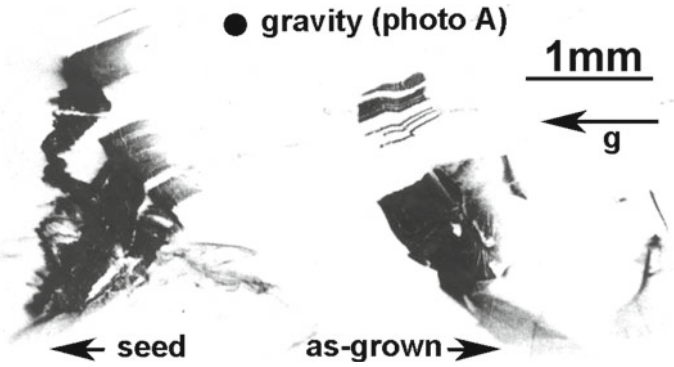

Fig. 6.23 ZnSe (IS)-5 reflection topograph from position A

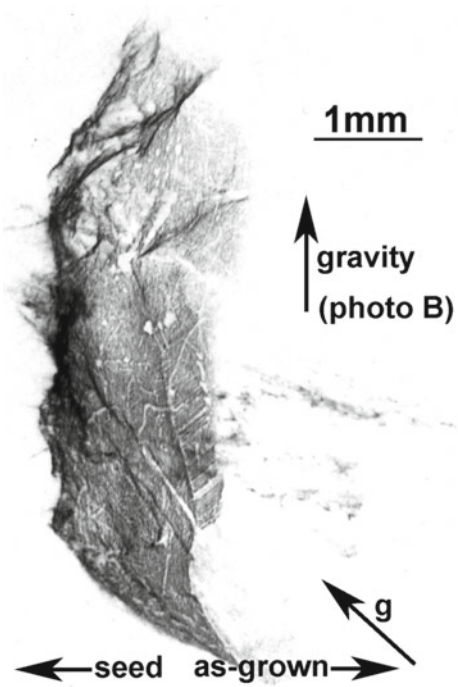

Fig. 6.24 ZnSe(IS)-5 reflection topograph from position B

crystal seed as planned. Both the seed region as well as the end of growth region exhibit large strains while the middle regions corresponding to steady growth show fairly low strains. Twin bands possibly nucleated from the seed are clearly seen. In Figs. 6.25 and 6.27 orientation contrast is absent from the twin but strain contrast from the twin boundaries is visible in both cases. In Fig. 6.26, orientation contrast from the twin boundaries is observed.

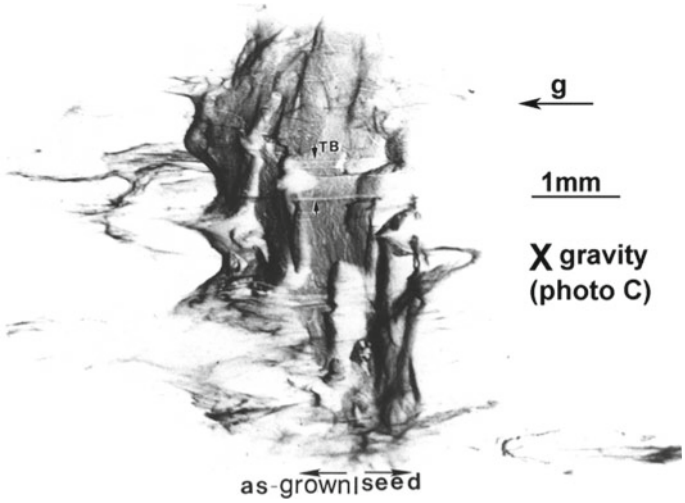

Fig. 6.25 ZnSe(IS)-5 reflection topograph from position C (g = 111)

Fig. 6.26 ZnSe(IS)-5 reflection topograph from position C (g = 220)

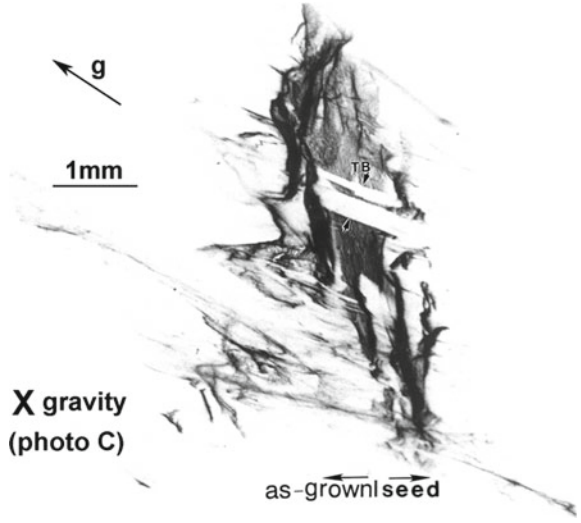

The X-ray film recorded in position D with the gravity vector pointing down on the image (the growth axis in the horizontal direction) shows the presence of multiple grains most of which are characterized by strains. The topograph given in Fig. 6.28 reveals that certain parts of the crystal shows good crystalline quality with some distorted image in the middle section due to the strains.

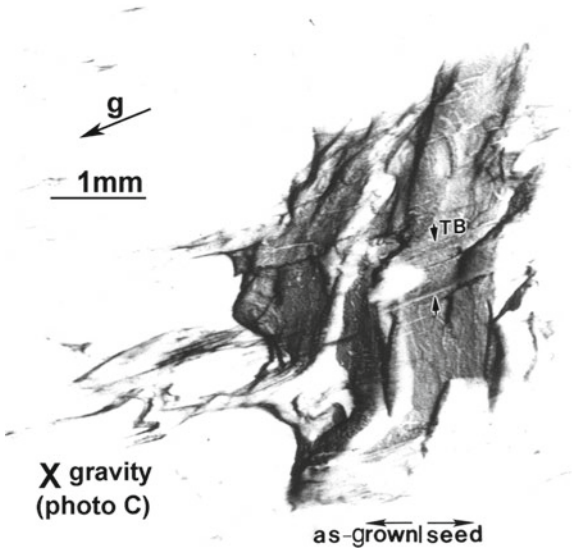

Fig. 6.27 ZnSe(IS)5 reflection topograph from position C (g = 224)

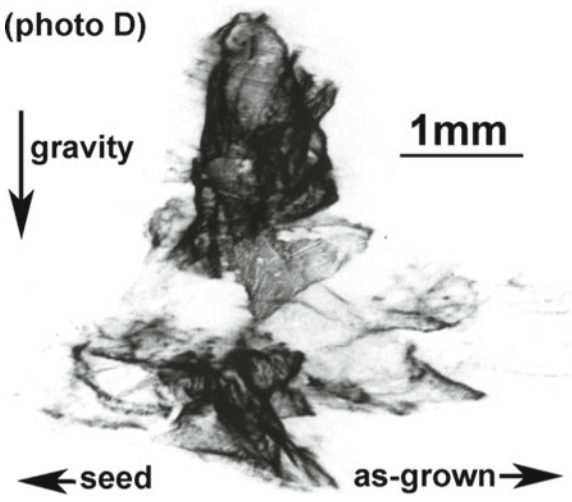

Fig. 6.28 ZnSe(IS)-5 reflection topograph from position D

6.2 Chemical Etching

Chemical etching was applied to polished crystal surface with certain orientation to delineate dislocation pits.

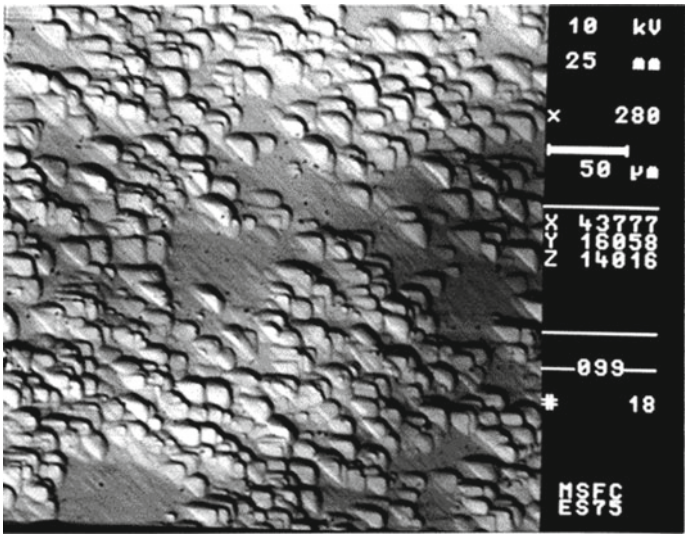

Fig. 6.29 Micrograph of an etched surface of a ZnSe-15H (111) wafer after NaOH etch. An etch pit density of $1 \times 10^5 \text{cm}^{-2}$ was estimated

6.2.1 Etching of ZnSe Crystals

For the chemical etching of ZnSe, (111) wafers were sliced from oriented boules of ZnSe-15H and then were chemico-mechanical polished with Al_2O_3/sodium hypochlorite solution. The polished (111) wafers were etched in boiling 30% NaOH solution for 10 min. Figure 6.29 shows the micrograph of an etched surface and the etch pit density was estimated to be 1×10^5 cm^{-2}.

6.2.2 Etching of CdTe Crystals

For the chemical etching of CdTe, discs were sliced perpendicular to the growth direction from two seeded grown crystals, CdTe(s)-10 and -22. The crystals were mechanically polished on both surfaces. Then they were chemically polished with E solution for 1 min prior to being etched. The E solution was composed of 10 ml of HNO_3, 20 ml of H_2O and 4 g of $K_2Cr_2O_7$. The EAg-1 etch-ing solution was selected since it produces etch pit configuration that varies in shape depending on both the surface orientation of the crystal and the Ag + ion configuration. The samples were etched with fresh EAg-1, which is composed of 10 ml of E solution and 0.5 mg of $AgNO_3$, for 1 min.

Results of the etching study in Fig. 6.30a show that the CdTe(s)-10 crystal consists of several grains with two different kinds of etch pits on different sides of the

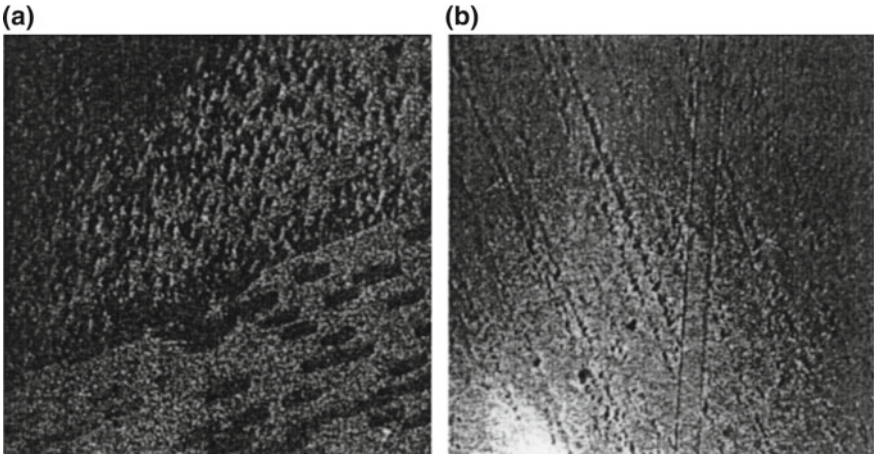

Fig. 6.30 The chemical etching pictures showing the etch pits and the grain boundaries of the two crystals **a** etch pits for CdTe(s)-10 near the grain boundary, the long sides of the rectangular pits are parallel to the grain boundary when the neighboring pits are pyramidal. **b** Small etch pits that are roughly triangular for CdTe(s)-22, and there are no pits in the twinned region (taken from Fig. 6 of Ref. [6])

grain boundary. The pyramidal pits indicate a (111) A orientation whereas the rectangular pits indicate a (100) orientation. Figure 6.30b shows the etch-pits on the CdTe(s)-22 crystal. Only one kind of etch-pit lined up along the straight parallel lines. Twin boundaries were observed in this crystal grown on a (211) seed. This is inconsistent with the reported results that single CdTe crystal without twins were successfully grown using homo-epitaxial growth by sublimation on the (211) seed [4]. The CdTe(s)-10 crystal grown on the (111) seed has a larger number of grain boundaries than the crystal grown on the (211) seed. Similar results were reported by Shetty et al. [5], although in their case, the CdTe crystals were grown by the Bridgman method.

Figure 6.31 shows the etch pits from the self-seeded grown CdTe-7 crystals. The triangular pits show on the (111) plane that was cut by either a narrow twin lamellae, as shown in Fig. 6.31a, or multiple parallel twins (shown in Fig. 6.31b).

6.2.3 Etching of CdS Crystals

Slices of CdS were polished and etched in HPC etchant (35% phosphoric acid saturated with CrO_3 with 65% HC1) for 10 to 20 s at room temperature. Figure 6.32a shows the SEM micrograph of dislocation etch-pits on a CdS slice following etching. The typical dislocation etch-pit densities ranged from 1 to 2×10^4 cm^{-2}. Figure 6.32b gives a close-up image of the hexagonal pit.

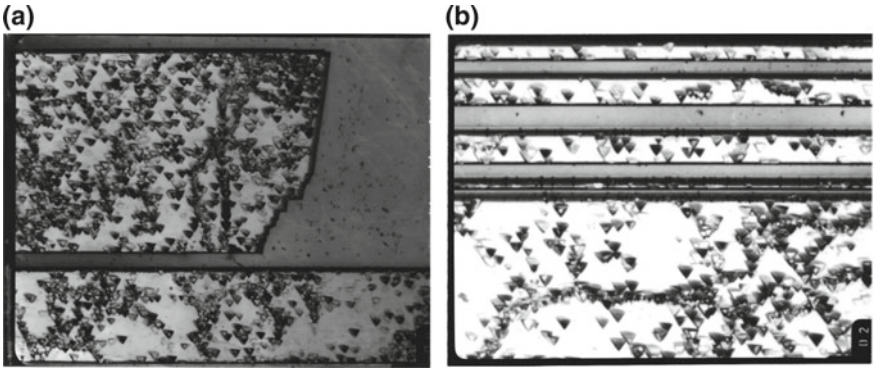

Fig. 6.31 The triangular etch pits of CdTe-7 crystal only shown on the (111) plane which was cut by a narrow twin (**a**) and multiple parallel twins (**b**)

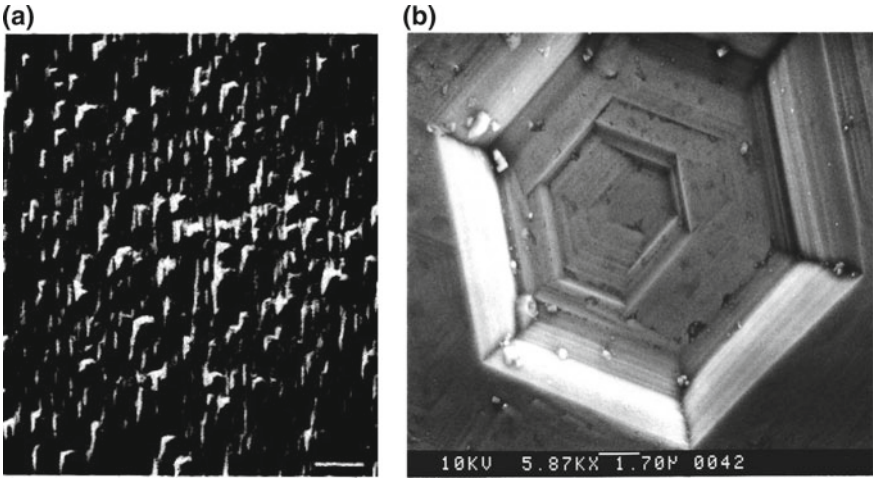

Fig. 6.32 **a** SEM photo shows the etch pits of CdS with densities ranging from 1 to 2 × 10^4 cm^{-2} (marker represents 50 μm) **b** a close-up photo the hexagonal pit (marker represents 1.7 μm)

6.3 Cathodoluminescence (CL)

A ZnSe-6H (110) wafer was polished by the Al_2O_3/H_2O solution then chemically polished with a 0.25% Br_2/methanol solution and the CL images were taken when sample was at 80 K. Figure 6.33 shows a CL image of the ZnSe-6H (110) wafer. From the separation of the dislocation clusters, 20–40 μm, the dislocation density was estimated to be in the high 10^4 to low 10^5 cm^{-2}. Comparing with the chemical etching, Fig. 6.29 shows the SEM micrograph of an etched surface and the etch pit density was estimated to be 1 × 10^5 cm^{-2}.

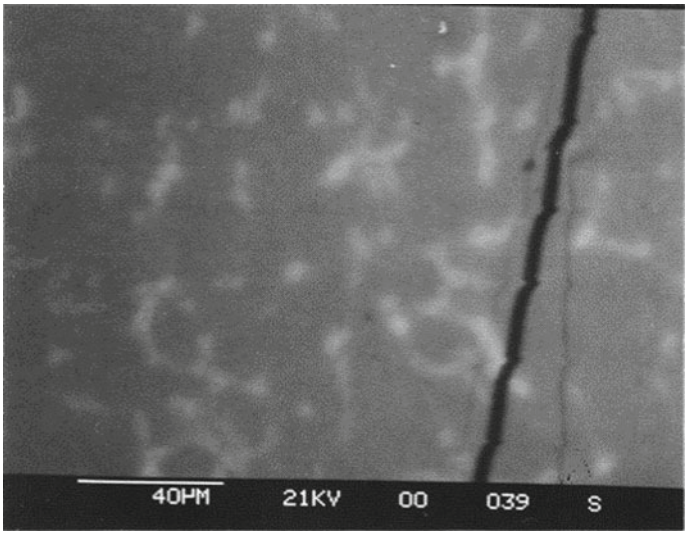

Fig. 6.33 Cathodoluminescence image of the ZnSe-6H (110) wafer. Dislocation and dislocation clusters are visible. From the separation, 20–40 μm, the dislocation density is estimated to be high 10^4 to low 10^5 cm^{-2}

6.4 Characterization on Distributions of Impurities and Point Defects

The impurity and defect distributions in the grown ZnSe crystals were examined by secondary ion mass spectroscopy (SIMS), photoluminescence (PL) and Glow Discharge Mass Spectroscopy (GDMS). The Cr doping level in the Cr-doped ZnSe crystals was determined by optical absorption measurements.

6.4.1 Secondary Ion Mass Spectroscopy (SIMS)

Secondary Ion Mass Spectroscopy (SIMS) is a technique to analyze the elemental contents of solid surfaces by sputtering the specimen with a focused primary ion beam and collecting and analyzing ejected secondary ions. It can detect very low concentrations of dopants and impurities although for quantitative analyses, a standard sample is needed. Hence, SIMS was performed to study the distribution of impurities in the ZnSe grown crystals [7]. The SIMS analyses were performed by a Cameca IMS-4f machine to provide the oxygen ion beam with spatial resolution of 25–30 μm in diameter and 100 μm in depth. The standards were mounted together with the sample in the chamber and the beginning-of-day and end-of-day analyses of the standards were performed to remove possible error from instrument drift over that particular day. The absolute concentration of a specific element in the samples

was determined from the relative sample/standard signal ratio of the element and the concentration of that element in the standards determined from GDMS. A total of 13 points and 36 points were mapped on the ZnSe-40H and the ZnSe-16V wafers, respectively.

The SIMS samples were sliced and polished on both sides with an Al_2O_3/H_2O solution and then the side of the SIMS measurements was polished again with diamond paste of 0.3 μm particle size. Four ZnSe samples were prepared for the SIMS measurements. Two of them were used as standards. One standard was a solid chunk of high-purity grade starting material provided by Eagle-Picher, Inc. The other standard was a specimen sliced from a vertically (stabilized) grown crystal, ZnSe-35V. Before the SIMS measurements the impurity levels in both standards were analyzed using glow discharge mass spectroscopy (GDMS) by the National Research Council of Canada and the results are listed in Table 6.1. Among the 55 trace elements measured most of the impurity levels in the two standards were below 50 ppb (atomic) except for the elements O, Al, Si, Ca, Fe, Cu, Cd and Te. The effect of purification during the vapor growth process was evidenced by comparing the impurity levels of the volatile elements in the starting material with those in the grown crystal the amounts of Li and Na were reduced by orders of magnitude after growth. The

Table 6.1 Impurity levels ppb (atomic) in starting materials from Eagle Picher, (E-P), and in the ZnSe-35 crystal by GDMS

Element	E-P	ZnSe-35	Element	E-P	ZnSe-35	Element	E-P	ZnSe-35
Li	85	<0.3	Mn	1	5	I	<0.6	<2
Be	<0.2	<0.2	Fe	250	300	Cs	<0.1	<20
B	<0.3	<2	Co	6	0.6	Ba	<2	720
C	75	20	Ni	300	30	La	<0.05	<0.03
N	10	10	Cu	500	150	Ce	<5	<1
O	4000	1500	Ga	<1	30	Hf	<0.03	<0.05
F	<5	<5	Ge	<3	<15	W	<0.2	<0.3
Na	70	2	As	<7	<13	Pt	1	4
Mg	3	30	Rb	<0.1	<0.2	Au	<10	<10
Al	2	1700	Sr	<0.07	<0.4	Hg	<0.3	<0.3
Si	<1	15000	Y	<0.06	<0.1	Tl	<0.08	<0.07
P	<0.2	9	Zr	<0.08	4	Pb	28	<0.09
S	100	<20	Nb	<0.1	<0.2	Bi	<0.06	<0.05
Cl	3	9	Mo	<0.2	<0.1	Th	<0.02	<0.02
K	<20	<15	Ag	<20	<2	U	<0.02	<0.02
Ca	6	500	Cd	70	800	V	<0.06	1
Sc	<0.1	<0.07	In	2	4	Sb	<0.1	<0.6
Ti	0.1	32	Sn	<0.2	<0.5			
Cr	7	25	Te	64	600			

hydrogen reduction heat treatment on the starting materials also reduced the oxygen content. However, the contamination of the grown crystal from the fused silica ampoule was also evidenced from the increase in the Si and Al contents. The cause of the observed increases in the Cd, Te and Ba contents is not clear. It is speculated that the sample was contaminated by Cd and Te during pre-growth processes.

Figure 6.34a–c shows the [Si], [Fe] and [Cu] contour map generated using the SIMS technique on the horizontally grown ZnSe-40H as-grown surface. From the SIMS results, [Si] and [Fe] show a clear tendency to segregate toward the bottom and [Cu] segregates toward the bottom at the first grown region and toward the top at the middle region of the facet. SIMS was also performed on a vertically grown ZnSe-16V wafer cut perpendicular to the growth axis. Figure 6.35a, b give, respectively, the [Si] and [Cu] contour maps, which show that these impurities tend to segregate toward the edge of the wafer. In general, the measured impurity levels, especially [Cu], in ZnSe-40H are lower than that in ZnSe-16V. This difference might be the result of the impurity segregation along the axial growth direction since the mapping

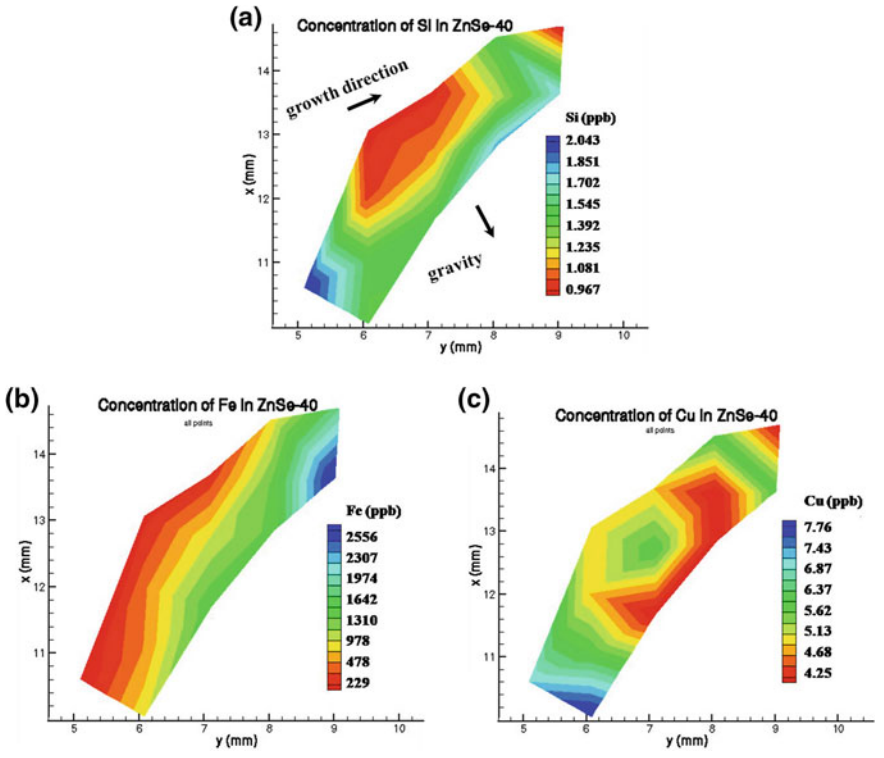

Fig. 6.34 Impurity concentration map generated using the SIMS technique on the ZnSe-40H as-grown facet. **a** Si concentration [Si], **b** Fe concentration [Fe] and **c** Cu concentration [Cu] (taken from Fig. 1 of Ref. [7])

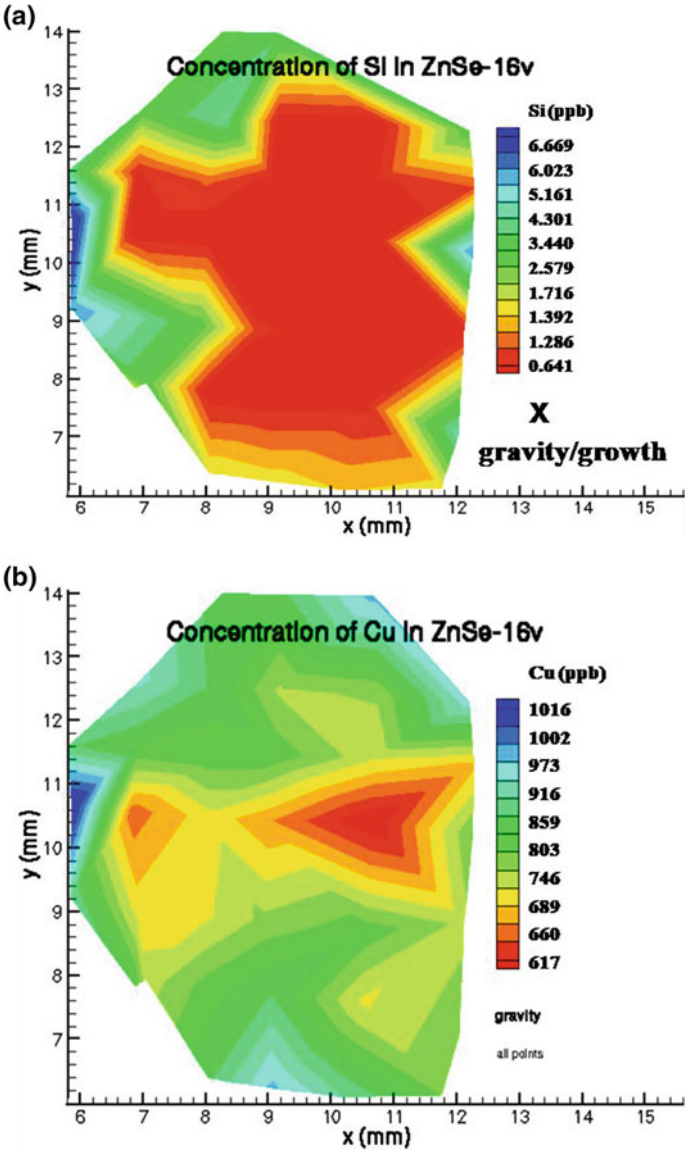

Fig. 6.35 SIMS derived, impurity contour mapping of a ZnSe-16V wafer cut perpendicular to the growth axis at 2.0 cm from the first grown tip. **a** Si concentration, [Si], and **b** Cu concentration [Cu]

on ZnSe-40H covered the area at 1.2–1.7 cm from the first-grown tip whereas the mapping on the ZnSe-16VS wafer was sliced at 2.0 cm from the first grown tip.

6.4.2 Photoluminescence (PL) Spectroscopy

Photoluminescence spectroscopy is mostly used on semiconductors for the identification of shallow level, and sometimes deep level that produce radiative recombination. When light, usually a laser, is directed onto a sample, the material goes through a process of *photo-excitation* which causes electrons to move into certain permissible excited states. When these electrons return to their equilibrium states, the excess energy is released through a radiative recombination process and results in the emission of light (photoluminescence). The energy of the emitted light relates to the difference in energy levels between the two electronic states involved in the transition and presents a signature of the level which can be attributed to certain point defects in the material. The important aspect of PL is that these point defects can include the substitutional impurity as well as the interstitial native elements and even point defects such as vacancy. The quantity of the emitted light is related to the relative contribution of the radiative process, or the quantity of the defects. In this study, the spatial distributions of impurities and point defects were mapped out by the PL measurements [8]. Experimentally, the samples were illuminated with the 364 nm line from a coherent Ar ion laser at a power density of about 0.8 W/cm^2 and a beam size of about 1.5 mm in diameter. The PL spectra were detected by a SPEX 1403 spectrometer with a typical slit width of 200 μm which corresponded to a resolution of 0.32 meV. The samples were maintained between 5 and 10 K, occasionally at 1.4 K, and the spectral data were recorded by a personal computer using SPEX DM3000 software. The intensity ratios between various emissions were calculated by taking the ratios of the integrated areas under the particular emission peaks.

6.4.2.1 PL Measurements on ZnSe Crystals

The surfaces of the PL measurements on ZnSe crystals were either as-grown (110) facet, cleaved (110) plane or wire-sawn surface polishing with Al_2O_3/H_2O solution to 0.3 μm particle size. Figure 6.36 shows a PL spectrum [8] of the Eagle-Picher starting material, ZnSe-SM, the same sample as that used in the GDMS measurements listed in Table 6.1. The spectrum is dominated by the near band edge emission from 2.64 to 2.82 eV, with a very small broad emission from 2.4 to 2.6 eV. Korostelin et al. [9] have assigned a broad green band, ranging from 2.34 to 2.65 eV with a maximum at 2.53 eV, as due to O impurity. By Comparing the O contents in the GDMS results and the corresponding PL spectra in Figs. 6.36 and 6.37 (next paragraph), it is concluded that this band is likely to be caused by O impurity. The near band edge emissions, as given in the inset, have an emission at 2.801 eV, designated as F_x, which is associated

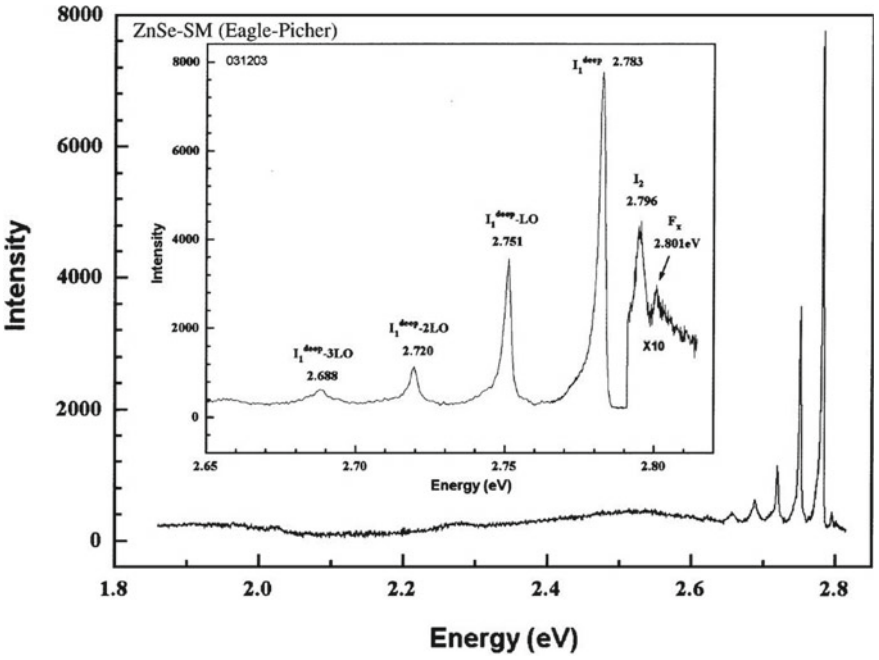

Fig. 6.36 PL spectrum of Eagle-Picher starting material, ZnSe-SM. The near band edge emissions are shown in the inset (taken from Fig.1 of Ref. [8])

with the free exciton [10–12]. The I_2 emission at 2.796 eV has been attributed to the exciton bound to a substitutional neutral donor, such as Al, Ga, In on the Zn site or Cl and F on the Se site [13–16]. The I_1^{deep} emission at 2.783 eV with its LO phonon replicas at energies spaced 32 meV [16] apart has been considered to be associated with the exciton bound to a deep Zn vacancy acceptor [14, 15, 17–20]. Figure 6.37 shows the broad PL spectrum from the GDMS specimen of ZnSe-35. The spectrum is dominated by the near band edge emissions and no deep-level DAP emissions were observed. The disappearance of the small broad emission band between 2.4 and 2.6 eV from the starting material is due to the reduction in O content (from 4000 to 1500 ppb) resulting from the pre-growth heat treatment. The spectrum at the near band edge section is also given in the figure. From the GDMS results on this sample the possible donor concentrations measured were: [Al] 1700 ppb, [Ga] 30 ppb, [Cl] 9 ppb, [In] 4 ppb and [F] below the detection limit of 5 ppb. Therefore, it was concluded that Al is the most likely donor associated with the I_2 emission in our grown crystals. The free exciton emission, F_x, is an intrinsic property of the samples. The strength of the emission of F_x is an indication of good crystalline quality and the emissions of F_x, I_2, and I_1^{deep} and their LO phonon replicas were observed in most of the grown crystals. The intensity ratio of a specific emission to that of the free exciton emission has been adopted by the Si industry [21] and by other research on the PVT grown ZnSe crystals [22] as a measurement of the defect concentration

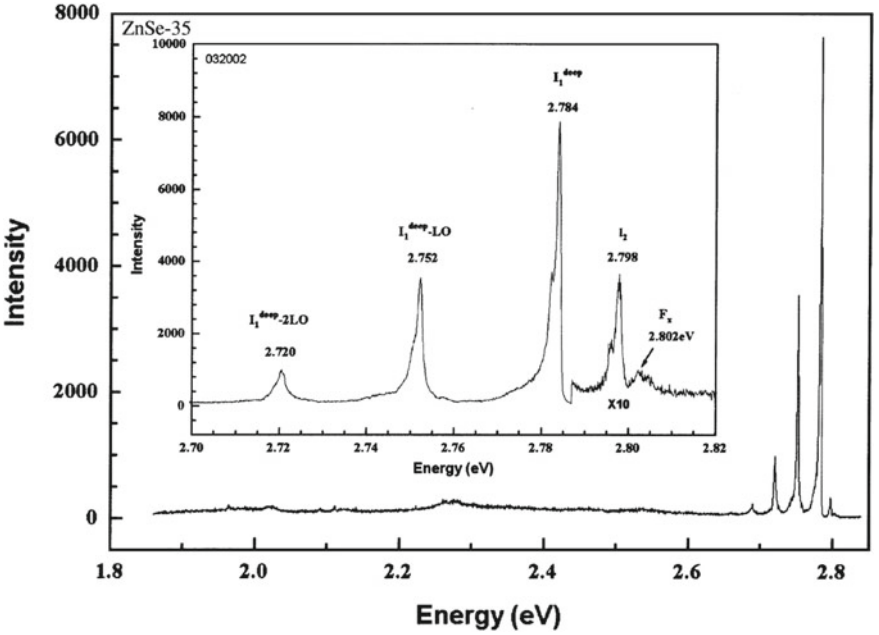

Fig. 6.37 PL spectrum of ZnSe-35, grown from Eagle-Picher starting material. The near band edge emissions are shown in the inset (taken from Fig. 2 of Ref. [8])

associated with that emission. The integrated area ratio of I_2 to F_x, $A(I_2)/A(F_x)$, was 3.172 for the starting material shown in Fig. 6.36 which had a total possible donor (Al, Ga, Cl, In and F) concentration of 13 ppb from the GDMS measurements. As shown in Fig. 6.37 this ratio increased to 4.88 in the grown crystal, ZnSe-35, which had a total donor concentration of about 1750 ppb, or 7.46×10^{16} cm^{-3}. On the other hand, the concentration of Zn vacancy, $[V_{Zn}]$, decreased as implied from the measured value of $A(I_1^{deep})/A(F_x) = 136.8$ in the starting material to 81.7 in the grown crystal. Using the intensity ratio mappings of various PL emissions, the effects of Earth gravity vector orientation on the distribution of point defects, [Al], [Li or Na] and $[V_{Zn}]$, were observed in the ZnSe samples grown by PVT under horizontal and vertical (stabilized and destabilized) configurations [7]. It should be noted that the ratios given above for ZnSe-35 were the values measured at a single point whereas in the GDMS measurements the average impurity concentration in a large volume (~20 mm^3) was determined.

For the measurements of PL mapping, two other samples were wafers sliced from two ZnSe grown boules for the impurity distribution mapping. One sample was sliced axially from the as-grown facet on the side of the crystal, ZnSe-40H, grown horizontally with no contact between the crystal and the ampoule wall. The other sample was sliced perpendicularly to the growth direction from the ZnSe-16V crystal grown in the vertical stabilized configuration. Except for the as-grown ZnSe-40H facet surface the other three samples were polished with diamond paste to 0.1 μm

particle size. Figure 6.38 shows the PL emission spectrum from 1.85 to 2.85 eV of the as-grown face of ZnSe-40H, the same face as shown in Fig. 6.34 for SIMS measurements. Figure 6.39 shows the near band edge emissions of the same spectrum which consists of: (1) F_x at 2.802 eV: free exciton, (2) I_2 at 2.798 eV: exciton bound to substitutional neutral donor (Al, Ga and In on the Zn site and Cl and F on the Se site) (3) I_1^{deep} at 2.783 eV: exciton bound to deep acceptor (Zn vacancy, V_{Zn}), (4) I_V^0 at 2.772 eV: Se vacancy (V_{Se}) or complex involving V_{Se} [13, 23, 24], (5) Ag_1^0 at 2.747 (2.745) eV: neutral Ga_{Zn}–Ag_{Zn} associate [25, 26] as well as LO phonon replicas of I_1^{deep} at 32 meV energy intervals and LO phonon and Stokes phonon replicas of Ag_1^0. An emission of $I_1^{x,y}$ at 2.792 eV was observed occasionally in some ZnSe crystals which was attributed to exciton bound to neutral Li or Na acceptors [12, 18, 25, 27].

To study the correlation between the stoichiometry (through I_1^{deep} peak) and the partial pressure of Zn during crystal growth, a 2 mm thick ZnSe crystal was annealed for 5 h inside two layers of evacuated fused silica coaxial ampoules (to prevent contamination from the furnace) which was placed inside a two zone furnace. The crystal was positioned in the hot zone at 1104 °C and pure elemental Zn was at the cold zone of 556 °C. The partial pressure of Zn inside the ampoule was such that the crystal was in equilibrium with a condition corresponding to $P_{Zn} = 6.1 \times 10^{-3}$ atm or $\alpha = P_{Zn}/P_{Se2} = 6.05$. Figure 6.40 shows the near band edge PL emissions of the crystal before and after the annealing. The intensity ratios, $A(I_1^{deep})/A(F_x) = 64.5$ and $A(I_2)/A(F_x) = 0.58$ before annealing and $A(I_1^{deep})/A(F_x) = 7.52$ and $A(I_2)/A(F_x) = 2.10$ after annealing imply that (1) I_1^{deep} emission is related to the exciton bound to the

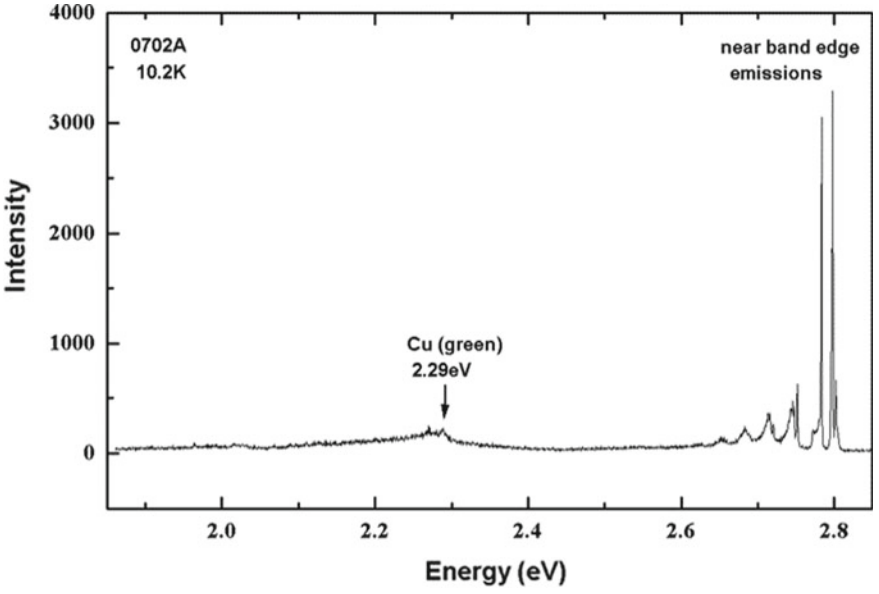

Fig. 6.38 PL emission spectrum of the as-grown facet of ZnSe-40H from 1.85 to 2.85 eV

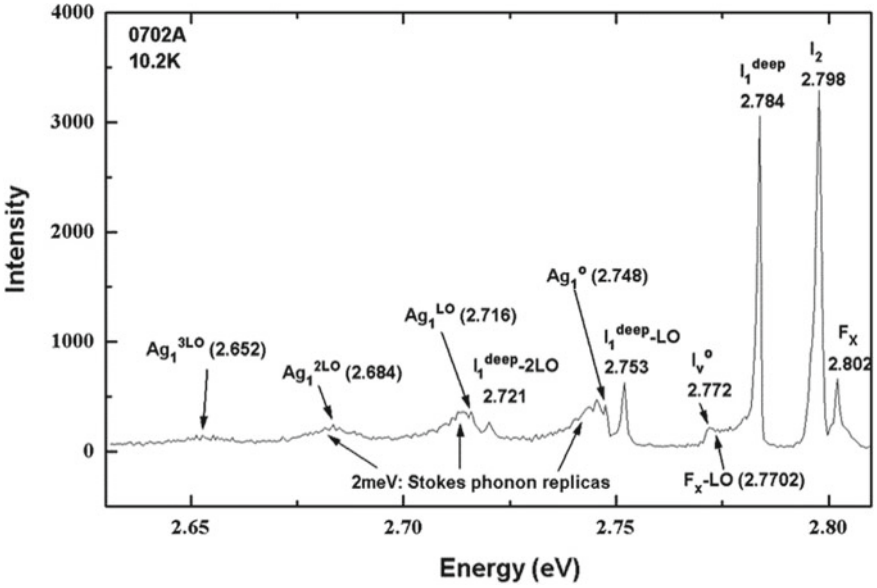

Fig. 6.39 Near band edge emissions of the PL spectrum for ZnSe-40H. See text for descriptions of the peaks and features in the figure

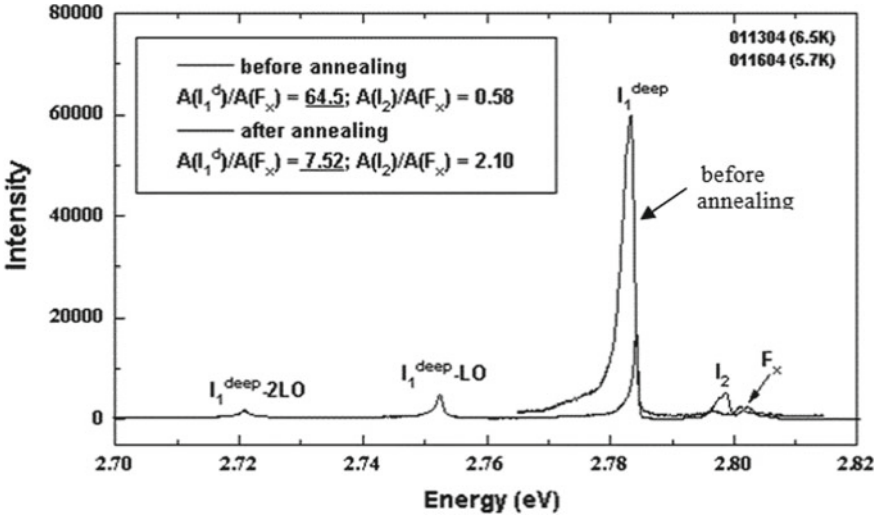

Fig. 6.40 Near band edge PL emissions for the ZnSe crystal before and after the annealing in Zn over pressure (taken from Fig. 4 of Ref. [6])

Zn vacancy acceptor and (2) the increase in I_2, presumably from Al contamination, originated from the fused silica ampoule wall. A second Zn vapor annealing was performed. The crystal was also annealed at 1104 °C and the Zn reservoir was at 575 °C. The Zn partial pressure in this case was 9.0×10^{-3} atm or $\alpha = 19.43$. The intensity ratio $A(I_1^{deep})/A(F_x)$ after annealing was 5.18. The reaction during Zn vapor annealing can be described as:

$$Zn_{Zn} \rightarrow V_{Zn} + Zn(g) \tag{6.43}$$

and the equilibrium constant for the reaction

$$K = [V_{Zn}] \times P_{Zn} = K_1 \times A(I_1^{deep})/A(F_x) \times P_{Zn} \tag{6.44}$$

At 1104 °C, the measured $A(I_1^{deep})/A(F_x) \times P_{Zn} = 0.0459$ atm and 0.0466 atm, respectively, for these two annealing studies. As shown in Fig. 6.41, the two annealing experiments agreed well with the equilibrium constant $K/K_1 = 0.04624$ at 1104 °C. The significance of the result is that the local Zn pressure in equilibrium with the crystal during the growth can be derived from the measured $A(I_1^{deep})/A(F_x)$.

PL mapping was performed on various ZnSe crystals by taking 20 to 90 PL spectra over the sample surface to study the impurities and V_{Zn} distribution on the surface

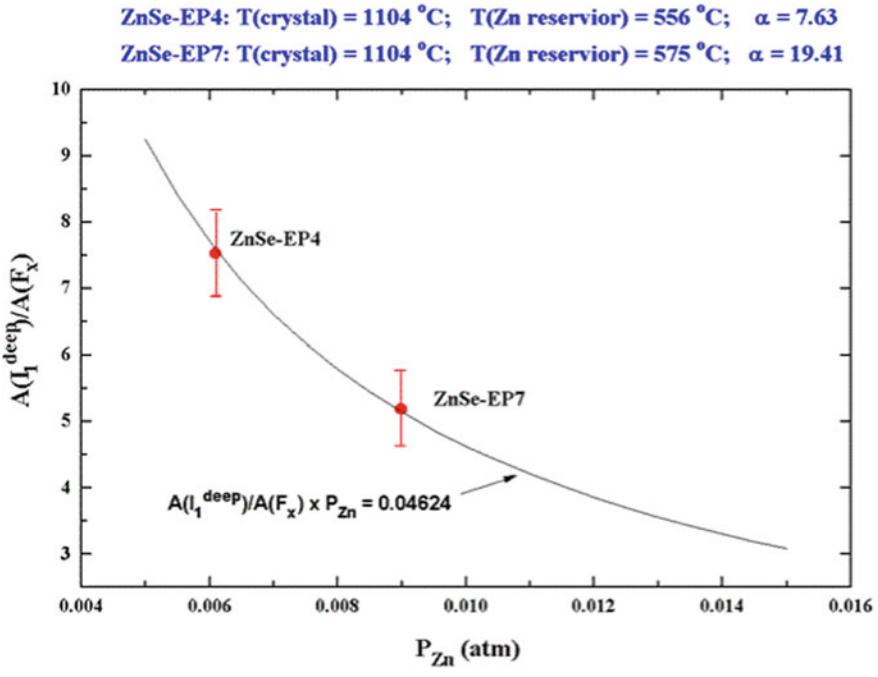

Fig. 6.41 Effects of Zn vapor annealing on $A(I_1^{deep})/A(F_x)$

and the results are summarized below. Figure 6.42a shows the $A(I_2)/A(F_x)$ contour map on the as-grown facet of the horizontally grown ZnSe-40H relative to the gravity direction and growth direction. The map indicates that Al impurity concentration, [Al], segregates radially slightly toward the top and axially toward the first grown region. Figure 6.42b shows the $A(I_1^d)/A(F_x)$ contour map on the same surface. The equilibrium local Zn pressure during the growth is also given in the figure. The map implies that $[V_{Zn}]$ segregates radially toward the bottom and axially toward the last grown region. PL mapping was also performed on a polished horizontally grown ZnSe-15H wafer cut perpendicular to the growth direction. Figure 6.43a, b show the contour maps of $A(I_2)/A(F_x)$ and $A(I_1^d)/A(F_x)$ on the wafer. Trends in the [Al] and $[V_{Zn}]$ segregation similar to ZnSe-40H were observed. Figure 6.44 shows the near band edge emission spectrum of the as grown surface of a seeded vertically (stabilized) grown ZnSe crystal, same as the one shown earlier for the SIMS measurements, ZnSe-16V. Besides the F_x, I_2 and I_1^d emissions, the emission of $I_1^{x,y}$ at 2.792 eV was attributed to the exciton bound to neutral Li or Na. Figure 6.45a, b, c show the contour mappings of $A(I_2)/A(F_x)$, $A(I_1^{x,y})/A(F_x)$ and $A(I_1^d)/A(F_x)$. These

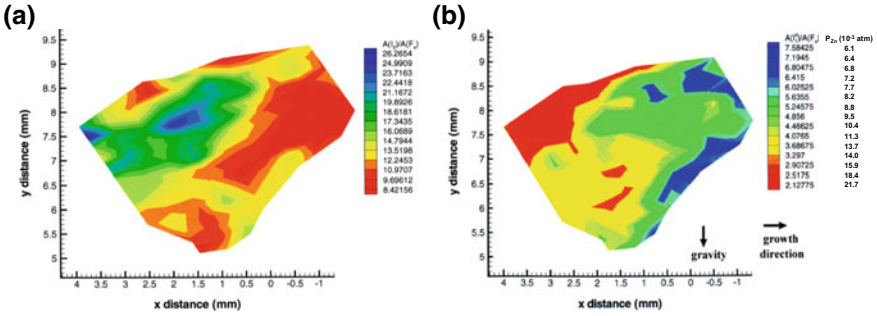

Fig. 6.42 PL contour map of ZnSe-40H as-grown facet, **a** $A(I_2)/A(F_x)$ and **b** $A(I_1^d)/A(F_x)$ (taken from Fig. 5 of Ref. [6])

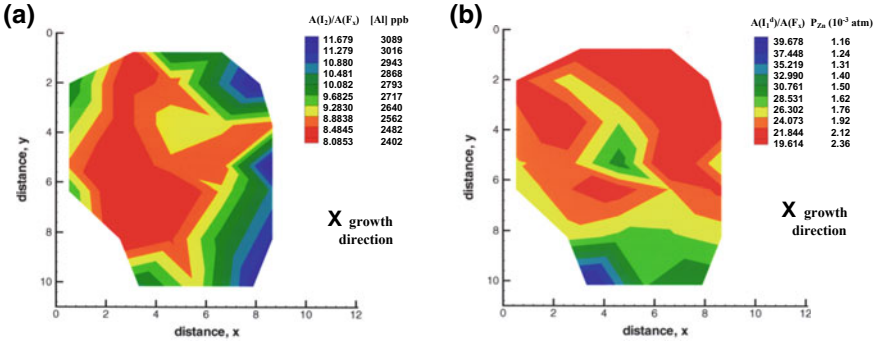

Fig. 6.43 PL contour maps of **a** $A(I_2)/A(F_x)$ and **b** $A(I_1^d)/A(F_x)$ on the ZnSe-15H wafer cut perpendicular to the growth direction (taken from Fig. 6 of Ref. [6])

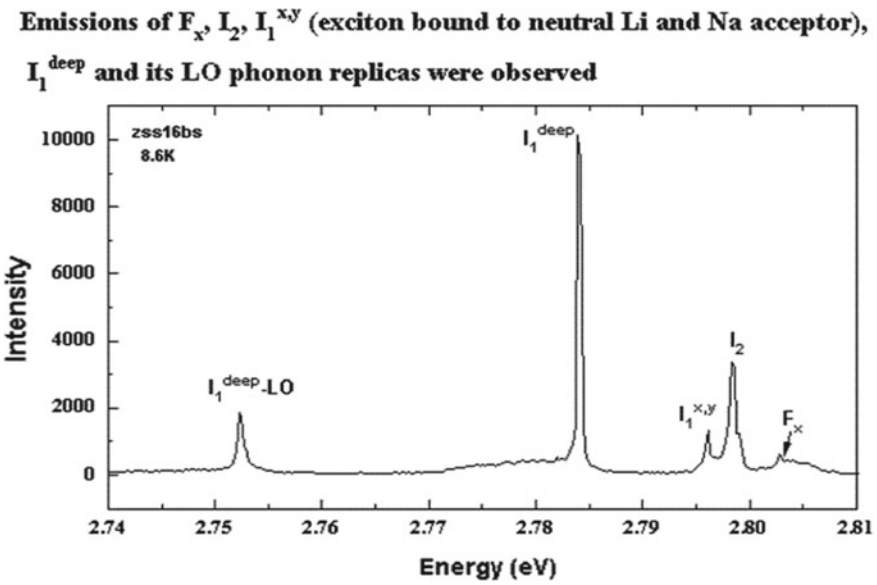

Fig. 6.44 Near band edge PL emission spectrum of the as-grown surface of the seeded vertically (stabilized) grown crystal of ZnSe-16V (taken from Fig. 7 of Ref. [6])

mappings indicate that [Al], [Li] or [Na] and [V_{Zn}] segregate radially toward the center. Figure 6.46a, b show the contour mapping of $A(I_2)/A(F_x)$, and $A(I_1^d)/A(Fx)$ on the as-grown surface of an self-seeded vertically (destabilized) grown ZnSe crystal, ZnSe-31V. The implication from the mappings is that [Al] and [V_{Zn}] segregate without an apparent pattern.

One possible explanation for the distribution in the horizontally grown ZnSe crystals is that the Al atom is less dense than the Zn atom and Se_2 species. Thus, radially, P_{Al} was higher toward the top of the ampoule due to the buoyancy force. This resulted in higher [Al] toward the top. At the same time, the Zn atom is 2.4 times less dense than Se_2, hence, radially, P_{Zn} was higher toward the top of the ampoule and resulted in higher [V_{Zn}] toward the bottom.

6.4.2.2 PL and IR Absorption Measurements on ZnTe Crystals

The data of photoluminescence spectrum, recorded on the ZnTe wafer, is shown in Fig. 6.47. In contrast to the PL of ZnSe described above, the PL spectrum of ZnTe looks very clean with the free exciton (light hole to conduction band) peak at 2.375 eV and its LO phonon replica at an interval of 26 meV. The high purity of the samples was also studied by low temperature infrared absorption measurements [28, 29]. The sample was cooled to 4.6 K and the measurements were recorded with a resolution of 0.25 cm^{-1}. As given in Fig. 6.47b, the optical absorption of PVT sample shows

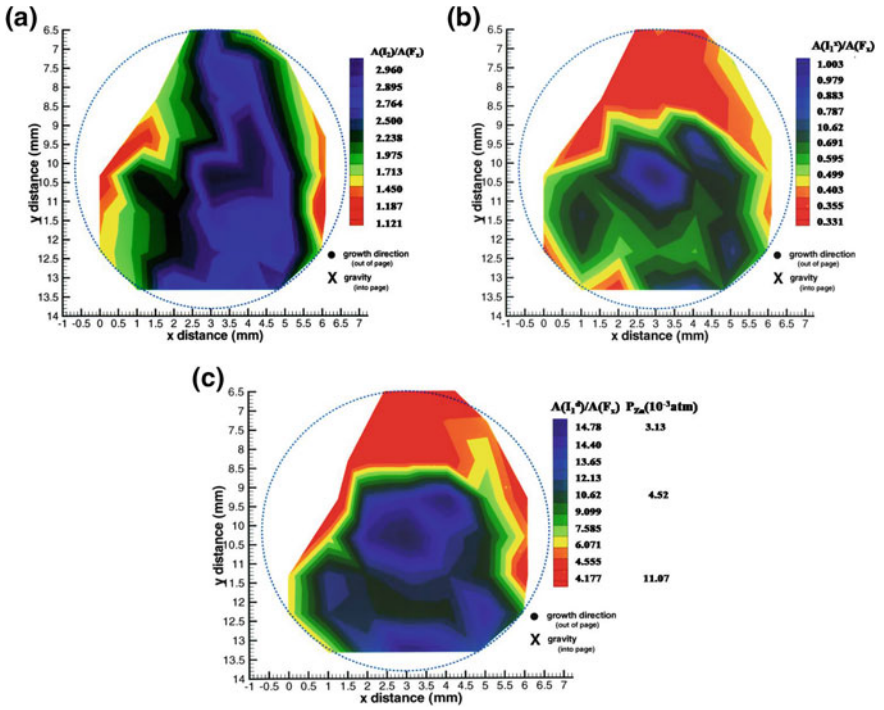

Fig. 6.45 PL contour mappings of **a** $A(I_2)/A(F_x)$, **b** $A(I_1^{x,y})/A(F_x)$ and **c** $A(I_1^d)/A(F_x)$ on the as-grown surface of the seeded vertically (stabilized) grown ZnSe-16V crystal. The partial pressure of Zn in equilibrium with the crystal surface during growth has also been derived as shown in **c**. (take from Fig. 8 of Ref. [6])

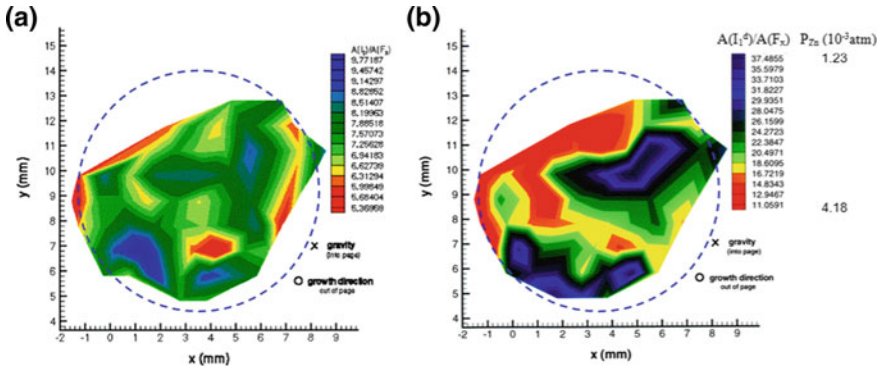

Fig. 6.46 PL contour mapping of **a** $A(I_2)/A(F_x)$, and **b** $A(I_1^d)/A(F_x)$ on the as-grown surface of the self-seeded vertically (destabilized) grown ZnSe-31V crystal (taken from Fig. 9 of Ref. [6])

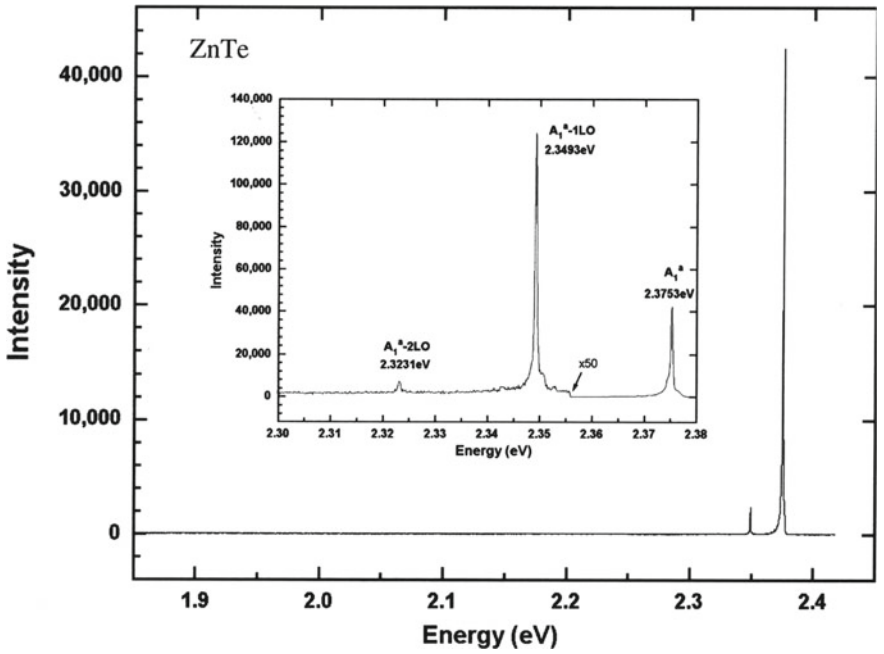

Fig. 6.47 Low temperature photoluminescence (PL) spectrum of ZnTe grown by PVT

a smooth line without any noticeable peaks. The IR absorption of another ZnTe sample, grown in-house by the travelling heater method (THM), was also measured as shown in Fig. 6.48a. A set of irregularly-spaced absorption peaks was observed between 1069 and 1200 cm^{-1}, and were repeated at intervals of 210 cm^{-1}, which corresponds to the 26 meV, i.e., the LO phonon energy discussed above. The peaks were identified to be related to Cu impurity by the following experiment of Cu doping by thermal diffusion. A disc was sliced from a ZnTe crystal grown by PVT and, after depositing a thin film of Cu, the sample was annealed in Te atmosphere at 250 °C for 1 h. The IR absorption spectrum of the sample is shown in Fig. 6.48c. After comparing the spectra of Fig. 6.48a, c, it is clear that the absorption peaks in THM sample can be attributed to Cu impurity. A detailed analysis [29] suggests that the irregular spacing of the absorption peaks is caused by a dynamic Jahn-Teller interaction acting on the excited 2E state and a linear Jahn-Teller coupling between an orbital doublet and a 2-fold vibrational model was able to accurately account for the irregular spacing. Since the starting materials for THM and PVT techniques were the same, i.e., 99.9999% grade Zn and Te elements provided by Cominco American (now Johnson Matthey), the purification characteristics of PVT technique through the sublimation-condensation process is evident.

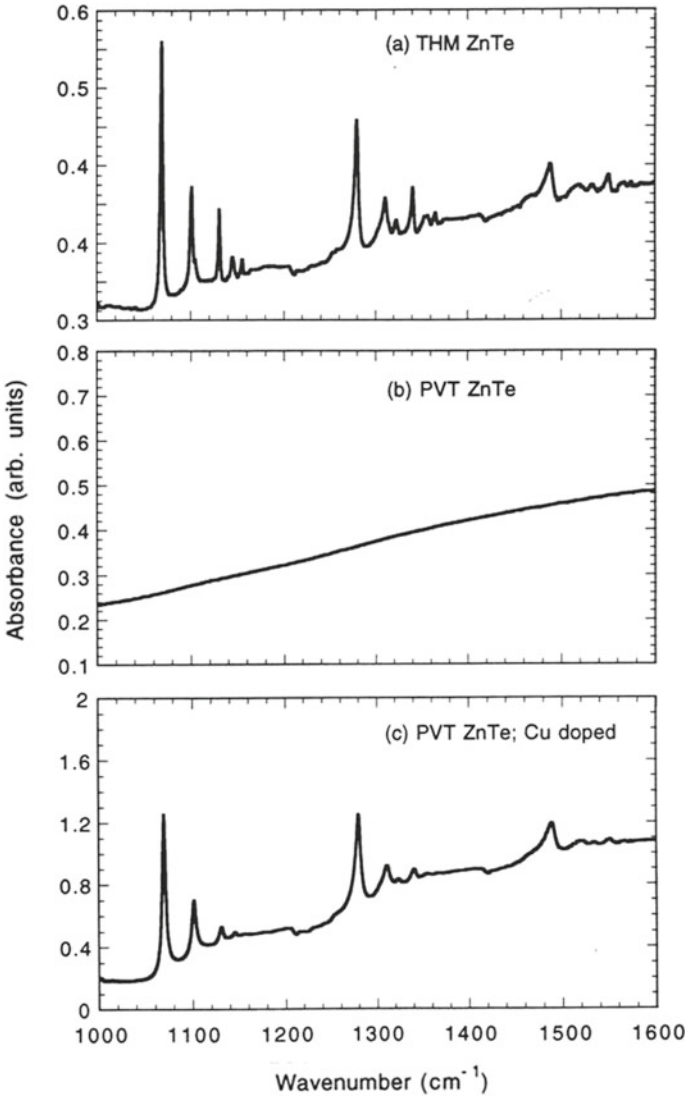

Fig. 6.48 Infrared absorption spectra at 4.6 K for ZnTe crystals **a** grown by THM, **b** grown by PVT, and **c** grown by PVT and then doped with Cu by thermal diffusion (taken from Fig. 3 in Ref. [29])

6.4.2.3 PL Measurements on CdTe Crystals

The low temperature (11 K) PL spectrum of CdTe-10, shown in Fig. 6.49, is a typical result for most of CdTe crystals grown by regular PVT [6]. The spectrum has dominant bound exciton peaks that consist of a weak emission of the free exciton

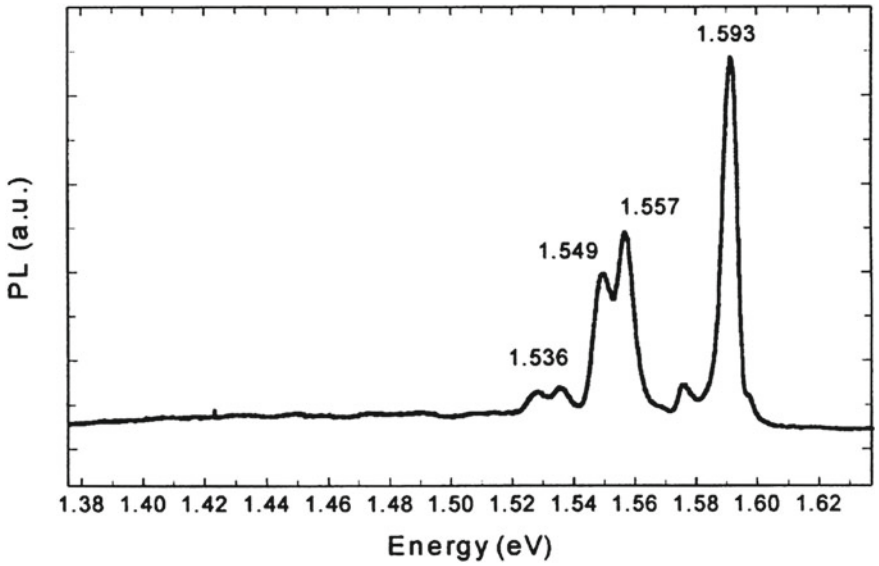

Fig. 6.49 Low temperature (11 K) PL spectrum showing bound exciton (D_o,X) peak for CdTe-10 sample (taken from Fig. 3 in Ref. [6])

at 1.598 eV and a shallow donor peak (D_o,X) at 1.593 eV. It has been reported [30] that the (D_o,X) line mainly originates from Cl_{Te} (Cl substituting Te site). However, the results of Spark Source Mass Spectroscopy (SSMS) analysis indicate the Cl content is less than 0.01 ppm in the crystal. Indium is the other possible donor with an appreciated amount, i.e., 1 ppm from the SSMS analyses. The origins of other two peaks at 1.557 and 1.549 eV with their LO phonon replicas are not clear. The peaks in this region have been previously observed in As and Sb-doped CdTe crystals [31], and were assigned as peaks due to electron-acceptor (e-A^o) recombination and a shallow donor-acceptor pair (DAP) recombination, respectively. In this case, the presence of an appreciable amount of In as an impurity in the CdTe might have led to the occurrence of these peaks. No deep level donor-acceptor-pair (DAP) lines around 1.45 eV were observed.

The PL spectrum of another crystal, CdTe-22, which was grown in the BN coated ampoule, was measured for comparison. The BN coating inside the ampoule wall was accomplished by high-temperature treatment of BN powder which resulted in the fusion of BN to the silica tubing. The empty ampoule was cleaned and loaded with high-purity grade BN powder supplied by Union Carbide, Inc. Radially uniform heating was applied using a hydrogen-oxygen torch on the ampoule which was mounted on a glass blowing lathe. After 10–20 min under white flame the ampoule was cooled and the excess BN powder was removed with distilled water. A uniform foggy appearance on the inside wall of the ampoule was visible. After heating the ampoule again by the torch, the hazy appearance disappeared and a green emission could be seen from the ampoule inner wall under the heat of the torch. The measured

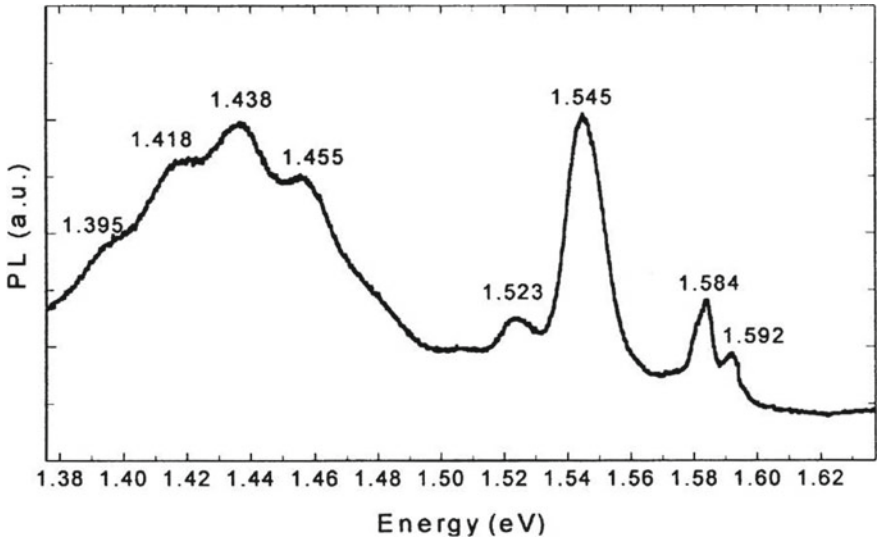

Fig. 6.50 Low temperature (11 K) PL spectrum showing bound acceptor peak due to boron doping for CdTe-22 sample (taken from Fig. 4 in Ref. [6])

spectrum for CdTe-22 is shown in Fig. 6.50. The (D_o,X) line is observed at 1.592 eV. It was a common feature to observe peaks near 1.584 eV in high-resistivity CdTe crystals doped with group III elements, such as 1.584 [32] and 1.585 [33] eV for Ga and similar lines for In and Al-doped CdTe. [34]. The line at 1.584 eV in Fig. 6.50 is therefore assumed to be caused by the unintentional doping of boron from the BN coating of the ampoule. There is a strong emission line at 1.545 eV followed by its phonon replica at 1.523 eV. It is believed that this peak is due to a DAP recombination. The peak at 1.545 eV is due to an impurity or dopant, and in this case the diffused boron enhances the intensity of the emission. At lower energy the DAP emission at 1.455 eV and its phonon replicas (DAP-1LO, DAP-2LO and DAP-3LO) were observed. Similar DAP emission bands were also observed in Ga- [32], In- [34] and Al-doped [35] CdTe crystals.

6.5 Impurity and Dopant Analyses on ZnSe Crystals by Glow Discharge Mass Spectroscopy (GDMS)

The impurity analyses were performed by GDMS on the crystal of ZnSe-48VS, grown by vertical stabilized PVT and three horizontal grown crystals of un-doped ZnSe, Cr-doped ZnSe and Fe-doped ZnSe. The contents of 70 elements were reported and only those impurity elements with concentration higher than 0.5 ppm (atomic) are presented here in Table 6.2. The analyses give the effects of different vendors of

Table 6.2 The source materials, contents of impurity elements in two ZnSe crystals, one Cr-doped and one Fe-doped ZnSe. The unit is in ppm (wt.)

Element	ZnSe-48VS[#1] 2.0 cm	ZnSe-F2[#2] 1.7 cm	Cr-ZnSe #1[#3] 1.6 cm	Fe-ZnSe #3[#4] 1.5 cm
Na	0.19	0.14	2.7	0.69
Mg	0.03	0.07	2.8	0.21
Al	0.41	0.82	2.4	3
Si	2.1	5.3	5.9	0.77
P	0.12	0.1	0.45	0.04
S	0.41	4.6	5.4	1.5
Cl	0.49	0.4	0.95	0.72
Ca	<0.5	<0.5	20	<0.5
Cr	0.008	<0.005	15	<0.005
Fe	0.25	0.06	0.8	7.1
Ni	0.01	0.14	0.38	0.16
Cu	1.7	0.33	1	1.2
Pb	5.6	12	29	0.97

Starting materials: [#1] Furukawa Co. Ltd. 99,9999%; [#2] Alfar Aesar 99.999%; [#3] source #1 + CrSe powder 99.5% from Alfa Aesar; [#4] source #1 + FeSe powder 99.9% from Alfa Aesar

source materials on the impurity contents in the grown crystals. On the growths of ZnSe crystals, 99.9999% purity of ZnSe from Furukawa Co. results in lower contents of Al, Si, S, Ni and Pb than 99.999% from Alfar Aesar but higher in the contents of Fe and Cu. The CrSe introduced impurities of Na, Mg, Al, Ca and Pb whereas FeSe introduced some extra Al content but actually reduced the contents of Si and Pb. The contents of Cr and Fe of 15 and 7.1 ppm (wt.) in Cr-ZnSe #1 and Fe-ZnSe #3 correspond to the dopant concentrations of 9.2×10^{17} cm^{-3} and 4.0×10^{17} cm^{-3}, respectively. Also, comparing these contents with the compositions of the starting materials, $(Zn_{0.987}Cr_{0.013})Se$ and $(Zn_{0.980}\ Fe_{0.020})Se$ in Cr-ZnSe #1and Fe-ZnSe #3, the dopant segregation coefficients for the vapor growth, defined as x_C/x_S (x_C and x_S are the doapnt concentrations in the crystal and source, respectively), are 3.2×10^{-3} and 9.3×10^{-4} for Cr and Fe, respectively.

6.6 Dopant Levels in Cr-Doped ZnSe Crystals Measured by Optical Absorption

The Cr concentration, [Cr], in the grown Cr doped crystals was determined by the optical absorption coefficient, α, at 5650 cm^{-1}, or 1770 nm wavelength [36, 37]. A linear relation between the absorption coefficient and [Cr] was established by Vallin et al. [38] as

$$\alpha\left(\mathrm{cm}^{-1}\right) = 11.4 \times 10^{-19}[Cr]\left(\frac{\mathrm{atom}}{\mathrm{cm}^{-3}}\right) \tag{45}$$

The [Cr] contents were determined in two wafers cut perpendicular to the growth axis, one from the horizontally grown ZnSe-36H, 1.13 cm from the first grown tip and the other from the vertically stabilized grown ZnSe-38VS, 1.10 cm from the first grown tip. The values of α, determined from the measured transmission and reflectance, were 13.4 and 80.6 cm^{-1}, respectively, for the ZnSe-36H and ZnSe-38VS wafers. The [Cr] contents and the segregation coefficients were calculated to be 1.2×10^{19} cm^{-3} and 0.015, respectively for the ZnSe-36H wafer and 7.1×10^{19} cm^{-3} and 0.085, respectively, for the ZnSe-38VS wafer. The values of the Cr contents and segregation coefficient are much higher than those values determined from the GDMS results, described in the last section, could becaused by the errors by the activations of defects during the absorption measurements.

6.7 Characterizations of ZnSeTe Crystals

In addition to the regular characterization methods described above, the compositional distribution of the ternary as-grown crystals of $ZnSe_{1-x}Te_x$ is an important issue which needs to be studied by different characterization techniques [39]. To determine the axial growth direction Laue X-ray diffraction patterns were taken on the cleaved surfaces near the first-grown region as well as across the as-grown surfaces of the grown boules. The boules were then sliced perpendicular to the growth direction by wire saw and the axial composition variation was determined from the precision density measurements on the sliced wafers. The errors in other slices were estimated to be about 4×10^{-5} $\mathrm{g/cm}^3$. The wafers were then polished by a Al_2O_3/H_2O solution to a particle size of 0.05 μm. The radial compositional variations across the wafers were determined from wavelength dispersive X-ray spectroscopy (WDS) using a JEOL JXA-8900R as well as from optical transmission mapping across the wafers using a Mattson Instruments Sirius spectrometer.

6.7.1 Compositional Variation by Wavelength Dispersive X-ray Spectroscopy (WDS)

During the WDS measurements a ZnSe single crystal was used as the standards for Zn and Se while a ZnTe single crystal was used as the standard for Te. The typical error in WDS was estimated to be 0.4% of the measured value for x, the mole fraction of ZnTe. Two wafers were polished to a thickness of about 1.3 mm for the optical transmission mapping. The spot size of the beam was 400 μm in diameter and a step size of 1 mm was used. A total of 117 spectra were taken on the ZST-1V wafer

(diameter 12 mm) sliced at 1.83 cm from the first-grown tip and a total of 76 spectra on the ZST-2H 1.43 cm wafer (diameter 10 mm).

The WDS measurements were performed on polished surfaces cut perpendicularly to the axial growth direction. The data were taken on each wafer along two diameters perpendicular to each other. Figure 6.51 shows some of the typical WDS results on the vertically grown wafers sliced from the ZST-6V, -1V and -5V crystals. The ZnTe content across each wafer was quite uniform which was also the case for other WDS results on the two horizontally grown crystals ZST-7H and -2H as illustrated in Fig. 6.52.

The WDS results on the other horizontally grown crystal, ZST-3H, are shown in Fig. 6.53. On the wafer surfaces at 1.4 and 1.6 cm from the first-grown tip, as shown in Fig. 6.53a, b, the WDS results indicate a core with uniform ZnTe contents, about 0.38, surrounded by a thin region of high ZnTe content of $x = 0.8$. In Fig. 6.53c, the WDS results on the ZST-3H 2.0 cm wafer show a rather uniform ZnTe content across the wafer with a slightly radial segregation, i.e. a higher ZnTe content, 0.40 at the center to a value of 0.37 at the edge. The ZnTe-rich rings on the ZST-3H wafers were confirmed by the SEM back scattering electron images and Fig. 6.54 shows the image on the 1.4 cm wafer. Due to the large difference in ZnTe content, the back scattering image shows a sharp contrast between the ZnTe-rich ring and the core area. The wire saw mark at the edge indicates the top of the boule in the gravity orientation. The

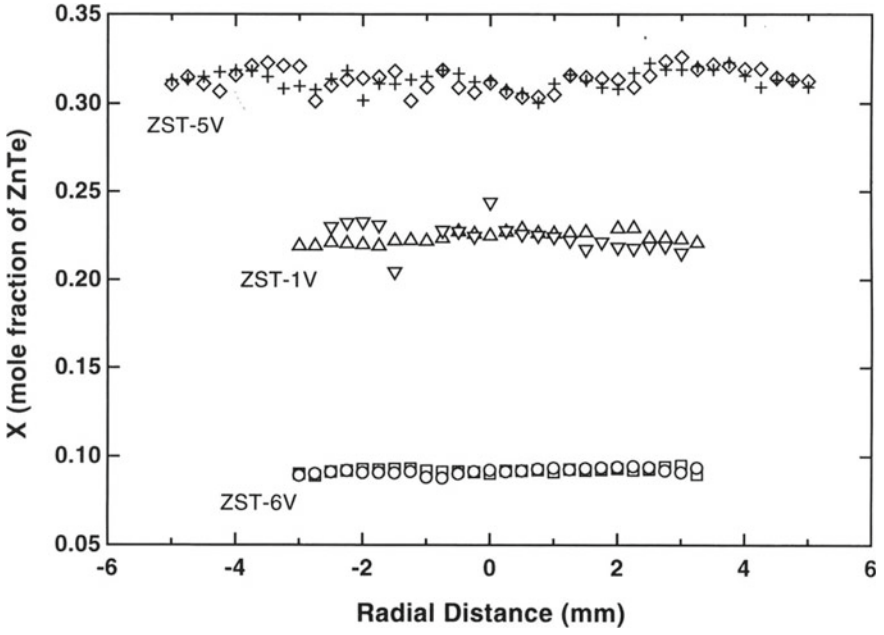

Fig. 6.51 The WDS results on the ZST-6V 1.3 cm, ZST-1V 0.8 cm and ZST-5V 1.9 cm surfaces. Two different data symbols for each wafer were taken along two perpendicular diameters (taken from Fig. 2 of Ref. [39])

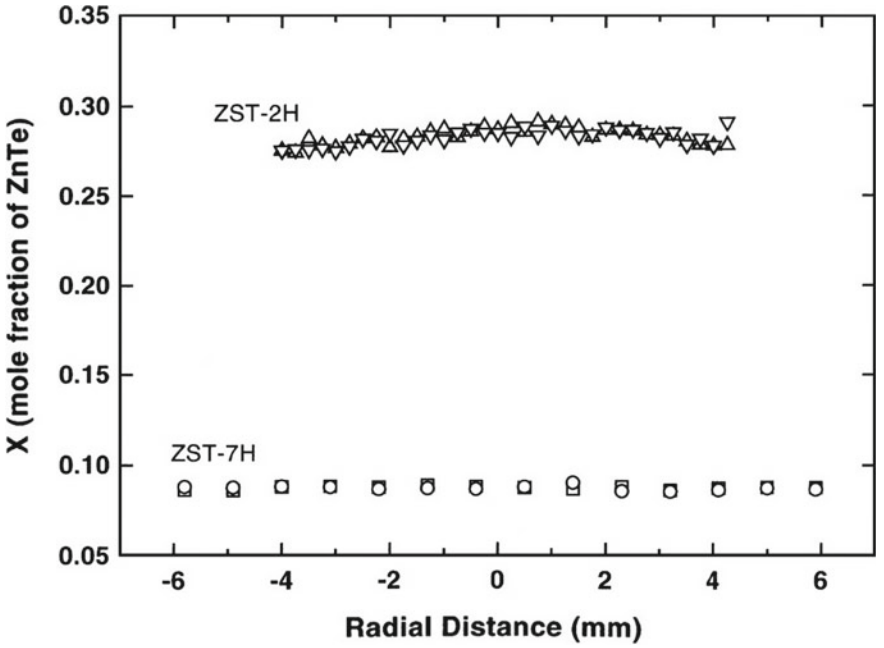

Fig. 6.52 The WDS results on the ZST-7H 2.6 cm and ZST-2H 1.35 cm surfaces. Two different data symbols for each wafer were taken along two perpendicular diameters with one of them parallel to the gravity orientation (taken from Fig. 3 of Ref. [39])

ZnTe-poor core region is positioned a little towards the bottom of the crystal which is also evidenced in Fig. 6.53a. Using back scattering electron imaging the ZnTe-rich ring feature was observed on all the ZST-3H wafers. As the imaging surface moved toward the last grown region of the boule, the thickness of the ZnTe-rich ring became smaller. In fact, it was so thin on the 2.0 cm surface that the WDS data in Fig. 6.53c did not reveal the characteristics of the ZnTe-rich ring although it was observed in the back scattering image. From the fact that this ZnTe-rich ring was not observed in the vertically grown ZST-5V crystal it was speculated that buoyancy-driven convection might have played a role. During PVT growth under horizontal configuration the density difference in the predominant transported species of Zn atom (atomic weight 65.37), Se_2 molecule (molecular weight 157.92) and Te_2 molecule (255.2) caused density gradient driven convection in the vapor phase. This convection resulted in compositional nonuniformity in the vapor phase adjacent to the growing surface and caused compositional nonuniformity in the grown crystal. It was not clear how this convective effect resulted in such a sharp change in crystal composition, from $x =$ 0.8 to 0.4 in a distance of about 200 μm, and why a similar feature was not observed in the other two horizontally grown ZST-7H and -2H crystals. It should be noted that

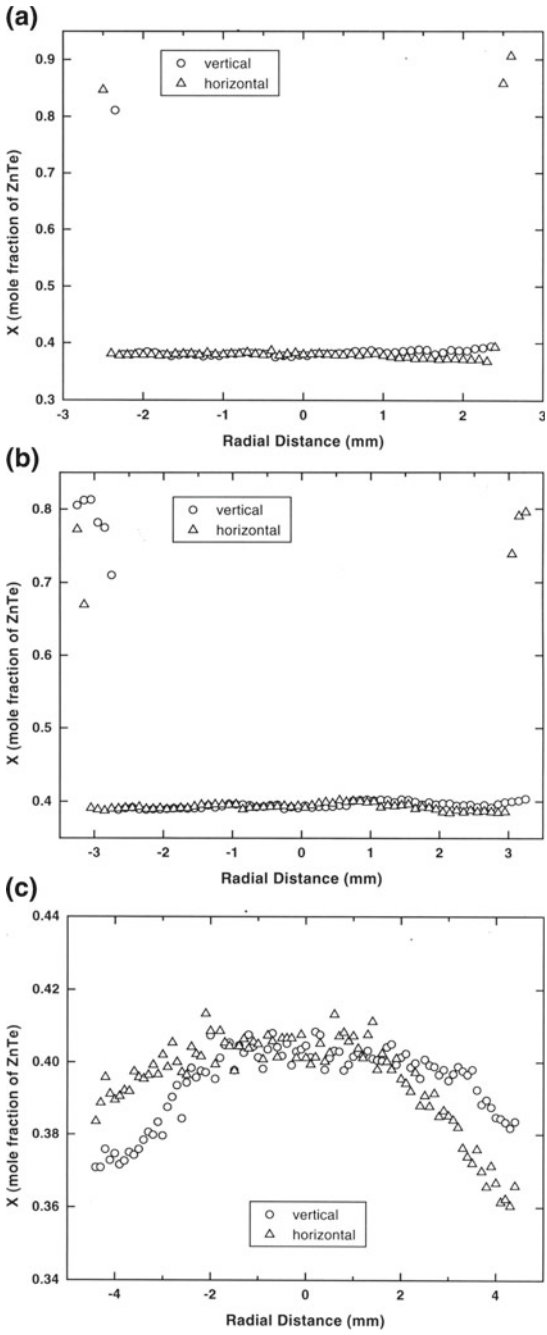

Fig. 6.53 The WDS results on **a** the ZST-3H 1.4 cm, **b** ZST-3H 1.6 cm and **c** ZST-3H 2.0 cm surfaces. Two different symbols show data taken along the diameters parallel (vertical) and perpendicular (horizontal) to the gravity orientation

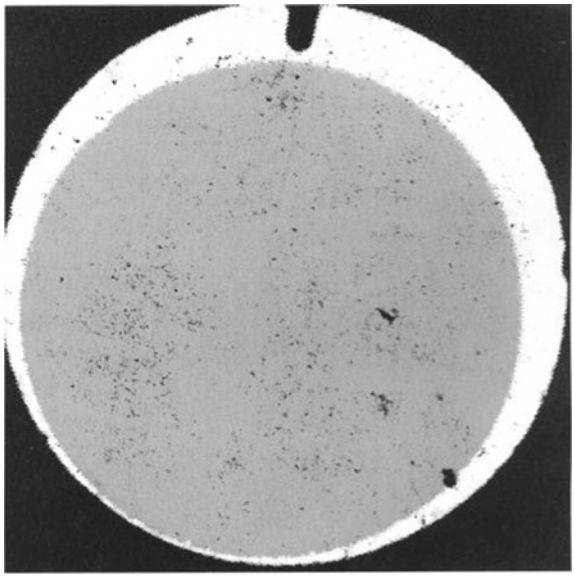

Fig. 6.54 The SEM back scattering electron image on the ZST-3H 1.4 cm surface. The wire saw mark at the top indicates the top of the gravity orientation during growth (taken from Fig. 5 of Ref. [39])

the source material composition for ZST-3H, -7H and -2H was, respectively, $x = 0.30, 0.10$ and 0.20 and, therefore, differences in the vapor composition are expected for these runs. As discussed earlier, the effects of earth gravity vector orientation on the distributions of point defects have been observed in ZnSe samples grown by PVT under horizontal and vertical (stabilized and destabilized) configurations [6].

The axial compositional data for ZST-6V and -7H, determining by taking the average of the WDS results on the surfaces of the wafers, are shown in Fig. 6.55. The measured compositions, x, for both crystals were within 0.090 ± 0.0025 except at the data point 0.5 cm from the tip of ZST-7H. From the results of a one-dimensional diffusion analysis on the mass flux of the ZnSeTe PVT system [40], the composition of condensation, x_C, was mainly determined by the parameter $\alpha = P_{Zn}/P_{Se2}$ over the source. The calculated value of x_C is essentially the same as the source composition, x_S, if $\alpha < 1$ and, as α increases from 1 to 10, the calculated x_C gradually increases from x_S and reaches a steady value about 1.5 times x_S when α is larger than 10. The results in Fig. 6.55, showing x_C (=0.090) smaller than x_S (=0.10), suggest that the transport mechanism in the system cannot be interpreted by the simple one-dimensional diffusion model.

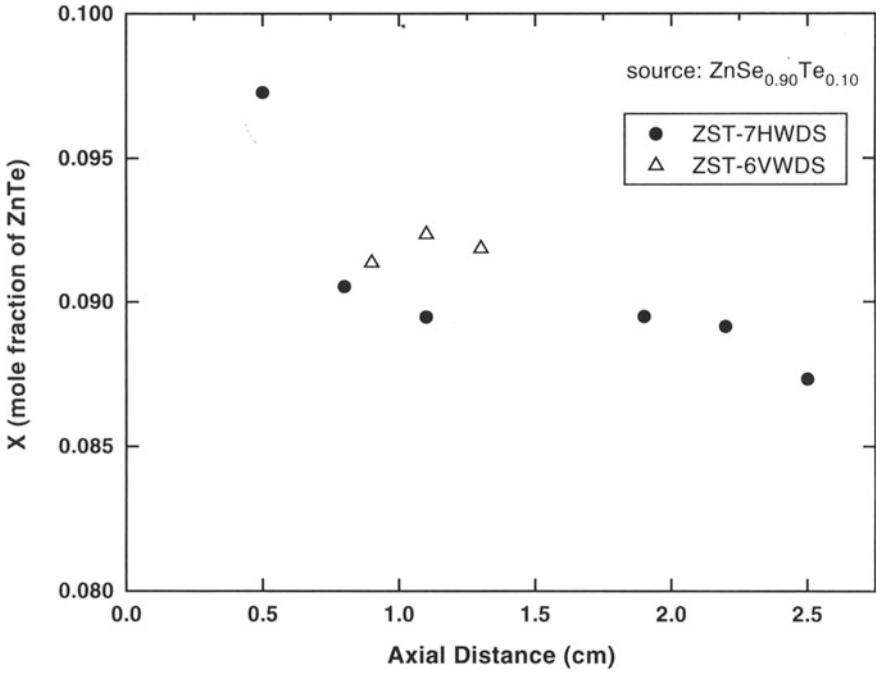

Fig. 6.55 The axial composition variations for ZST-7H and -6V by averaging the WDS results on the surfaces (taken from Fig. 6 of Ref. [39])

6.7.2 Compositional Variation by Optical Transmission Measurements

The contour maps of constant cut-off wavenumber measured by the optical transmission mapping on the ZST-1V and -2H wafers are given in Fig. 6.56a, b, respectively. The composition, x in $ZnSe_{1-x}Te_x$, corresponding to the transmission cut-off wavelength, was derived from the expression [41]:

$$E_{cutoff}(\text{eV}) = 2.59479 - 1.84431x + 1.45954x^2 (0 < x < 0.4) \qquad (6.46)$$

In both wafers the radial compositional distribution was quite uniform and the measured ZnTe mole fraction, x, was slightly higher at the center than that around the edge. For the ZST-1V 1.78–1.88 cm wafer, the composition x varies from 0.272 near the edge to 0.280 at the center. For the ZST-2H 1.38–1.48 cm wafer, the distribution was slightly radially asymmetrical with the higher ZnTe section positioning toward the top of the wafer and the composition x varied from 0.290 around the edge to 0.304 at the center.

Optical absorption experiments were performed using diamond-anvil cells to measure the hydrostatic pressure dependence of the fundamental bandgap of $ZnSe_{1-x}Te_x$ alloys over the entire composition range [42]. The first- and second-order pressure

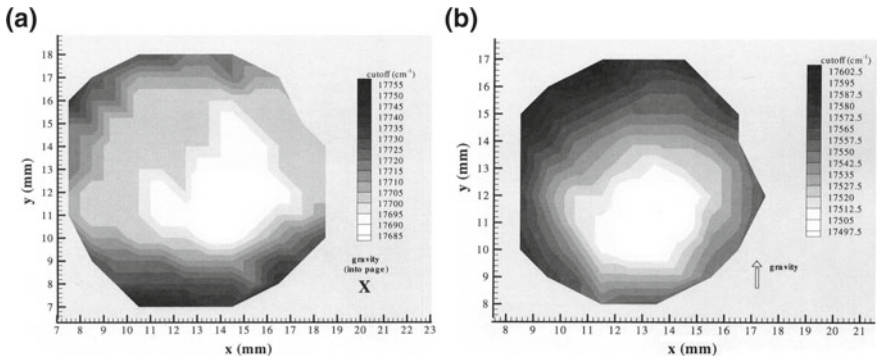

Fig. 6.56 The constant cut-off wavelength contour maps for **a** ZST-1V 1.78–1.88 cm and **b** ZST-2H 1.38–1.48 cm. Gravity orientation is also shown (taken from Fig. 7 of Ref. [39])

coefficients were obtained as a function of composition. The coefficients do not vary linearly between the ZnSe and ZnTe end-point values. Starting from the ZnSe side, the magnitude of both coefficients increases slowly until $x = 0.7$, which is the point where the ambient-pressure bandgap shows a minimum. At larger values of x the coefficients rapidly approach the values of ZnTe. The large deviations of the pressure coefficients from the linear interpolation between ZnSe and ZnTe are explained in terms of the band anti-crossing model. Photomodulated reflection, optical absorption, and photoluminescence spectroscopy have also been used to measure the composition dependence of inter-band optical transitions in $ZnSe_{1-x}Te_x$ alloys [43]. The results reveal entirely different origins of the large band-gap bowing for small and large Te content. On the Te-rich side, the reduction of the band gap is well explained by the band anticrossing interaction between the Se localized states and the ZnTe conduction-band states. On the Se- rich side, an interaction between the localized Te states and the degenerate Γ valence bands of ZnSe is responsible for the band-gap reduction and the rapid increase of the spin-orbit splitting with increasing Te concentration. The band-gap bowing in the entire composition range was accounted for by a linear interpolation between the conduction-band anticrossing and valence-band anticrossing models.

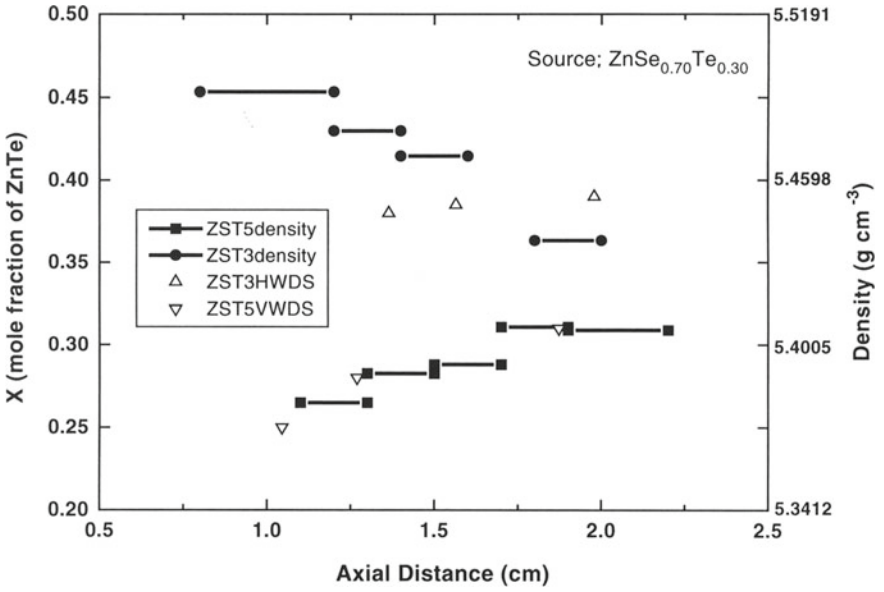

Fig. 6.57 The axial compositional variations for ZST-5V and -3H from the precision density and WDS measurements (taken from Fig. 8 of Ref. [39])

6.7.3 Axial Compositional Variation by Precision Density Measurements

The average density measured for each wafer from ZST-3H and -5V is plotted in Fig. 6.57 (right ordinate) as the horizontal bar versus the axial distance from first-grown tip. The averages of the ZnTe mole fraction from the WDS results (only the ZnTe-poor core region for ZST-3H) on the surfaces of the wafers are also shown as symbols in the figure. Since the experimental data on the density of $ZnSe_{1-x}Te_x$ solid solution as a function of x are not available, two WDS results on ZST-5V were selected as standards in the composition range of $0.2 < x < 0.4$. The composition, x, for the slices at 1.1–1.3 cm and 1.7–1.9 cm from first-grown tip were set to match the WDS surface results as 0.265 and 0.31 and this yielded.

$$\rho\left(\text{density of } ZnSe_{1-x}Te_x \text{ in g/cm}^3\right) = 5.2226 + 0.593x \qquad (6.47)$$

Using this relationship the average ZnTe mole fractions of the slices were calculated from the density results and are given in the figure according to the left ordinate. For the horizontally grown ZST-3H the composition derived from the density measurements was high, $x = 0.45$ in the first-grown region and gradually reduced to 0.35 toward the last-grown region. Since the density measurements yielded the average composition of the slice this trend is consistent with the observation from the back scattering imaging that the volume percentage of the ZnTe-rich ring region was high

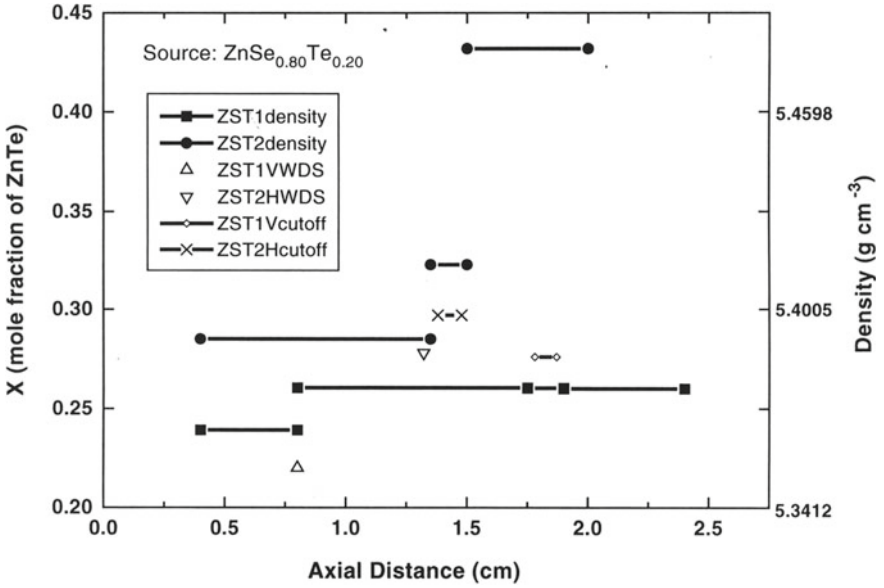

Fig. 6.58 The axial compositional variations for ZST-1V and -2H from the precision density, WDS and optical transmission cut-off wavelength measurements (taken from Fig. 9 of Ref. [39])

in the first-grown region and slowly reduced to almost zero toward the last-grown region. The density results and the average compositions measured by WDS and optical transmission on the ZST-1V and -2H slices were also derived and are shown in Fig. 6.58. It should be noted that the high ZnTe content in the last slice of the ZST-2H boule resulted from the power outage of the furnace central zone at the end of growth. The sudden decrease in temperature caused massive spontaneous condensation on the growing surface which was visible as a 1 mm thick layer at the end of the grown crystal. As shown in Fig. 6.57 and 6.58, the axial composition for the vertically grown ZST-1V and -5V crystals was fairly uniform with a slight increase in x toward the last-grown region. Similar to the results in Fig. 6.55, the initial composition of ZST-5V, showing x_C (=0.25) smaller than x_S (=0.30), suggests that the transport mechanism in this ampoule cannot be interpreted by the simple one-dimensional diffusion model.

References

1. W. Zhou, J. Wu, M. Dudley, C.-H. Su, M.P. Volz, D.C. Gillies, F.R. Szofran, S.L. Lehoczky, Mater. Res. Soc. Symp. Proc., Infrared Detectors—Materials, Processing, and Devices, A. Applebaum and L. R. Dawson (eds.) 299, 203 (1994)
2. W. Zhou, M. Dudley, J. Wu, C.-H. Su, M.P. Volz, D.C. Gillies, F.R. Szofran, S.L. Lehoczky, Mater. Sci. Eng. **B27,** 143 (1994)

3. C.-H. Su, M. Dudley, R. Matyi, S. Feth, S.L. Lehoczky, J. Crystal Growth **208**, 237 (2000)
4. Y. Yoshioka, H. Yoda, M. Kasuga, J. Crystal Growth **115**, 705 (1991)
5. R. Shetty, W.R. Wilcox, L.L. Regel, J. Crystal Growth **153**, 103 (1995)
6. K. Chattopadhyay, S. Feth, H. Chen, A. Burger, C.-H. Su, J. Crystal growth **191**, 377 (1998)
7. C.-H. Su, S. Feth, D. Hirschfeld, T.M. Smith, L.J. Wang, M.P. Volz, S.L. Lehoczky, J. Crystal Growth **204,** 41 (1999)
8. C.-H. Su, S. Feth, L.J. Wang, S.L. Lehoczky, J. Crystal Growth **224** 32 (2001)
9. Y. Korostelin, V.I. Kozlovsky, A.S. Nasibov, P.V. Shapkin, J. Crystal Growth **197**, 449 (1999)
10. K. Yoneda, Y. Hishida, T. Toda, H. Ishii, T. Niina, Appl. Phys. Lett. **45**, 1300 (1984)
11. K.P. Giapis, D.-C. Lu, K.F. Jensen, Appl. Phys. Lett. **54**, 353 (1989)
12. Z. Zhu, G.D. Brownlie, P.J. Thompson, K.K. Prior, B.C. Cavenett, Appl. Phys. Lett. **67**, 3762 (1995)
13. J.L. Merz, H. Kukimoto, K. Nassau, J.W. Shiever, Phys. Rev. B **6**, 545 (1972)
14. M. Isshiki, T. Yoshida, K. Igaki, W. Uchida, S. Suto, J. Crystal Growth **72**, 162 (1985)
15. M. Isshiki, T. Yoshida, T. Tomizono, S. Satoh, K. Igaki, J. Crystal Growth **73**, 221 (1985)
16. P.J. Dean, D.C. Herbert, C.J. Werkhoven, B.J. Fitzpatrick, R.N. Bhargava, Phys. Rev. B **23**, 4888 (1981)
17. J.L. Merz, K. Nassau, J.W. Shiever, Phys. Rev. B **8**, 1444 (1973)
18. J.C. Bouley, P. Blanconnier, A. Herman, Ph. Ged. P. Henoc, J.P. Noblanc, J. Appl. Phys. **46,** 3549 (1975)
19. S.-M. Huang, Y. Nozue, K. Igaki, Jpn. J. Appl. Phys. **22**, L420 (1983)
20. E. Tournie, C. Morhain, G. Neu, M. Laugt, C. Ongaretto, J.-P. Faurie, R. Triboulet, J.O. Ndap, J. Appl. Phys. **80**, 2983 (1996)
21. M. Tajima, T. Masui, D. Itoh, T. Nishino, J. Electrochem. Soc. **137**, 3544 (1990)
22. M. Isshiki, K. Masumoto, W. Uchida, S. Satoh, Jpn. J. Appl. Phys. **30**, 515 (1991)
23. K. Shahazad, D.J. Olego, D.A. Cammach, Phys. Rev. B **39**, 13016 (1989)
24. T. Yodo, T. Koyama, K. Yamashita, J. Appl. Phys. **64**, 2403 (1988)
25. P.J. Dean, B.J. Fitzpatrick, R.N. Bhargava, Phys. Rev. B **26**, 2016 (1982)
26. Z. Zhu, H. Mori, T. Yao, J. Appl. Phys. **73**, 1146 (1993)
27. J.M. DePuydt, T.L. Smith, J.E. Potts, H. Cheng, S.K. Mohapatra, J. Crystal Growth **86**, 318 (1988)
28. C.-H. Su, M.P. Volz, D.C. Gillies, F.R. Szofran, S.L. Lehoczky, M. Dudley, G.-D. Yao, W. Zhou, J. Crystal Growth, **128**, 627 (1993)
29. M.P. Volz, C.-H. Su, S.L. Lehoczky, F.R. Szofran, Phys. Rev. **B46**, 76 (1992)
30. B. Yang, Y. Ishikawa, Y. Doumae, T. Miki, T. Ohyama, M. Isshiki, J. Crystal Growth **172**, 370 (1997)
31. M. Soltani, M. Certier, R. Errard, E. Kartheuser, J. Appl. Phys. **78**, 5626 (1995)
32. S. Seto, A. Tanaka, K. Suzuki, M. Kawashima, J. Crystal Growth **101**, 430 (1990)
33. J.M. Wrobel, J.J. Dubowski, P. Becla, J. Vac. Sci. Technol. A **7**, 338 (1989)
34. N.C. Giles, S. Hwang, J.F. Schetzina, S. McDevitt, C.J. Johnson, J. Appl. Phys. **64**, 2656 (1988)
35. P. Siffert, A. Cornet, R. Stuck, R. Triboulet, Y. Marfaing, IEEE Trans. Nucl. Sci. **NS-22**, 211 (1975)
36. A. Burger, K. Chattopadhyay, J.-O. Ndap, X. Ma, S.H. Morgan, C.I. Rablau, C.-H. Su, S. Feth, R. page, K.I. Schaffers, S.A. Payne, J. Crystal Growth **225**, 249 (2001)
37. C.-H. Su, S. Feth, M.P. Volz, R. Matyi, M.A. George, A. Burger, S.L. Lehoczky, J. Crystal Growth **207**, 35 (1999)
38. J.T. Vallin, G.A. Slack, S. Roberts, Phys. Rev. B **2**, 4313 (1970)
39. C.-H. Su, Y.-G. Sha, M.P. Volz, P. Carpenter, S.L. Lehoczky, J. Crystal Growth **216**, 104 (2000)
40. Y.-G. Sha, C.-H. Su, S.L. Lehoczky, J. Crystal Growth **171**, 516 (1997)
41. C.-H. Su, unpublished
42. J. Wu, W. Walukiewicz, K.M. Yu, J.W. Ager III, E.E. Haller, I. Miotkowski, A.K. Ramdas, C.-H. Su, Phys. Rev. **B 68**, 033206(1–4) (2003)
43. J. Wu, K.M. Yu, W. Walukiewicz, J.W. Ager III, E.E. Haller, I. Miotkowski, A.K. Ramdas, Ching-Hua Su, I.K. Sou, R.C.C. Perera, J.D. Denlinger, Phys. Rev. **B 67**, 035207(1–5) (2003)

Chapter 7
Measurements on Thermal and Electrical Properties and Characterizations on Annealed Samples

Abstract The temperature dependences of thermal, electrical conductivity and Seebeck coefficients provide the critical information on the thermoelectric properties of the materials. The recent advancements in the converting efficiency of thermoelectrics have been attributed to the modification on material inhomogeneity of microstructures by hot pressing or simply cooling the melt to reduce the thermal conductivity. On the other hand, due to its time-consuming preparation/processing and unnecessary good crystalline quality (for thermoelectric applications), the processing of thermoelectric materials by crystal growth resulted in very few investigations. In this section, the thermoelectric properties of CdTe, grown by PVT, will be presented and compared with CdZnTe grown by directional solidification from the melt. Two different types of CdS crystals were produced from the PVT process in our laboratory, i.e., the "clear" and the "dark", even though the growth parameters were kept essentially the same. To investigate the cause of this optical difference, the studies were emphasized on the stoichiometry changes of the crystals through the formation of point defects and their complexes. In the study, the approach was to subject the CdS crystals to heat treatments in the presence of Cd, S, and Se vapor and then compared their low-temperature photoluminescence (PL) spectra complemented with the measurements of electrical properties.

Keywords Thermal conductivity · Electrical conductivity · Seebeck coefficient · Thermoelectric property

7.1 Thermal, Electrical Conductivity and Seebeck Coefficient of CdTe Grown by PVT

The temperature dependences of thermal, electrical conductivity and Seebeck coefficients provide the critical information on the thermoelectric properties of the materials. The recent advancements in the converting efficiency of thermoelectrics have been attributed to the modification on material inhomogeneity of microstructures by hot pressing or simply cooling the melt to reduce the thermal conductivity. On the other hand, due to its time-consuming preparation/processing and unnecessary good crystalline quality (for thermoelectric applications), the processing of thermoelectric

© Springer Nature Switzerland AG 2020

C.-H. Su, *Vapor Crystal Growth and Characterization*,
https://doi.org/10.1007/978-3-030-39655-8_7

materials by crystal growth resulted in very few investigations. In this section, the thermoelectric properties of CdTe, grown by PVT, will be presented and compared with CdZnTe grown by directional solidification from the melt [1].

7.1.1 Thermal Conductivity

The thermal conductivity, electrical conductivity, and Seebeck coefficient of the vapor-grown CdTe-15 crystal was measured from room temperature to 780 °C. The thermal conductivity, κ, was determined from the following equation.

$$\kappa = \rho C_p \alpha \tag{7.48}$$

where ρ, C_p, and α are density, heat capacity, and thermal diffusivity, respectively.

The thermal diffusivity was measured by the Flashline 3050 System from Anter Corp. (now TA Instruments). In the flash technique, when the sample was heated and in equilibrium with a preset temperature, the radiant energy of a high-intensity light pulse was absorbed on the front surface of the disc and the resultant temperature rise on the rear face was recorded. The diffusivity was calculated from the thermogram using the Clark and Taylor analysis [2]. The room temperature lattice constants have been reviewed by Williams [3] to be 0.6481 Å for CdTe. The density at elevated temperature was determined by the lattice constant at room temperature and their linear thermal expansion coefficients values reviewed in Ref. [3] for CdTe. Figure 7.1 shows that the thermal conductivity of the CdTe-15 ingot grown by PVT, derived from Eq. (7.48), was slightly above 0.08 W/cm-K at room temperature, decreased to about 0.035 W/cm-K when temperature reached above 200 °C, stayed there, and slowly decreased when temperature was above 700 °C. The thermal diffusivity of CdTe has been measured by a similar laser-flash method between 930 and 1085 °C [4]. Their thermal diffusivity data were multiplied by the values of heat capacity and density at the temperatures, as described above, to obtain the values for thermal conductivity which are also shown in Fig. 7.1. Those data are in line with the extension of present data from the lower temperature range.

The measured thermal conductivities from room temperature to 750 °C for CdTe together with two $Cd_{0.8}Zn_{0.2}Te$ samples are given in Fig. 7.1 for comparison. The crystals of $Cd_{0.80}Zn_{0.20}Te$ were grown by unseeded vertical directional solidification under controlled Cd over-pressure to optimize the stoichiometry of the grown materials [5]. After about 90 g of starting material has been loaded inside the growth ampoule, a fused silica basket holding about 2 g of pure Cd was fixed below the seal-off location at the top of the ampoule to serve as the Cd reservoir to control Cd overpressure during growth. The sample, CZT-34, was sliced from a crystal grown from starting material of $Cd_{0.80}Zn_{0.20}Te$ whereas CZT-30 was grown from starting material of $Cd_{0.80}Zn_{0.20}Te$ with In doping of 5.0 ppm atomic. The furnace translation rate and Cd reservoir temperature were 1.0 mm/h and 785 °C, respectively for CZT-30 and 1.2 mm/h and 845 °C for CZT-34, respectively.

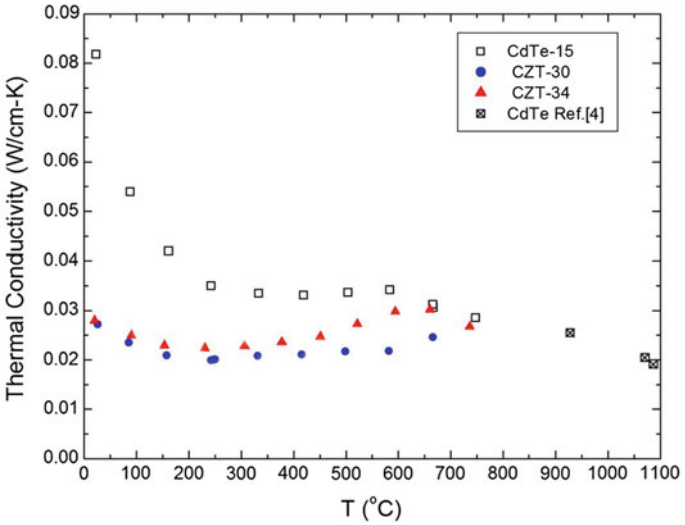

Fig. 7.1 The measured thermal conductivity for PVT grown CdTe-15, In-doped (CZT-30) and un-doped (CZT-34) $Cd_{0.80}Zn_{0.20}Te$ samples, grown from the melt, plotted against temperature. The three data for CdTe at temperature above 900 °C are from Ref. [4] (taken from Fig. 1 of Ref. [1])

The thermal conductivity for the In-doped CdZnTe, CZT-30, stayed below 0.03 W/cm-K in the low temperature range with a shallow minimum at about 250 °C. The un-doped CdZnTe sample, CZT-34, has the thermal conductivity similar to that of CZT-30 in the low temperature range and increased to a slight maximum of 0.03 W/cm-K at about 650 °C. All three sets of the thermal conductivity data merged together at about 750 °C—an implication that the samples became intrinsic as the phonon contribution to thermal conductivity started to dominate at elevated temperatures.

7.1.2 Electrical Conductivity

The electrical conductivity was measured by the ULVAC ZEM-3 instrument, which performed the electrical conductivity and Seebeck coefficient measurements simultaneously from room temperature to 800 °C. The samples were sliced into the shape of roughly 2 × 2 ×15 mm rectangular prism from the thermal diffusivity samples. The electrical conductivity was determined from ten measured I-V points and the Seebeck coefficient was derived from the values of Seebeck voltages measured over 6 mm distance along the sample under three different applied thermal gradients.

The CdTe crystal grown by PVT showed low values of electrical conductivity at low temperature range and increased exponentially as the temperature increased. The CdTe crystal, grown from a starting material being heat-treated to approach congruent

sublimation condition, contains small amount of native defects (donor or acceptor) and hence is close to be intrinsic This is evidenced from the almost linear dependence of its electrical conductivity (in log scale) versus 1000/T(K) shown in Fig. 7.2, especially for temperature above 440 °C, or 1000/T(K) < 1.4. Another sample, CdTe-10, grown under similar conditions has been reported to have a resistivity in the range of high-10^8 Ω cm [6], or a conductivity of low 10^{-7} S/cm at room temperature. This value is roughly in line with the extrapolation of the current high temperature results. Electrical conductivity of CdTe single crystals have been measured at elevated temperature while controlling the partial pressures of either Cd or Te_2 in equilibrium with the samples [7]. It reported that the measured electrical conductivity for two un-doped CdTe crystals near Te-saturation condition were 0.07 and 0.17 S/cm at 330 °C, increased slowly to 0.14 and 0.20 S/cm, respectively, at 580 °C and approached 0.30 S/cm at 680 °C, which is a little higher than our interpolating value of about 0.24 S/cm at 680 °C. High temperature electrical conductivity of CdTe single crystals have also been measured in the temperature range from 400 to 1200 °C [8]. Their data started to approach intrinsic at temperature above 636 °C, or 1000/T(K) = 1.1 and are roughly 0.25 and 0.6 S/cm at 636 and 727 °C, respectively, comparing to our interpolating values of 0.17 and 0.41 S/cm, respectively.

The data for the In-doped melt-grown CdZnTe, CZT-30, also showed low values of electrical conductivity in the low temperature range and increased exponentially as the temperature increased. When plotting on the scale of $\log_{10}$ versus 1000/T as shown in Fig. 7.2, they also show the intrinsic characteristics by forming a linear line roughly parallel but lower to those data for CdTe due to the larger band gap of CdZnTe. It has been shown that the intrinsic carrier concentration of CdTe can

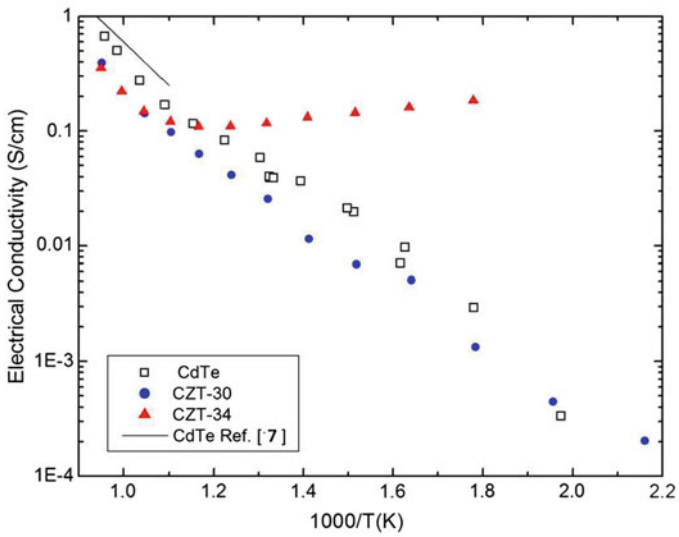

Fig. 7.2 The measured electrical conductivities plotted in a scale of $\log_{10}$ versus 1000/T(K). The line segment at the upper left corner shows data from Ref. [7] (taken from Fig. 3 of Ref. [1])

be fitted well [9] by the following form for a non-degenerate semiconductor with parabolic valence and conduction bands:

$$n_i = NT^{3/2}\exp\left(-E_g/2kT\right) \tag{7.49}$$

where N is a constant (related to band structure parameters), T in K, E_g the effective band gap energy, and k the Boltzmann constant. From the measurements of optical transmission at 300 K on CdZnTe [10], the measured cut-on energy for x = 0 and 0.20 was 1.464 and 1.572 eV, respectively. Assuming the band gap difference, 0.108 eV, to be the same and similar band structure parameters at elevated temperatures, the ratio of intrinsic carrier concentration of $Cd_{0.8}Zn_{0.2}Te$ to that of CdTe would be:

$$n_i(Cd_{0.8}Zn_{0.2}Te)/n_i(CdTe) = \exp(-0.108eV/2kT) \tag{7.50}$$

Assuming that the mobilities for the carriers are the same for $Cd_{0.8}Zn_{0.2}Te$ and CdTe at a fixed temperature, this ratio in Eq. (7.50) will also be the ratio for their electrical conductivity. At the temperature of 1000 K, this ratio of n_i would be 0.534 from Eq. (7.50) which is comparable to the ratio of the measured electrical conductivity at 1000 K, as interpolating from Fig. 7.2 to be, respectively, 0.22 and 0.41 S/cm for $Cd_{0.8}Zn_{0.2}Te$ and CdTe, a ratio of 0.54. The electrical conductivity of the un-doped CZT-34 sample started with a value of 0.3 S/cm at around 300 °C and decreased to a minimum of about 0.1 S/cm and then merged with the In-doped sample at temperature above 650 °C.

7.1.3 Seebeck Coefficient

The types of electrical conduction were revealed from the Seebeck coefficient measurements as shown in Fig. 7.3. For the CdTe sample, in the low temperature range, the Seebeck coefficients were positive—indicating a p-type dominant conduction, presumably from native acceptors of either Te interstitial or Cd vacancy, resulted from non-stoichiometry. The measured Seebeck coefficients showed a rather high value of 1.1 mV/K at the lowest measured temperature of 346 °C. For comparison, de Nobel had measured the Seebeck coefficient for a large number of n- and p-type CdTe samples [11] using Ga baths as electrical contacts and reported values for p-type CdTe ranged from 0.79 to 0.98 mV/K, presumably near room temperature. As temperature increased, our measured Seebeck coefficients decreased slowly as sample approached to be intrinsic and the conduction type converted to n-type around 680 °C due to the mobility difference—about 300 cm^2/V-s for electrons and 15 cm^2/V-s for holes at 680 °C as reported by Smith [7].

The Seebeck coefficients for the CZT-30 sample indicated n-type conduction at low temperature, converted to p-type at about 250 °C, reached a maximum of 0.9 mV/K between 400 and 500 °C, and converted back to n-type at 770 °C. The In was usually intentionally doped in CdZnTe to increase its electrical resistivity for the

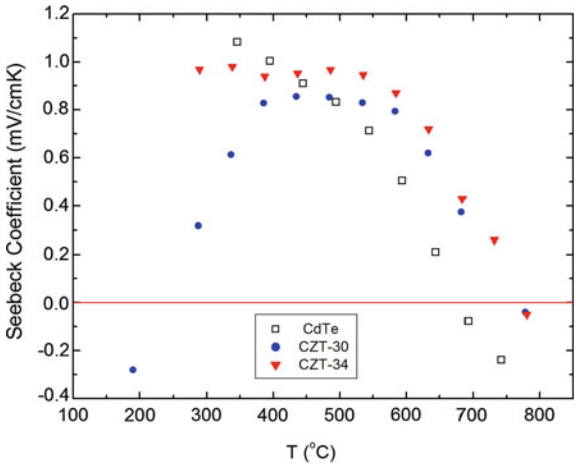

Fig. 7.3 The measured Seebeck coefficient of CdTe, In-doped (CZT-30) and un-doped (CZT-34) $Cd_{0.80}Zn_{0.20}Te$ samples plotted against temperature. Positive and negative Seebeck coefficients represent, respectively, p-type and n-type dominant electrical conduction (taken from Fig. 4 of Ref. [1])

application as high-energy radiation detector at room temperature. The small amount of n-type In doping compensated the residual native acceptor (either Cd/Zn vacancy or Te interstitial), formed during the solidification from the Te-rich stoichiometric range, and showed n-type characteristics in the low temperature range. As temperature increased, the ionization of native acceptors converted the sample into the p-type conduction until at even higher temperatures when the sample approached to be intrinsic and the conduction type converted to back n-type because of the high mobility of electrons. In the case of CZT-34, the Seebeck coefficients in Fig. 7.3 showed p-type conduction at low temperatures with a plateau of 0.97 mV/K between 250 and 550 °C then merged with In-doped CZT-30 and converted to n-type at 770 °C. The trend confirms that, for the un-doped sample, the native acceptor formed during the solidification from the Te-rich range of stoichiometry.

7.2 Effects on Post-growth Annealing of CdS Crystals Grown by PVT

Two different types of CdS crystals were produced from the PVT process in our laboratory, i.e., the "clear" and the "dark", even though the growth parameters were kept essentially the same. To investigate the cause of this optical difference, the studies were emphasized on the stoichiometry changes of the crystals through the formation of point defects and their complexes. Most of the PL measurements of CdS were studied in the context of intentionally doped crystals [12–14]. Other reported the results of the effects of post-growth heat and illumination treatments on the general features of their luminescence spectra [15–17].

In our study, the approach was to subject the CdS crystals to heat treatments in the presence of Cd, S, and Se vapor and then compared their low-temperature

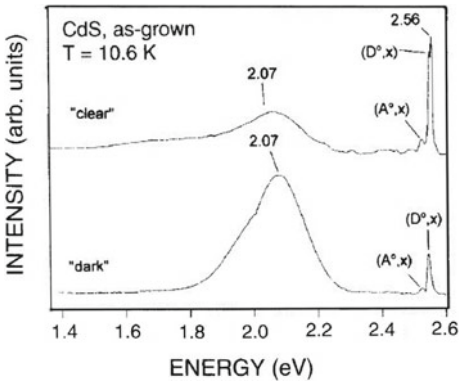

Fig. 7.4 Photoluminescence spectra of as-grown CdS samples by PVT at 10.6 K: (top) "clear"-type crystal, (bottom) "dark"-type crystal. Excitation at 457.9 nm, 15 mW/mm^2 (taken from Fig. 1 of Ref. [18])

photoluminescence (PL) spectra complemented with the measurements of electric properties [18]. Several 2 mm thick CdS discs, sliced from the as-grown crystals, were annealed with heat treatments which were performed at 500 °C for 48 h under Cd or S atmosphere. The Se-annealing experiment was performed at 700 °C for 240 h. Low-temperature PL measurements were performed on these crystals at 10.6 K. The excitation, with a power density of 15 mW/mm^2, came from the 457.9 nm line of an ILT 5500 A air-cooled argon-ion laser. The PL spectra were recorded using a SPEX 1877D triplemate spectrophotometer and a liquid nitrogen cooled CCD detector. In the monochromator stage of the spectrometer, a 30 μm slit and a 300 grooves/mm grating were employed.

The low-temperature photoluminescence spectra of the as-grown CdS "clear" and "dark"-types crystals are shown in Fig. 7.4. In the region close to the absorption edge (2.4-2.6 eV), the spectra are dominated by shallow-level excitons bound to neutral donors (D°X) or neutral acceptors (A°X) with the presence of free exciton around 2.56 eV in the spectrum of clear type crystal. The PL spectra in the deep-level range of 1.4-2.2 eV show the similarity between the as-grown "dark"-type and the "clear"-type crystal with the main emission peak around 2.07 eV but with a difference in the ratio of peak height between this deep level to that of the exciton level. Several studies indicated that this deep emission is related to a donor that is present in Cd-rich crystals [19, 20] Even with the similar heat treatment of dynamic vacuum baking of the starting material, the grown crystals seem to show slightly different stoichiometry. The PL spectrum for CdS sample after post-growth annealing in Cd pressure, as shown in Fig. 7.5, is similar to the spectra associated with the as-grown "clear"-type crystal. In Fig. 7.5, the intensity of the acceptor bound exciton (A°X) in the S-annealed sample became almost equal to the intensity of the donor bound exciton (D°X), indicating that a high level of electrical compensation took place after this heat treatment. This conclusion is supported by the electrical measurements showing the highest room temperature resistivity (10^{12} Ω cm) being achieved in this sample. The same spectrum shows a clear emission peak at 2.41 eV. A similar emission band was sometimes observed in Cd-treated CdS samples [21, 22] but was not seen in our Cd treated sample. A shallow level at 2.48 eV was observed in the

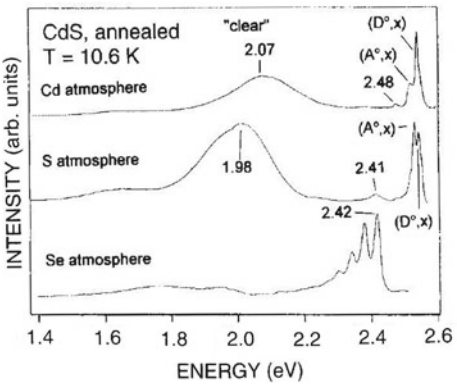

Fig. 7.5 Photoluminescence spectra at 10.6 K of heat-treated "clear"-type CdS crystals: (top) after annealing in Cd vapour at 500 °C for 48 h, (center) after annealing in S vapour at 500 °C for 48 h, and (bottom) after annealing in Se vapour at 700 °C for 240 h. Excitation at 457.9 nm, 15 mW/mm^2 (taken from Fig. 2 of Ref. [18])

Cd-treated crystal which was previously reported to exist in the Cd-rich CdS crystals and assigned [23] to the transition between a donor and the conduction band, most likely due to a Cd interstitial or a S vacancy-related center. The PL spectrum of the Se-treated sample shows a minimal contribution from donor-acceptor pair (DAP) radiative recombination. Based on data found in the literature [24, 25], it appears that the effect of this treatment was the diffusion of Se into this sample to the extent that it modified the crystal composition from CdS to a ternary of $CdS_{1-x}Se_x$, where x ~ 0.07. The emission from the solid-solution crystal is qualitatively different from that of the parent (binary) crystals with the bound exciton emissions lines are replaced by one broader band (around 2.42 eV) and its phonon replicas.

It is interesting to point out the absence of significant emission around the 1.6–1.7 eV region for all of the CdS crystals studied here. An emission peak was frequently reported in this spectral region and was related to a copper impurity [13, 16]. With copper being a notorious impurity in most the II-VI compound crystals, this finding indicates that the crystals prepared by the PVT method have low copper impurity content. As discussed in 6.4.2.2, it was concluded from the low temperature IR absorption spectra measurements that the THM grown ZnTe crystals were contaminated by Cu impurity but the PVT processed ZnTe was free of Cu [26, 27]. The electrical resistivity has been measured at room temperature on these five CdS samples. The as-grown "clear" and "dark" crystals showed a resistivity in the range of 10^8 Ω cm. The sample after the post-growth annealing of S pressure, as discussed in the last paragraph, showed a resistivity of 10^{12} Ω cm, an increase of 4 orders of magnitude. The result from the Cd-treated sample, as expected, reduced the resistivity to 10^3 Ω cm. Finally, the CdS annealed under Se pressure showed a resistivity of 10^{10} Ω cm.

References

1. S. Ching-Hua, AIP Adv. **5**, 057118 (2015)
2. L.M. Clark, R.E. Taylor, J. Appl. Phys. **46**, 714 (1975)
3. D.J. Williams, *Properties of Narrow Gap Cadmium-based Compounds*, edited by P. Capper, emis Datareviews series, INSPECT publication (1994) p. 399
4. S. Sen, W.H. Konkel, S.J. Tighe, L.G. Bland, S.R. Sharma, R.E. Taylor, J. Crystal Growth **86**, 111 (1988)
5. C.-H. Su, S.L. Lehoczky, J. Crystal Growth **319**, 4 (2011)
6. K. Chattopadhyay, S. Feth, H. Chen, A. Burger, C.-H. Su, J. Crystal growth **191**, 377 (1998)
7. F.T.J. Smith, Met. Trans. **1**, 617 (1970)
8. P. Hoschl, E. Belas, L. Tujanska, R. Grill, J. Franc, R. Fesh, P. Moravec, J. Crystal Growth **220**, 444 (2000)
9. S. Ching-Hua, J. Appl. Phys. **103**, 084903 (2008)
10. S.M. Johnson, S. Sen, W.H. Konkel, M.H. Kalisher, J. Vac. Sci. Technol **B9**, 1987 (1991)
11. D. de Nobel Philips Res. Repts. 14, 361 (1959)
12. M. Avinor, G. Meijer, J. Chem. Phys. **32**, 1456 (1960)
13. S.G. Patil, J. Woods, J. Lumin. **4**, 231 (1971)
14. N. Susa, H. Watanabe, M. Wada, Jpn. J. Appl. Phys. **14**, 173 (1975)
15. F.J. Bryant, A.F.J. Cox, Brit. J. Appl. Phys. **16**, 463 (1965)
16. F.J. Bryant, A.F.J. Cox, Brit. J. Appl. Phys. **16**, 1065 (1965)
17. T.A.T. Cowell, J. Woods, J. Phys. **D2**, 1053 (1969)
18. K.-T. Chen, Y. Zhang, S.U. Egarievwe, M.A. George, A. Burger, C.-H. Su, Y.-G. Sha, S.L. Lehoczky, J. Crystal Growth **166**, 721 (1996)
19. J.S. Sharman, Solid State Electron. **8**, 17 (1965)
20. S.G. Patil, J. Phys. **D5**, 1692 (1972)
21. R. Boyn, O. Goege, S. Kushnerus, Phys. Status Solidi **12**, 57 (1965)
22. G.H. Hershman, F.A. Kroger, J. Solid State Chem. **2**, 483 (1970)
23. N. Susa, H. Watanabe, M. Wada, Jpn. J. Appl. Phys. **15**, 2365 (1976)
24. F.A. Majumder, S. Shevel, V.G. Lyssenko, H.E. Swoboda, C. Klingshim, Z. Phys. B **66**, 409 (1987)
25. S. Permogorov, A. Reznitsky, J. Lumin. **52**, 201 (1992)
26. C.-H. Su, M.P. Volz, D.C. Gillies, F.R. Szofran, S.L. Lehoczky, M. Dudley, G.-D. Yao, W. Zhou, J. Crystal Growth **128** 627 (1993)
27. M.P. Volz, C.-H. Su, S.L. Lehoczky, F.R. Szofran, Phys. Rev. **B46**, 76 (1992)

Chapter 8
Two-Dimensional and Three-Dimensional Numerical Simulation of Vapor Transport Process

Abstract In this chapter, the PVT process is numerically investigated using both two-dimensional and three-dimensional formulation of the governing equations and associated boundary conditions. Both the incompressible Boussinesq approximation and a compressible model are tested to determine the influence of the thermal environments, the residual gas pressure as well as the gravity direction and magnitude on the process and to discern the differences between the two approaches. The results on the ZnSe system show that both the incompressible and compressible approximations provide comparable results and the presence of a residual gas tends to measurably reduce the mass flux in the system. Detailed flow patterns and velocities as well as thermal and concentration profiles were calculated and the shear flow velocity in the horizontal configuration supports the step growth mechanism observed experimentally.

Keywords Two-dimensional numerical simulation · Three-dimensional numerical simulation · Boussinesq approximation

The one-dimensional diffusion model, encompassing both binary and ternary systems, has been presented in Sects. 2.2 and 3.4, respectively. The calculated results of mass flux, or the transport rate, have provided the important guidance on the parameters for the experimental conditions. However, from the comparisons of the experimental results, such as the grown crystal morphology and distributions of point defects and impurities, between the vertical and horizontally configurations, it is clear that gravity has extra effects on the transport process other than diffusion. Therefore, the PVT process is numerically investigated using both two-dimensional and three-dimensional formulation of the governing equations and associated boundary conditions. Both the incompressible Boussinesq approximation and a compressible model are tested to determine the influence of gravity on the process and to discern the differences between the two approaches. The influence of a residual gas is included in the models. The results show that both the incompressible and compressible approximations provide comparable results and the presence of a residual gas tends to measurably reduce the mass flux in the system. Detailed flow, thermal and concentration profiles are provided.

© Springer Nature Switzerland AG 2020

C.-H. Su, *Vapor Crystal Growth and Characterization*,
https://doi.org/10.1007/978-3-030-39655-8_8

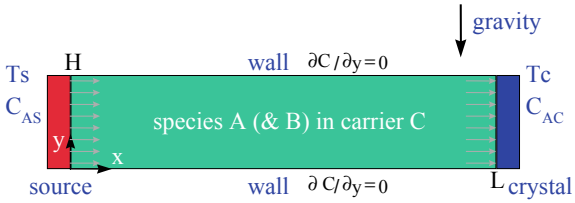

Fig. 8.1 Schematic of the modeling problem in horizontal configuration

8.1 The Problem Set Up

A schematic of the problem is shown in Fig. 8.1. It essentially consists of an ampoule of diameter H and length L with a source at one end of the ampoule and the growing crystal at the other end. The figure depicts the set up used in both 2-D and 3-D calculations. In order to determine the gravitational effects on the thermo-fluid characteristics of the system, a Cartesian section (axes shown in the figure) of the ampoule is utilized in the 2-D computations. The source and crystal are at temperatures T_S and T_C respectively, and the ampoule side walls are subjected to a known temperature profile. The system is comprised typically of species A (and B, in a two species system) in an inert carrier component C. The mass fractions of A at the source and crystal, C_{AS} and C_{AC}, respectively, are determined from system thermodynamics as discussed earlier assuming local equilibrium conditions. In the case of two species the mass fraction of the second species B, C_{BS} and C_{BC}, at the source and crystal respectively are also specified. No slip velocity boundary conditions and zero species gradient conditions are imposed on the ampoule side walls.

8.2 Governing Equations

The governing equations for the PVT growth are the transport equations for momentum, heat and mass transfer as given below in standard vector notation.

$$\rho_t + \nabla \rho u = 0 \tag{8.51}$$

$$\rho u_t + \rho u \cdot \nabla u = -\nabla p + \rho g + \mu \nabla^2 u \tag{8.52}$$

$$\rho T_t + \rho C_p u \cdot \nabla T = k \nabla^2 T \tag{8.53}$$

$$\rho C_i + \rho u \cdot \nabla C_i = \rho \alpha_c \nabla^2 C_i \tag{8.54}$$

In Eq. (8.54), C_i represents the mass fraction of a species. If the system consists of 2 species A and C (n = 2) then only 1 species equation (n−1) is solved. So for the H_2–I_2 system, H_2 is treated as the carrier gas and only the species equation for I_2 is

solved. For the Zn–Se system with a residual gas component, two species equations (for Zn and Se_2) are solved. In general, for a mixture of n species (total) the following can be written:

$$\sum_{i=1}^{n} C_i = 1 \Rightarrow C_N = 1 - \sum_{i=1}^{n-1} C_i \tag{8.55}$$

where the suffix N represents the carrier gas attributes. The net molecular weight can be written as:

$$\frac{1}{M} = \sum_{i=1}^{n} \frac{C_i}{M_i} \tag{8.56}$$

In the fully compressible formulation, the fluid is treated as an ideal gas and the gas density is calculated from

$$\rho = \frac{Mp}{RT} \tag{8.57}$$

For multiple species this leads to

$$\rho = \frac{pM_N}{RT\left[1 + \sum_{i=1}^{n-1}\left(\frac{M_N}{M_i} - 1\right)C_i\right]} \tag{8.58}$$

In instances where the gas density is not a strong function of pressure the so called quasi-compressible formulation for density is adopted. This formulation is mathematically simpler to implement and the local density is now expressed as:

$$\rho = \frac{\rho_o[1 - \beta_T(T - T_o)]}{\left[1 + \sum_{i=1}^{n-1}\left(\frac{M_N}{M_i} - 1\right)C_i\right]} \tag{8.59}$$

In the incompressible formulation, the density is held constant for all terms in the momentum equation except the source term which is treated using the Boussinesq approximation to account for the thermal and solutal buoyancy effects. The buoyancy source term can be written as:

$$(\rho - \rho_o)g_e = \frac{-\rho_o\left[\beta_T(T - T_o) + 1 + \sum_{i=1}^{n-1}\left(\frac{M_N}{M_i} - 1\right)C_i\right]g_e}{1 + \sum_{i=1}^{n-1}\left(\frac{M_N}{M_i} - 1\right)C_i} \tag{8.60}$$

where g_e is the gravity vector. The latter two formulations were used in the present study.

8.3 Benchmark Simulations

In order to verify the proper problem set up and coding, the H_2–I_2 system was studied in a series of benchmark simulations. The system has been studied extensively by Rosenberger et al. [1–5]. For this problem, iodine is the deposited species (A) and hydrogen is the carrier gas (C). The following are the system parameters:

H = 1 cm, L = 5 cm, T_S = 370.5 K, T_C = 358.1 K (isothermal source and crystal sections).

The upper and lower walls have a linear temperature variation and zero gradient for the species as mentioned previously. The molecular weights are M_A = 254, M_C = 2.016 and the system total pressure is P_T = 100 Torr (133.3 kPa). The partial pressure of I_2 is a function of the local temperature of source and can be calculated from

$$P_A(T) = 760 \exp(30.795 - 8088.64/T - 2.013 \ln T) \text{ Torr; where T is in K} \tag{8.61}$$

Using Eq. (8.61), the partial pressures can be calculated to give $P_A(T_S)$ = 40.046 Torr, $P_C(T_S)$ = 59.954 Torr and $P_A(T_C)$ = 20.137 Torr and $P_C(T_C)$ = 79.863 Torr. The mass fraction C_A can now be evaluated at the source and crystal ends from the relation:

$$C_A = 1/[1 + (P_T/P_A - 1)M_C/M_A] \tag{8.62}$$

Using Eqs. (8.61) and (8.62) the mass fractions for the system can be calculated as

$$C_{AS} = 0.98835 \text{ and } C_{AC} = 0.96972$$

The sublimation/condensation boundary conditions are derived from the diffusion equations of the participating species and are rather unique (see Rosenberger et al. [1–5]).

$$\text{At the source (x = 0) sublimation occurs: } u = \frac{-D_{AC}}{(1 - C_{AS})} \frac{\partial C_A}{\partial x} \tag{8.63}$$

$$\text{At the crystal (x = L) deposition occurs: } u = \frac{-D_{AC}}{(1 - C_{AC})} \frac{\partial C_A}{\partial x} \tag{8.64}$$

where D_{AC} is the diffusivity of species A in the carrier gas C. The property values used in the computations are $D_{AC} = 1.25 \times 10^{-4}$ m^2/s, dynamic viscosity $\mu = 1.5 \times 10^{-5}$ kg/m s, specific heat for H_2 = 1005 J/kg K (property for air was used), thermal conductivity = 0.02547 W/m K and the thermal expansion coefficient β_T is taken as $(1/T_{avg})$, where $T_{avg} = (T_S + T_C)/2$.

The governing equations and boundary conditions were solved using a finite element code (Fidap) set in primitive variables. A separate equation is solved for pressure in addition to the momentum, energy and an equation for each species in the system. Typical spatial discretization consisted of 625 elements, (9 noded quadrilateral), with an increased grid density near the wall regions. The equations were solved iteratively using the Newton-Raphson scheme and the solutions were carried to convergence till the sum of normalized residuals was less than 10^{-5}. Only the steady state problem was solved (i.e., the transient term in Eqs. (8.51) and (8.52) was omitted). The specialized boundary conditions for the sublimation velocity at the source and the condensation velocity at the crystal were implemented using a user subroutine to the code. Since the system is completely confined with internal mass fluxes a special scaling procedure for velocity was adopted to ensure mass conservation. The efficiency of this scaling and the implementation of the boundary conditions were tested in the benchmark simulations.

The results from a parametric variation of gravity are shown in Fig. 8.2. As indicated in the figure the calculations are for the g vector aligned normal to the system temperature (indicated in color) gradient (worst case scenario). The wide disparity in the molecular weights of the system components results in strong convection in the system due to solutal effects which overrides thermal buoyancy effects as evidenced by flow going down along the heated wall at $x = 0$. At $g = 1\ g_o$ (where g_o denotes terrestrial gravity) there is substantial flow recirculation in the system which leads to severe asymmetry. Such asymmetry cannot be seen in axisymmetric calculations. As the gravity level is reduced, the buoyancy effects are reduced as well resulting in less distortion of the streamlines eventually resulting in a symmetric flow pattern that approaches purely diffusion limited (D/L) flow conditions. It is

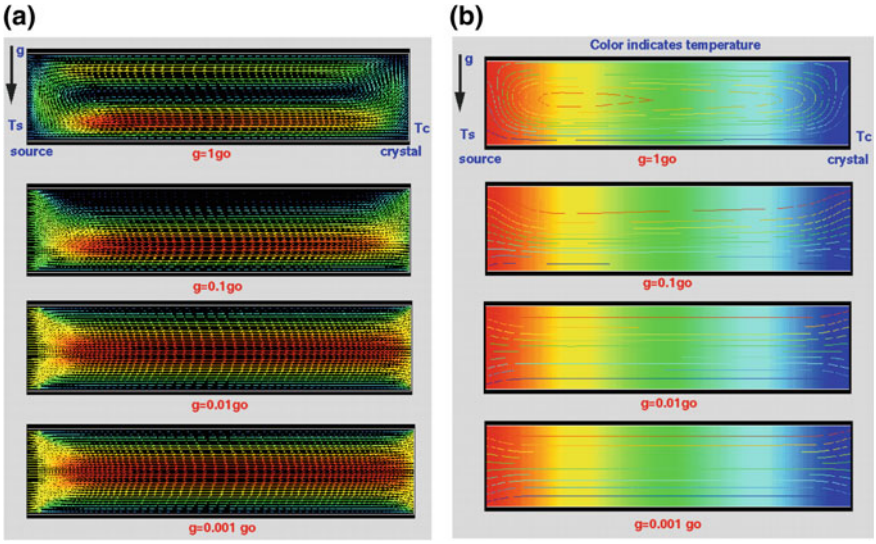

Fig. 8.2 Benchmark simulations for the hydrogen/iodine system (a) velocity vector and (b) stream function

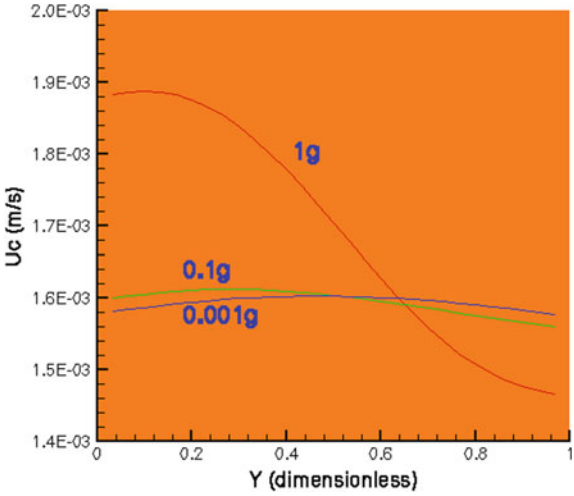

Fig. 8.3 Comparison of crystal growth rate at terrestrial and reduced gravity levels. *Note* $U_c = 1.6 \times 10^{-3}$ m/s = 5.32 mm/day (taken from Fig. 8.2 of Ref. [8])

interesting to note that even at g = 0.001 g_o there is significant streamline distortion next to the source and crystal ends. This phenomenon (also seen when g is turned off, purely diffusive conditions), stems from the no slip velocity boundary condition imposed on the ampoule side walls. The calculations are in good agreement with those existing in literature. The growth rate along the vertical crystal surface, Y, from the simulations is summarized in Fig. 8.3 The figure shows that when the buoyancy effects are dominant the growth rate is significantly enhanced from D/L conditions but is accompanied with non-uniform growth across the crystal interface. A 10% reduction in the g-level, however, causes a dramatic reduction in the growth rate non-uniformity. A Peclet number analysis for the problem shows a reduction from 1.27 (for 1 g_o) to 1.07 (for 0.1 g_o). This substantiates the fact that as Pe ~ 1near D/L growth conditions are realized. Both the quasi-compressible density formulation and the Boussinesq approximation were tested for the problem. As far as the flow, temperature and concentration profiles in the system are concerned, both approaches yielded very similar results. The quasi-compressible case predicted a slightly higher average growth rate (7 mm/day) compared to 5.3 mm/day predicted by the incompressible calculations for diffusion limited growth. Other parametric simulations also showed that the crystal growth rate is inversely proportional to the ampoule length yielding reduced growth rates as the length is increased.

8.4 The Zn–Se System with a Residual Gas Component

For these calculations, Zn and Se_2 are treated as two species transported in a carrier gas of molecular weight 28. This model for the residual gas uses a lumped approach for the CO (26%) and N_2 (26%), the major components of the system as discerned

from experimental findings given early. The system parameters for the computations are provided in Table 8.1.

The binary diffusion coefficients in the above table were calculated using the Chapman-Ensog formula, described in the earlier chapter. Typical calculations were performed for a stoichiometry parameter at the source $\alpha = P_{Zn}/P_{Se_2} = 2.9$which is close to the initial experimental growth conditions. For given values of T_S, T_C and α, the partial pressures P_{Zn} and P_{Se_2} are calculated at the source from the equilibrium condition given by Eq. (9) in Chap. 2. For an assumed partial pressure of the residual gas, the total pressure which remains constant throughout the system is then determined. Following this step, P_{Zn} and P_{Se_2} at the crystal temperature are determined using Eq. (9) and the partial pressure of the residual gas is found. The procedure is iterated for different values of the residual gas pressure until the average residual gas pressure over the entire length of the ampoule matches the experimentally determined pressure of the residual gas. Once the partial pressures of the various components are known the mass fractions at the source and crystal are evaluated. For $\alpha = 2.9$ the mass fraction of Zn at the source is 0.5456 and at the crystal is 0.7025. The corresponding mass fractions of Se_2 are 0.4544 and 0.2975 respectively. Specially derived boundary

Table 8.1 Properties used in simulations. $M_{Zn} = 65.39$, $M_{Se_2} = 157.92$, $M_{N_2} = 28$

Length	10 cm
Diameter	1.5 cm
Source temperature, T_S	1160 °C
Crystal temperature, T_C	1130 °C*
Density	1.2×10^{-5} gm/cm^3
Dynamic viscosity	4.3×10^{-5} Pa s
Diffusivity (Zn in carrier, N_2)	64.59 cm^2/s
Diffusivity (Se_2 in carrier, N_2)	71.46 cm^2/s
Thermal expansion coefficient	7.1×10^{-4} 1/K
Prandtl number, Pr	0.439
Schmidt number, Sc_{Zn}	0.557
Schmidt number, Sc_{Se_2}	0.503
System stoichiometry (α)	2.9$^+$, 20$^\wedge$
Residual gas partial pressure, source	0.01 atm
Residual gas partial pressure, crystal	0.01358 atm
Total system pressure	0.02316 atm
Zn partial pressure, source ($\alpha = 2.9$)	9.7887×10^{-3} atm
Zn partial pressure, crystal ($\alpha = 2.9$)	8.1533×10^{-3} atm
Se_2 partial pressure, source ($\alpha = 2.9$)	3.3754×10^{-3} atm
Se_2 partial pressure, crystal ($\alpha = 2.9$)	1.43×10^{-3} atm

* Some calculations have a Tc profile
+ Typical growth stoichiometry
^ Off stoichiometry computations

conditions are again required for treating sublimation at the source and condensation at the crystal. Similar to the approach adopted for the H_2–I_2 system the boundary conditions are derived from the mass flux equations for the three components:

$$\dot{m}_{Zn} = \rho(VC_{Zn} - D_{Zn}\nabla C_{Zn}) \tag{8.65}$$

$$\dot{m}_{Se} = \rho(VC_{Se} - D_{Se}\nabla C_{Se}) \tag{8.66}$$

$$\dot{m}_{N} = \rho(VC_{N} - D_{N}\nabla C_{N}) = 0 \tag{8.67}$$

As noted in Eq. (8.67) the mass flux of the residual gas in and out of the source and crystal respectively is zero. Assuming the binary diffusion coefficients of Zn and Se_2 in the residual gas to be the same (a fairly good approximation) the velocity boundary condition can be derived for the source and crystal as:

$$V\left(\frac{\frac{M_{Se}}{\alpha M_{Zn}}}{1+\frac{M_{Se}}{\alpha M_{Zn}}} - C_{Zn}\right) = -D\nabla C_{Zn} \tag{8.68}$$

8.4.1 Two-Dimensional Calculation

Calculations were performed with an experimentally determined temperature profile imposed on the ampoule side walls. The governing equations for momentum, temperature and two species equations were non-dimensionalized and solved. To gauge what effects are produced by the buoyancy forces a sequence of velocity difference plots are generated. The reasoning stems from the fact that in the PVT growth of ZnSe the diffusive flux (Stefan flow) tends to dominate the system and thereby tends to mask the underlying subtle buoyancy effects. In order to evaluate the buoyancy effects it is necessary to subtract the purely diffusive flow. The first of these plots is shown in Fig. 8.4. It represents the differences in axial (u) and transverse (v) velocities from calculations for the horizontal geometry between 0 g (D/L conditions) and 1 g_o conditions. The magnitude of the maximum difference velocities is about 0.3 mm/s in the u velocity and 50 μm/s in the v velocity. The axial velocity difference contours are symmetric about the ampoule centerline but the transverse velocity difference is asymmetric. In fact, the latter component shows buoyancy introduced transverse velocity of the order of 50 μm/s (in the positive y direction, going up) next to the crystal face. This velocity is 1400 times the crystal growth rate of 0.035 μm/s, i.e., 3 mm/day. This transverse velocity is comparable to the velocity of step growth estimated from the surface morphology of as-grown ZnSe crystals in Sect.5.2.5. The transverse component is much stronger ~0.2 mm/s adjacent to the source. The buoyancy effects are again due to solutal buoyancy (downward flow next to the heated

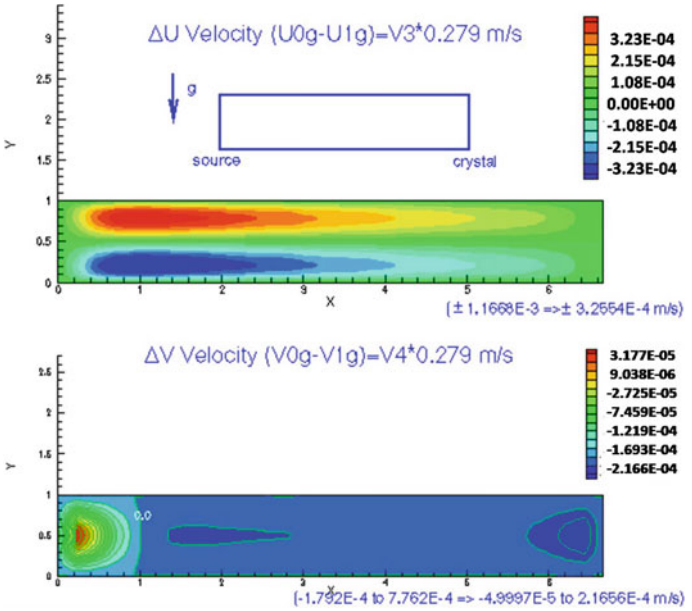

Fig. 8.4 Distribution of velocity differences, ΔU (axial) and ΔV (transverse) are the velocity differences, in m/s, between (1 g_o–0 g_o); d = 1.5 cm, L = 10 cm; α = 2.9

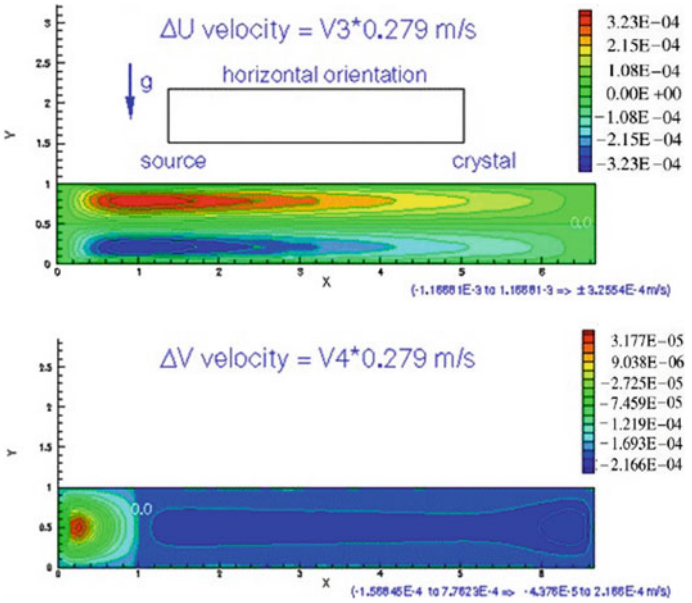

Fig. 8.5 Distribution of velocity differences, differences in ΔU (axial) and ΔV (transverse), in m/s, between (1 g_o–0 g_o); d = 1.5 cm, L = 10 cm; α = 2.9. (with variation in T_C)

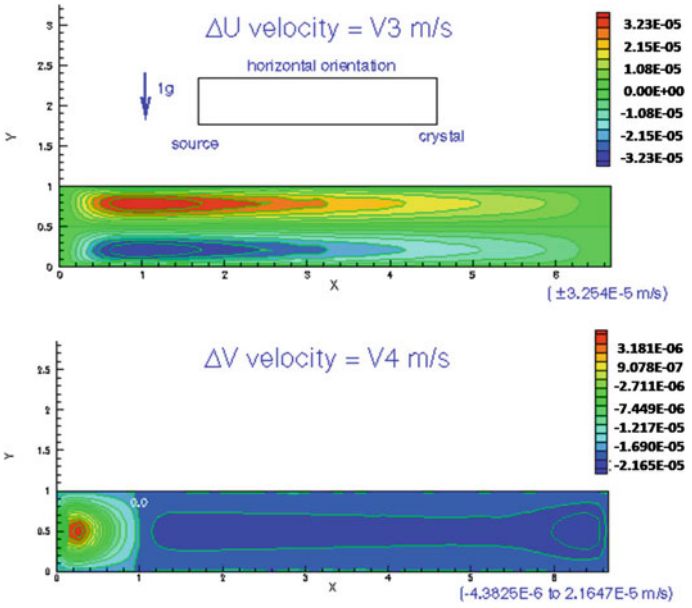

Fig. 8.6 Velocity differences in (0 g_o–0.1 g_o), given in m/s, $\alpha = 2.9$ (with variation in T_C)

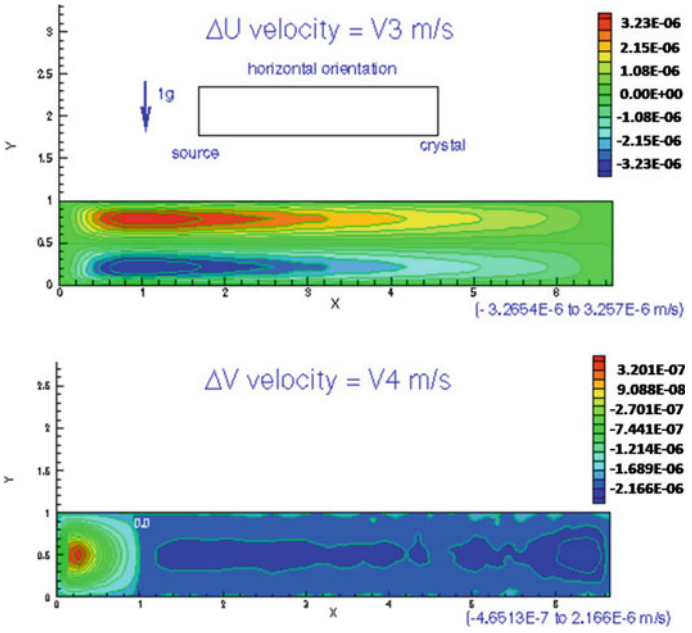

Fig. 8.7 Velocity differences in (0 g_o–0.01 g_o), in m/s, $\alpha = 2.9$ (with variation in T_C)

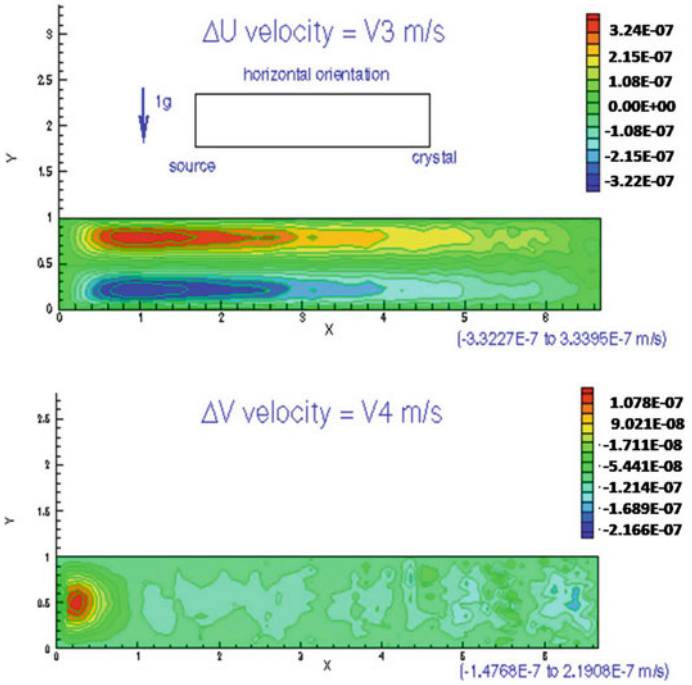

Fig. 8.8 Velocity differences in (0 g_o–0.01 g_o), in m/s, $\alpha = 2.9$ (with variation in T_C)

source) and not due to thermal buoyancy effects. The effect of a temperature profile at the crystal end, $T_C(y)$ is next gauged. A symmetric, quadratic temperature profile with a 2 °C drop in the middle of the crystal is imposed in the calculations. This profile was numerically computed from a thermal model of the system. The crystal face temperature profile is due to the different thermal conductivities of the crystal and the ampoule material. The velocity difference plot is shown in Fig. 8.5. Similar to the earlier plot a $\Delta u \sim 0.3$ mm/s and a $\Delta v \sim 43.7$ μm/s (slightly less than 50 μm/s in Fig. 8.4) are calculated. This marginal reduction is due to the opposing thermal buoyancy in the vicinity of the growing crystal from the imposed crystal temperature profile. A series of g-sensitivity velocity difference plots were generated for successive reductions in the g-level as shown in Fig. 8.6, 8.7 and 8.8 with the range of the calculated velocity shown on the lower right corner of each figure. The value of maximum Δv keeps decreasing to 4.4, 0.47, and 0.15 μm/s for 0 g_o minus 0.1 g_o, 0.01 g_o and 0.001 g_o, respectively. It is noted that in all the calculations herein a temperature profile with a 2 °C drop in the middle is imposed on the crystal, i.e. $T_C = T_C(y)$.

Calculations were also carried out for different g orientations. Figure 8.9 shows the velocity difference plot for the vertically stabilized (maximum temperature above the crystal with g in the positive x direction). Again, the purely diffusive case (0 g_o) calculations are taken as the reference case in calculating the velocity differences.

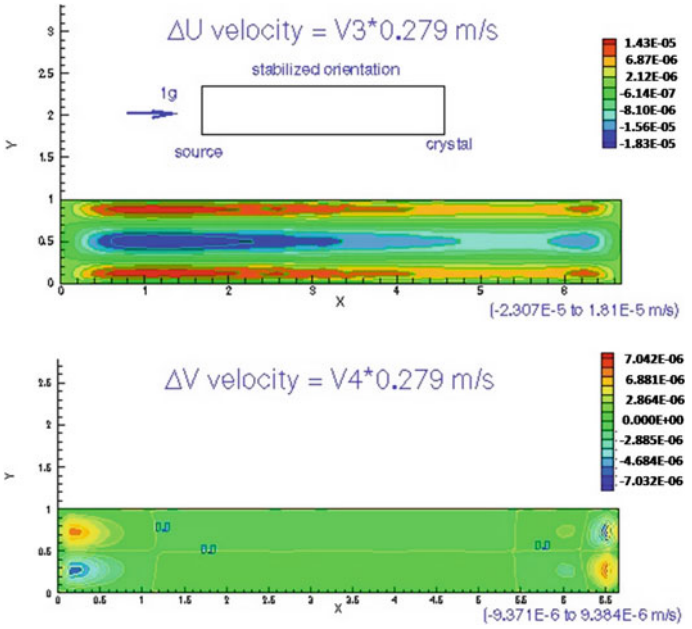

Fig. 8.9 Distribution of velocity differences in vertical stabilized configuration, ΔU (axial) and ΔV (transverse) are the velocity differences between (1 g_o–0 g_o) in m/s ; d = 1.5 cm, L = 10 cm; α = 2.9. (with variation in T_C)

The plot shows Bernard type convective behavior giving rise to symmetric convection rolls going up (towards the source along the axis) and coming down along the side walls of the ampoule. A similar plot for the thermally destabilized orientation of the ampoule to the g-vector shows flows that are reversed from the previous case but the difference in velocities are almost the same, Δu is 18 μm/s and Δv is 9.4 μm/s. So as far as the transverse velocity (v) is concerned both vertically stabilized and destabilized orientations have similar buoyancy effects. A transverse streaming flow of 9.4 μm/s is considerably less than the 50 μm/s flow velocity computed for the horizontal orientation. Similar to the horizontal case, a g-sensitivity plot can be generated from calculations for successively reduced g-levels in the vertical case.

8.4.2 Three-Dimensional Calculations

3-D calculations for the Zn–Se system with residual gas were implemented. A customized multi-physics, time-dependent, code was developed for this purpose [6]. It encompasses the ability to simulate the entire growth furnace, the growth process, conjugate heat transfer of the entire system, dynamic simulation of the macroscopic growth morphology of the crystal, gravitational effects, and the modeling of thermal

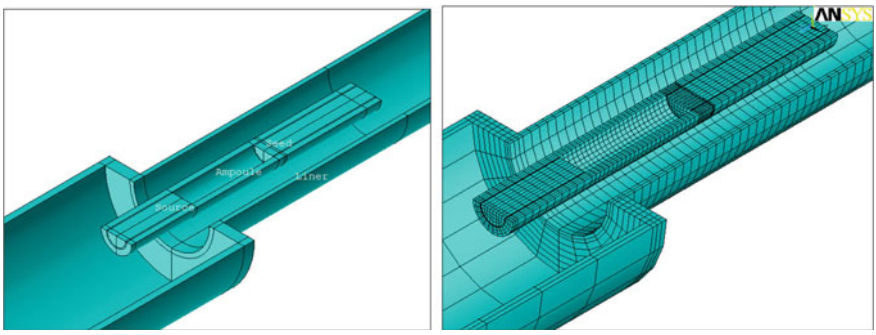

Fig. 8.10 A cut view of the translational furnace, showing the furnace liner and the ampoule which is translated down the furnace and the 3-D mesh for calculations

stresses. Figure 8.10 shows a typical PVT crystal growth furnace geometry and the corresponding 3-D grid used in the simulations. A Monte Carlo technique is used to solve the radiant heat transfer equation for arbitrary, complex enclosures filled with inhomogeneous, participating media. The code is parallelized in order to achieve fast execution times for the thermal solution of complex and evolving 3-D geometries. The code can simulate both 2-D and 3-D geometries and has been validated by comparing

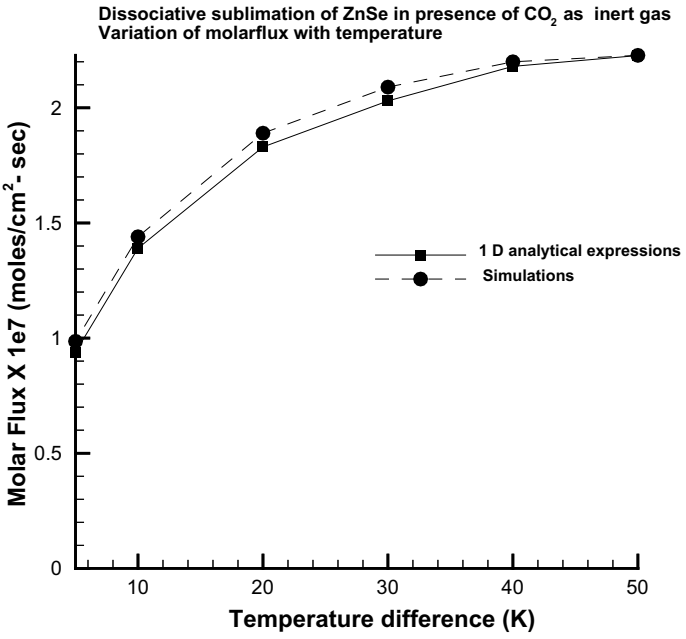

Fig. 8.11 A comparison of mass flux at the growth surface with temperature difference between the source and crystal in presence of an inert gas calculated analytically in Sect. 2.2 and by simulation

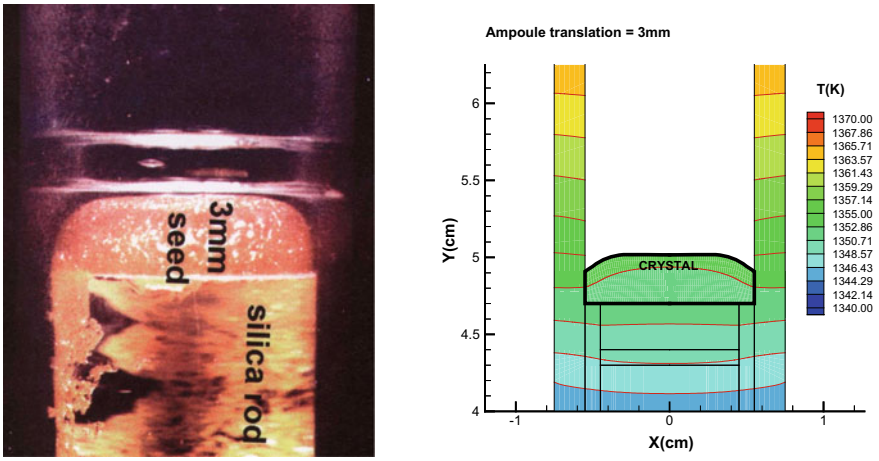

Fig. 8.12 Comparison of the shape of grown crystal with the crystal shape calculated using 2-D simulations

simulation results to those obtained from analytical expressions as shown in Fig. 8.11. A sampling of results for ZnSe growth simulated under the exact growth conditions is compared directly with experimental results and shown in Fig. 8.12 [6–8]. A multi-banded radiation model was used in the simulations and the temperature field was re-calculated periodically as the crystal growth interface evolves, typically 2 h of growth. This evolution from 2-D simulations for a stoichiometry ratio of 2.9 is shown in Fig. 8.13. As can be seen from this figure the crystal is thicker near the center due to viscous and thermal effects that lead to a lower molar flux at the edges. The temperature at the surface of the crystal for the various crystal growth stages shows that crystal is about 1.5 K hotter at the edge than at the center. These two effects together lead to a higher growth rate there and causes the crystal to be thicker near the center. It is noted that the simulation also captures the deformation of the source during the crystal growth process.

The 3-D crystal shape evolution under 1 g_o conditions is shown in Fig. 8.14 [7]. These are essentially the same as those obtained using 2-D calculations—i.e. the crystal is thicker in the center due to the cooler temperatures at the center and the fact that the fluid is slowed down near the edges. The thickness of the crystal in the center at all stages is the same as calculated from the 2-D simulations. The temperature contours (not shown in this figure) show that similar to the results obtained in 2-D, the crystal cools down by 3 K as growth progresses. Similar results were obtained for g orientation parallel and perpendicular to the ampoule axis indicating that the system is dominated by the Stefan diffusive flux and the g effects if any are secondary in nature. Similar to the 2-D results presented earlier, the 0 g velocity field is subtracted from the 1 g_o velocity field to bring out the differences between the two velocity fields. Velocity fields obtained this way are plotted in Fig. 8.15. Iso-contours of the component of the velocity normal to the ampoule axis are shown. As can be seen from this figure the fluid sinks near the source and rises near the seed. The maximum

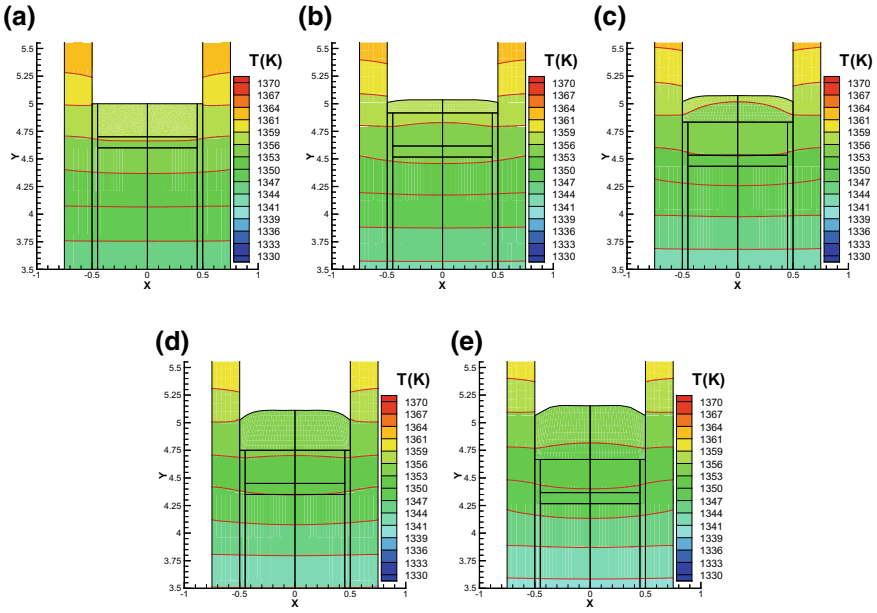

Fig. 8.13 Temperature contours in the growing crystal for case 1 at various stages of crystal growth. **a** t = 0 h, **b** t = 2 h, **c** t = 4 h, **d** t = 6 h and **e** t = 8 h

velocity difference in the velocity component (i.e. in the direction of gravity) of the velocities is ~100 μm/s, similar to what was reported from the 2-D simulations.

8.4.3 Limitations of Mathematical Modeling and Future Developments

In the current formulations the stoichiometry is fixed and not allowed to vary. In principal, any source material with incongruent partial pressure ratio, i.e., $\alpha \neq 2.0$, will keep on changing its stoichiometry when it sublimes. A realistic simulation needs to take into account of the changing of stoichiometry with a specific total source mass and an initial α value. Also, it is important to note that the presence of the non-planar growing crystal surface modifies the thermal profile and, consequently, alters the partial pressure profiles inside the ampoule and should also be considered in the numerical calculations. In practice, a moving and deformable boundary condition poses a serious problem in the mathematical modeling if bulk transport favors growth at a particular point in the ampoule. One important area envisioned in the

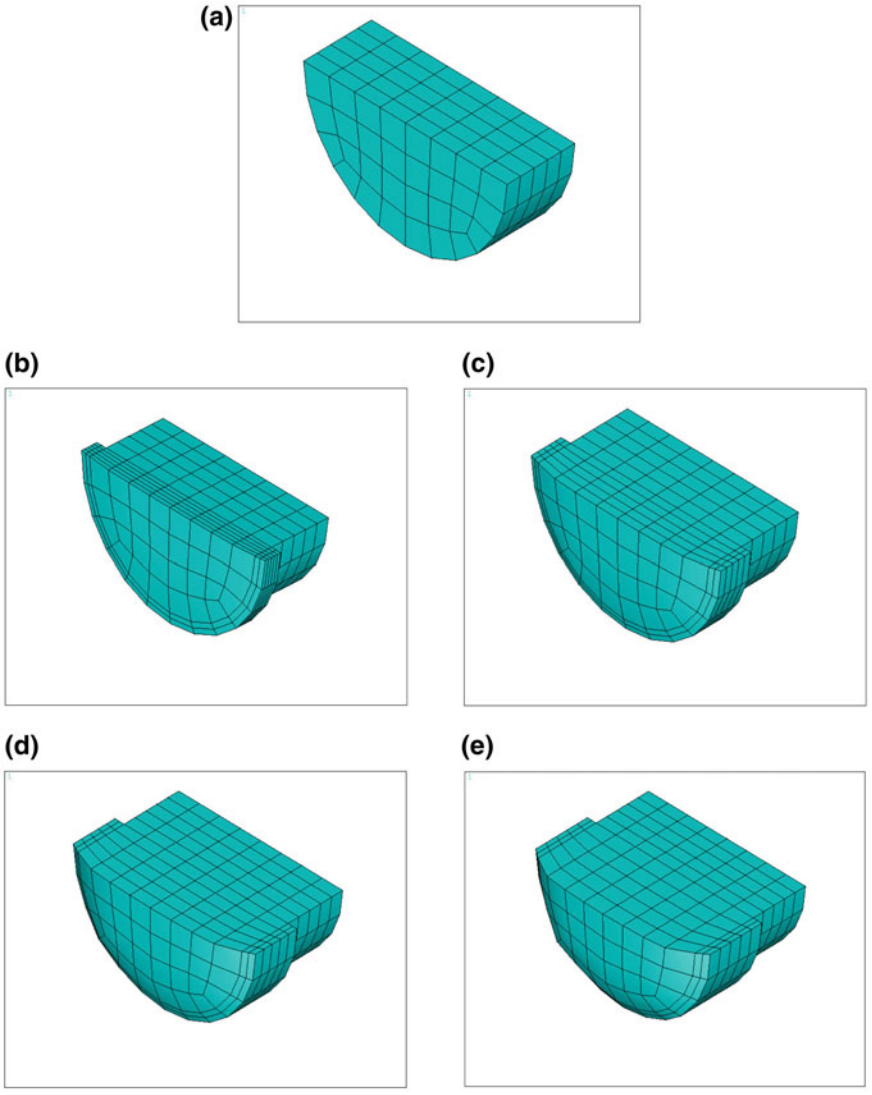

Fig. 8.14 Shape of the crystal calculated by the 3D model at various stages of crystal growth **a** t = 0 h, **b** t = 2 h, **c** t = 4 h, **d** t = 6 h and **e** t = 8 h

future calculations is the simulation of non-planar growth fronts. Finally, the other limitation on the present modeling capabilities is the treatment on the transport and incorporation of the dopant or impurities, such as Al, Cu, Cr, etc.

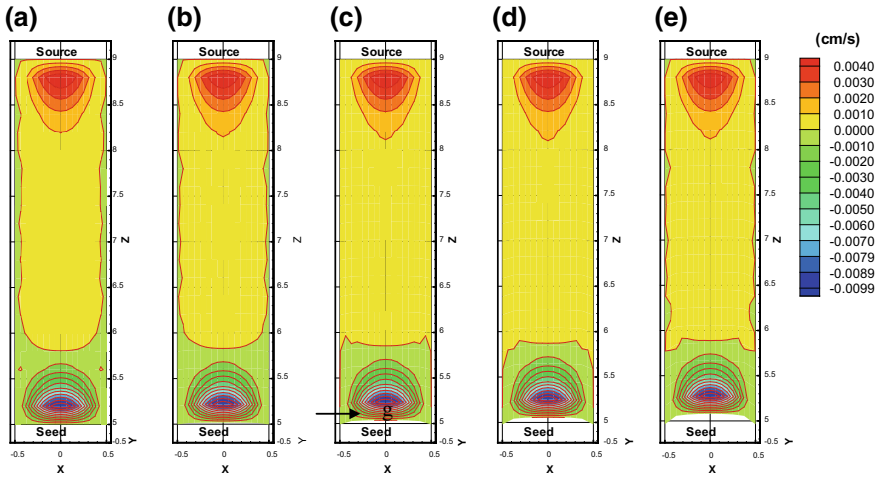

Fig. 8.15 Contours of $\Delta v = V_{1go} - V_{0g}$ (i.e. difference in the transverse velocities for the 1 g_o and 0 g case) plotted at various stages of crystal growth. **a** t = 0 h, **b** t = 2 h, **c** t = 4 h, **d** t = 6 h and **e** t = 8 h

References

1. B.L. Markham, F. Rosenberger, Chem. Eng. Comm. **5**, 287 (1980)
2. D.W. Greenwell, B.L. Markham, F. Rosenberger, J. Cryst. Growth **51**, 413 (1981)
3. D.W. Greenwell, B.L. Markham, F. Rosenberger, J. Cryst. Growth **51**, 426 (1981)
4. A. Nadarajah, F. Rosenberger, J.I.D. Alexander, J. Cryst. Growth **118**, 49 (1992)
5. G.H. Schiroky, F. Rosenberger, Int. J. Heat Mass Transf. **27**, 587 (1984)
6. S. Motakef, et al., Virtual Environment for Design and Analysis of vapor Transport Crystal Growth Processes, Phase II SBIR Final Report, Cape Simulations (2000)
7. N. Ramachandran, A. Worlikar, C.-H. Su, presented at ICCG-13, Kyoto, Japan, July 30–August 4 (2001)
8. N. Ramachandran, C.-H. Su, S.L. Lehoczky, J. Cryst. Growth **208**, 269 (2000)